Technische Universität München

Fakultät für Physik
Lehrstuhl für Struktur der Hadronen und fundamentelle Symmetrien (E18)

Dissertation

Scattering of Ultracold Neutrons in Condensed Deuterium and on Material Surfaces

Stefan DÖGE

aus Leipzig

Vollständiger Abdruck der von der Fakultät für Physik der Technischen Universität München zur Erlangung des akademischen Grades eines

Doktors der Naturwissenschaften (Dr. rer. nat.)

genehmigten Dissertation.

Vorsitzender:	Prof. Dr. Martin Zacharias
Prüfer der Dissertation:	1. Prof. Dr. Stephan Paul
	2. Prof. Dr. Winfried Petry

Die Dissertation wurde am 20.12.2018 bei der Technischen Universität München eingereicht und durch die Fakultät für Physik am 03.05.2019 angenommen.

Abstract

Ultracold neutrons (UCNs) are a versatile tool for fundamental physics experiments, such as the exact determination of the free neutron lifetime or the search for a possible non-zero neutron electric dipole moment.

For several decades, the ultracold neutron facility PF2 (also called "Turbine") at Institut Laue–Langevin, Grenoble, has been providing the highest density of ultracold neutrons worldwide. This density is a crucial parameter in any UCN storage experiment. Nevertheless, the accuracy of most experiments performed at PF2 has been limited by UCN counting statistics, which triggered the development of new UCN converters based on solid deuterium (sD_2) across Europe and North America. Initial simulations and test measurements predicted a significant increase in UCN density compared to PF2. The actual UCN output of these new converters is lower than expected.

This discrepancy can be explained by the scattering of UCNs from rough surfaces and from defects inside the sD_2 crystal. Both were taken into account here quantitatively for the first time in UCN transmission experiments. Within this thesis, a sample container for cryogenic liquids and solids that addresses both these issues was conceived, constructed and tested. With the help of this sample container, the proper preparation of the sample can be verified optically before the neutron measurement is started. Its highly polished silica windows allow for growing a sample with a smooth surface, and thus reduce surface scattering as much a possible. Due to the high rigidity of silica compared to commonly used aluminum windows, the container does not bulge under pressure differentials of 1 to 2 bar.

This sample container was used in the work on this thesis in time-of-flight (TOF) experiments and allowed to measure the total scattering cross sections of liquid and solid deuterium for ultracold neutrons. The new data for liquid deuterium overlap well with a theoretical model that has been published previously. The data on solid deuterium allowed for the first time to estimate the size and concentration of defects inside the crystal. These results will help gain a realistic understanding of the scattering processes inside sD_2-based UCN converters. In addition, ultracold-neutron transmission experiments were performed on various metal foils, which proved conclusively the large effect that rough sample surfaces have on the transmission of ultracold neutrons. The results allow to draw conclusions as to how the mean free path λ_{mfp} of UCNs in solid deuterium can be increased, which may be interesting to the operators of sD_2-based UCN converters and may help to increase their extractable UCN density.

Kurzfassung

Ultrakalte Neutronen (UCNs) sind ein vielseitiges Werkzeug und Objekt physikalischer Grundlagenexperimente, wie zum Beispiel bei der genauen Bestimmung der Lebensdauer freier Neutronen oder der Suche nach einem möglichen elektrischen Dipolmoment des Neutrons verschieden von null.

Während einiger Jahrzehnte hat die PF2-Anlage (auch „Turbine“ genannt) am Institut Laue–Langevin in Grenoble die weltweit höchste UCN-Dichte zur Verfügung gestellt. Diese Dichte ist ein wesentlicher Parameter in allen UCN-Speicherexperimenten. Trotzdem war die Genauigkeit der meisten am PF2 durchgeführten Experimente durch die UCN-zählrate beschränkt, was zur Entwicklung neuer UCN-Konverter auf Grundlage von festem Deuterium (sD_2) in Europa und Nordamerika geführt hat. Anfängliche Simulationen und Testmessungen hatten eine deutliche Steigerung der UCN-Dichte im Vergleich zum PF2 vorhergesagt. Die tatsächliche Abgabe von UCNs aus diesen neuen Konvertern ist niedriger als erwartet.

Diese Abweichung kann durch UCN-Streuung an rauhen Oberflächen und an Defekten im sD_2-Kristall erklärt werden. Beide wurden hier erstmals im Zusammenhang mit UCN-Transmissionsmessungen quantitativ berücksichtigt. Im Rahmen dieser Arbeit wurde ein Probenbehälter für kryogene Flüssigkeiten und Feststoffe entworfen, gebaut und getestet, welcher die Lösung beider Probleme ermöglicht. Mit Hilfe dieses Probenbehälters kann die ordnungsgemäße Präparation der Probe vor Beginn der Neutronenmessung optisch überprüft werden. Seine hochglanzpolierten Silicafenster ermöglichen es, Proben mit glatten Oberflächen zu ziehen und so die Oberflächenstreuung so weit wie möglich zu reduzieren. Aufgrund der hohen Steifigkeit von Silica im Vergleich zu herkömmlichen Aluminiumfenstern wölbt sich der Behälter bei Druckdifferenzen von 1 bis 2 bar nicht.

Dieser Probenbehälter wurde im Rahmen dieser Arbeit in Flugzeitexperimenten (TOF) verwendet und ermöglichte die Messung der Gesamtstreuquerschnitte von flüssigem und festem Deuterium für ultrakalte Neutronen. Die neuen Daten für flüssiges Deuterium stimmen gut mit einem früher publizierten theoretischen Modell überein. Die Daten für festes Deuterium erlaubten es erstmals, die Größe und Konzentration von Defekten im Inneren des Kristalls abzuschätzen. Diese Ergebnisse werden dazu beitragen, eine realistische Vorstellung der Streuprozesse im Innern von UCN-Konvertern auf Basis von sD_2 zu entwickeln. Darüber hinaus wurden Transmissionsexperimente mit ultrakalten Neutronen an verschiedenen Metallfolien durchgeführt, die den großen Einfluss rauher Probenoberflächen auf die Transmissivität ultrakalter Neutronen eindeutig belegt haben. Die Ergebnisse lassen

Rückschlüsse darauf zu, wie die mittlere freie Weglänge λ_{mfp} von UCNs in festem Deuterium erhöht werden kann. Das kann für die Betreiber von UCN-Konvertern auf Basis von sD_2 interessant sein und kann helfen, die aus ihnen extrahierbare UCN-Dichte zu erhöhen.

Résumé

Les neutrons ultrafroids (UCN) sont un outil polyvalent pour les expériences de physique fondamentale, telles que la détermination exacte de la durée de vie des neutrons libres ou la recherche d'un moment dipolaire électrique de neutrons non nul possible.

Depuis plusieurs décennies, l'installation de neutrons ultrafroids PF2 (également appelée « Turbine ») de l'Institut Laue-Langevin, Grenoble, a fourni la plus forte densité de neutrons ultrafroids au monde. Cette densité est un paramètre crucial dans toute expérience de stockage UCN. Néanmoins, la précision de la plupart des expériences réalisées à PF2 a été limitée par le taux de comptage de UCN, qui a déclenché le développement de nouveaux convertisseurs UCN sur la base du deutérium solide (sD_2) en Europe et en Amérique du Nord. Les simulations initiales et les expériences d'essai ont prédit une augmentation significative de la densité UCN par rapport au PF2. La sortie UCN réelle de ces nouveaux convertisseurs est inférieure aux prévisions.

Cet écart peut s'expliquer par la diffusion des UCNs à partir de surfaces rugueuses et de défauts à l'intérieur du cristal sD_2. Ici, ces deux éléments ont été pris en compte en termes quantitatifs pour la première fois dans les expériences de transmission de l'UCN. Dans le cadre de cette thèse, on a conçu, construit et testé un récipient d'échantillon pour des liquides et solides cryogéniques qui traite de ces deux questions. A l'aide de ce récipient d'échantillon, la préparation correcte de l'échantillon peut être vérifiée optiquement avant le début de la mesure utilisant des neutrons. Ses fenêtres en silice hautement polies permettent de faire croître un échantillon avec une surface lisse et donc de réduire autant que possible la diffusion en surface. En raison de la grande rigidité de la silice par rapport aux fenêtres en aluminium couramment utilisées, le récipient ne gonfle pas sous des différentiels de pression de 1 à 2 bar.

Ce récipient d'échantillon a été utilisé dans le cadre de cette thèse pour des expériences de temps de vol (TOF) et a permis de mesurer les sections efficaces du deutérium liquide et solide pour la diffusion des neutrons ultra-froids. Les nouvelles données sur le deutérium liquide recoupent bien un modèle théorique qui avait été publié précédemment. Les données sur le deutérium solide ont permis d'estimer, pour la première fois, la taille et la concentration des défauts à l'intérieur du cristal. Ces résultats aideront à acquérir une compréhension réaliste des processus de diffusion à l'intérieur des convertisseurs UCN utilisant du sD_2. De plus, des expériences de transmission de neutrons ultra-froids ont été effectuées sur diver-

ses feuilles métalliques, ce qui a prouvé de façon concluante l'effet important des surfaces rugueuses des échantillons sur la transmission des neutrons ultra-froids. Les résultats permettent de tirer des conclusions sur la manière d'augmenter le libre parcours moyen λ_{mfp} des UCNs dans le deutérium solide, ce qui peut être intéressant pour les opérateurs de convertisseurs UCN à base de sD_2 et peut aider à augmenter leur densité UCN extractible.

Аннотация

Ультрахолодные нейтроны (УХН, UCN) являются широко применяемым средством для проведения экспериментов в различных областях фундаментальной физики, таких как точное определение времени жизни свободного нейтрона или поиск возможного ненулевого электрического дипольного момента нейтрона.

В течение нескольких десятилетий установка PF2 (также называемая « Турбина ») в Институте Лауэ-Ланжевена, Гренобль, имела самую высокую плотность выхода УХН во всем мире. Эта плотность является ключевым параметром в любом эксперименте по хранению УХН. Тем не менее, точность большинства экспериментов, проведенных на PF2, была ограничена скоростью счета УХН, что привело к разработке новых конвертеров УХН на основе твердого дейтерия (sD_2) в Европе и Северной Америке. Первоначальное моделирование и тестовые измерения предсказали значительное увеличение плотности УХН по сравнению с PF2. Фактический выход УХН из этих новых конвертеров ниже, чем ожидалось.

Это расхождение может объясняться рассеянием УХН на шероховатостях поверхностей и рассеянием на дефектах внутри дейтериевого кристалла. В данной работе, при проведении экспериментов по пропусканию УХН, оба явления впервые учтены количественно. Для этого, в рамках работы над настоящей диссертацией, был разработан, сконструирован и испытан специальный контейнер для крио-жидкостей и кристаллов, позволяющий учитывать оба описанные выше явления. С помощью изготовленного контейнера можно оптически контролировать правильность подготовки образца до начала измерений с нейтронами. Окна контейнера выполнены из высоко полированного кварцевого стекла, что позволяет вырастить образец с гладкими поверхностями, существенно снижающими рассеяние нейтронов на шероховатостях. Вследствие высокой жесткости кварцевых окон по сравнению с широко применяемыми окнами из алюминия, контейнер не изгибается при перепадах давления от 1 до 2 бар.

В рамках настоящей диссертации использование этого контейнера в нейтронных измерениях, проведенных по методике времени пролета (TOF), позволило экспериментально измерить полное сечение рассеяния жидкого и твердого дейтерия для ультрахолодных нейтронов. Новые экспериментальные результаты для жидкого дейтерия хорошо согласуются с результатами, полученными для теоретической модели, опубликованной ранее. Экспериментальные данные по

твердому дейтерию позволили оценить размеры и концентрацию дефектов внутри кристалла. Полученные результаты внесут вклад в понимание реальных процессов рассеяния внутри источников УХН на основе твердого дейтерия. В дополнение, в работе проведены эксперименты по пропусканию УХН через различные металлические фольги, результаты которых окончательно подтвердили существенное влияние шероховатостей поверхности на пропускание УХН. Полученные результаты позволяют сформулировать требования для увеличения длины свободного пробега λ_{mfp} УХН в твердом дейтерии, что в свою очередь будет полезно для управляющих таких источников УХН, поскольку приведет к увеличению плотности извлекаемых ультрахолодных нейтронов.

Contents

List of Tables

List of Figures

Introduction and Motivation

A variety of particle physics experiments rely on ultracold neutrons (UCN), i.e. very slow neutrons with a kinetic energy of less than a few hundred nano-electronvolts. Neutrons have no electric charge and therefore interact only weakly with matter when they pass through. Neutrons with an energy of a few milli-electronvolts easily go through slabs of most metals and concrete, for example. If neutrons are slowed down to very low energies – in the range of a few hundred nano-electronvolts – they can no longer penetrate matter that has a neutron-optical potential higher than the neutron's kinetic energy. This effect entails that ultracold neutrons can be retained in material bottles as long as their kinetic energy perpendicular to the bottle wall is less than the wall material's neutron-optical potential. Certain materials with high potentials, e.g. nickel and fluorinated hydrocarbons, are used as surface coatings on the inside of bottles to store neutrons of higher kinetic energies.

The idea of storing ultracold neutrons in bottles was discussed informally and without much avail in the reactor physics community of the early days. Bruno Pontecorvo claimed[1] that Enrico Fermi was the first to have had the idea of storable neutrons: Enrico Fermi, Emilio Segrè and Bruno Pontecorvo were going home after work on a rainy day. Segrè jumped over a puddle when a drop of water fell off the sole of his shoe and dropped into the puddle. Waves on the puddle's surface emanated from the drop and they were reflected off the brink of the puddle. Looking on as the waves reverberated back and forth, to Fermi's mind came the idea that neutrons, which can also be described as material waves, can be stored in a bottle.

The first documented report of the idea, including rough estimates of the UCN density and possible materials for the bottle, was published by Yakov Borisovich Zel'dovich, member of the Russian Academy of Sciences, in 1959 [1]. It was about a decade later, in 1968, that ultracold neutrons were experimentally observed for the first time by the group of Fyodor L'vovich Shapiro in Dubna (Russia) [2, 3] and by Albert Steyerl in Munich (Germany) [4].

Since then, ultracold neutrons have been used in experiments measuring the lifetime of the free neutron [5], verifying the zero electrical dipole moment of the neutron [6, 7], bound states of the free neutron in the Earth's gravitational field [8, 9, 10], fundamental neutron optics [11, 12, 13], and others. What is common

[1] Alexander Vladimirovich Strelkov (Joint Institute of Nuclear Research, Dubna, Russia), priv. comm.

to all these experiments is the limited accuracy due to the feeble flux of ultracold neutrons. As the statistical error σ_{stat} is related to the number of neutrons N used in a measurement by $\sigma_{\text{stat}} \propto 1/\sqrt{N}$, it could be substantially reduced if the UCN flux to these experiments was one to two orders of magnitude higher than at the moment.

Recently, a comparison [14] of most UCN sources in operation has been made and found the mechanical "Turbine" [15, 16] (UCN and VCN facility PF2) at the research reactor Institut Laue–Langevin (ILL) in Grenoble (France) to be the forerunner in terms of UCN density (≈ 20 UCN/cm^3) issuing from a continuously operating source. Strictly speaking, the Turbine is not a source of UCN, because it acts collectively on all neutrons and thus, according to Liouville's theorem, does not increase the phase-space density in the UCN region compared to the Maxwell–Boltzmann spectrum of neutrons issuing from the cold source (liquid deuterium reservoir) [15]. The UCN source at the Paul Scherrer Institut (PSI) in Villigen (Switzerland) [17] has an UCN density slightly higher than that of the Turbine, but is coupled to a spallation neutron source and produces UCNs in pulses.

For years, research has been ongoing to develop UCN sources based on solid deuterium (sD_2), the source at PSI being one of them. Originally, sD_2-based sources were supposed to surpass the UCN density of the Turbine by about two orders of magnitude [18, 19]. However, tests showed that they perform equally well at best. One likely reason is the formation of defects in the deuterium converter crystals [20, 21].

It is the aim of this PhD thesis to quantify the size and concentration of these defects, their dependence on temperature, and additional effects that drastically reduce the density of UCNs that is extractable from sD_2-based sources. The Incoherent Approximation (IA) for the calculation of 1-phonon up-scattering of UCNs is revisited and corrections for strongly coherently scattering isotopes, such as deuterium, are presented. Over the course of this work it became apparent that UCN scattering on rough surfaces introduces large errors to experimental results. Therefore, UCN scattering on metal foils is treated theoretically and experimental results are presented in this thesis.

Part I

Theoretical Basics

1 Properties of the Neutron, Neutron Scattering, and Ultracold Neutrons

Protons give an atom its identity, electrons its personality.
— Bill Bryson, *A Short History of Nearly Everything*

Neutrons are electrically uncharged subatomic particles, hence their name. First published by Harkins [22], the term "neutron" has been used since 1921 for an electrically neutral constituent of atomic nuclei that had only been postulated at the time by Ernest Rutherford. Bothe and Becker were the first to observe free neutrons experimentally [23], but did not recognize them as a new type of radiation. James Chadwick was the first to correctly interpret them as moving particles with about the same mass as protons [24, 25]. In the Standard Model of physics, neutrons are classified as hadrons (subgroup baryons) as they consist of three quarks that are held together by the strong nuclear force. These three quarks (one up-quark – charge $+2/3$, two down-quarks – charge $-1/3$) are responsible for the zero electric charge of the neutron. Its spin is $1/2$ and so it belongs to the fermions.

Louis de Broglie wrote in his 1924 doctoral thesis on wave mechanics [26, 27]

> "Certes, cette idée que le mouvement d'un point matériel dissimule toujours la propagation d'une onde, aurait besoin d'être étudiée et complétée, mais, si l'on parvenait à lui donner une forme entièrement satisfaisante, elle représenterait une synthèse d'une grand beauté rationnelle."[1]

Next to the early work on black-body radiation by Planck and the photo-electric effect by Einstein and Millikan, this was the origin of the idea of wave–particle duality. The behavior of any sufficiently light particle can in part be described by wave equations, especially its interference and scattering. De Broglie postulated this effect for electrons, which was proven experimentally by Davisson and Germer in 1927 [28]. In the meantime it has been shown to be true also for protons,

[1] Admittedly, this idea that the movement of a material point always conceals the propagation of a wave, would need to be studied and completed, but if one succeeded in giving it a fully satisfactory form, it would represent a synthesis of great rational beauty.

neutrons [29, 30], and even macroscopic objects like C_{60} fullerene molecules [31, 32] and porphyrin derivates with an atomic mass exceeding 10 000 g/mole [33].

As a consequence, all non-relativistic particles can be assigned a de Broglie wavelength λ

$$\lambda = \frac{h}{p},\ p = |\mathbf{p}|, \tag{1.1}$$

where $h = 2\pi\hbar$ is the Planck constant and p is the scalar value of the particle's momentum $\mathbf{p}$. The momentum vector of a neutron is given by $\mathbf{p} = m_\mathrm{n}\mathbf{v}$, where $\mathbf{v}$ denotes the neutron's velocity vector. The wave vector $\mathbf{k}$ of a neutron is related to its momentum by $\mathbf{p} = \hbar\mathbf{k}$. The change of momentum in a scattering process, i.e. the momentum transfer, is usually denoted by $\mathbf{q} = \mathbf{k}' - \mathbf{k}$. The aforementioned quantities are interrelated by the following equations

$$\lambda_\mathrm{n} = \frac{2\pi}{k} = \frac{h}{p_\mathrm{n}} = \frac{2\pi\hbar}{m_\mathrm{n} v} \text{ and} \tag{1.2}$$

$$E_\mathrm{kin} = k_\mathrm{B}\, T_\mathrm{n} = \frac{1}{2} m_\mathrm{n}\, v^2 = \frac{\hbar^2\, k^2}{2\, m_\mathrm{n}}, \tag{1.3}$$

where E_kin denotes the neutron's kinetic energy, T_n its temperature, and $m_\mathrm{n} = 1.6749 \times 10^{-27}\,\mathrm{kg}$ its mass. A handy overview of conversions from one physical quantity of the neutron to another in common units is given in Tab. 1.1. Fig. 1.1 shows their relations graphically.

Phys. Qty [Unit]	**Kinetic Energy E_kin [meV]**	**Wavelength λ [Å]**	**Wave vector k [Å^{-1}]**	**Velocity v [m/s]**	**Temp. T [K]**
$E_\mathrm{kin} =$	—	$81.776/\lambda^2$	$2.071\, k^2$	$5.225 \times 10^{-6}\, v^2$	$8.617 \times 10^{-2}\, T$
$\lambda =$	$9.043/\sqrt{E}$	—	$2\pi/k$	$3956/v$	$30.81/\sqrt{T}$
$k =$	$0.695\,\sqrt{E}$	$2\pi/\lambda$	—	$1.588 \times 10^{-3}\, v$	$0.2040\,\sqrt{T}$
$v =$	$437.4\,\sqrt{E}$	$3956/\lambda$	$629.7\, k$	—	$128.4\,\sqrt{T}$
$T =$	$11.60\, E$	$949.0/\lambda^2$	$24.03\, k^2$	$6.066 \times 10^{-5}\, v^2$	—

Table 1.1: Conversion factors frequently used in neutron scattering as functions of neutron kinetic energy, wavelength, wave vector, velocity, and temperature using typical dimensions for cold neutron scattering.

1.1 Creation and moderation of free neutrons

On Earth, neutrons are normally bound inside atomic nuclei. However, as a result of spontaneous nuclear decay or nuclear reactions – e.g. the absorption of an

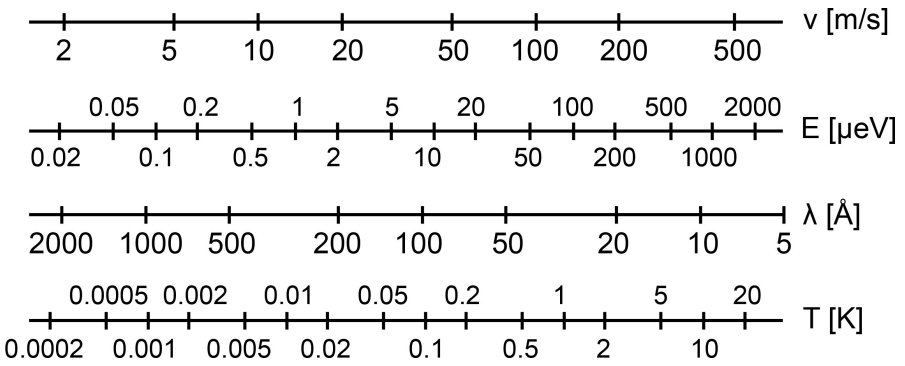

Figure 1.1: Direct comparison of the neutron's velocity v with its corresponding kinetic energy E_{kin}, wavelength λ and temperature T.

α-particle by a light nucleus and the subsequent release of a neutron (α,n), the impact of a very fast proton on a heavy nucleus, or a neutron-induced nuclear fission reaction (n,f) – they can be released from nuclei. Free neutrons interact with matter through the strong nuclear and electromagnetic forces. They are also subject to gravity, which plays an important role in the case of slow neutrons. Free neutrons are unstable. Their β-decay is governed by the weak force.

Before the discovery of neutron-induced nuclear fission, free neutrons were produced by (α,n) nuclear reactions [30, 34]. A widespread routine [35] at that time was the irradiation of beryllium-9 with α-particles from the decay of radium-226,

$$^{9}_{4}\mathrm{Be} + ^{4}_{2}\mathrm{He} \rightarrow ^{12}_{6}\mathrm{C} + n + 13.2\,\mathrm{MeV}. \tag{1.4}$$

With the advent of the world's first nuclear reactor, Chicago Pile-1, and dedicated research reactors, such as FRM-I in Munich and the ILL reactor in Grenoble, a whole new field of research was opened up. Neutron fluxes from reactors are many orders of magnitude higher than those from (α,n) sources and also have a lower background of γ rays. Some isotopes of heavy elements, such as uranium-235 and plutonium-239, can be efficiently fissioned by thermal neutrons, e.g. as follows

$$n + ^{235}_{92}\mathrm{U} \rightarrow ^{236}_{92}\mathrm{U}^{*} \rightarrow ^{144}_{56}\mathrm{Ba} + ^{89}_{36}\mathrm{Kr} + 3n + 177\,\mathrm{MeV}. \tag{1.5}$$

Usually, these fission reactions are more likely to happen the slower the neutrons are.

When neutrons are released as a result of such a fission reaction, they have energies of a few mega-electronvolts (MeV) and are called fast or fission neutrons. After passing through a moderator at room temperature, usually light or heavy water, they retain a kinetic energy E_{kin} of around 25 milli-electronvolts (meV) and are called thermal neutrons (ThN).

In each collision with a water molecule (mostly with its hydrogen atoms), the neutron transfers some kinetic energy to the water molecule. This process is called

thermalization and ends when the neutron spectrum has adopted the same mean temperature $T = E_{\mathrm{kin}}/k_{\mathrm{B}}$ as the moderating agent. The transfer of energy $\Delta E = E_{\mathrm{initial}} - E_{\mathrm{final}}$ depends on the standard atomic weight A of the moderating nuclei. The mean logarithmic energy loss ξ of the neutron is constant and can be calculated as follows [36]

$$\xi = \overline{\ln \frac{E_{\mathrm{initial}}}{E_{\mathrm{final}}}} = 1 + \frac{(A-1)^2}{2A} \ln\left(\frac{A-1}{A+1}\right). \tag{1.6}$$

It takes n collisions to slow down the neutron from its initial energy $E_{\mathrm{initial}} = 2\,\mathrm{MeV}$ to the final (thermal) energy $E_{\mathrm{final}} = 25\,\mathrm{meV}$, where

$$n = \frac{\ln\left(\frac{E_{\mathrm{fast}}}{E_{\mathrm{thermal}}}\right)}{\xi}. \tag{1.7}$$

In light water, the fast neutron needs to undergo 18 collisions, in heavy water 25 to reach E_{final}. Further slowing down is achieved by passing thermal neutrons through a volume of liquid deuterium, which they leave as cold neutrons (CN) with about 1.5 meV. The cooling-down mechanism in this step is the same as described above.

Any delineation of above-mentioned neutron energy classes must be arbitrary to a certain degree due the Maxwell–Boltzmann velocity distribution of neutrons that are fully thermalized with the moderating medium. One possible energy classification of neutrons was given by Furrer et al. [37].

The wavelengths of thermal and cold neutrons are a few Ångströms and correspond to interatomic distances in liquids and solids of all sorts, and their kinetic energy is in the range of elementary excitations like phonons, rotons, and magnons. This makes these neutrons perfect probes for investigating the structure and dynamics of a wide range of materials in the field of condensed matter, magnetism and superconductors, biology, and materials science.

Fig. 1.2 shows the velocity-dependent flux $\phi(v)$ of thermal and cold neutron spectra with their respective mean temperatures T_0 and T_{c}. $\phi(v) = N(v) \times v$, with $N(v)$ the Maxwell–Boltzmann velocity distribution

$$N(v) = N_0 \left(\frac{m}{2\pi k_{\mathrm{B}} T}\right)^{3/2} 4\pi v^2 \mathrm{e}^{-\frac{mv^2}{2k_{\mathrm{B}}T}}. \tag{1.8}$$

The red circle in Fig. 1.2 marks roughly the UCN energy region and demonstrates that UCNs are present at low densities in both the ThN and CN spectra. It illustrates also the significantly higher UCN density in a cold compared with a thermal neutron spectrum. In the experiments that first observed UCNs, they were extracted from a thermal neutron spectrum through a bent horizontal guide [2] and a bent vertical guide [4].

The following gain factor G [38] gives the gain in UCN density for cooling the neutron spectrum from room temperature (thermal neutrons, $T_0 = 300\,\mathrm{K}$) to liquid

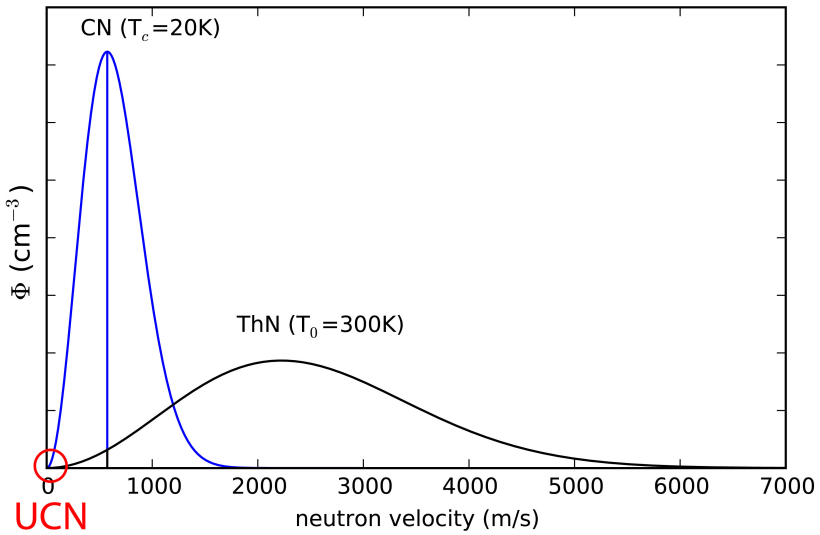

Figure 1.2: The neutron flux density $\phi(v)$ is plotted over neutron velocity v for thermal (ThN) and cold neutrons (CN) in thermal equilibrium with their respective moderators at temperatures T_0 and T_c. The spectrum takes the form of a Maxwell–Boltzmann distribution. In both spectra UCNs are present, but it is obvious that they are much more abundant in the cold neutron spectrum.

deuterium temperature (cold neutrons, $T_c = 20\,\mathrm{K}$)

$$G \simeq e^{-1} \left(\frac{T_0}{T_c}\right)^{3/2} \approx 20. \tag{1.9}$$

Due to Liouville's theorem, the UCN density in the moderator puts an effective limit on the UCN density extractable from UCN sources for experiments. Conversion methods using non-conservative forces can circumvent this limitation, see Section 1.3.

At the Institut Laue–Langevin, neutrons from one of the cold sources are guided vertically inside a bent beam guide. Neutrons that are too fast leave the bent guide through its wall. Slower neutrons, called very cold neutrons (VCN), fulfill the total-reflection condition and are extracted at the top end of the bent guide. A part of these neutrons is fed into the so-called "ultracold-neutron Turbine" [15, 16, 39, 40], which constitutes the instrument PF2 (physique fondamentale 2) at ILL. It consists of a paddlewheel featuring smooth nickel–copper composite replica blades. The wheel rotates at 250 rotations per minute, see Section 4.10, and takes advantage of the Doppler shift to slow VCNs down to ultracold neutrons (UCN) with an energy of less than 2000 neV. The Turbine's blades exert a conservative force on the incoming VCNs. It follows from Liouville's theorem that the phase-space density is conserved and, therefore, the final UCN density extractable from the Turbine

cannot be increased above that which is present in the primary source of CN – the deuterium moderator. Ignatovich [41, 42] described the theory of UCN moderation in detail and is recommended for further reading.

1.2 Properties of UCNs

The idea that neutrons below a certain velocity have additional properties compared to faster neutrons, especially total reflection from surfaces under any angle of incidence, was first published by Zel'dovich [1]. He estimated the attainable UCN density from a reactor neutron flux of $10^{12}\,(\mathrm{cm^2 s})^{-1}$ moderated in a tank of 1 $\mathrm{m^3}$ of liquid ^{4}He and graphite walls to be 50 UCN/$\mathrm{cm^3}$.

The interaction of UCNs with a single bound nucleus can be described by the Schrödinger equation,

$$-\frac{\hbar^2}{2m_\mathrm{n}}\nabla^2\Psi(\mathbf{r}) = \left[U_\mathrm{Fermi}(\mathbf{r}) - E_\mathrm{kin}(\mathbf{r})\right]\Psi(\mathbf{r}), \tag{1.10}$$

where m_n is the neutron mass, $\mathbf{r}$ is the position of the nucleus, E_kin is the neutron's kinetic energy, $\Psi(\mathbf{r})$ is the neutron wave function, and

$$U_\mathrm{Fermi}(\mathbf{r}) = \frac{\hbar^2}{2m_\mathrm{n}} 4\pi b_{\mathrm{coh},i}\,\delta^3(\mathbf{r}-\mathbf{r}_i) \tag{1.11}$$

is the Fermi pseudo-potential that solves the Schrödinger equation in the first Born approximation. For a detailed derivation of this potential the reader is referred to the books of Ignatovich [41, 42] and Golub [43].

UCNs have a wavelength of the order of 800 Å, which corresponds to about $800\text{Å}/\sqrt[3]{N_\mathrm{V}^{-1}} \approx 800\text{Å}/\sqrt[3]{(3\times10^{22}\mathrm{cm^{-3}})^{-1}} \approx 250$ intermolecular distances in solid deuterium and most other materials. An UCN thus does not interact with individual nuclei, but rather with the average of a large ensemble. If the Fermi pseudo-potential is averaged over all nuclei in a sample, one obtains the neutron-optical potential[2], also called the scattering potential, see Eq. 1.12. In the case of more than one isotope of an element being present in the sample, their bound coherent scattering lengths b_coh have to be weighted according to their concentrations, $\overline{b_\mathrm{coh}} = \sum_i b_{\mathrm{coh},i} N_{\mathrm{V},i}/N_\mathrm{V}$.

$$U_\mathrm{opt} = \frac{\hbar^2}{2m_\mathrm{n}} 4\pi N_\mathrm{V} b_\mathrm{coh}, \tag{1.12}$$

where m_n is the neutron mass, N_V is the number of particles per unit volume and b_coh is the bound coherent scattering length of one nucleus of the respective element. This equation is in a strict sense only true for media in which UCNs

[2] Even though it is not correct in a strict sense, this quantity is also called "Fermi potential" in many publications.

cannot be lost. Total reflection from material walls occurs for neutrons with a kinetic energy component in the z-direction $E_{\mathrm{kin},z} < U_{\mathrm{opt}}$. Tab. 1.2 gives neutron-optical potentials for the most relevant substances used in this work, calculated using Equation 1.12 and values from Sears [44] for the bound coherent scattering lengths. An experimental value for U_{opt} of solid deuterium was provided by Altarev et al. [45] and the molecular densities of deuterium and hydrogen at various temperatures were taken from Souers [46].

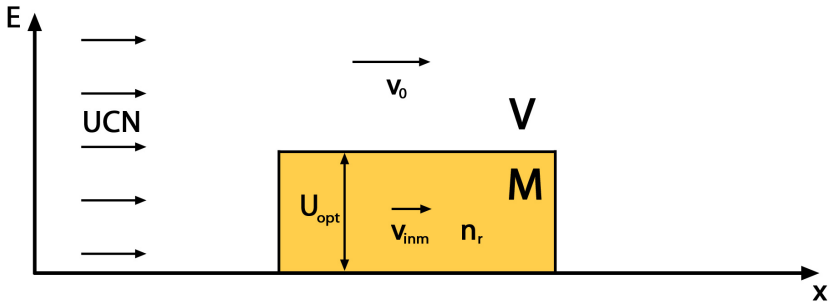

Figure 1.3: UCNs with a vacuum velocity, i.e. out-of-medium velocity v_0, entering from vacuum (V) into matter (M) with the following associated quantities: in-medium velocity v_{inm}, index of refraction n_{r}, neutron-optical potential (of the medium M) U_{opt} compared to the kinectic energy of the neutron E, plotted over distance x.

The neutron-optical potential can be separated into a real part V, which describes UCN scattering, and an imaginary part iW, which describes UCN loss by absorption or energy gain (up-scattering),

$$U_{\mathrm{opt}} = V - iW. \tag{1.13}$$

Associated to both parts is the probability of an UCN being lost (loss per bounce)

$$f = \frac{W}{V} = \frac{(\sigma_{\mathrm{abs}} + \sigma_{\mathrm{up\text{-}scatt}}^{\mathrm{1\text{-}ph}})k}{4\pi(b_{\mathrm{coh}} + b_{\mathrm{inc}})}. \tag{1.14}$$

Fermi deduced from theory that matter must have an index of refraction for neutrons and observed it experimentally together with Zinn [47]. For matter, the index of refraction for neutrons is given by

$$n_{\mathrm{r}} = \frac{k'}{k_0} = \frac{v_{\mathrm{inm}}}{v_0} = \sqrt{1 - \frac{N_{\mathrm{v}} b_{\mathrm{coh}} \lambda_n^2}{\pi}} \tag{1.15}$$

where N_{v} is the particle number density, b_{coh} the coherent scattering length of each particle, and λ_{n} is the neutron wavelength. The UCN velocity in medium and in vacuum is given by v_{inm} and v_0, where

$$v_{\mathrm{inm}} = \sqrt{v_0^2 - v_{\mathrm{crit}}^2}. \tag{1.16}$$

The associated wave vectors for neutrons in medium and out of medium are k' and k_0, respectively. Fig. 1.3 illustrates the out-of-medium and in-medium quantities connected with UCNs.

The critical velocity v_{crit} of a material with atomic particle density N_{V} and bound coherent scattering length b_{coh} arises directly as a result of the relation $U_{\mathrm{opt}} = m_{\mathrm{n}} v_{\mathrm{crit}}^2/2$

$$v_{\mathrm{crit}} = \frac{2\hbar}{m_{\mathrm{n}}}\sqrt{\pi N_{\mathrm{V}} b_{\mathrm{coh}}}. \tag{1.17}$$

Substance	**Bound Coh. Scat. Length b_{coh} [fm]**	**Volum. Particle Density N_{V} [cm^{-3}]**	U_{opt} **[neV]**	v_{crit} **[m/s]**
D_2 (solid)	6.671 (per atom)	3.021×10^{22} at 5 K	105.0	4.48
		exp. at 5 K [45]	99 ± 7	4.4±0.2
		3.016×10^{22} at 10 K	104.8	4.48
		2.998×10^{22} at 14 K	104.2	4.46
		2.990×10^{22} at 15 K	103.9	4.46
		2.956×10^{22} at 18 K	102.7	4.43
D_2 (liquid)	6.671 (per atom)	2.593×10^{22} at 19.0 K	90.1	4.15
		2.546×10^{22} at 20.6 K	88.5	4.11
		2.501×10^{22} at 22.0 K	86.9	4.08
		2.468×10^{22} at 23.0 K	85.7	4.05
H_2 (solid)	-3.7406 (per atom)	2.611×10^{22} at 5.0 K	-50.9	$3.12i$
		2.607×10^{22} at 9.0 K	-50.8	$3.12i$
SiO_2 (amorphous)	15.755 (per SiO_2 unit)	2.209×10^{22} at 10 K	90.6	4.16
		2.208×10^{22} at RT	90.6	4.16
Be	7.79	12.35×10^{22} at RT	250.5	6.92
Al	3.449	6.026×10^{22} at RT	54.1	3.22
Cu	7.718	8.45×10^{22} at RT	169.2	5.69
Zr	7.16	4.29×10^{22} at RT	80.0	3.91
Fe	9.45	8.492×10^{23} at RT	209.0	6.32
Ni (nat.)	10.3	9.140×10^{22} at RT	245.1	6.85
^{58}Ni	14.4	9.140×10^{22} at RT	342.7	8.10
Fomblin®[3]			106	4.50

Table 1.2: Neutron-optical potentials for selected materials [44]. RT signifies room temperature.

1.3 Superthermal UCN sources

The naming convention for ultracold neutrons follows that for faster neutrons: hot neutrons are in thermal equilibrium with a hot moderator (graphite at 2300 K), thermal neutrons are in equilibrium with a moderator at room temperature (usually heavy or light water) and cold neutrons are in equilibrium with a cold secondary neutron source (usually liquid deuterium at 20 K). UCNs, however, are not in thermal equilibrium with the moderator that produce them. For their temperature is in the range of a few mK, the moderator would have to have the same temperature. A technical solution to this problem is close to impossible as the heat deposited in the moderator by the incoming faster neutrons would significantly heat up the moderator. Therefore, the maximum UCN density in a thermal UCN source, i.e. a cold moderator, is limited by the Maxwell–Boltzmann distribution of neutrons in that source and the gain factor, see Eq. 1.9.

In 1975, Golub and Pendlebury [48] proposed the idea of producing UCNs through inelastic scattering events in a converter material. The material needs to have a phonon or roton spectrum such that cold neutrons of a certain energy can be down-scattered to UCN energies in a single scattering event by creating an elementary excitation in a converter. Up-scattering of UCNs is suppressed by low converter temperatures, which suppress low-energy excitations due to the principle of detailed balance.

Since the neutrons produced are not in thermal equilibrium with the converter material, this kind of source is called "superthermal". Also, the source material is called converter rather than moderator. As the conversion mechanism from cold to ultracold neutrons does not act on all neutrons collectively, the phase-space density of the slowed-down neutrons can be higher than in the incoming beam.

One of the materials that fulfill the requirements for a superthermal source of UCNs is solid *ortho*-deuterium (sD_2). The $J = 0$ *ortho* species is the lowest rotational state of the deuterium molecule and the only species that meets the requirements set forth by Golub and Pendlebury. Details about deuterium are given in Chapter 2.

First tests of liquid *normal*-hydrogen and *normal*-deuterium as moderators for thermal neutrons and, at the same time, as UCN converters were published in 1980 by a group from the Leningrad Nuclear Physics Institute of the Academy of Sciences [49].

In 1983, Golub and Böning [50] proposed a thin-film converter instead of a large converter volume. This required a converter material with a scattering cross section higher than that of helium (see below), e.g. hydrogen or deuterium. Due to incoherent scattering, there is a much greater chance of scattering a cold neutron

[3] Fomblin is the name of a group of fluorinated hydrocarbons used in vacuum tubing to drive out water. The linear formula of Fomblin Y is $CF_3O[\text{-}CF(CF_3)CF_2O\text{-}]_x(\text{-}CF_2O\text{-})_yCF_3$ (CAS number 69991-67-9). Fomblin is a registered trademark of Solvay Solexis S.P.A. The critical velocity v_{crit} of Fomblin was taken from Golub et al. [43].

down to UCN energies where the kinematic region of the incoming neutrons overlap with the phonon frequency spectrum of hydrogen and deuterium, see Fig. 1.4. This overlap has its maximum for incoming neutrons with a temperature of $T = 30\,\mathrm{K}$ (2.6 meV) [51]. The high absorption cross section for UCNs in hydrogen leads to a very short UCN lifetime of about 200 μs in solid H_2, which makes it inferior to deuterium (UCN lifetime $\approx 200\,\mathrm{ms}$) as an UCN converter material. For the same converter film thickness, temperature and incoming neutron energy, a deuterium film has an UCN density of at least one order of magnitude higher than a hydrogen film. As calculations show, the exact form of the phonon density of states of H_2 and D_2, i.e. whether a Debye model or a more realistic model derived from experimentally measured dispersion curves is used, has little to no effect on the UCN densities achieved [51].

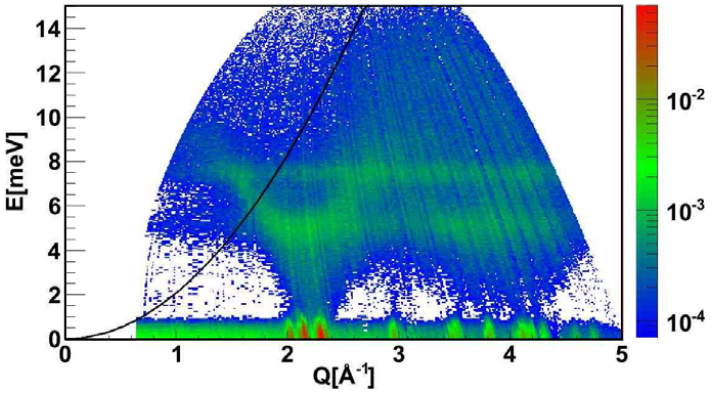

Figure 1.4: The scattering law $S(Q, E)$ (arib. units) of sD_2 with an *ortho*-deuterium concentration of $c_{\mathrm{ortho}} = 95.2\%$ is shown as measured at $T = 4$ K on the IN4 instrument at ILL. The black parabola represents the dispersion curve of the free neutron. This figure was taken from [52] and reprinted with permission from the European Physical Society.

In the 1990s, the idea of using sD_2 as a superthermal converter gained momentum and led to a number of publications about expected UCN output densities [18, 53] and molecular effects in deuterium [54]. In the 2000s, experimental work was published on the actual UCN production rates of various deuterium converter prototypes, e.g. [20, 55, 56, 57], and on the generalized density of states of solid deuterium, e.g. by Frei et al. [52, 58].

When UCN sources based on solid deuterium were planned and designed, their UCN output was projected to be up to 10^4 UCN/cm^3 [18, 53], which is about a factor of 100 better than the Turbine at ILL [19]. However, when they were built and started operation, their neutron density output was comparable to or lower than that of the Turbine [14].

A host of reasons can explain this underperformance. The two most important ones are the scattering of UCNs on rough surfaces and on defects inside the sD_2

crystal. Both were not taken properly into account during the measurement of the sD_2 scattering cross sections that provided the reference data used in computer simulations today, see Section 3.1.

Besides solid deuterium, superfluid helium (^{4}He-II) at $T \leq 1\,\mathrm{K}$ has been proposed as a suitable converter material [59, 60, 61]. The phonon–roton dispersion curve of helium crosses the dispersion curve of the free neutron $\omega \propto q^2/(2m_\mathrm{n})$ at one point, e.g., for cold neutrons with $\lambda_\mathrm{n} = 9\,\text{Å}$: $E = 1\,\mathrm{meV}, q = 0.7\,\text{Å}^{-1}$ [39]. Since neutron scattering in helium is purely coherent, only neutrons with a kinetic energy in the vicinity of that value can be down-scattered to the UCN region in a single scattering event by exciting a phonon in the helium bath. Due to the compact structure of the helium nucleus, it has zero absorption cross section for neutrons. This is because the ground state of a system of two protons and three neutrons is an α-particle and a free neutron. The low temperature of the helium bath largely prevents UCNs from being up-scattered by phonons. Helium-based UCN converters are currently in operation at the Institut Laue-Langevin (SUN-1 [62] and SUN-2), have been operated in Japan [63, 64], and are under construction at TRIUMF in Vancouver, Canada [65]. The disadvantage of the small, exclusively coherent scattering cross section of helium is offset by a large converter volume in the range of 10 to 40 liters. At the moment, the extractable UCN density is lower than that of some sD_2-based converters and the Turbine at the ILL [14].

In addition to solid *ortho*-deuterium and superfluid helium, various other substances have been tested as potential UCN converters. Among them were solid oxygen O_2 in the α-phase [66, 67], which has a significantly lower UCN production rate than sD_2, but no incoherent scattering cross section due to the zero nuclear spin of the isotope ^{16}O, and solid nitrogen $^{15}N_2$, also in the α-phase [68]. While oxygen can be used in its natural isotopic composition due to the low absorption cross section of its most abundant isotopes ^{16}O and ^{18}O, only the rare nitrogen isotope ^{15}N (abundance 0.37%) can be used as an UCN converter. Since the latter needs to be purified at least to $> 99.9\%$, it is not able to compete with deuterium and oxygen financially. When directly compared to each other (same cold neutron beam, UCN production volume, detector setup, etc.), solid D_2 is the far better choice of UCN converter than solid deuterated methane CD_4 and solid O_2 [69].

Recently, modified and new types of UCN converters have been proposed. Lychagin et al. proposed to surround a ^{4}He-II-based UCN converter with a medium of high reflectivity for cold neutrons, such as solid methane in phase II at 4 K [70] or a wall made from diamond nanoparticles [71]. This leads to multiple passages of cold neutrons through the helium bath and increases the chances of phonon creation and UCN production. Zimmer proposed to use deuterated O_2 clathrates for a stepwise removal of kinetic energy from cold neutrons by electronic spin flip of the paramagnetic converter material [72].

1.4 Select experiments using UCNs

Apart from the books of Ignatovich [42] and Golub [43], the last comprehensive review of experiments with UCNs and efforts to increase the UCN density extractable from sources – to the knowledge of the author – has been given by Ignatovich in 1996 [73]. In the following subsections it is attempted to give a brief overview of recently and currently ongoing research using UCNs. A more comprehensive overview would go beyond the scope of this chapter about properties and basic applications of UCNs and needs to be left to a more talented writer.

1.4.1 The lifetime of the free neutron measured in material bottles

Bound inside atomic nuclei and interacting with protons via the strong force, neutrons are stable. Free neutrons, however, are not stable. If it is not absorbed by matter, a free neutron decays into a proton, an electron and an electron-antineutrino

$$n \rightarrow p + e^- + \overline{\nu}_\mathrm{e} + 0.78\ \mathrm{MeV}. \tag{1.18}$$

This decay is governed by the weak interaction, namely the transformation of a down quark d into an up quark u. Therefore, measuring the lifetime τ_n of the free neutron as well as decay correlation coefficients is a way of determining key quantities of the weak interaction in the Standard Model of particle physics (SM) with high precision.

In the SM, the transformation of one quark into another upon interaction with a W boson is described by the Cabibbo–Kobayashi–Maskawa (CKM) matrix or quark mixing matrix. The absolute squares of the CKM matrix elements give the transition probability of differently flavored u-type quarks (up u, charm c, top t) into d-type quarks (down d, strange s, bottom b). The value $|V_\mathrm{ud}|^2$ represents the transition probability between up and down quarks, which is related to the neutron lifetime τ_n. Unitarity of the CMK matrix indicates that our understanding of quarks is complete, i.e. there exist no quark transitions that are not quantitatively explained by the electroweak interaction. This is a cornerstone aspect of the SM. In the mathematical model unitarity is assumed, but experimentally it still has to be proven to an acceptable certainty. The unitarity condition for the first row of matrix elements reads

$$|V_\mathrm{ud}|^2 + |V_\mathrm{us}|^2 + |V_\mathrm{ub}|^2 = 1, \tag{1.19}$$

where the subscripts indicate the transition between different flavor generations. The connection between the free-neutron lifetime τ_n and the CKM matrix element V_ud is given by

$$\tau_\mathrm{n} = \frac{(4908.7 \pm 1.9)\,\mathrm{s}}{|V_\mathrm{ud}|^2 \times (1 + 3\lambda^2)}, \tag{1.20}$$

where $\lambda = g_A/g_V$ represents the ratio of the axial-vector weak coupling constant to the vector weak coupling constant. The error in the numerator comes from the uncertainty of electroweak radiative corrections. For a detailed derivation and a review of the SM observables accessible through neutron decay, the reader is referred to Abele [74] as well as Dubbers and Schmidt [75].

The neutron lifetime also enters into Big-Bang nucleosynthesis (BBN) models as a key parameter [76]. BBN theory predicts the primordial abundances of D, ^{3}He, ^{4}He, and ^{7}Li. Just after the Big Bang, neutrons and protons existed with the following ratio

$$n/p = e^{\frac{-\Delta E}{k_B T}}, \tag{1.21}$$

where $\Delta E = 1.293$ MeV is the energy difference $\Delta E = mc^2$ (and, equivalently, the mass difference) between neutrons and protons and T the temperature of the Universe. As the temperature of the Universe fell faster than the Hubble expansion rate, the particles therein departed from chemical equilibrium. This is called the "freeze-out" (at $T_{\text{freeze}} \approx 1$ MeV) and took place when the Universe was about one second old. After this event, neutrons were free to undergo β decay. Nearly all neutrons quickly ended up bound in the most stable light element, ^{4}He. The ratio of bound baryons to free baryons, Y_p, depended most importantly on the lifetime of the free neutron. The formation of light elements and their ratios to one another was fixed already 180 seconds after the Big Bang. Experimentally, near-primordial ratios of light elements can be observed on astrophysical sites with low metal abundance and thus little stellar nucleosynthesis in the past. For further reading about the astrophysical importance of neutron decay parameters, the following publications are recommended [75, 76, 77].

The lifetime of the free neutron is measured by either counting decay events directly or by counting the surviving neutron population after a certain amount of time. The number of neutron β-decays per infinitesimally short period of time $\mathrm{d}N(t)/\mathrm{d}t$ can be described by the following ordinary differential equation, where $N(t)$ is the total population of free neutrons in the decay volume and λ is the decay constant

$$\frac{\mathrm{d}N(t)}{\mathrm{d}t} = -\lambda N(t) = \frac{-N(t)}{\tau_n}. \tag{1.22}$$

The mean lifetime of a neutron of this population is $\tau_n = 1/\lambda$. It is the same time after which the 1/e-th fraction of the initial population is left over. The half-life $t_{1/2}$ of a free neutron is related to its mean lifetime τ_n by

$$t_{1/2} = \frac{\ln(2)}{\lambda} = \ln(2)\tau_n. \tag{1.23}$$

There are two methods for measuring the lifetime of a free neutron. The "beam" method employs cold neutrons beams and measures the absolute rate of neutron decay $\mathrm{d}N/\mathrm{d}t$ in a well defined reference volume and the total number of neutrons

$N(t)$ present in that volume. Since a continuous beam is used, $N(t) = N$ is constant over time. The lifetime is then deduced via the differential form of the decay equation 1.22. The difficulty with this method is that the absolute neutron flux needs to be known very well and the neutron decay needs to be detected with high efficiency. Currently, the mean free-neutron lifetime accepted by the Particle Data Group (PDG)[4] is 880.0 ± 1.0 s [5]. It has been calculated from the results of two beam experiments and five bottle experiments. Both the results from beam and bottle experiments (see below) differ by 8.4 seconds and lie 3.8σ (standard deviations) apart from each other [78]. This means that the results of both types of experiments do not fall within each other's 95% confidence intervals.

Due to their property of being reflected from material walls that have a neutron-optical potential U_{opt} higher than the neutron's kinetic energy, see Section 1.2, and their interaction with magnetic fields [79], UCNs can be stored in material bottles and magnetic fields, where they decay. The wall coating material of choice in current "bottle" neutron lifetime experiments, the second type of experiment to determine the free-neutron lifetime, is fomblin grease[5]. After filling the bottle – which is usually an aluminum or steel drum of several tens of liters – with a certain number of UCNs $N(t = 0)$, the number of surviving neutrons $N(t)$ is counted after various time intervals. The initial number of neutrons present in the bottle, $N(t = 0)$, cannot be measured directly, but has to be extrapolated from subsequent measurements: $N(t = 0) = \lim_{t\to 0} N(t)$. Divided by the volume of the storage bottle, it represents the maximum attainable UCN density (in units of UCN/cm^3), which is a figure of merit for UCN sources.

During storage, UCNs are lost via a number of processes, so-called loss channels. All of them have to be understood as well as possible in order to calculate the true neutron lifetime τ_{n} with good accuracy. The main equation governing these processes is

$$N(t) = N_{(t=0)} \mathrm{e}^{-t\times(1/\tau_{\text{n}}+1/\tau_{\text{abs}}+1/\tau_{\text{up}})}, \tag{1.24}$$

where τ_{abs} represents the capture lifetime of an UCN, i.e. the time before an UCN is *absorbed* by a wall atom or a residual gas atom. τ_{up} stands for the lifetime of an UCN before it gains kinetic energy above the neutron-optical potential U_{opt} through *up-scattering* on a wall atom or on residual gas or other impurities in the storage vessel.

[4] The PDG is an international collaboration that provides a comprehensive summary of Particle Physics and related areas of Cosmology: the Review of Particle Physics. It is led by a team at Lawrence Berkeley National Laboratory (LBNL), USA.

[5] Perfluoropolyether chains with a high molecular weight.

1.4.2 The electric dipole moment of the neutron (nEDM)

One fundamental question in cosmology is the observed dominance of matter over antimatter in the Universe. Matter consists chiefly of baryons (like protons and neutrons) as opposed to antimatter, which consists of *anti*baryons. The process by which the imbalance between baryons and antibaryons came to be, is called baryogenesis.

One of the mainstays of particle physics is the CPT theorem. A system is called CPT symmetric when it is invariant under the combined reversal of charge C, parity (spatial coordinates) P, and time T. Standard local quantum field theory, under which interactions are CPT invariant, predicts that particles and antiparticles have the same properties other than the signs of their charges. However, according to the three Sakharov principles the C and CP symmetries must be violated in order for baryogenesis to take place.

Sources of CP violation known so far are insufficient to explain the observed dominance of matter over antimatter in the Universe. One additional source of CP violation could be the neutron, among others, if it had a non-zero electric dipole moment (nEDM). Researchers searching for the nEDM have published ever lower upper limits during the past decades. In doing so, they ruled out many theories that go beyond the Standard Model and require a CP violation that would imply a nEDM larger than the current upper limit for the neutron electric dipole moment of $d_\mathrm{n} < 3 \times 10^{-26} e\,\mathrm{cm}$ [5, 7]. The Supersymmetry model (Susy) predicts as much CP violation as the current nEDM limit allows. Therefore, if the nEDM upper limit can be decreased further, a theory like Susy, or aspects thereof, could be dismissed.

Dubbers and Schmidt published an extensive review on the neutron's role in fundamental physics experiments [75], which is recommended to the interested reader. A comprehensive, recent overview of the state of nEDM experiments worldwide was given by Schmidt-Wellenburg [80].

1.4.3 Neutrons in the gravitational potential

Ultracold neutrons can be used to test Newton's law of gravity on the micrometer scale. Free neutrons are massive particles and on Earth they are trapped in the Earth's gravitational potential well. If quantum mechanics is universal, neutrons trapped in a potential well must have quantized bound energy states. Their direct observation has long been made difficult by the weakness of the gravitational force – the transistion energies between bound states $n \to (n+1)$ is only in the range of pico-electronvolts. In 2002, Nesvizhevsky et al. [8] demonstrated the quantization of the energy states of the neutron in the gravitational well. To this date, groups continue to use ultracold neutrons in their search for quantum effects, exotic particles [81] as well as hypothesized fields that extend the Standard Model and dark matter [82].

1.4.4 UCN interference and the microscope

Ultracold neutrons can interfere with themselves, just as photons can. In a simple experiment, Steinhauser [11] demonstrated the wave character and interference of UCNs by reflecting them off an Al–Cu–Al–Cu quadruple layer sandwich. UCNs reflected from the first Al–Cu interface interfered with those that were reflected from the second Al–Cu interface, which is analogous to Fabry–Perot experiments with photons. The intensity of reflected UCNs showed a marked dip at the neutron wavelength that corresponded fairly well to the thickness of the Cu–Al bilayer of 1100 Å, see Fig. 1.5.

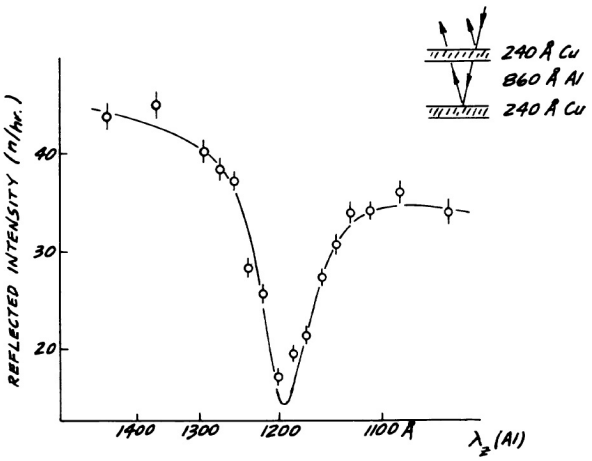

Figure 1.5: The reflectivity of UCNs from a sandwiched multilayer system of aluminum and copper is shown over the neutron wavelength for the velocity component in z-direction (normal to the multilayers). The thin aluminum top layer is not shown in the inset. Original plot by Steinhauser [11], redrawn by Shull [83]. Reprinted with permission from the American Physical Society.

An optical microscope using UCNs with their long wavelengths would allow for the investigation of large atomic structures, such as biological molecules, in the range of a few micrometers. Different elements (and isotopes thereof) would be visible in various shades of gray [12, 84, 85]. The idea seems to have first been published by I. M. Frank [86] and was called one of the more exotic applications of UCNs by Shapiro [87].

Indeed, it is hard to construct and operate such a microsope beyond the mere proof of principle [88, 89] due to high radiation background, which is always a problem in UCN applications, aberration due to the strong influence of gravity on slow neutrons, and extremely low count rates due to small apertures and monochromatized UCN beams. Only an UCN source significantly stronger than current sources will make it possible to operate an UCN microscope.

2 Theoretical Background for the Transmission Experiment

The elements of the physical reality cannot be determined by a priori philosophical considerations, but must be found by an appeal to results of experiments and measurements.
— Einstein, Podolsky, Rosen, *Phys. Rev. 47:777, 1937*

2.1 Basic idea behind a transmission experiment

A transmission measurement is an experiment in which waves or particles are passed through a sample to determine some of its properties. In the simplest case, the sample in question is homogenous, has the geometry of a slab, a well defined thickness along the beam path and no surface roughness (or a surface roughness to which the applied waves are insensitive). Due to the quantum-mechanical principle of wave–particle duality, photons, electrons, neutrons and other small particles have both wave and corpuscular properties.

Assume that an incoming beam of neutrons has the intensity I and traverses a sample of thickness d along the z-axis, i.e. horizontally. If the sample is cut into slices of thickness Δd perpendicular to the beam direction, the intensity of the incoming beam is reduced by the sample according to $\Delta I = -\Sigma I \Delta d$, where ΔI is the number of neutrons scattered away from the beam axis in each sample slice of thickness Δd, I is the neutron intensity incident on Δd, and Σ is the attenuation factor of the sample material for a given neutron velocity. In differential notation one can write

$$\frac{\mathrm{d}I}{\mathrm{d}d} = -\Sigma I. \tag{2.1}$$

This is an ordinary differential equation with the solution

$$I(d) = I_0 \mathrm{e}^{-\Sigma d}, \tag{2.2}$$

where $I(d)$ represents the neutron beam intensity at any one point d along the z-axis inside the sample, I_0 is the neutron beam intensity impinging on the sample, and Σ is the attenuation coefficient, which is the product of the volumetric particle density N_v inside the sample and the total scattering cross section σ_tot of the sample

particles for neutrons. The total scattering cross section is dependent on the in-medium velocity of the incoming neutrons, $\sigma_{\mathrm{tot}}(v_{\mathrm{m}})$. The quantities I_0 and $I(d)$ are the count rates of the respective velocity channel $v_{\mathrm{m}} \pm \Delta v_{\mathrm{m}}$ if polychromatic neutrons are used.

The mean free path λ_{mfp} of neutrons in a medium is

$$\lambda_{\mathrm{mfp}} = \frac{1}{N_{\mathrm{v}}\sigma_{\mathrm{tot}}}. \tag{2.3}$$

The transmission equation, Eq. 2.2, is similar to Lambert–Beer's law [90, 91] used in chemistry to relate the intensity of light transmitted through a solution to the concentration of the dissolved substance. Fig. 2.1 illustrates this equation graphically.

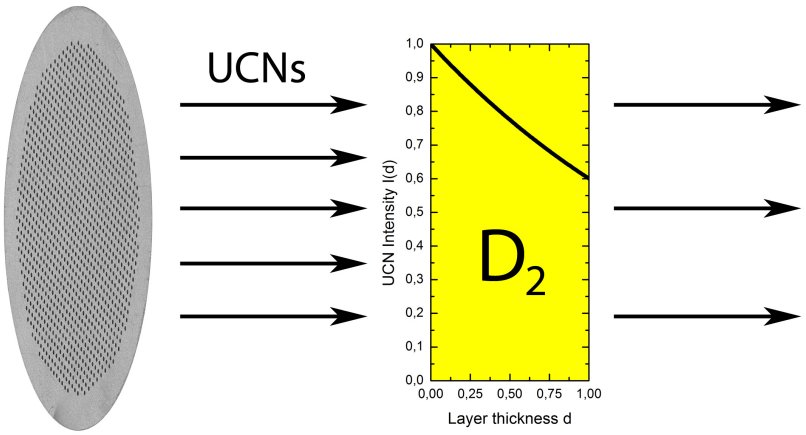

Figure 2.1: Illustration of the transmission geometry using collimated, i.e. parallelized, neutrons. The black curve inside the yellow sample shows the exponential decay of the transmitted neutron intensity over sample thickness.

In the experiments carried out for this thesis, the quantity I_0 was measured as the total number of ultracold neutrons (UCNs) per measurement run passing through the empty sample container with a vacuum of about 10^{-2} mbar inside, while $I(d)$ was the number of UCNs passing through the sample container filled with a sample. Dimension d represents the sample thickness, which is equivalent to the distance between the inner walls of the sample container's windows. The molecular or atomic particle density was taken from the literature (liquid and solid deuterium as well as liquid and solid hydrogen [46]). The quantity to be determined by the method given above is the total scattering cross section σ_{tot} per deuterium molecule. It is composed of the neutron absorption cross section in deuterium σ_{abs}, energy gain of the UCN (so-called inelastic or up-scattering to cold neutron energies) σ_{inel} and the elastic scattering cross section σ_{el}. The absorption

cross section is well known for thermal energies and is strictly proportional to the inverse of the velocity of the incoming neutron, $\sigma_{\mathrm{abs}} \propto 1/v$. Therefore, it can easily be subtracted from the measured quantity σ_{tot}.

$$\sigma_{\mathrm{tot}} = \underbrace{\sigma_{\mathrm{abs}}}_{=c_{\mathrm{abs}}/v} + \underbrace{\sigma_{\mathrm{inel}} + \sigma_{\mathrm{el}}}_{=\sigma_{\mathrm{scatt}}} \tag{2.4}$$

It may help to understand this experimental approach by likening it to the passage of sunlight through a glass window. If a window pane is perfectly homogenous, well polished and clean, all light passes through it unencumbered. If, on the other hand, it has manufacturing faults inside, such as small air bubbles, or was intentionally made non-transparent by adding dispersed particles, as is done in milk glass, much less or no light passes through, even if the surface is perfectly polished (Willis–Tyndall scattering). This behavior is similar to that of a low-roughness deuterium crystal with defects, which was investigated in this dissertation. If the window pane is ground (as in ground or frosted glass), light gets scattered at the pane's surface and only a significantly reduced fraction passes straight through the window. This is the equivalent of having a perfect deuterium crystal with a rough surface due to a rough-surface sample container. All these processes depend on the wavelength of the incident particles. As with light, long-wavelength photons are scattered less in the cases described above. Ultracold neutrons scatter stronger as their wavelength increases.

A transmission measurement along the z-axis, as described here, can only measure integral losses of UCN in all spatial directions (4π). It is , therefore, not possible to measure the angular distribution of the scattered UCNs, i.e. $\mathrm{d}\sigma/\mathrm{d}\Omega$. An UCN spectrometer which can indeed measure the angular distribution of the scattered slow neutrons was built by Pokotilovski [92] and has been used for a few transmission measurements on metal and polyethylene samples at the Institut Laue–Langevin. Its beam axis is vertical, which prohibits the use of thin slices of cryogenic liquids and solids. This is one reason why a horizontal beam axis was chosen for the experiments discussed here; the other being the higher UCN intensity, which leads to better statistics and shorter measuring times in the integral transmission experiment.

This comes at the cost of several side effects, which need to be accounted for in order to extract the correct scattering cross section σ_{scatt} of the measured material:

- scattering losses on the sample surface
- forward scattered neutrons
- multiply scattered neutrons

Scattering losses on the sample surface were minimized by using a sample container with highly polished windows, see Chapter 5. During their growth process

the deuterium crystals took on the surface roughness of the windows and were, therefore, very smooth. UCNs that were scattered forward, i.e. with a negligible momentum transfer $q \to 0$, ended up in the detector and were counted as unscattered neutrons. This effect was small enough to be neglected, see Section 6.4. Multiple scattering, i.e. the effect that UCNs scatter twice elastically and end up in the detector, can also be neglected for the experiments described here due to the samples being thinner than one mean free path for UCNs and the small detector acceptance angle.

2.2 The kinematic region

When a neutron gains or loses energy in a scattering event, that scattering process is called inelastic (superscript *inel* in the general case, *1ph* for up-scattering due to phonon annihilation). If no or only little energy is exchanged, the process is called elastic (superscript *el*) and quasi-elastic (superscript *qel*), respectively.

Since total energy and total momentum are conserved in a scattering event, energy and momentum transfer with respect to the sample are described by

$$\Delta E = \hbar\omega = \frac{\hbar^2 \mathbf{k}_\mathrm{i}^2}{2m_\mathrm{n}} - \frac{\hbar^2 \mathbf{k}_\mathrm{f}^2}{2m_\mathrm{n}} \text{ and} \tag{2.5}$$

$$\Delta p = \hbar|\mathbf{q}| = \hbar|\mathbf{k}_\mathrm{i} - \mathbf{k}_\mathrm{f}|\,, \tag{2.6}$$

where $\mathbf{q} = \mathbf{k}_\mathrm{i} - \mathbf{k}_\mathrm{f}$ denotes the scattering vector, i.e. the momentum transfer, and $\mathbf{k}_\mathrm{i}$ is the incoming (or initial) and $\mathbf{k}_\mathrm{f}$ the outgoing (or final) neutron wave vector.

From the equations above one can derive expressions for $q(\omega)$ representing the energy and momentum limits, in which a scattered neutron with initial momentum $\mathbf{k}_\mathrm{i}$, initial energy $\hbar\omega_\mathrm{i}$, momentum transfer $\mathbf{q}$ and energy transfer $\hbar\omega$ can be found after a scattering event. The area delimited by $q_{1/2}(\omega)$ in the q-ω plot is called the *kinematic region* and is shown in Fig. 2.2.

When the effective scattering cross section for a given substance in a given state for a given incident neutron energy is to be calculated, one has to integrate the respective scattering law $S(q, \omega)$ over the kinematic region.

The two parabolas in q marking off the kinematic region (for UCN up-scattering) are

$$q_1(\omega) = k_0 \left[-1 + \sqrt{1 + \frac{\omega}{\omega_0}}\right] \tag{2.7}$$

$$q_2(\omega) = k_0 \left[+1 + \sqrt{1 + \frac{\omega}{\omega_0}}\right]. \tag{2.8}$$

For UCNs the kinematic region is only a very small band because of the low initial neutron energy $\hbar\omega_\mathrm{i}$. The area for neutron energy loss above the abscissa

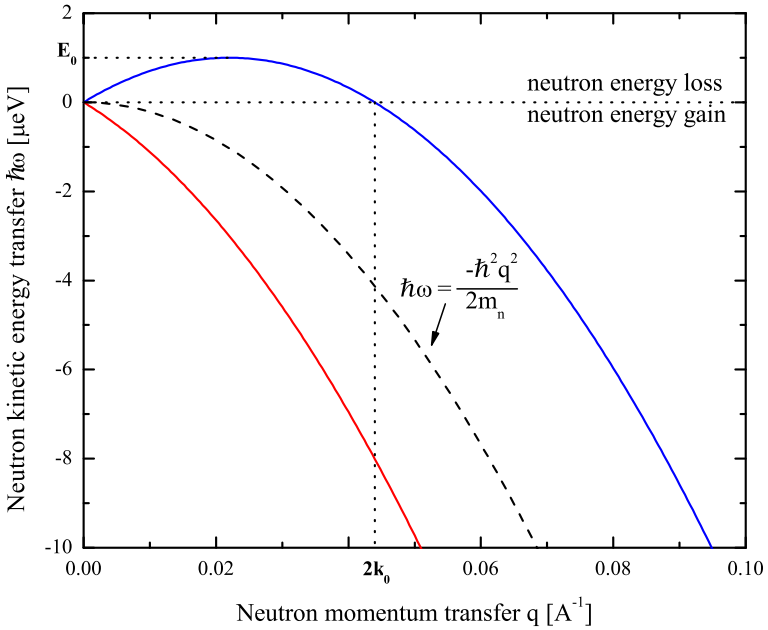

Figure 2.2: Plot of the kinematic region, i.e. accessible momentum–energy space, for a neutron of incident energy $E_0 = 1\,\mu$eV.

is negligible because UCN energies are very small compared to both the thermal energy $k_\mathrm{B}T$ of the sample even at low temperatures like 10 K, and typical phonon energies.

The effective scattering cross section for neutrons of a certain incident energy (E_0 in Fig. 2.2 represents the incident neutron energy) in a given material is calculated by integrating the scattering law of that material $S(q,\omega)$ over the kinematic region defined by the incident neutron energy.

The integration is carried out as follows

$$\sigma_\mathrm{eff} = \int \left(\frac{\mathrm{d}^2\sigma}{\mathrm{d}\Omega \mathrm{d}E} \right) \mathrm{d}\Omega \mathrm{d}E \tag{2.9}$$

$$\sigma_\mathrm{eff} = \int \left(\frac{\mathrm{d}^2\sigma}{\mathrm{d}\Omega \mathrm{d}E} \right) \frac{2\pi q \mathrm{d}q}{k_\mathrm{i} k_\mathrm{f}} \mathrm{d}E \tag{2.10}$$

$$\sigma_\mathrm{eff} = \int_{-\infty}^{E_0} \int_{q_1(E)}^{q_2(E)} \left(\frac{1}{k_\mathrm{i} k_\mathrm{f}} \frac{\mathrm{d}^2\sigma}{\mathrm{d}\Omega \mathrm{d}E} \right) 2\pi q \mathrm{d}q \mathrm{d}E \tag{2.11}$$

The scattering laws derived for UCN scattering on defects as well as those for 1-phonon up-scattering using the Incoherent Approximation, refer to Sections 3.3 and 3.2, have to be integrated over the kinematic region to obtain effective cross sections σ_eff. For large energy transfers from the sample to the neutron (up-scattering), the scattering law $S(q,\omega)$ is suppressed by the detailed balance factor.

For slow neutrons, the effective inelastic scattering cross section behaves like $\sigma_{\text{eff}} \propto \frac{\text{const.}}{v}$. This $1/v$ dependence, also called the $1/v$ law, is due to the small width of the kinematic region for slow neutrons and the definition of the cross section. It is not a property of the scattering law. Contrary to the inelastic cross section, the incoherent elastic cross section does not show a $1/v$ dependence. Its $\frac{\mathrm{d}\sigma}{\mathrm{d}\Omega} \propto S(q,0)$ is integrated only along the abscissa. Since the integral is normalized and no change of momentum takes place during the scattering event ($k_{\text{f}}/k_{\text{i}} = 1$), no v-dependence is introduced to the effective scattering cross section. UCNs have a wavelength much longer than the Bragg cut-off of any substance. Therefore, they show no coherent elastic (Bragg) scattering.

2.3 Basic properties of the hydrogens

In 1927, theoretical physicist Werner Heisenberg predicted that a homonuclear diatomic molecule, where each atom has a nuclear spin of $I = 1/2$, has two different "systems" A (*ortho*, antiparallel nuclear spins[1]) and B (*para*, parallel nuclear spins), with corresponding statistical weights 1 and 3, respectively [93]. This was hypothesized to manifest itself in molecular spectra, where the peaks of the para–para transitions would be three times as high as those of the ortho–ortho transitions; something that was thought of as an anomaly at the time and was called "Intensitätswechsel"[2] [94]. This intensity ratio of 3:1 approaches unity for molecules composed of atoms with higher nuclear spin. Heisenberg and Friedrich Hund predicted that the hydrogen molecule ^{1}H–^{1}H exhibits such a behavior [95].

The molecular spectra are not the only observable affected by spin–spin interactions in homonuclear diatomic molecules. The heat capacity was found by Eucken [96] to have an unusual drop at low temperatures. Dennison was able to explain this by the non-interaction of the "symmetrical" and "anti-symmetrical" states of hydrogen over the time of a typical experiment[3] [98].

Bonhoeffer and his team, who worked at the Kaiser-Wilhelm Institut für Chemie in Berlin[4], were the first to experimentally prove the separation of hydrogen into two species and to produce 99.7% pure *para*-hydrogen. They systematically investigated the conversion from *normal*-hydrogen to *para*-hydrogen, its dependence on temperature, pressure, liquid and gaseous state, and catalysts. Among the tested materials, activated carbon was shown to be the best catalyst at cold temperatures.

[1] It should be noted that throughout this paragraph, where Heisenberg's work is quoted, the meaning of the terms *ortho* and *para* as they pertain to the hydrogen molecule ^{1}H–^{1}H are used inversely to today's convention.

[2] English: change of intensity; or rather: an intensity differing from expectations that were based on the knowledge of molecular interactions at that time.

[3] In fact, without a catalyst, a *normal*-deuterium mixture would take months to reach the low-temperature *ortho–para* equilibrium [97].

[4] More about the early research on the hydrogen species can be found here [99] and in an article by Bonhoeffer [100].

Within only two years, the emerging theory of quantum mechanics was able to predict interactions of atoms in a homonuclear diatomic molecule, from which the temperature-dependent behavior of observable properties were derived, and experimental physicists confirmed those predictions. In 1932 the Nobel Prize in Physics was awarded to Werner Heisenberg[5]

> for the creation of quantum mechanics, the application of which has, *inter alia*, led to the discovery of the allotropic forms of hydrogen.

The behavior described above together with quantum-mechanical constraints demand that a hydrogen molecule (two fermions) have an anti-symmetric total wave function and a deuterium molecule (two bosons) have a symmetric total wave function with regard to the exchange of both atoms in the molecule. The wave functions are composed of a part for vibration, nuclear spin, and rotation: $\Psi_{\text{vib}} \times \Psi_{\text{spin}} \times \Psi_{\text{rot}}$. For a more detailed treatment of the spin physics of hydrogen and deuterium, the reader is referred to a comprehensive review article written by Silvera [97].

Vibrational excitations, which lie in the range of hundreds of milli-electronvolts, can be neglected in a cold solid and liquid around 20 K and with neutrons of an energy of around one micro-electronvolt. Due to the low temperature, the molecule will be in the lowest vibrational state, $\nu = 0$.

Excited rotational states are, however, present in hydrogen and deuterium at low temperatures. Hydrogen with a total nuclear spin of $I = 0$ is called *para*-hydrogen and has even-numbered rotational states, $J = 0, 2, \ldots$. Hydrogen with $I = 1$ has odd-numbered rotational states, $J = 1, 3, \ldots$. In deuterium the situation is similar, but slightly more complex. Total nuclear spins of $I = 0, 2$ give rise to even-numbered rotational quantum numbers, while a total nuclear spin of $I = 1$ requires rotational odd-numbered rotational quantum numbers, $J = 1, 3, \ldots$. Molecules with an even J are called *ortho*-deuterium, those with an odd J are called *para*-deuterium. This means that the term "*ortho*-deuterium" does not refer to a *single* rotational state, but rather a collection of states. Therefore, *ortho*-deuterium is referred to as a spin "species", as is *para*-deuterium. *Normal*-deuterium (nD_2), i.e. deuterium at room-temperature equilibrium, consists of 67% *ortho*-deuterium and 33% *para*-deuterium. This is a direct consequence of the multiplicities of the total nuclear spins in each species.

The energy of the rotational levels J can be calculated by applying a linear rigid rotor model, which gives the energy spectrum of (homonuclear) diatomic molecules with a moment of inertia

$$I_{\text{rot}} = m \times r^2, \tag{2.12}$$

where m is the mass of one nucleus and $r = 0.74/2$ Å [97] is half the equilibrium distance between two deuterons.

[5] "The Nobel Prize in Physics 1932". Nobelprize.org. Nobel Media AB 2014. Web. 16 Oct 2018. http://www.nobelprize.org/nobel_prizes/physics/laureates/1932/

The rotational energy of a state J is

$$E_J = \frac{\hbar^2}{2I_{\mathrm{rot}}} \times J(J+1) = \frac{7.4\,\mathrm{meV}}{2} \times J(J+1). \tag{2.13}$$

The energy released in the transition $J = 1 \rightarrow 0$ is $E_{1\rightarrow 0} = 7.4$ meV and it is orders of magnitude larger than the kinetic energy of UCNs. Therefore, if an UCN scattering event leads to the de-excitation of a rotational level, the UCN only needs to pick up a fraction of that energy (with the rest creating a phonon in the sample) to be "up-scattered" to a higher neutron energy, i.e. very cold or cold neutron. It is then lost for measurements with ultra-cold neutrons. That is why up-scattering is often treated similarly to absorption of UCNs.

The population of a rotational state N_J with the rotational quantum number J can be calculated using the Boltzmann distribution

$$\frac{N_J}{N_0} = (2J+1) \times \exp\left(-\frac{E_J}{k_{\mathrm{B}}T}\right), \tag{2.14}$$

where k_{B} is the Boltzmann constant, T is the temperature of the sample and $(2J+1)$ is the degeneracy factor of the rotational level J. For typical liquid and solid deuterium temperatures, the fraction of molecules in the $J = 2$ state and higher can safely be neglected.

When cooled from room temperature to cryo-temperatures, hydrogen and deuterium will assume the *ortho–para* equilibrium for that particular temperature over time. For this to happen, the molecules need to be able to collide with each other. An isolated single molecule cannot change its rotational state from $J = 1 \rightarrow 0$ as this transition is quantum-mechanically forbidden. Natural spin conversion, i.e. without a catalyst, from the room-temperature to the cryo-temperature equilibrium takes weeks. If the molecules are brought in contact with a substance that has a large magnetic moment, e.g. (paramagnetic) oxygen or various metal oxides, that conversion time can be as short as a few hours. Comprehensive overviews of the spin conversion mechanisms in deuterium are given in [97, 101, 102]. Fig. 2.3 shows the equilibrium *ortho–para* ratios for deuterium and hydrogen from 0 K to 160 K, at which point the room-temperature equilibrium is reached.

An overview of molecular densities for hydrogen and deuterium at the temperatures relevant for this thesis are given in Tab. 1.2. These values and many more important properties of hydrogen and deuterium, like the averaged square displacement $\langle u^2 \rangle = 0.25\,\mathrm{Å}^2$ (important for the Debye–Waller factor), the speed of sound, heat capacity, lattice constants, hard-sphere radius, etc., are summed up in a review book by Souers [46].

2.4 Scattering cross sections of deuterium

As early as 1946 Hamermesh and Schwinger [104], and later Young and Koppel [105], calculated the scattering cross sections of deuterium for slow neutrons.

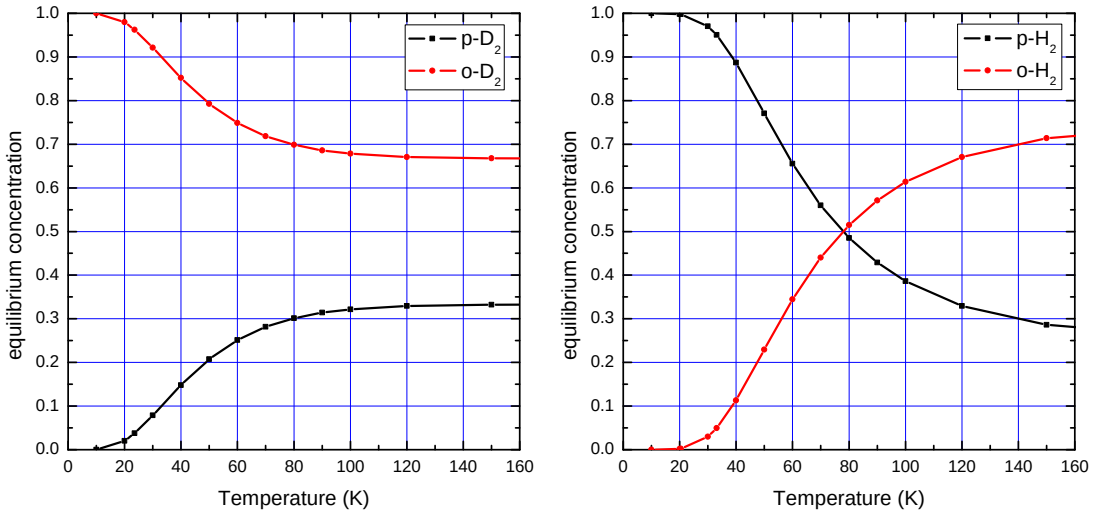

Figure 2.3: Left: Ortho–para equilibrium of deuterium; right: Para–ortho equilibrium of hydrogen from cryogenic to room temperature [103].

According to the theory from these two papers, the *nuclear* scattering cross sections $\sigma_{J\to J'}$ of deuterium *molecules* are

$$\sigma_{00}^{\text{inc}} = 4\pi \times 2\left(\frac{5}{4}b_{\text{inc}}^2\right) = 5.13\,\text{barn} \tag{2.15}$$
$$\sigma_{00}^{\text{coh}} = 4\pi \times 4(b_{\text{coh}}^2) = 22.37\,\text{barn} \tag{2.16}$$
$$\sigma_{01}^{\text{inc}} = 18\pi \times b_{\text{inc}}^2 = 9.23\,\text{barn} \tag{2.17}$$
$$\sigma_{01}^{\text{coh}} = 0.0\,\text{barn} \tag{2.18}$$
$$\sigma_{11}^{\text{inc}} = 4\pi \times 2\left(\frac{1}{2}b_{\text{inc}}^2\right) = 2.05\,\text{barn} \tag{2.19}$$
$$\sigma_{11}^{\text{coh}} = 4\pi \times 4(b_{\text{coh}}^2) = 22.37\,\text{barn} \tag{2.20}$$
$$\sigma_{10}^{\text{inc}} = 4\pi \times 2\left(\frac{3}{2}b_{\text{inc}}^2\right) = 6.15\,\text{barn} \tag{2.21}$$
$$\sigma_{10}^{\text{coh}} = 0.0\,\text{barn}, \tag{2.22}$$

where J represents the initial rotational species (before the scattering event) and J' after the event. Cross sections with an initial species of $J = 0$ represent *ortho*-deuterium, those with $J = 1$ stand for *para*-deuterium. The squared values for the bound scattering lengths of deuterium *nuclei*, $b_{\text{coh}}^{\text{D}} = 6.671 \times 10^{-15}\,\text{m}$ and $b_{\text{inc}}^{\text{D}} = 4.04 \times 10^{-15}\,\text{m}$, were taken from Sears [44].

These nuclear scattering cross sections are used in the double-differential scattering cross sections, which is then integrated over the kinematic region in q–E space allowed by the conservation of total momentum and energy, see Section 2.2. The Incoherent Approximation, see Section 3.2, uses the total nuclear scattering

cross section, $\sigma_{00}^{\mathrm{tot}} = \sigma_{00}^{\mathrm{coh}} + \sigma_{00}^{\mathrm{inc}}$.

The incoherent elastic scattering cross section of deuterium, which is constant over the entire UCN spectrum, is 5.13 barn per molecule, not 4.1 barn as often reported [106, 107, 108]. This stems from the fact that the incoherent cross section of the *ortho*-species needs to be averaged over both rotational spin states $J = 0$ and $J = 2$ [104, 109], which introduces a factor of 5/4

$$\frac{\langle J(J+1)\rangle}{4} = \frac{1}{6} \times \langle 0\rangle + \frac{5}{6} \times \langle 6\rangle = \frac{5}{4}. \tag{2.23}$$

Therefore, the incoherent elastic scattering cross section of a deuterium *molecule* is $\sigma_{00}^{\mathrm{inc,el}} = 5/4 \times 2 \times 2.05\,\mathrm{barn}$, where 2.05 barn is the incoherent cross section of one deuterium *atom*.

In the case of deuterium, in addition to the nuclear scattering cross sections, molecular form factors in the form of squared spherical Bessel functions enter into the double-differential scattering cross section, where $a = 0.74$ Å stands for the equilibrium separation of the two deuterons in a molecule.

$$\sigma_{00} \text{ requires } \left[j_0^2\left(\frac{aq}{2}\right)\right] \tag{2.24}$$

$$\sigma_{11} \text{ requires } \left[j_0^2\left(\frac{aq}{2}\right) + 2 \times j_2^2\left(\frac{aq}{2}\right)\right] \tag{2.25}$$

$$\sigma_{10} \text{ and } \sigma_{01} \text{ require } \left[j_1^2\left(\frac{aq}{2}\right)\right] \tag{2.26}$$

Since the neutron absorption cross section shows a $1/v$ dependence, not only for the UCN energy region but for thermal neutron energies ($v_{\mathrm{n}} = 2200$ m/s) and less [44], the tabulated thermal absorption cross sections can be extrapolated to UCN velocities. For H_2 the thermal absorption cross section is 0.3326 barn per *atom*, for D_2 this is 0.000519 barn per *atom*.

3 New Aspects: Scattering on Rough Surfaces, Defects, and Phonons

[. . .] sve je mogućno; ništa nije stvarno, ali ništa nije neverovatno ni potpuno isključeno.

— Ivo Andrić, *Na Drini ćuprija, poglavlje 15 (1945)*

3.1 Previous UCN transmission experiments on light and heavy hydrogen

The very first neutron transmission measurements on hydrogen were made by Halpern et al. in 1937 [34], only one year after the wave nature of neutrons had been confirmed and only five years after the discovery of neutrons at all. This experiment was mainly fueled by the desire to verify theoretical predictions by Schwinger and Teller [110, 111], who showed that the slow neutron scattering cross sections of *para*- and *ortho*-hydrogen must differ significantly, if the neutron–proton interaction depended on the spin of both.

To the knowledge of the author, the first very cold neutron (VCN) transmission measurements on solid deuterium were done by a group at PNPI, Gatchina (Russia) [20]. They froze out deuterium from the liquid phase at four different speeds (freezing time 20 min, 1 hour, 2 hours, 3 hours). It was expected to see an unambiguous correlation between freezing speed and VCN transmission. The slower the crystal was frozen, the more transparent for VCNs it should be. The results, however, painted a different, unclear picture, see Fig. 3.1.

One problem was that the sample container was made from machined (unpolished) titanium. The amount of surface scattering on the container windows could not be quantified. It was equally impossible to optically verify both the fill height of the liquid in the sample container and the uniform freezing of the solid. Instead, the fill level was inferred from the container volume and the pressure difference in the gas reservoir. Therefore, the exact sample thickness was not well known. Also, it is possible that part of the liquid froze out on the walls of the sample container above the liquid level, thereby reducing the sample thickness. The VCN transmission was measured vertically.

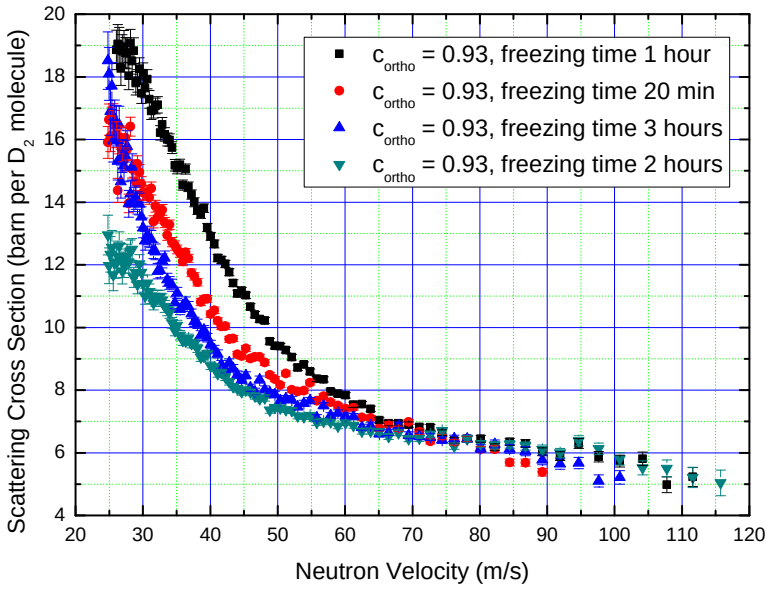

Figure 3.1: Scattering cross sections for solid deuterium crystals of various freezing speeds as inferred from VCN transmission. Adapted from Ref. [20] with permission. Copyrighted by the Russian Academy of Sciences.

The only other direct slow neutron transmission experiments on deuterium that the author is aware of, were carried out by a group from Paul Scherrer Institut (PSI) in Switzerland [21, 107] and used UCNs. These experimenters employed an aluminum sample container with machined aluminum neutron windows. During the experiments these windows bulged due to pressure differentials and introduced an error to the cross sections of about 10%. The final results were modeled using an effective sample thickness as a fit paramter. The crystals could be observed laterally through a sapphire window. Photos from [21] suggest cracks being present in the crystals, which had been frozen from the liquid phase. The rough surfaces of the aluminum windows, and consequently also the rough surfaces of the deuterium crystals, attenuated the UCN beam by an unquantified magnitude.

The experimentally determined scattering cross sections for solid deuterium at 18 K seemed to match their calculations well, see Fig. 3.2, while the cross sections of all colder crystals were significantly higher than the calculated 1-phonon up-scattering and incoherent elastic cross sections. This discrepancy, which is most likely due to a combination of scattering on crystal defects and the rough deuterium surface, was entirely attributed to defect scattering. However, the correlation between freezing procedure and the "additional isotropic elastic scattering process" introduced by Bryś et al. [21, 107] could not be quantified. The qualitative conclusion was that the total scattering cross section increases as the crystal is cooled down. The cross section also increased as a result of temperature cycling [21].

The discrepancy between the experimental data from Brys [21] for colder crys-

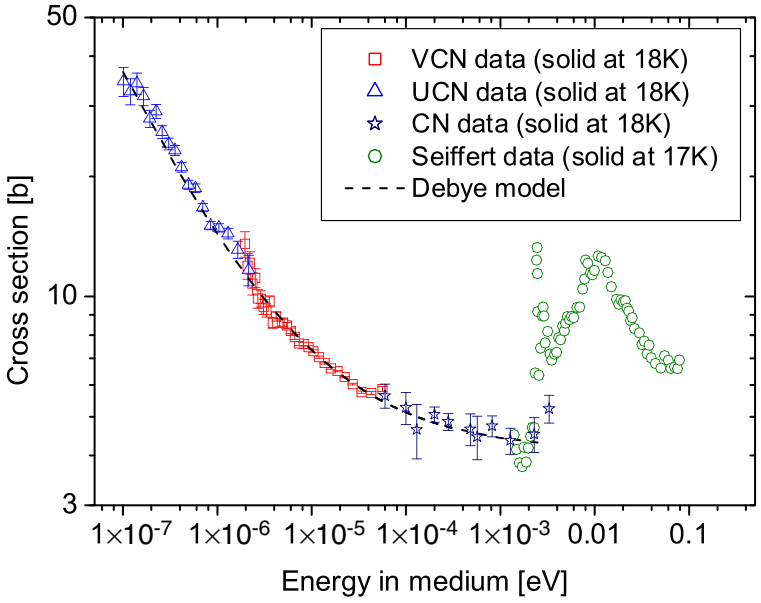

Figure 3.2: Measured cross sections per deuterium molecule. Included in the plot is the data of [112]. The expected cross section is dominated by thermal up-scattering and was calculated using the Debye model. The UCN data for other crystal temperatures are not shown. Reprinted from Ref. [107] with permission. Copyrighted by the American Physical Society.

tals and the Incoherent Approximation for 1-phonon up-scattering, see Section 3.2 for details, as well as the rough-surface neutron windows used in previous experiments [20, 21, 107, 113, 114] were the main motivation for the development of a sample container with low-roughness windows and the re-measurement of deuterium scattering cross sections. Low-roughness sample container windows allow for the determination of the unperturbed total cross section inside the medium, which in turn helps improve calculation models for superthermal UCN converters [115].

As part of this thesis, a sample container for cryogenic liquids and solids that reduces surface scattering to a minimum, was conceived, constructed and tested, see Chapter 5. With the help of this sample container, the proper preparation of the sample can be verified optically before the neutron measurement is started. The highly polished silica windows suppress surface scattering as much a possible and prevent bulging under pressure. This improved sample container was used in new UCN transmission measurements reported in this thesis and made possible the estimation of the defect concentrations in several sD_2 crystals.

Mindful of what has been said above, the determination of the true, unperturbed scattering cross section of real – rather than ideal – solid deuterium crystals for

UCNs has been a desideratum for the UCN research community for more than a decade now. The present work makes a contribution to remedy this lack of data.

Note: A part of this section has previously been published as
S. Doege et al. Optical Observation of Hydrogen and Deuterium Crystal Growth and Implications for Ultracold Neutron Transmission Experiments. ISINN-25 Conference Proceedings, JINR Dubna (Russia), pp. 31-40 (2018).

3.2 The Incoherent Approximation and corrections

For the experimental determination of defect scattering in the deuterium crystal, it is important to understand all other significant UCN loss mechanisms so that they can be calculated and subtracted from the experimental total cross section σ_{tot}. Absorption of UCNs by deuterium nuclei σ_{abs} (and, to a lesser extent, by hydrogen impurities) is well understood. It scales with $1/v_{\mathrm{UCN}}$. The incoherent elastic nuclear cross section $\sigma_{\mathrm{inc}}^{\mathrm{el,nuc}}$ is constanly 5.1 barn per D_2 molecule, see Section 2.4. The other remaining effect that removes UCNs from the direct beam, see Fig. 2.1, is 1-phonon up-scattering, i.e. energy transfer from the sample to the UCN.

When a neutron is scattered inelastically, it either gains energy from an elementary excitation, e.g. a phonon, or it creates a phonon and loses the corresponding energy ΔE. As for UCNs, they do not have enough energy to excite elementary excitations[1] and can therefore only gain kinetic energy. That energy gain is in almost all cases large enough (several μeV to meV) for these neutrons to leave the UCNs range. This up-scattering process is an important loss mechanisms in UCN traps, see Subsection 1.4.1.

1-Phonon neutron scattering can be coherent or incoherent. Both kinds can be separately described and contribute to the total double-differential cross section

$$\frac{\mathrm{d}^2\sigma}{\mathrm{d}\Omega\mathrm{d}E} = \frac{1}{4\pi}\frac{k_{\mathrm{f}}}{k_{\mathrm{i}}}\left[\sigma^{\mathrm{coh}} \times j_n^2\left(\frac{aq}{2}\right) \times S_{\mathrm{coh}}^{\mathrm{1ph}}(q,\omega) + \sigma^{\mathrm{inc}} \times j_n^2\left(\frac{aq}{2}\right) \times S_{\mathrm{inc}}^{\mathrm{1ph}}(q,\omega)\right] \tag{3.1}$$

Shape and spin state change, i.e. the type of rotational transition $J \to J'$, of the deuterium molecule are represented by the squared spherical Bessel functions $j_n^2\left(\frac{aq}{2}\right)$, where a denotes the equilibrium distance between the two deuterons in a molecule (0.74 Å) and n the order of the Bessel function, see Eq. 2.24ff. In monoatomic media, no Bessel functions are used in the double-differential cross section.

[1] An exception to this might be inelastic spin-flip scattering in substances with large hyperfine splitting energies, as was conjectured in 1968-69 [116, 117] and possibly observed in deuterium by Döge et al. [118].

In many cases, experimenters use the simplifying approach of the *Incoherent Approximation* [35], see Eq. 3.2, to compare their experimental results with calulations, e.g. Atchison et al. [107]. It neglects the coherent scattering law $S_{\mathrm{coh}}(q,\omega)$ and weights the incoherent one with both coherent and incoherent nuclear cross sections $\sigma_{\mathrm{tot}} = \sigma^{\mathrm{coh}} + \sigma^{\mathrm{inc}}$ instead. In the liquid state, σ^{coh} has to be weighted with the structure factor $S(q)$, which can be determined experimentally, to include the macroscopic structure of the liquid.

$$\frac{\mathrm{d}^2\sigma}{\mathrm{d}\Omega\mathrm{d}E} \simeq \frac{1}{4\pi}\frac{k_{\mathrm{f}}}{k_{\mathrm{i}}}\left[(\sigma^{\mathrm{coh}} + \sigma^{\mathrm{inc}}) \times j_n^2\left(\frac{aq}{2}\right) \times S_{\mathrm{inc}}^{1\mathrm{ph}}(q,\omega)\right] \tag{3.2}$$

3.2.1 The Incoherent Approximation (IA)

The quantification of inelastic up-scattering (1-phonon annihilation, inelastic scattering) of UCNs has been done for decades using the Incoherent Approximation (IA), for example in [51, 55, 107]. In the case of UCN scattering ($E_{\mathrm{n}} \to 0$) in solid deuterium, contributions from 2-phonon and higher-order phonon scattering can be neglected as their scattering cross section is less than 3% that of 1-phonon scattering[2] [35]. In the metals investigated in this thesis (Al, Zr, Cu), the 2-phonon scattering cross section is well below one percent of the 1-phonon cross section.

The standard form of the Incoherent Approximation is given in Eq. 3.3. For a detailed derivation see, for instance, Turchin [35]. The IA neglects interference of scattered waves from neighboring nuclei. In essence, it acts as if all scattering events were fully incoherent.

For isotopes with low coherent and high incoherent cross sections, e.g. hydrogen, the IA works well. Its applicability to isotopes with comparably high coherent cross sections, especially at low temperatures, is subject to restrictions and requires an interference correction, see the following subsection.

The calculation model for the phonon annihilation part of the IA (superscript *-1ph*) is given, for example, in Tarasov and Gurevich [109] as

$$\sigma_{00}^{\text{-}1\mathrm{ph}} = 24\sigma_{00}^{\mathrm{tot}}\left(\frac{m_{\mathrm{n}}}{m_{\mathrm{mol}}}\right) \times \left(\frac{E_0}{k_{\mathrm{B}}\Theta_{\mathrm{D}}}\right)^3 \int\int \mathrm{d}\xi\mathrm{d}\eta \mathrm{e}^{-2W(\eta)} \frac{j_0^2(ak_0\eta)}{\exp\left(\xi E_0/k_{\mathrm{B}}T\right) - 1} \tag{3.3}$$

using the dimensionless variables $\eta \equiv \frac{q}{2k_0}$ and $\xi \equiv \frac{\hbar\omega}{E_0}$. The spherical Bessel function $j_0^2(ak_0\eta)$ was added to the equation to account for the shape of the *ortho*-deuterium molecule. Phonon creation can be neglected in the case of UCNs.

Since the UCN parabola in the kinematic region is narrow, see Section 2.2, the Debye–Waller factor (DWF) and the Bessel function can be calculated for an average value of their integration variables. That way, they become constants in

[2] Calculated using the Debye temperature Θ_{D} for *ortho*-deuterium as determined by Nielsen and Møller [119] (114 K at 0 K). For temperatures from 5 K to 18 K Θ_{D} decreases from 110 K to 100 K [120].

η and can be pulled out of the η integral. Now the inner integral over η can be solved analytically, which yields

$$\sigma_{00}^{\text{-1ph}} = 24\sigma_{00}^{\text{tot}} \left(\frac{m_\text{n}}{m_\text{mol}}\right) \times \left(\frac{E_0}{k_\text{B}\Theta_\text{D}}\right)^3 \int_0^{k_\text{B}\Theta_\text{D}/E_0} \text{d}\xi \text{e}^{-2\overline{W}(\overline{\eta})} \times \frac{1}{8} \times \sqrt{1+\xi} \times (2+\xi) \times \\ \times \left[j_0^2 \left(\frac{ak_0\sqrt{1+\xi}}{2} \right) \times \frac{\xi}{\exp\left(\xi E_0/k_\text{B}T\right) - 1} \right], \quad (3.4)$$

where $2\overline{W} = \frac{1}{3}\langle u^2 \rangle k_0^2(\xi+1)$, $\sigma_{00}^{\text{tot}} = \sigma_{00}^{\text{coh}} + \sigma_{00}^{\text{inc}} = 27.5$ barn the nuclear total cross section of an *ortho*-deuterium molecule, m_n the neutron mass, m_mol the mass of one deuterium molecule, T the sample temperature, E_0 the energy of the incoming slow neutron and Θ_D the Debye temperature of the sample at temperature T. This integral has to be solved numerically. Tab. 3.2 shows the 1-phonon up-scattering cross sections for *ortho*-deuterium (00) in the IA.

A simplification of the IA is the so-called Stepanov equation [121]

$$\sigma_\text{inc}^{\text{1ph-Stepanov}} \simeq \frac{45}{8}\zeta\left(\frac{7}{2}\right)\sqrt{\pi}\sigma_{00}^{\text{tot}} \left(\frac{m_\text{n}}{m_\text{mol}}\right) \times \sqrt{\frac{k_\text{B}T}{E_0}} \times \left(\frac{T}{\Theta_\text{D}}\right)^3, \quad (3.5)$$

where $\zeta(x)$ is the Riemann zeta-function.

This equation neglects the exact forms of the Debye–Waller factor (DWF) and the Bessel function j_0^2 by setting both of them equal to 1. Doing so, the integration of the double-differential cross section over the kinematic region simplifies greatly and can be done analytically. This, however, comes at the price of limited validity. The Stepanov equation is only valid at low temperatures ($T < 5$ K for deuterium) and low neutron energies. At a deuterium temperature of $T = 18$ K, the Stepanov equation delivers 1-phonon cross sections about 40% above the full incoherent approximation. Therefore, it is not suited for calculating the 1-phonon up-scattering cross section in warm deuterium crystals of $T = 12$ to 18 K.

3.2.2 Coherent corrections to the IA, the case of solid deuterium

Lavelle et al. [113] found that the up-scattering of UCNs due to 1-phonon annihilation in solid deuterium is much less temperature-dependent than predicted by the IA. Their experimental results were better explained by an up-scattering cross section that was two to four times smaller than the IA. A paper that Liu et al. [122] wrote based on these findings, taking into account a modeled realistic density of states and deuterium crystal properties, did unfortunately not appear in a journal.

Golub provided in his book [43] a method to estimate the *coherent* 1-phonon scattering cross section. The result of this calculation for deuterium is given here to understand by how much the IA has to be corrected in the case of strong

coherent scatterers. When the real hcp lattice (2 molecules per unit cell) of solid deuterium is approximated by an fcc structure (1 molecule per unit cell) of the same density, the *coherent* 1-phonon up-scattering in *ortho*-deuterium at $T = 10$ K and for $v = 10$ m/s is 0.45 barn/molecule (b/m). After a small correction of 10% for optical phonon modes (to compensate for neglecting the hcp crystal structure) is applied, this value becomes $\sigma_{00}^{\mathrm{coh,\text{-}1ph}} = 0.50$ b/m.

When dividing the value for $\sigma_{00}^{\mathrm{IA}}$ from the IA for $T = 10$ K, see Tab. 3.2, into a coherent and incoherent part by applying $\sigma_{00}^{\mathrm{coh}} = 22.4$ b/m and $\sigma_{00}^{\mathrm{inc}} = 5.1$ b/m as weighting factors, one gets

$$\sigma_{00}^{\mathrm{IA}} = 2.0\,\mathrm{b/m} = \sigma_{00}^{\mathrm{coh,IA}} + \sigma_{00}^{\mathrm{inc,IA}} = (1.63 + 0.37)\,\mathrm{b/m}. \tag{3.6}$$

When replacing the coherent part, 1.63 b/m, by the value obtained by the Golub approximation, 0.50 b/m, the sum total is 0.87 b/m, which is a only 0.435 times the value calculated by using the IA. In other words, the IA is a factor of 2.3 too high for solid *ortho*-deuterium. This finding is in very good agreement with the factor of 2.6 for $T = 10$ K presented in the unpublished paper by Liu et al. [122].

Placzek and van Hove [123] provided an even more rigorous method to calculate the coherent correction to the IA for low temperatures and low neutron energies. In analogy to Eq. 3.1, they write

$$\sigma^{\mathrm{corrIA}} = \sigma_{\mathrm{nuc}}^{\mathrm{inc}} \times S^{\mathrm{inc}} + \sigma_{\mathrm{nuc}}^{\mathrm{coh}} \times S^{\mathrm{coh}}. \tag{3.7}$$

Here, S^{inc} and S^{coh} refer to the *integrals* of the dynamic structure factor over the kinematic region. The Bessel functions and all other material properties are included in $S^{\mathrm{inc/coh}}$. After some rearrangement of the terms in this equation, one gets

$$\sigma^{\mathrm{corrIA}} = \underbrace{\sigma_{\mathrm{nuc}}^{\mathrm{tot}} \times S^{\mathrm{inc}}}_{\sigma^{\mathrm{IA}}} \times \underbrace{\left[1 + \frac{\sigma_{\mathrm{nuc}}^{\mathrm{coh}}}{\sigma_{\mathrm{nuc}}^{\mathrm{tot}}} \times \left(\frac{\delta S}{S^{\mathrm{inc}}}\right)\right]}_{\text{correction term}}, \tag{3.8}$$

where $\frac{\delta S}{S^{\mathrm{inc}}}$ is the Placzek–van Hove correction factor and for *ortho*-deuterium $\sigma_{\mathrm{nuc}}^{\mathrm{coh}} = \sigma_{00}^{\mathrm{coh}}$ and $\sigma_{\mathrm{nuc}}^{\mathrm{tot}} = \sigma_{00}^{\mathrm{tot}}$.

Placzek and van Hove provided a way to calculate $\frac{\delta S}{S^{\mathrm{inc}}}$, the values of which are given in Tab. 3.1 for various temperatures. It is obvious that the IA used hitherto yields cross sections that are, depending on the temperature, a factor of 2 to 5 too high. The corrected 1-phonon up-scattering cross sections compare very well with those obtained by Liu et al. [122], who used a completely different approach. The good agreement between the two different approaches underlines the pertinence of the corrections presented here.

Including the corrections to the IA described above, the various means of calculating the 1-phonon up-scattering (coherent and incoherent) are shown and compared in Tab. 3.2 for a selection of typical solid deuterium temperatures and an UCN (in-medium) velocity of 10 m/s. The values for $\sigma_{\mathrm{inc}}^{\mathrm{el}}$ follow from Section 2.4,

Temp. [K]	$\frac{\delta S}{S^{\mathrm{inc}}}$	OEF	$\chi_{\mathrm{D2}} = \sigma^{\mathrm{corrIA}}/\sigma^{\mathrm{IA}}$	$\chi_{\mathrm{D2}}^{\mathrm{Liu}}$
5	-0.9904	5.19	0.19	–
10	-0.8227	3.03	0.33	0.39
15	-0.6588	2.16	0.46	0.50
18	-0.5976	1.95	0.51	0.56

Table 3.1: The Placzek–van Hove correction factors $\frac{\delta S}{S^{\mathrm{inc}}}$ are given for various temperatures. Inserting these factors along with the nuclear cross sections for *ortho*-deuterium molecules into Eq. 3.8 gives χ_{D2}, the ratio of corrected IA to "old" IA. These ratios compare well with those obtained by Liu et al., $\chi_{\mathrm{D2}}^{\mathrm{Liu}}$. The inverse of χ_{D2} tells by which factor the "old" IA overestimates the actual 1-phonon up-scattering cross section, hence overestimation factor (OEF).

$\sigma_{\mathrm{abs}}^{\mathrm{H2}} + \sigma_{\mathrm{abs}}^{\mathrm{D2}}$ was taken from Sears [44], and $\sigma_{10}^{\mathrm{0ph}}$ and $\sigma_{10}^{\pm 1\mathrm{ph}}$ (relaxation of rotational excitation) from Liu et al. [54]. The values for $\sigma^{\mathrm{Stepanov}}$, σ^{IA} and σ^{corrIA} were calculated as explained above.

Temp. K	$\sigma_{\mathrm{inc}}^{\mathrm{elast}}$ [barn]	$\sigma_{\mathrm{abs}}^{\mathrm{H2}}$ [barn]	$\sigma_{\mathrm{abs}}^{\mathrm{D2}}$ [barn]	$\sigma_{10}^{\mathrm{0ph}}$ [barn]	$\sigma_{10}^{\pm 1\mathrm{ph}}$ [barn]	$\sigma^{\mathrm{Stepanov}}$ [barn]	σ^{IA} [barn]	σ^{corrIA} [barn]
5	5.1	146.3	0.23	24.8	1.0	0.2	0.2	0.04
10	5.1	146.3	0.23	24.8	1.2	2.4	2.0	0.66
15	5.1	146.3	0.23	24.8	1.8	9.7	7.3	3.4
18	5.1	146.3	0.23	24.8	2.3	18.4	12.9	6.6

Table 3.2: Comparison of various methods for calculating 1-phonon up-scattering cross sections (three columns on the right) for different *ortho*-deuterium temperatures. In addition, other UCN loss channels are given with their cross sections per molecule (four columns in the center), as well as the incoherent elastic cross section (second column from the left). All cross sections are given for one *molecule* and have been calculated for an UCN velocity of 10 m/s using $\Theta_{\mathrm{D}} = 110$ K.

The cross section of 1-phonon up-scattering in solid deuterium has been calculated above. The experimental data for solid deuterium $\sigma_{\mathrm{tot}}^{\mathrm{exp}}(v)$, take for example $T = 10$ K, is fitted by taking the relevant cross sections from Tab. 3.2 and Subsec-

tion 6.5.1,

$$\sigma_{\mathrm{tot}}^{\mathrm{exp}}(v) = \sigma_{\mathrm{def}}(v) + \left(\underbrace{5.1}_{\text{incoh. el.}} + \underbrace{\frac{6.6}{v}}_{\text{corrIA}} + \underbrace{\frac{0.025}{v} \times 260}_{\sigma_{10}^{0/\text{-}1\mathrm{ph}}} + \underbrace{\frac{0.001 \times 1463 + 2.3}{v}}_{\sigma_{\mathrm{abs}}^{\mathrm{H2}} + \sigma_{\mathrm{abs}}^{\mathrm{D2}}} \right). \quad (3.9)$$

The only free fit parameter is the defect scattering cross section, $\sigma_{\mathrm{def}}(v)$, for which the Guinier and spherical form factor models are employed, see Section 3.3.

3.2.3 Corrected IA for metal foils

The total cross section of matter is composed of bulk scattering, surface scattering, and absorption. From Tab. 6.2 the absorption cross sections at thermal neutron energies ($E_{\mathrm{kin}} = 25\,\mathrm{meV}$, $v_{\mathrm{UCN}} = 2200\,\mathrm{m/s}$) can be taken and extrapolated to UCN energies by using the relation $\sigma_{\mathrm{abs}} \times v_{\mathrm{UCN}} = \mathrm{const}$.

Tab. 3.3 lists the 1-phonon up-scattering cross section using the IA, the 1-phonon up-scattering cross section using corrections to the Incoherent Approximation (corrIA), and the absorption cross section for all three metals under investigation: Al, Cu, and Zr. The corrections to the IA can only strictly be calculated for cubic crystals. Since Zr has an hcp crystal structure at room temperature, it was assumed to have an fcc structure of the same density for the sake of calculating the correction. The coherent correction to the IA are not significant compared to absorption, which is the dominant UCN loss channel for all three metals at room temperature. For the copper samples, up-scattering can be neglected altogether.

Sample	σ^{IA} [b]	σ^{corrIA} [b]	$\sigma_{\mathrm{abs}}^{10\mathrm{m/s}}$ [b]	Sum [b]	$\sigma_{\mathrm{tot}}^{\mathrm{exp}}$ [b]
Al	6.3	7.4	50.8	58.2	175 ± 78
Cu	18.8	17.3	832	849	803 ± 73
Zr	12.7	10.1	40.7	50.8	636 ± 348

Table 3.3: 1-Phonon up-scattering calculated according to the Incoherent Approximation (IA) and the IA corrected for coherent effects (corrIA), see Section 3.2, as well as absorption for Al, Cu, and Zr. The sum column gives the combined values of corrIA and absorption, while the right-hand column gives the experimental values from Chapter 7.3 extrapolated to 10 m/s. All cross section values are calculated for room temperature and $v_{\mathrm{UCN}} = 10\,\mathrm{m/s}$. The cross sections for absorption and incoherent scattering scale with $1/v$ in the UCN energy region.

With up-scattering and absorption being known, the remaining loss of UCNs in the transmission experiment on pure metal foils can be attributed to surface

scattering. Coherent elastic scattering in the bulk can be neglected due to the UCNs' large wavelengths, which go far beyond any Bragg cutoff wavelength. Due to the high purity of the foils, no small-angle scattering from impurities is expected.

3.3 Scattering on crystal defects

The presence of defects in a homogenous medium does not change significantly the 1-phonon up-scattering process and the imaginary part of the neutron-optical potential [124]. In the case of cryogenic temperatures, these changes are of the order of 10^{-6}. Frei et al. [58] have demonstrated this experimentally by showing that the generalized density of states (gDOS), i.e. the phonon spectrum, of solid deuterium depends neither on the crystal preparation method (frozen from the liquid or gaseous phase) nor on the freezing speed, which resulted in crystals with different transparency.

However, the mean free path of UCNs in solid deuterium can be significantly reduced by density fluctuations caused by cracks and crystal defects that have dimensions similar to the UCN wavelength [43].

In some of the VCN and UCN transmission experiments described above, defects were conjectured to cause additional scattering, but no quantitative estimate for this effect has been provided.

Lavelle et al. [113] estimated the elastic cross section for UCNs due to defects to be a few barn per molecule, in the same range as the incoherent elastic (nuclear) cross section (5.1 barn). This result was based on cold neutron transmission data and Monte Carlo simulations. No direct measurement of these defects had been performed.

One way to estimate the size and concentration of defects in solid deuterium is to apply the two-phase model by Guinier [125, 126]. This model assumes homogeneously distributed, sharp-edged, non-correlated particles of phase 1 inside a matrix of phase 2. All particles of phase 1 have the same size. Applied to a real deuterium crystal this is, of course, a simplification; one that allows for the first estimate of the defect size in solid deuterium. In addition, all particles of phase 1 are assumed to be of spherical shape with a generalized radius of gyration R_g. This radius of gyration is related to the radius of the spheres, R_s, by $R_\mathrm{g} = \sqrt{(3/5)}R_\mathrm{s}$. The Guinier model is valid for $k_0 R_\mathrm{g} < 1.2$ [126], which is fulfilled for typical UCN velocities and defect sizes of about 100 Å and less.

The double-differential cross section for the Guinier two-phase model is

$$\frac{\mathrm{d}\sigma}{\mathrm{d}\Omega}(q) = \underbrace{\frac{N_\mathrm{p}}{N_\mathrm{s}}}_{c_\mathrm{p}} \underbrace{([N_\mathrm{s} b_\mathrm{s}^\mathrm{coh} - N_\mathrm{p} \underbrace{b_\mathrm{p}^\mathrm{coh}}_{=0}]^2 \, V_\mathrm{p}^2)}_{(\Delta\rho)^2} \times \exp\left(-\frac{q^2 R_\mathrm{g}^2}{3}\right), \tag{3.10}$$

where N_p is the number density of defects, N_s the number density of the sample

molecules, i.e. deuterium, c_p the defect concentration per sample molecule, $b_\mathrm{s}^\mathrm{coh}$ the coherent scattering length of the sample (needs to be taken times two for the two deuterium atoms in a molecule), $b_\mathrm{p}^\mathrm{coh} = 0$ the scattering length of the empty (defect) phase, $\Delta\rho$ the difference in scattering length density between the sample bulk and the defects (vacuum), V_p the volume of the spherical defects, and k_0 the wave vector of the incoming UCN.

When this formula is integrated from 0 to $2k_0$, it gives an expression for the removal cross section due to crystal defects

$$\sigma^\mathrm{el,Guinier}(k_0) = 5\pi \times c_\mathrm{p} \times [N_\mathrm{s} b_\mathrm{s}]^2 V_\mathrm{p}^2 \times \frac{1}{(k_0 R_\mathrm{s})^2} \times \left[1 - \exp^{-\frac{4}{5}(k_0 R_\mathrm{s})^2}\right], \tag{3.11}$$

which is valid for $k_0 R_\mathrm{s} \lesssim 1.5$.

An extension for neutrons of larger k_0 can be added to the model by using the spherical form factor, $F_\mathrm{k}(q) = 3 \times j_1(qR_\mathrm{s})/qR_\mathrm{s}$,

$$\frac{\mathrm{d}\sigma}{\mathrm{d}\Omega}(q) = \underbrace{\frac{N_\mathrm{p}}{N_\mathrm{s}}}_{c_\mathrm{p}} \left([N_\mathrm{s} b_\mathrm{s}]^2 V_\mathrm{p}^2\right) \times \left[\frac{3 j_1(qR_\mathrm{s})}{qR_\mathrm{s}}\right]^2, \tag{3.12}$$

which has a Porod-like behavior ($\mathrm{d}\sigma/\mathrm{d}\Omega \propto 1/q^4$) for $q \to \infty$.

After integration, this expression yields

$$\sigma^\mathrm{el,sph\text{-}form}(k_0) = c_\mathrm{p} \times [N_\mathrm{s} b_\mathrm{s}]^2 V_\mathrm{p}^2 \times \frac{9\pi}{2k_0^2 R_\mathrm{s}^2} \times \left[1 - j_0^2(2k_0 R_\mathrm{s}) - j_1^2(2k_0 R_\mathrm{s})\right], \tag{3.13}$$

where j_0 and j_1 are spherical Bessel functions.

In the limit of very slow neutrons ($k_0 \to 0$), this reduces to the same expression as Eq. 3.11.

In the limit of very fast neutrons ($k_0 \to \infty$), Eq. 3.13 reduces to

$$\sigma^\mathrm{el,sph\text{-}form}(k_0) = 4\pi \times c_\mathrm{p} \times [N_\mathrm{s} b_\mathrm{s}]^2 V_\mathrm{p}^2 \times \frac{9}{8} \times \left[\frac{1}{(k_0 R_\mathrm{s})^2} - \mathcal{O}\left(\frac{1}{k_0^4 R_\mathrm{s}^4}\right)\right]. \tag{3.14}$$

It is obvious that this kind of scattering does not play a role for faster neutrons as $\sigma^\mathrm{el,sph\text{-}form} \to 0$ for $k_0 R_\mathrm{s} \gg 1$.

3.4 UCN reflection from rough surfaces

Ultracold neutrons are highly sensitive to rough surfaces, which can be regarded as irregularities on the nanometer or micrometer scale. Since UCN wavelengths (100 to 1000 Å) are of the same order as the microscopic roughness of a wide range of materials, they can interact with these irregularities. A typical, simplified measure for roughness is the centerline-average roughness R_a, see Section 3.5. Two related – but in a practical application somewhat different – effects have to be considered.

The first one, which is important to this work, is the scattering of UCNs incident perpendicularly on a rough metal or sample surface. In a transmission experiment, see Section 2.1 for details, these UCNs are supposed to traverse the sample and get scattered only by the sample bulk. If instead they are scattered on the rough sample surface, they do not reach the detector and introduce an error, i.e. an apparently higher scattering cross section, to the measurement that needs to be corrected for.

The second effect is the diffuse reflection of UCNs from rough surfaces. In a neutron guide, UCNs are supposed to move in the direction of the exit by specular reflections from the guide's inner walls. That is, the angle of incidence is the same as the angle of reflection and both incoming and reflected beam are co-planar. The neutron retains its velocity component in the direction of flight, v_z. If the guide tube is not sufficiently well polished on the inside, neutrons can be reflected diffusely, which means they significantly change their direction of travel and can even move backwards inside the guide (so-called retro-diffusion). In the case of diffuse reflection, the velocity components of the neutron, v_x, v_y, v_z are mixed. The angle of reflection no longer depends on the angle of incidence, but follows a cosine distribution with respect to the surface normal (for $R_a \ll \lambda_n$) [43] and shows a more complicated behavior for surfaces with smaller roughness [42]. Diffuse reflection of UCNs, which is also called non-specular or off-specular reflection, has been studied to better understand UCN transport in guide tubes [127] and to build an extraction mechanism for UCN sources that is sensitive to the neutron's direction of flight [128]. To date, there exists no comprehensive theory to predict the ratio of specular to diffuse scattering for a given material with a given surface roughness. In UCN transport simulations using Monte Carlo methods, free or semi-free parameters are usually used for diffuse scattering, e.g. in Atchison et al. [55].

Surface roughness also plays a role in increased absorption of UCNs in traps [121], such as those used in neutron lifetime experiments.

The following points are to be considered when improving the UCN density extractable from superthermal UCN sources. They stress the role UCN scattering on rough surface plays in this process.

1. Maximize the mean free path λ_{mfp} of UCNs inside the source material, see Subsection 3.3,

2. minimize the surface roughness of the UCN converter medium, e.g. solid D_2,

3. minimize the surface roughness of any vacuum separator foil in the UCN beam path, and

4. lose as little as possible UCN density on the way from the converter medium to the experimental installation due to diffuse reflection.

3.5 UCN transmission through metal foils with rough surfaces

As Lavelle et al. [113] found out experimentally in 2010, the rough aluminum windows of their sample cell caused UCN losses of up to 3/4. Alas, this effect was not further studied and has not been taken into account quantitatively in the previously cited recent literature on UCN *transmission* experiments, where rough-surface sample containers were used.

But rough surfaces on sample containers are not the only reason why UCNs are lost from the direct beam. At the place where UCNs leave the converter volume, a so-called exit window is necessary to protect the converter volume at a temperature of 5 K or less from attracting gaseous impurities. Also, in a lot of cases it is necessary to separate the insulation vacuum of the UCN source, such as the Turbine at the ILL, from the neutron guide vacuum and the vacuum of the experimental equipment. The material of choice for these vacuum diaphragms are thin aluminum foils of thicknesses between 30 and 100 μm, which scatter a significant fraction of the UCNs due to their surface roughness (and inhomogeneities if aluminum alloys are used).

Studies of exit window materials for the UCN sources Mini-D2 in Mainz [129] and PSI [130] investigated the best choice of materials for this application. Aluminum and zirconium were identified as the best candidates. These studies used thin metal foils of a few hundred micrometers thickness. They noticed a significantly lower transmission than expected. Surface scattering was considered to be one of the causes but no quantitative explanation or estimate was provided. One could say that surface scattering of UCNs has this far been a known unknown.

UCN transmission measurements on deuterium using aluminum sample windows with rough surfaces [131] suggested that a significant fraction of UCNs got scattered out of the beam by the rough surfaces of both the deuterium sample and the aluminum windows. Therefore, I hypothesize that the thickness of metal foil samples (and that of sample container windows) has only a limited influence on the total transmission through thin metal foils. Much more important than its thickness is the surface roughness of the foil.

In Frei at al. [129] and Atchison et al. [130] the different sample thicknesses were achieved by layering several thinner foils on top of each other[3]. By doing that, the bulk material was increased, but so was the number of surfaces. It is therefore not

[3] In the study by Atchison et al. [130], no mention was made of how the different foil thicknesses were achieved. The lead author, M. Daum, revisited the experiment's notebooks and could not find a note about whether the foils reported in Fig. 9 (top) were single foils or stacked on top of each other. The unitization of foils reported in the paper (multiples of 100 μm) suggests stacked foils. This is supported by the fact that the 5+1 data points describe a nearly perfect exponential decay over thickness – something that is not to be expected for single foils of different thicknesses, see Eq. 3.17. The re-examination of the results from [130], see Tab. 7.3, strongly supports this "stacked foils" conjecture.

surprising that the thickness-dependent transmission curves show an exponential decay with increasing foil thickness, or better: with an increasing number of rough surfaces traversed by the UCN beam.

This made it necessary to repeat UCN transmission experiments with metal foils of the same bulk material and surface preparation but with different thicknesses. In doing so, the bulk thickness can be varied and the number of surfaces traversed by the neutrons remains constant at two. Mathematically speaking, transmissivity data of two foils of different thickness is enough to solve an equations with two independent variables – one for the bulk scattering cross section σ_{tot} and one for the surface scattering term A.

The first treatment of surface scattering of UCNs was proposed by Steyerl [132]. He developed a mathematical model for the interference of neutrons scattering from correlated peaks ξ on a plane surface. For UCNs that are incident perpendicularly on a rough sample surface ("macroroughness") and have a wave vector (out of medium) $k \gg |k_{\mathrm{l}}|$, the total fraction of UCNs that is scattered out of the direct beam by one surface is

$$L_{\mathrm{t}} = \frac{I_{\text{1-surf}}}{I_0} = \frac{1}{4}\frac{b^2 k_{\mathrm{l}}^4}{k^2}, \tag{3.15}$$

where $k_{\mathrm{l}} = m \times v_{\mathrm{crit}}/\hbar$, b the coherent scattering length of the scattering nuclei, I_0 the intensity incident on the rough surface and $I_{\text{1-surf}}$ the intensity of UCNs scattered out of the direct beam. The condition $k \gg |k_{\mathrm{l}}|$ is fulfilled for deuterium and the metals treated in this thesis for all except the very slow UCNs of $v \lesssim 5$ m/s (out of medium).

In analogy to the scattering of light on particles considerably smaller than (Rayleigh scattering, $d \ll \lambda$) or of about the same size (Mie scattering, $d \approx \lambda$) as the photon wavelength λ, it is assumed that UCN scattering on surface roughness and defects in the range of up to a few hundred Ångströms is mostly elastic.

Some of the UCNs scattered elastically at the surface only change their direction slightly and form an angle with the beam axis that is accepted by the detector. As shown in Section 6.4, the error introduced by these scattered neutrons and the non-vanishing detector solid angle is negligible.

Assuming the same surface treatment, and thence the same surface roughness, for each foil of the same metal, the transmission equation for uniformly absorbing and scattering media,

$$T = \frac{I_{\mathrm{n}}}{I_0} = \mathrm{e}^{-N\sigma_{\mathrm{tot}} d_{\mathrm{n}}} \tag{3.16}$$

can be expanded as

$$T = \frac{I_{\mathrm{n}}}{I_0} = \mathrm{e}^{-N\sigma_{\mathrm{tot}} d_{\mathrm{n}} - 2A}, \tag{3.17}$$

where T represents the measured absolute transmissivity of sample n, and A the UCN loss factor on *each* one of the two surfaces of the foil for a given neutron velocity. The particle number density N_{v} is known, as well as the sample thickness d.

In order to determine both the total cross section σ_{tot} and A, the transmissivities T_1 and T_2 through foils of at least two different thicknesses need to be recorded. Then, the transmission equations can be divided by one another, whereupon the surface loss term $-2A$ vanishes

$$T_1 = \frac{I_1}{I_0} = \mathrm{e}^{-N\sigma_{\text{tot}}d_1} \times \mathrm{e}^{-2A} \tag{3.18}$$

$$T_2 = \frac{I_2}{I_0} = \mathrm{e}^{-N\sigma_{\text{tot}}d_2} \times \mathrm{e}^{-2A} \tag{3.19}$$

$$\frac{T_1}{T_2} = \mathrm{e}^{(d_2-d_1)N\sigma_{\text{tot}}}. \tag{3.20}$$

Rearranging the latter equation yields an expression for the bulk's total cross section

$$\sigma_{\text{tot}} = \frac{\ln\left(\frac{T_1}{T_2}\right)}{(d_2-d_1)N}. \tag{3.21}$$

This total cross section σ_{tot} can then be plugged into both equations for T_1 and T_2 to determine the surface scattering term and estimate the corresponding error.

The UCN loss factor A can be related to the Steyerl equation, Eq. 3.15, by

$$L_{\text{t}} = \frac{I_{\text{1-surf}}}{I_0} \approx \left(1-\mathrm{e}^{-A}\right), \text{ for } A \lesssim 0.25\text{:}\;\; L_{\text{t}} \approx A \tag{3.22}$$

and the surface roughness parameter b as seen by the neutrons can thus be derived as follows

$$b \approx \sqrt{\frac{(1-\mathrm{e}^{-A}) \times 4 \times k^2}{k_{\text{l}}^4}}. \tag{3.23}$$

This surface roughness is represented by the mean square amplitude of elevations above and below the reference plane of the surface. For surfaces with a relatively even distribution of peaks and valleys and no extreme peaks, the mean square amplitude is quite similar to the center-line average roughness, also called the arithmetical mean deviation of the assessed roughness profile, R_{a}. A line profile of the surface is taken and then the average deviation from the imaginary center plane is calculated as

$$R_{\text{a}} = \frac{1}{n}\sum_{i=1}^{n}\left|y_i\right|. \tag{3.24}$$

Generally, it is difficult to obtain the same roughness values for measurements of the same sample using different techniques. For example, the non-zero curvature radius of the stylus used in an atomic-force microscope (AFM) will lead to smaller roughness readings than those obtained by non-contact optical methods [133]. One single roughness parameter is often not enough to describe the entire surface roughness with short-range and long-range correlations. An overview of roughness parameters was published by Gadelmawla et al. [134].

How the mechanically determined roughness parameter R_{a} of metal foils compares to that obtained by UCN transmission and the use of Steyerl's theory, b, is shown in Section 7.3.

Part II

Methods and Instruments

4 Experimental Setup and the UCN Beamline PF2-EDM at ILL

To measure is to know.
— Lord Kelvin

4.1 Experimental setup for UCN transmission measurements in TOF geometry

As described in Section 2.1, the transmission experiment requires collimated neutrons. To that end, the UCNs issuing from the Turbine at the beamline PF2-EDM first pass a titanium disk with holes of 0.5 mm in diameter. UCNs that impinge on the disk are absorbed. The collimated beam then passes a chopper, which chops the incoming beam into bunches of neutrons. This time-of-flight (TOF) technique is necessary for gaining velocity information about each measured neutron as the beam is polychromatic. Over the flight path, these bunches are smeared out due to the different neutron velocities present in each bunch. After the neutrons pass the thermal shield made of highly polished undoped silicon, they traverse the actual sample. Behind the sample lies the other half of the flight path and the neutron detector. Polyethylene foil is used as a liner for the last part of the flight path and removes from the beam those UCNs, whose flight path deviates too much from the beam axis. The removal takes place by either absorption on hydrogen atoms or up-scattering to thermal energies. The detector receives a trigger pulse from the chopper at the time the chopper window opens. This trigger signal, along with the measured flight time and the constant flight path, allows for calculating the neutrons' velocities. The total flight path was 358 mm when using a beam tube without a viewport (as used for measuring metal foils) and 455 mm with a viewport (as used for deuterium samples), see Fig. 4.1.

The setup is shown in Fig. 4.2. In the flight tube between the cryostat and the neutron detector, a horizontal viewport can be seen. A mirror on a rod above the viewport can be lowered down into the neutron beam path and the sample preparation process can be observed in real time. When the sample is ready to be measured with neutrons, the mirror can be raised out of the beam.

All parts of the experimental setup are described in detail in the following sections.

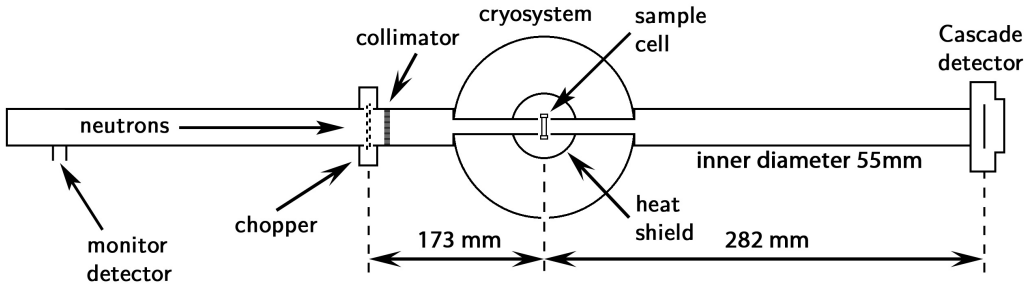

Figure 4.1: The TOF geometry as it was used for the deuterium transmission measurements.

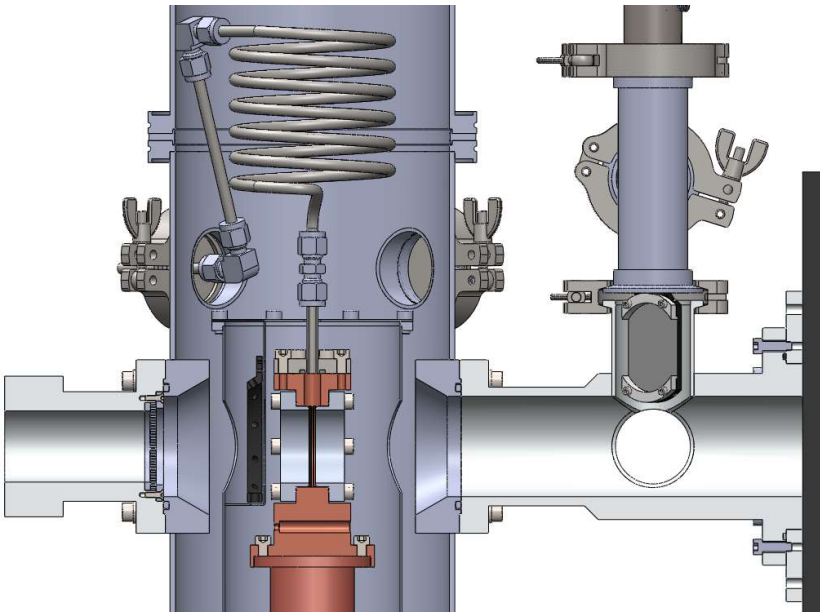

Figure 4.2: Cryostat with sample container and viewport in the right-hand part of the flight path. An oblique view and description is given in Fig. 5.7.

4.2 Cryostat and refrigerator

For the experiments described here, a closed-cycle refrigerator from Sumitomo (Japan), type RDK-408D2 was used. Its working fluid is ^{4}He and the waste heat was cooled away in a fan-based compressor. The two-stage (4 K and 70 K) Sumitomo cold-head had a cooling power of 1 W at 4 K, see the capacity map in Fig. 4.3. How the sample container was connected to the cold-head is described in detail in Chapter 5.

This cryostat has been used before in experiments at the ILL [114, 118, 135]. However, preparing for the experiments of this PhD thesis, the cryostat was improved in terms of cooling and vacuum performance. A test of the maximum heat

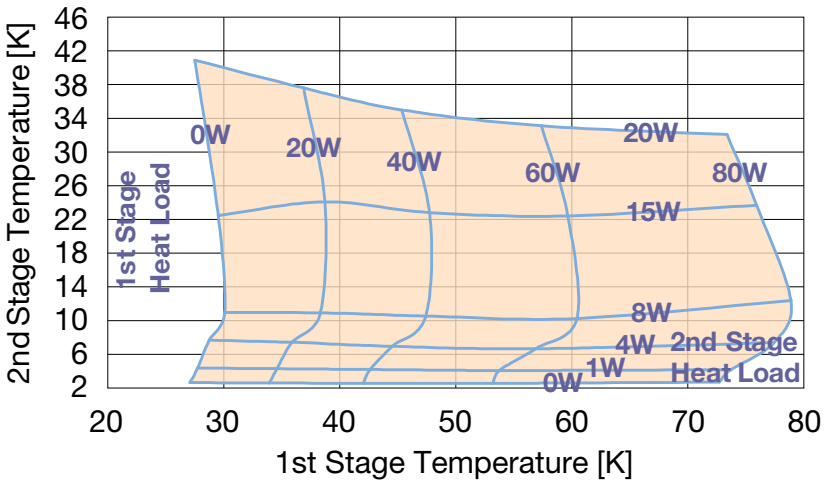

Figure 4.3: Capacity map of the cold head of the closed-cycle refrigerator Sumitomo RDK-408D2 operated at 50 Hz. Copyright by Sumitomo Heavy Industries Ltd., Japan.

load that the cold-head was able to cool away was performed, see Fig. 5.1, and was later used to simulate the temperature distribution in the sample container, see Section 5.1. Tab. 4.1 gives an overview of the improvements of the experimental setup compared to the experiments carried out in 2012 by Döge et al. [136].

In addition to the parameters shown in this table, the inner thermal shield of the cryostat was equipped with a heat radiation reflector facing the neutron beam tube. The reflector was a 0.5 mm thick double-side polished undoped silicon wafer with a diameter of 50.8 mm (2 inches). An aluminum foil, see Section 4.8, was used as a vacuum separator to prevent volatile substances that may possibly be present in the neutron beam tube, from migrating towards the cold parts in the cryostat.

After the first optical observations of solid hydrogen and deuterium were made at cryogenic temperatures, it became clear that there would always be a bubble in the middle of the sample container, see Section 5.7. It was therefore necessary to blind this bubble by covering it with a cadmium absorber flap. Since the UCN flux was the highest at the very spot where the bubble formed, it was decided to lift the sample container up. By doing so, the highest UCN flux was able to pass through the deuterium sample below the cadmium absorber. A 9 mm thick spacer disc made from commercial pure aluminum (~99% purity) was inserted between the cold-head and the sample container. The rather poor heat conductivity of aluminum entailed a rise in the minimum attainable sample temperature to 10 K.

The sample temperature could be raised to any arbitrary value between 5 K and room temperature by a restive heating wire attached to the top of the sample container and by another resistive heater that was inserted into the base of the

Specifications	**in 2012**	**in 2015-18**
Container body material	commercial pure aluminum	copper (ETP)
Min. T_{lower} [K]	13.0	4.0
$T_{\text{upper}} - T_{\text{lower}}$ [K]	— —	0.9 at 5 K (filled) 0.6 at 5 K (empty)
(gradient across sample container)	2.1 at 16 K (filled) 1.2 at 16 K (empty)	0.5 at 16 K (filled) 0.5 at 16 K (empty)
Cryo-vacuum at room temperature [mbar]	5.5×10^{-4}	$2...5 \times 10^{-5}$
Neutron background	$\approx 80\%$ (Al windows)	$\approx 25\%$ (Al windows)
over entire spectrum	—	$\approx 14\%$ (SiO_2 windows)
Signal-to-noise ratio at TOF peak using – Al windows	5 (for empty container) 2.9 (for solid D_2)	55 (for empty container) 15 (for solid D_2)
– SiO_2 windows	— —	54 (for empty container) 45 (for solid D_2)

Table 4.1: Overview of the improved experimental parameters of the cryostat comparing the measurements in 2015-18 to those from 2012 [136]. Both background and signal-to-noise ratio were obtained using the same 0.3 mm thick aluminum sample cell windows to allow for a good comparison.

sample container. Each was powered by a laboratory power source of max. 800 W. One of them was set to a constant heating power and the other was controlled by a PID (proportional–integral–derivative) controller through a LabView program. The latter also logged the temperatures at the top and the bottom of the container as well as the heating power.

4.3 Gas-handling system

A pivotal point in sample preparation is the safe handling of the high-purity gas. Not only must the gaseous deuterium be prevented from contact with oxygen while handled in one of the most sensitive areas of the ILL reactor, it must also be kept free of contaminants that could introduce additional errors to the measurement. The gas-handling system designed to this end is shown in Fig. 4.4 and is based

on the experience from previous experiments [135]. Before any gaseous sample is introduced, it can be evacuated via a diaphragm and a turbo pump connected in series. The pressure is monitored by pressure and vacuum (Pirani) sensors at three locations: the main ducts of the gas-handling system, the Oxisorb converter and the sample container. Once taken out of the bottle, the gaseous sample can be stored in three different volumes: the Oxisorb converter, the low-pressure gas tank (up to 2 bar absolute pressure) and the sample container. The Oxisorb converter, see Section 4.4, is cooled down to cryogenic temperatures and fed from the low-pressure tank. When enough sample gas has been condensed into the converter, valve V5 is closed. To avoid damage to the system in the event of overpressure in the converter, a check valve was installed in parallel to V5, and the valves V4 and V-Tank were always left open to provide the gas tank as a buffer volume. The sample container was equally protected by a check valve.

Condensing gas into the sample container and the Oxisorb converter took anything from about ten minutes to several hours, depending on the amount of sample to be transferred. The spiral duct on top of the sample container served as a heat insulator between the outer cryostat body and the sample container.

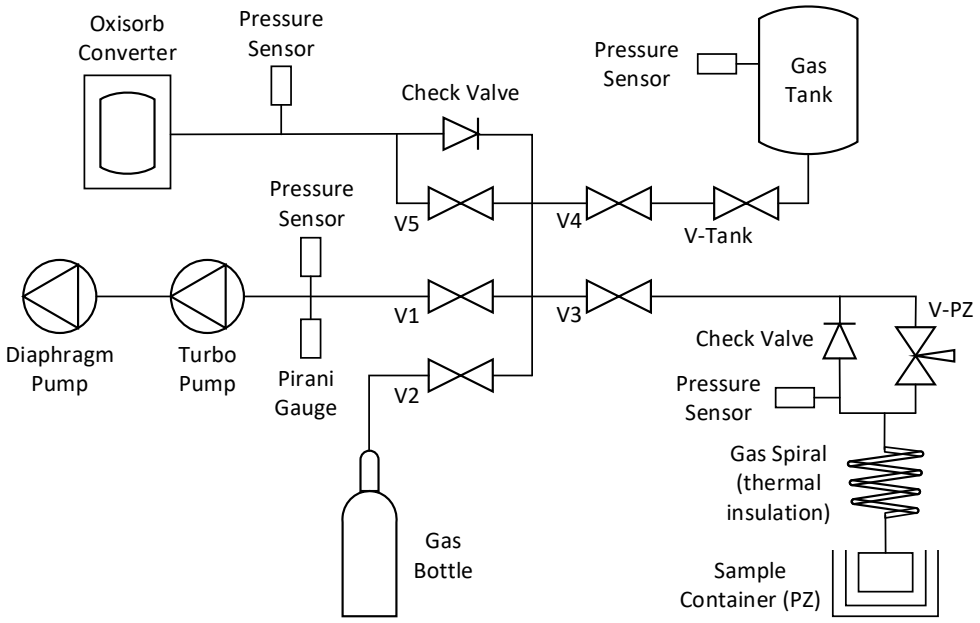

Figure 4.4: The gas-handling system connected the gas bottle (deuterium), the Oxisorb converter, the temporary low-pressure gas storage tank, pumps, and the sample container.

4.4 Spin converter unit

For the use as a cold-to-ultracold neutron converter material, deuterium must be in its lower rotational species, *ortho*, since the *para* species has a large up-scattering cross section due to its excited rotational level. When a neutron relaxes a rotational excitation, it carries away part of the released energy and is lost as an UCN.

Therefore, great care is taken by the operators of sD_2-based UCN converters that the *ortho* content is as large as possible. The natural conversion from the room-temperature equilibrium to the cryo-temperature equilibrium would take months. With the help of a spin-flip catalyst kept at cryogenic temperatures, this time can be reduced to about 12 hours.

The *para*→*ortho* converter unit shown in Fig. 4.5 consisted of a cryostat with a copper cup attached to a cold-head, which contained the spin-flip catalyst, Oxisorb[1], which is a trade name for CrO_3-coated[2] silica grains. Originally, it was intended for oxygen and moisture removal from large gas flows by chemisorption and physisorption, respectively. In 1990, it was discovered by Sullivan et al. [138] to be an efficient *ortho*→*para* converter for hydrogen, which works for deuterium as well. Oxisorb is less prone to poisoning than iron hydroxide gels.

The temperature of the converter cup was monitored using two Cernox temperature sensors. A wire heater around the base of the copper cup allowed for precise temperature adjustment with an uncertainty of $\delta T \approx 0.1$ K. The sensors and heater were both connected to a National Instruments interface. The temperature signals were fed into a custom LabView program, which employed a PID controller to set voltage and current for the heating wire to keep the copper cup at a pre-defined temperature. The pressure was monitored using a pressure gauge.

Efficient and quick conversion was achieved by keeping the deuterium (and hydrogen) in the converter cup around its boiling point to ensure good mixing with the Oxisorb grains. Normally, 20 hours of boiling at 21 K are sufficient to obtain almost pure ($c_{\mathrm{ortho}} = 98.5\%$) *ortho*-deuterium.

4.5 Raman measurement

The *ortho*-deuterium content of the liquid and solid deuterium samples used in this experiment was determined by drawing a gaseous sample from the sample container before and after an experimental run, and analyzing it in a Raman spectrometer

[1] Oxisorb® is a registered trademark of Messer Group GmbH, Bad Soden, Germany

[2] Chromium(VI) oxide (CrO_3, CAS No. 1333-82-0), which is contained in Oxisorb®, is prohibited from sale and use in the European Union by the Regulation (EC) No. 1907/2006 of 18 December 2006 concerning the Registration, Evaluation, Authorisation and Restriction of Chemicals (REACH) with effect from 21 September 2017. Alternative substances that can be used for the *para*→*ortho* conversion of hydrogen and deuterium are magnetic salts and oxides, such as iron(III) oxide [102, 137], and also activated carbon [100].

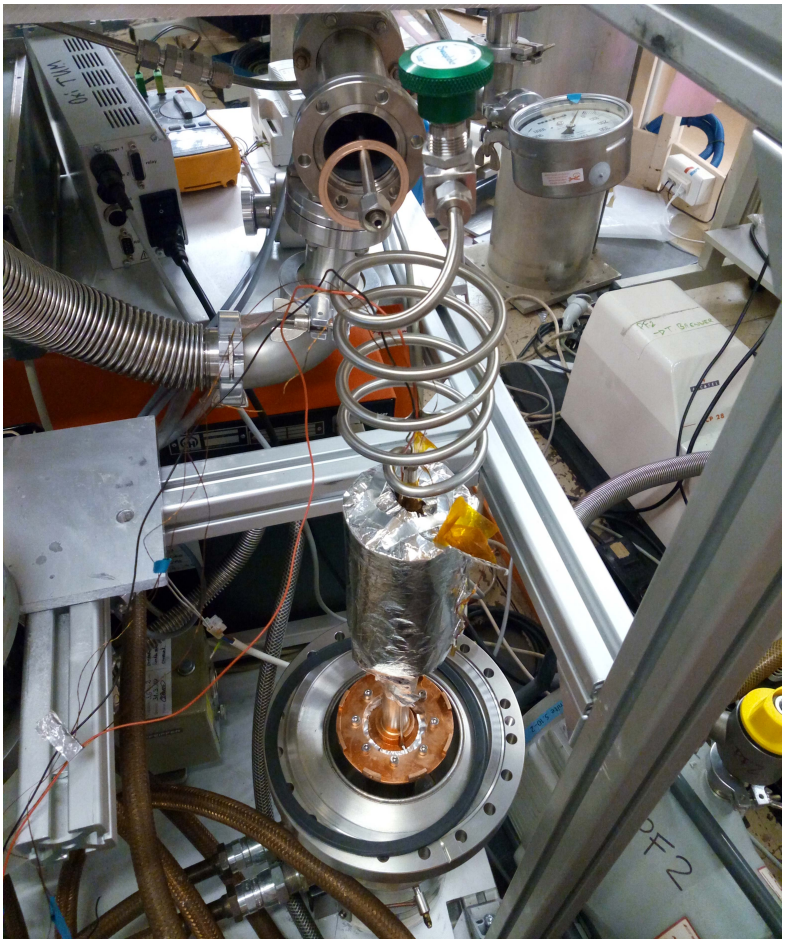

Figure 4.5: Spin converter unit built by T. Lauer with the vacuum vessel removed. Shown are the gas fill line and the converter vessel wrapped in super-isolation foil and mounted on the cold head below it.

(type RamanRXN1™, Kaiser Optical Systems, Inc.). These measurements were done with support from Bernhard Lauss and Nicolas Hild of the UCN group at Paul Scherrer Institut, Villigen, Switzerland [139]. Raman scattering provides information on occupied states by measuring the energy difference between photons from an laser beam and inelastically scattered photons as shown in Fig. 4.6.

For background correction, the spectra of *normal*-hydrogen (n-H_2) and *normal*-deuterium (n-D_2) straight out of the bottle were recorded. These *ortho–para* mixtures were in the room-temperature equilibrium[3] and therefore had a well determined *ortho* ratio. These spectra were also used for benchmarking and verifying the data treatment routine.

Because of a high gamma background radiation from the neighboring VCN beamline and the Turbine, the Raman measurements were subdivided into runs of 20

[3]hence the designation “normal”

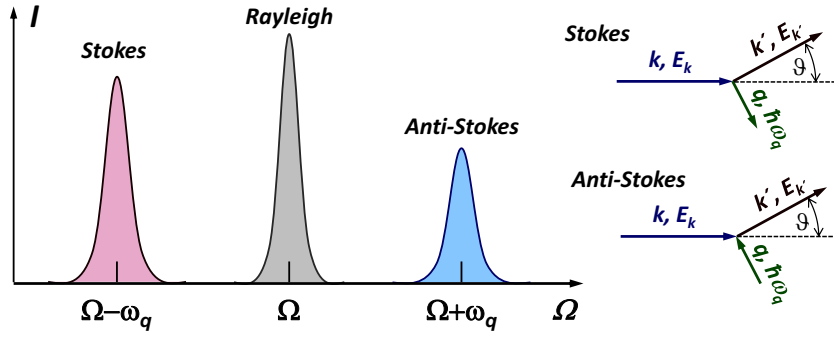

Figure 4.6: Raman scattering provides information on the energy $\pm\hbar\omega_{\mathrm{q}}$ of occupied (anti-Stokes lines) and unoccupied (Stokes lines) levels in matter. Illustration taken from [140].

seconds duration. For each run, the ratio of characteristic transition lines was determined. For both hydrogen and deuterium, the first four lines in the Raman spectrum were used: $S_0(0)$ ($J = 0 \rightarrow 2$), $S_0(1)$ ($J = 1 \rightarrow 3$), $S_0(2)$ ($J = 2 \rightarrow 4$) and $S_0(3)$ ($J = 3 \rightarrow 5$), see Fig. 4.7. They were paired as $S_0(0)/S_1(0)$ and $S_3(0)/S_4(0)$ and the statistical uncertainty for the ratio of the former pair was slightly lower than that of the latter pair. The ratios from each run of one measurement were plotted and fitted by a Gaussian. Those outliers that deviated more than 10σ standard deviations from the mean, were discarded. About 2% of all runs were discarded this way. Most of the faulty runs were due to gamma particles from the reactor or cosmic background on the CCD detector of the Raman spectrometer.

The Raman spectra are directly proportional to the number of molecules that are in the states that produce the lines, see for example Long [141]. It follows that the line ratios follow the same relative change with temperature. The slow conversion of the converted samples to the room-temperature equilibrium can be seen in Fig. 4.8.

From the measured transition line intensities, the *ortho*-D_2 and *para*-H_2fraction can be calculated as described by Silvera [97] and Souers [46].

Raman measurments were taken of each deuterium and hydrogen sample before and after the UCN measurements. For the *ortho*-deuterium measurements the ortho fraction was determined to be $c_{\mathrm{ortho}} = 97.2 \pm 0.02\%$ for the liquid samples and the solid deuterium sample of 11.5 mm thickness.

All hydrogen samples that were prepared, but delivered no useful results during the neutron measurements, had a *para*-hydrogen fraction of $c_{\mathrm{para}} = 99.8 \pm 0.02\%$.

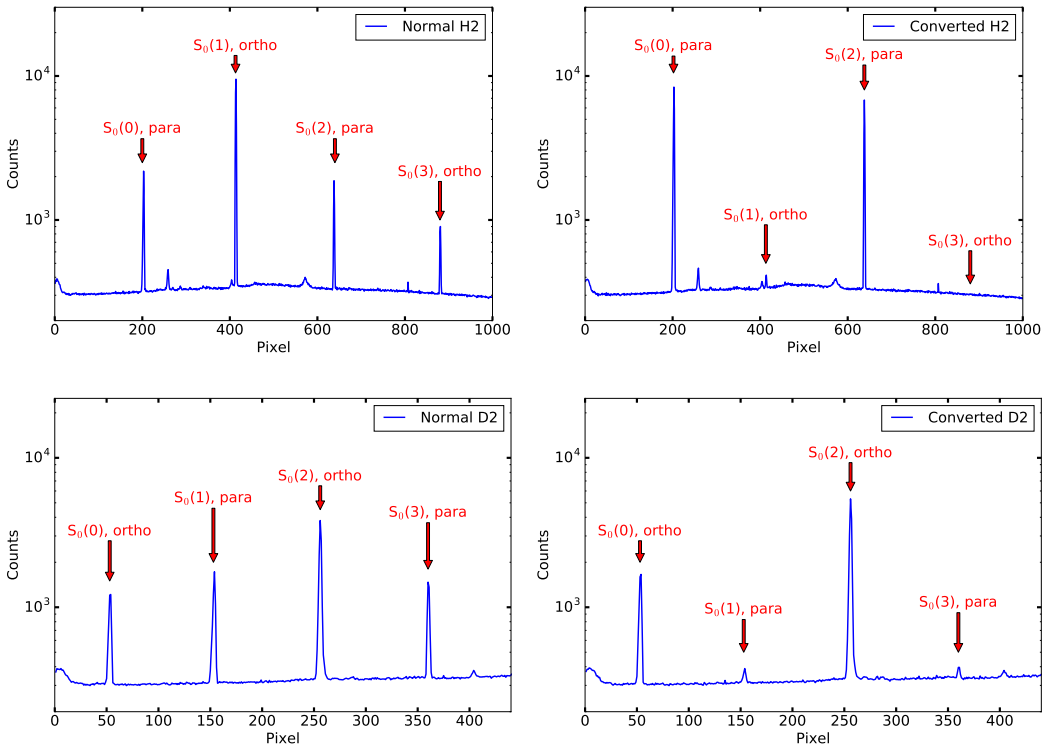

Figure 4.7: Observed Raman spectra (20 s exposure time) of *normal*-H_2 (upper left) and *para*-H_2 converted at 15.3 K (upper right), as well as *normal*-D_2 (lower left) and *ortho*-D_2 converted at 19.5 K (lower right). The observed peaks are the first four S-branch pure rotational Raman peaks.

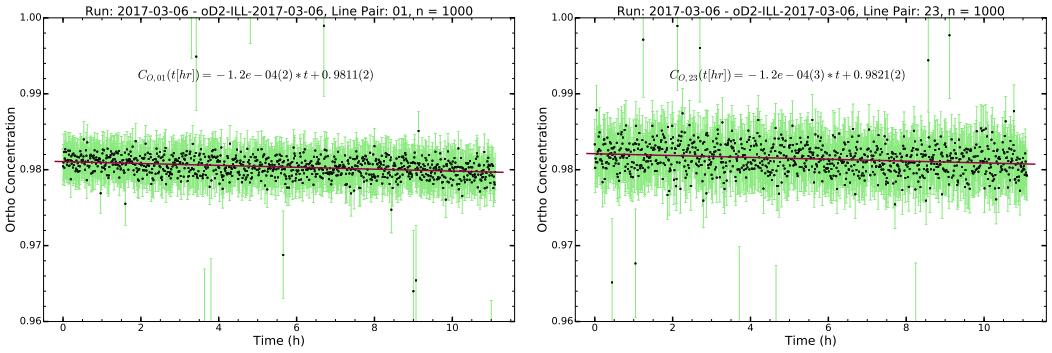

Figure 4.8: Measurement "2017-03-06 - oD2-ILL-2017-03-06" over time. The slow conversion from cryo-temperature equilibrium to room-temperature equilibrium is visible by a decreasing *ortho*-D_2 fraction.

4.6 UCN detectors

Neutrons are generally detected indirectly, for example by means of a capture reaction with the subsequent release of charged particles, usually (n,α). It is the energy and charge of the particles released in this reaction that can be registered in various ways by electronic readout systems. For efficient detection, it is conducive to use isotopes with high capture cross sections for neutrons, such as ^{3}He (5333 barn for thermal neutrons with $v = 2200$ m/s), ^{10}B (3835 barn), or ^{235}U (680.9 barn).

4.6.1 Cascade detector

The Cascade-U 100 detector is a boron-lined linear proportional detector [142]. It has a 100 μm thick aluminum entrance window with an inside coating of 200 nm ^{10}B (enriched to 96%). Neutrons faster than 3.2 m/s, i.e. the critical velocity of aluminum, can penetrate the entrance window and get absorbed by the boron layer on the aluminum foil. In the ensuing nuclear reactions, of which Eq. 4.1 shows the decay channel with 94% probability, charged particles are created. Those are then accelerated by a high voltage between gas electron multiplier (GEM) foils [143] and initiate an electron avalanche that is large enough to be detected, see Fig. 4.9.

$$^{10}\mathrm{B} + n \rightarrow [^{11}\mathrm{B}]^{*} \rightarrow \alpha + {}^{7}\mathrm{Li} + \gamma\,(0.48\ \mathrm{MeV}) + 2.31\,\mathrm{MeV}\ (94\%) \qquad (4.1)$$

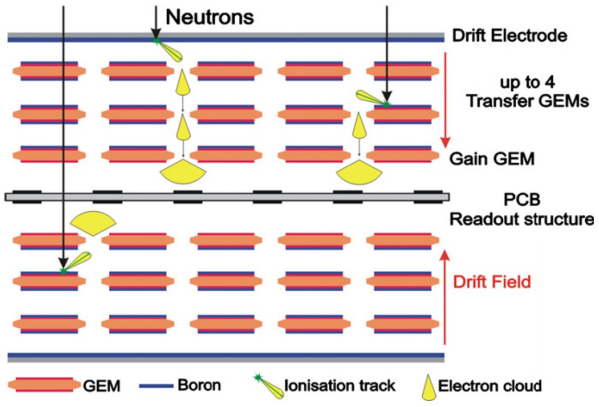

Figure 4.9: In this top view of the Cascade detector, the aluminum entrance windows and GEM foils are shown. The products from the neutron capture reaction cause ionisation tracks inside the counting gas. The acceleration of electrons in the high electric field towards holes in the GEM foils creates electron clouds that can then be detected. Taken from Klein et al. [142].

To slow down and eventually flush out reaction products and to protect the delicate electronics of the detector, a mixture of Ar/CO_2 (90/10) is used as a counting

gas. The name Cascade detector derives from the multiple cascaded GEM foils, see Fig. 4.10. Before the detector was used in UCN experiments, it was flushed with counting gas for several hours. Furthermore, the discriminator thresholds were set according to the real UCN spectrum and the optimal acceleration high voltage was determined[4] to be 1100 V.

The detection efficiency of this type of detector is reported to be about 90% for UCNs [144]. This, however, refers only to the efficiency of neutron conversion in the boron layer. A recent comparison between the Cascade and the Dunya detectors, see the following Subsection, yielded a relative efficiency of the Cascade of $(40 \pm 2)\%$ compared to the Dunya detector [145]. The Dunya has an absolute efficiency of 85 to 86% for UCNs. This was tested by varying the ^{3}He content of the detector and using various entrance windows [146]. Both efficiencies combined give an absolute efficiency of the Cascade detector of $(34 \pm 5)\%$[5] for the averaged UCN spectrum at the Turbine. The error of this efficiency is estimated to be 5% (absolute) due to the uncertainty of the absolute ^{3}He pressure in the Dunya at the time of measurement as well as differences in the acceleration voltage applied to the Cascade detector, which varies from 1100 to 1300 V, depending on the research group.

The solid angle of the detector was about 0.03 sr in the setup used here, see Section 6.4.

4.6.2 ^{3}He-based Dunya detector

As a neutron flux monitor the Dunya[6] detector developed by Alexander Strelkov at JINR Dubna (Russia) was used. It is a ^{3}He gas-filled proportional detector, see Fig. 4.11 for a photograph and Fig. 4.12 for a schematic sectional view. The ^{3}He partial pressure in the detector is 15 mbar, the stopping gas is composed of 10 mbar CO_2 and 1.1 bar Ar. Due to their low neutron-optical potential, either titanium or aluminum foils are used as the detector's entrance window. Neutrons are detected via the following nuclear reaction

$$^3\mathrm{He} + n \rightarrow ^3\mathrm{H} + ^1\mathrm{H} + 0.764\,\mathrm{MeV}. \tag{4.2}$$

This reaction is highly dependent on the orientation of the ^{3}He nuclear spin to the neutron spin. Since only unpolarized UCNs were used for the purposes of this dissertation, the spin-dependence did not play any role.

The Dunya detector has an absolute efficiency of 85 to 86% for UCNs [146]. In this work, it served as a beam monitor to track possible fluctuations of the

[4] with the help of M. Klein, inventor of the Cascade detector

[5] This surprisingly low value might be due to a worn down GEM foil in the Cascade detector, which perhaps had tiny holes inside due to high voltage discharges [147].

[6] Dunya (Дуня) is the Russian diminutive of the archaic Byzantine female name Eudokia, meaning "goodwill" or "affection" and A.V. Strelkov's tongue-in-cheek name for his detector series.

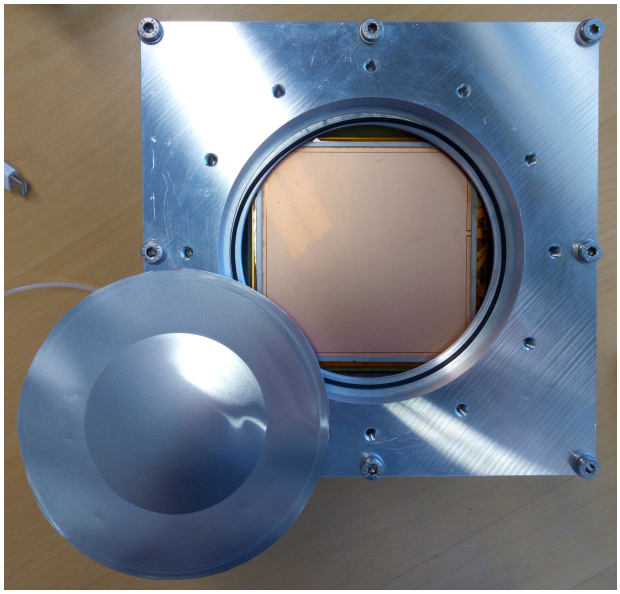

Figure 4.10: The Cascade detector with the beam tube flange and the aluminum entrance window removed (lower left-hand corner). The GEM foil stack can be seen in the center of the detector.

Figure 4.11: View of the Dunya ^{3}He proportional detector. Photo by Damien Roulier [148].

incoming UCN flux. To this end, it was placed between the UCN Turbine and the UCN chopper, and counted UCNs that fell through between the fitting edges of two stainless steel neutron guides. As can be seen in the representative example of Fig. 4.13, the count rate of the monitor only changed by less than $\pm 1\%$ during one day of measurements. The typical measurement time per sample was between 8

and 16 hours. Therefore, the change of the incoming UCN flux due to fluctuations in reactor power between associated measurement runs was of the order of 1% maximum.

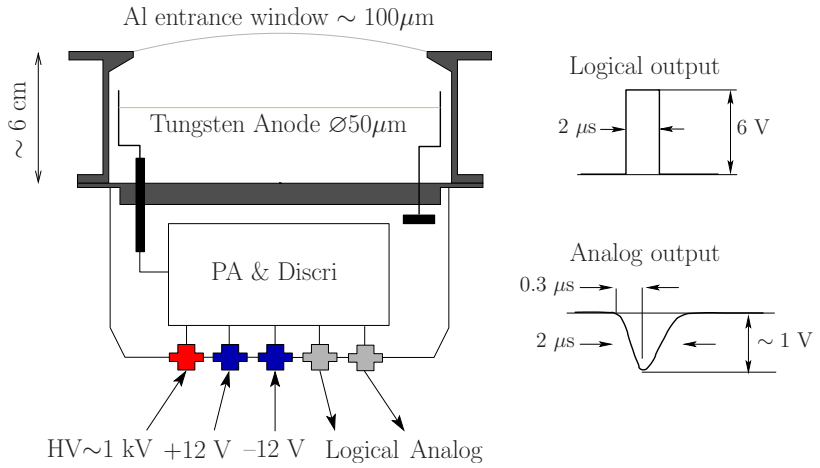

Figure 4.12: Sectional view of the Dunya ^{3}He proportional detector and shape of its electronic pulses. Drawing by Gwendal Rogel [149].

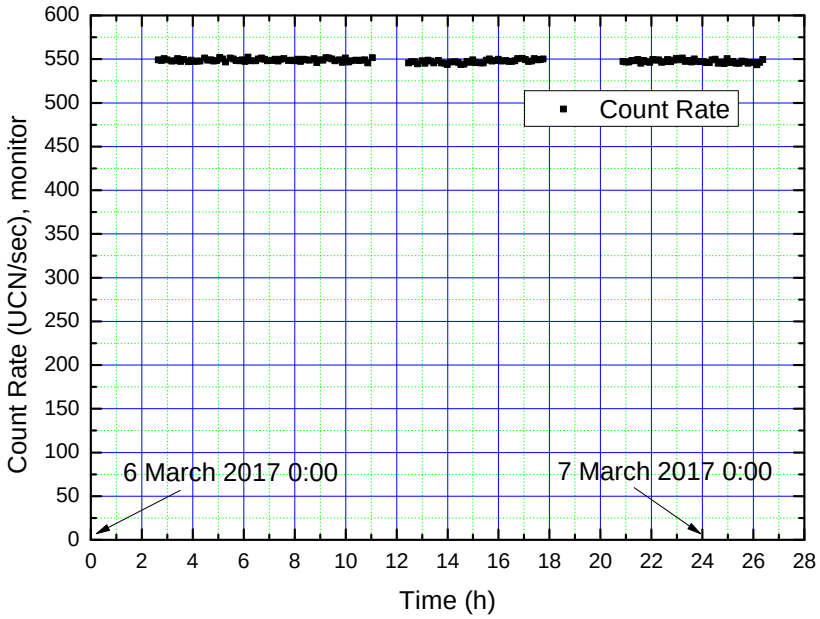

Figure 4.13: Count rate of the Dunya monitor detector over a 24 hour measurement during the ILL reactor cycle no. 171 in 2017.

4.7 UCN chopper

4.7.1 Chopper description

When using a polychromatic neutron beam for velocity-resolved measurements, a beam chopper needs to be employed. The chopper cuts the beam into small bunches, which stretch out over the flight path due to the different neutron velocities present in the bunch. Just before the chopper opens, it sends a TTL trigger signal to the Cascade detector electronics, which launches the measurement frame. Since the chopper was operated at a repetition rate of 5 Hz, the frame width was 200 ms. The flight time of each detected neutron between chopper and detector was recorded and could later be used to calculate the neutron's velocity. The chopper used for the work on this thesis resembles the one developed and described by Lauer [150].

It is made up of a rigid, vacuum-tight steel body with KF flanges for vacuum hoses and two linear actuators, each of which drives a titanium grid. In closed mode, these titanium grids overlap and the UCN beam is almost completely absorbed by the titanium. A few UCNs that escape the grid, cause a constant background in the measured transmission spectrum and can easily be subtracted from it, see Chapter 6. This UCN background is about 0.3% of the count rate with the chopper open. In open mode, the openings in the grid overlap maximally and 36% of the geometrical beam cross section are open. The linear actuators are controlled by controller electronics in a separate box. From that box, a TTL trigger signal is sent to the detector electronics via a coaxial cable. The chopper opening characteristics and repetition rate are programmable. For chopper calibration tests, see Section 4.7.2. During operation, the chopper was constantly being evacuated by a turbomolecular pump and a diaphragm pump in series.

4.7.2 Chopper parameters and time offset

Before the chopper was used in neutron transmission experiments, its programmable ("nominal") parameters like opening time, trigger-signal time offset and repetition rate were tested with neutrons in a typical TOF setup. Later, they were verified with an LED light source using the setup shown in Fig. 4.14. Opening time and repetition rate together give the "duty cycle", which is a measure for how many of the incoming neutrons pass the chopper: duty cycle [%] = opening time [s] $\times$ repetition rate [Hz].

The neutron measurements of the opening time were carried out as an integral measurement. A 2D neutron image was recorded over 60 sec while the chopper was i) completely closed (to determine the background count rate), ii) chopping at various rates, and iii) completely open (to determine the ratio of useful neutrons). The neutron count rates are shown in Tab. 4.2, where they can be compared with parameters from the measurements using visible light. The combined optical

and electronic background count rate in the measurements with visible light was typically 1.5% and that in UCN measurements was 9% for the preset opening of 8 ms and much less for longer opening times. Both were subtracted from the respective raw data.

For nominal opening times of 8 ms, 9 ms, and 20 ms and more, the integrated counts are quite similar to the duty cycle. For opening times less than 8 ms, the discrepancy is blatant. This is probably due to the inertia of the linear actuators and the titanium grids, which do not manage to open up enough and let neutrons pass before the next closing signal arrives. Taking this into account and searching for the right balance between neutron count rate and temporal resolution, a nominal opening time of 8 ms was selected for all subsequent experiments.

The neutron tests, which were carried out before the tests with light, revealed a problem with the chopper for nominal opening times between 10 ms and 20 ms. The integrated neutron counts for both settings were the same although the former was expected to be roughly half of the latter. These findings were confirmed by the measurements using visible light and two different nominal time offsets (10 ms and 20 ms), see and compare Figs. 4.15 and 4.16. This dysfunction did, however, not affect the UCN measurements presented here as the 8 ms chopper opening was used.

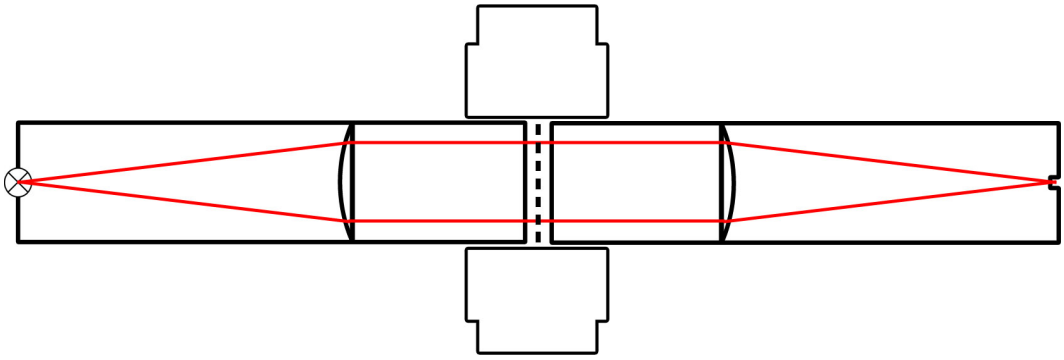

Figure 4.14: Schematic drawing (top view) of the chopper setup for measuring its opening function using light. From left to right the elements are: a light source (red LED), which is situated at the focal point of a plano-convex lens ($f = 14.5$ cm) that parallelizes the light rays; the titanium chopper blades and parts of the chopper housing in the middle of the drawing, and another plano-convex lens that gathers the light rays and focuses them onto a photodetector. The light rays are parallel to each other when they pass the chopper blades. The chopper blade area is evenly illuminated over a diameter of 50.8 cm (2 in.).

After taking the UCN spectra measured with different TOF paths, the chopper–detector offset is calculated by using the premise that the peak of both UCN spectra is at the same UCN velocity with a small margin of error. This can be

expressed as

$$v_{1/2}^{\text{peak}} = \frac{d_{1/2}^{\text{TOF}}}{t_{1/2}^{\text{peak}} - t_{\text{offset}}}, \tag{4.3}$$

Nominal time offset [ms]	**Nom. opening time [ms]**	**Real opening FWHM [ms]**	**Relative light int.**	**Realtive UCN int.**
10	5	no opening	—	—
10	8	13.6	1.00	—
10	10	17.7	2.12	—
10	20	18.0	2.16	—
10	40	37.6	4.59	—
10	80	77.6	9.41	—
10	100	98.0	11.85	—
10	150	148.0	17.95	—
20	5	no opening	0.01	0.01
20	6	6.9	0.12	0.15
20	7	10.4	0.41	0.50
20	8	13.7	1.00	1.00
20	9	15.7	1.53	1.59
20	10	17.7	2.17	2.24
20	20 (1)	17.8	2.16	2.29
20	20 (2)	17.9	2.19	2.38
20	40	37.6	4.64	—
20	80	77.8	9.65	—
20	100	98.0	12.17	12.42
20	150	148.0	18.44	—

Table 4.2: Overview of the nominal (theoretical) chopper opening times and the real opening times at the full width at half maximum (FWHM) of the opening function, as well as integrated light and UCN counts normalized to the a nominal opening time of 8 ms. The UCN transmission measurements were only carried out using the 10 ms preset time offset.

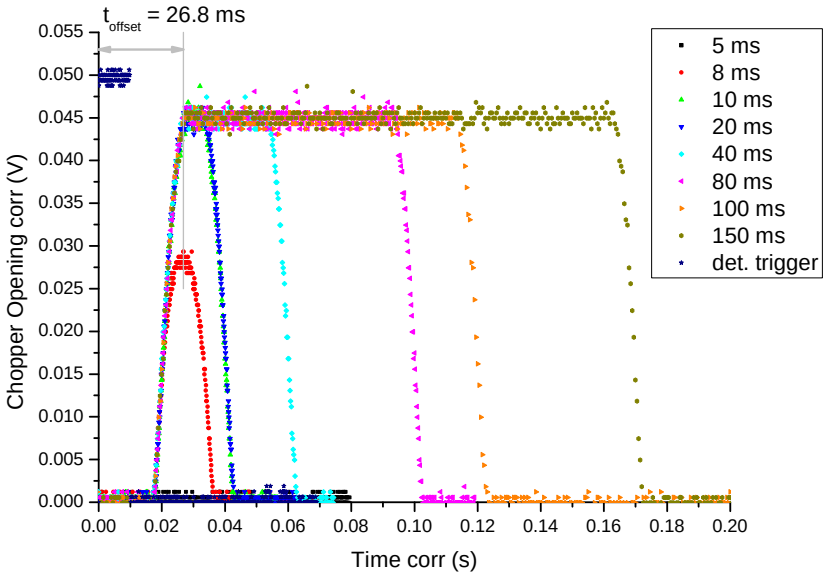

Figure 4.15: Comparison of the chopper opening functions for various opening times and a nominal chopper offset of 10 ms. The time scale starts at $t = 0$ with the start of the trigger signal that the chopper sends to the detector. It is 10 ms long. The real chopper offset for the nominal chopper opening of 8 ms, which was used in the UCN transmission experiments described here, was 26.8 ms as measured with light and 28.4 ms as measured with neutrons and two different TOF path lengths (458 mm and 609 mm), see Fig. 4.17.

where $v_{1/2}^{\text{peak}}$ are the (same) peak velocities of the UCN spectrum in the measurement with TOF path length d_1^{TOF} and TOF path length d_2^{TOF}. The flight times $t_{1/2}^{\text{peak}}$ are taken at the peak of the spectrum for the two TOF path lengths, respectively. The time offset is denoted as t_{offset}. Solving the two equations above for t_{offset} gives

$$t_{\text{offset}} = \frac{d_1 t_2 - d_2 t_1}{d_1 - d_2}. \tag{4.4}$$

When t_{offset} has been determined, both spectra can be corrected by this value and should overlap completely once converted to the velocity domain. Fig. 4.17 shows both corrected spectra and, indeed, the overlap is very good except for high UCN velocities with $v_z > 14$ m/s, which is due to the chopper opening function of 13.6 ms (FWHM) for which the temporal resolution decreases and the error increases. The real chopper offset for the nominal chopper opening of 8 ms and the nominal chopper offset of 10 ms was in fact 26.8 ms as measured with light, and 28.4 ms as measured with neutrons using two different TOF path lengths (458 mm and 609 mm), see Fig. 4.17. The two values agree well with each other. For data correction, the value obtained with neutrons was used.

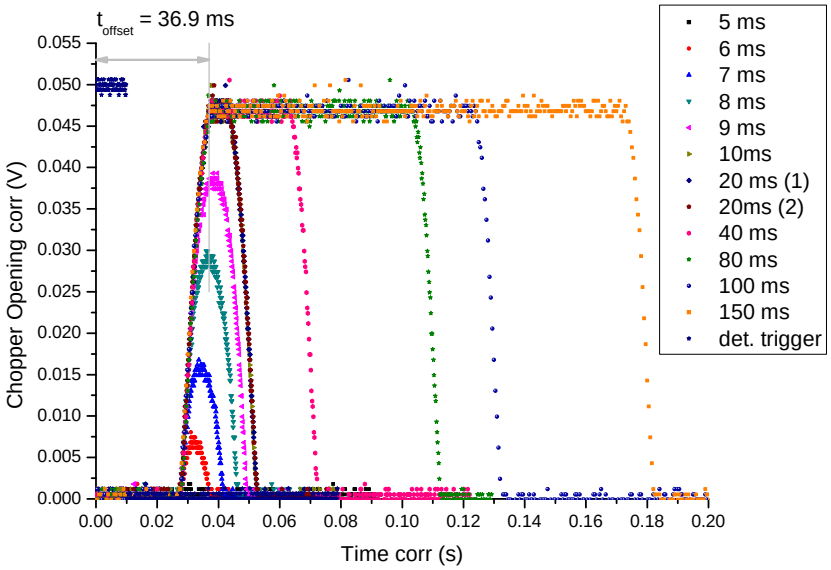

Figure 4.16: The same as Fig. 4.15, but for a chopper offset of 20 ms. The real chopper offset for the nominal chopper opening of 8 ms was 36.9 ms as measured with light. These settings were not used in the following UCN transmission experiments.

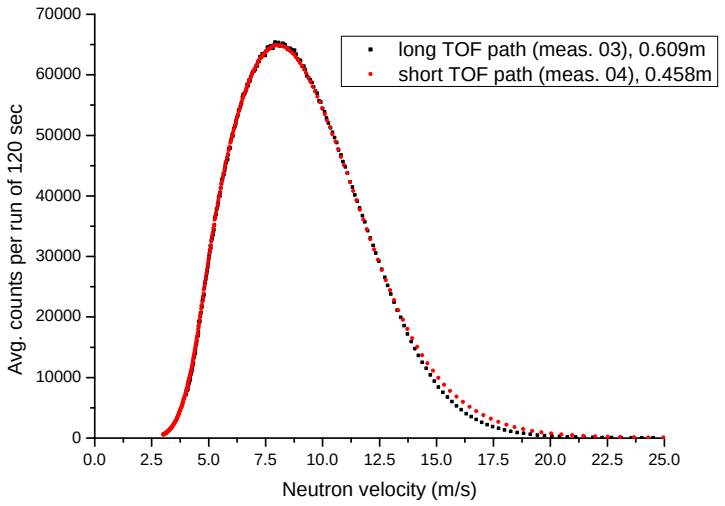

Figure 4.17: Velocity spectrum of the neutron beam port PF2-UCN as measured with two different TOF distances, reflecting beam guides, and no collimator. The maximum of the velocity component along the z-axis v_z is around 8.1 m/s.

4.8 Collimator

The transmission measurement requires a collimated[7], i.e. parallelized, neutron beam, see Section 2.1. This is to say that neutrons of different energies should have the same path length inside the sample. To this end, the collimator material serves either as absorber of UCNs (e.g. titanium) or up-scatters them to higher energies (e.g. materials containing hydrogen), thus removing them from the usable beam. The resulting UCN beam is strongly collimated in the forward direction. To this end, a perforated titanium disc of 3 mm thickness and 47.9 mm diameter was employed. It has 1225 holes of 0.5 mm diameter each, see Fig. 4.18. The resulting solid angle of the collimator aperture was $\Omega \approx \frac{0.2\,\mathrm{mm}^2}{(3\,\mathrm{mm})^2} = 2.2 \times 10^{-2}$ sr and in terms of apex angle $\delta = 2\arctan(0.5/3) \approx 1/3$ rad. This means a maximum deviation from the z-axis by $q_{\mathrm{xy}} = 2k_{0\mathrm{z}}\sin(\delta/2) \approx k_{0\mathrm{z}}\delta \approx k_{0\mathrm{z}}/3$. For an UCN of 100 neV kinetic energy this means a deviation from the z-axis by 2.3×10^{-3} Å^{-1} behind the collimator.

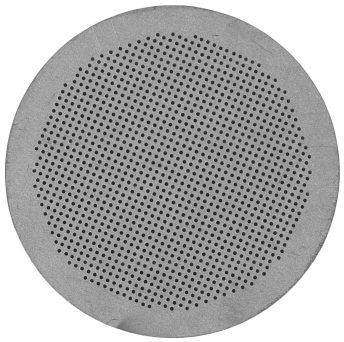

Figure 4.18: Titanium collimator as used for UCN transmission measurements.

Due to the sample container's dimensions and the polyethylene foil lining of a part of the neutron flight path, the UCN beam is effectively collimated again with a solid angle of $\Omega \approx 3.0 \times 10^{-2}$ sr, see Eq. 6.8. Thus it is ensured that for the most part only those UCNs with all their kinetic energy in the z-direction are detected.

For all deuterium and hydrogen measurements the titanium collimator was used. It was housed in an aluminum flange, see Fig. 4.19, which also provided for a groove to attach a steel ring with an aluminum foil ($d \approx 20$ μm) to separate the cryostat vacuum (down to 10^{-7} mbar) from the (poorer) vacuum in the neutron beam tube (low 10^{-3} mbar range). This was done to prevent rest gas and impurities from the beam tubes from freezing out on the cold sample container. For testing, the aluminum foil was replaced by a $d = 1$ mm vitreous silica disc. Both showed almost

[7] According to the Merriam-Webster dictionary, the English verb "collimate" derives from the Latin "collimare", which is itself a misreading of the word "collineare", meaning "to direct in a straight line". This misreading appeared in some editions of ancient Roman works and was perpetuated in the Middle Ages and the Early Modern Period by scientists writing in Latin.

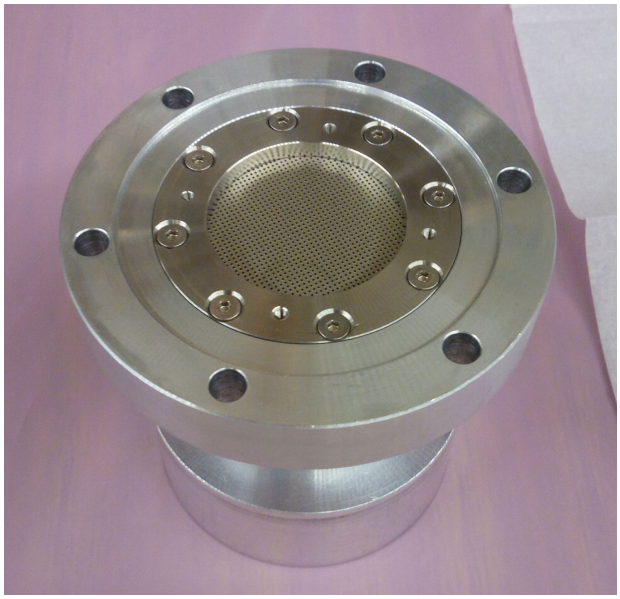

Figure 4.19: Titanium collimator built into the cryostant flange. The aluminum foil that serves as vacuum separator is sandwiched between a protuberance in the flange and the collimator.

identical transmission of UCNs, with slightly higher values for the aluminum foil. The latter was therefore chosen as a vacuum separator.

UCNs are slow enough to have a significant susceptibility to the gravitational field of the Earth. After having passed the collimator, the UCNs are parallel to the beam axis. However, as they progress along the flight path, gravity acts on them and accelerates them vertically. As slow UCNs spend a longer time between the chopper and the detector, they are naturally more susceptible to gravity than faster neutrons. Between the collimator and the detector the slowest usable UCNs of 6.0 m/s (out of medium) experience a vertical drop of 18.6 mm, the fastest usable UCNs of 15 m/s (out of medium) a drop of 3.0 mm. The diameter of the flight path inside the cryostat and its flanges, which is 55 mm, is large enough so that only few UCNs are lost on the polyethylene foil due to excessive vertical drop.

4.9 Transmission of UCNs through neutron guides

The transmission of UCNs through neutron guides is a long-standing and difficult problem in UCN physics. For maxiumum utilization of the UCN flux provided by sources and converters, UCN transport needs to be as efficient as possible. Loss of UCNs inside guide tubes on residual gas molecules, dust, absorption by the wall coating material as well as backwards diffusion due to diffuse scattering on rough surfaces have to be avoided. A few studies have been carried out on the ratio of

diffuse to specular reflectivity [127] and the transmissivity of beam tubes for very slow UCNs ($E \lesssim 200\,\mathrm{neV}$) by selecting UCN energies in a spectrum shaper or by reflection from materials with a high neutron-optical potential [151, 152, 153]. These works relied to a large extent on computer simulations to interpret their results and no energy- or velocity-dependent reflectivities have been reported.

4.9.1 Glass tubes coated with NiMo

The transmission of UCNs through NiMo-coated glass tubes (molar fraction 85% Ni, 15% Mo, unmagnetic, coating thickness 500 nm, coating directly on glass substrate, outer diameter ∅90 mm, inner diameter ∅80 mm) of different lengths was measured at the PF2-UCN beam in a TOF setup in collaboration with Tobias Rechberger, in part to provide a new experimental campaign of the "qBounce" experiment [154] with the optimal choice of beam guide and installation geometry. The TOF setup contained no collimator and the UCN velocities given in this section refer to the v_z component parallel to the beam guide.

For calibration purposes and the determination of the chopper–detector offset, the following beam tube combinations were installed downstream from the vacuum separator foil (aluminum) at the beam port:

1. 230 mm ∅81 mm Nocado tube, transition piece ∅81/90 mm, 450 mm ∅90 mm NiMo-coated glass tube, transition piece ∅90/90 mm, 600 mm ∅90 mm NiMo-coated glass tube, Cascade detector (integral count rate 642'000 UCN/sec)

2. 230 mm ∅81 mm Nocado tube, transition piece ∅81/90 mm, 450 mm ∅90 mm NiMo-coated glass tube, chopper, 600 mm ∅90 mm NiMo-coated glass tube, Cascade detector (TOF path 609 mm, integral count rate 8407 UCN/sec)

3. 230 mm ∅81 mm Nocado tube, transition piece ∅81/90 mm, 600 mm ∅90 mm NiMo-coated glass tube, chopper, 450 mm ∅90 mm NiMo-coated glass tube, Cascade detector (TOF path 458 mm, integral count rate 8461 UCN/sec)

During measurement 1) the Cascade detector was moved left and right a few millimeters with the transition piece ∅90/90 mm as a pivot. This was done to estimate the count rate error due to UCNs vanishing between the fitting edges of two connecting glass tubes. The count rate remained the same within the statistical error.

Measurements 2) and 3) were carried out to determine the chopper–detector time offset. The TOF path was different in both settings, but the total guide path traversed by the UCNs remained the same. Only the 450 mm and the 600 mm tubes were swapped. The integral count rate in both settings only differed by 0.6%. The corresponding UCN spectra are shown in Fig. 4.17.

A series of NiMo-coated glass tubes that were produced by the same technology, was tested for UCN transmission. The TOF path remained the same with the 450 mm tube between the chopper and the detector as in measurement 3) from above. The glass tube directly in front of the chopper was replaced for each new measurement as illustrated in Fig. 4.20.

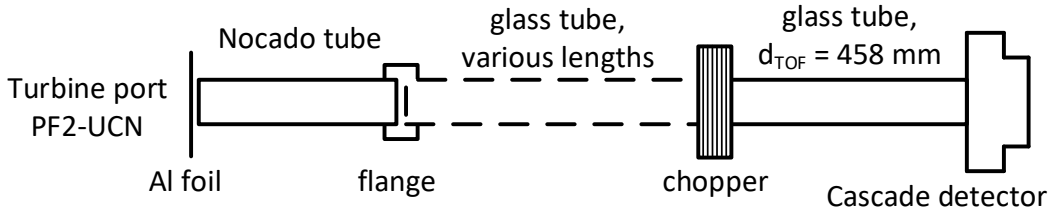

Figure 4.20: Test setup for comparing the transmissivity of different NiMo glass tubes with each other. The TOF path (chopper, 450 mm NiMo tube, Cascade detector) remained the same. Only the beam tube directly in front of the TOF setup was changed.

From the transmissivities of four beam tubes of different length the average velocity-dependent transmission per meter of NiMo-coated glass tube and the corresponding error, i.e. mean squared deviation from the average, were calculated.

4.9.2 Electropolished stainless steel tubes

Electropolished stainless steel tubes are commonly used standard UCN guides for experiments at the ILL and PSI. Their advantage over glass tubes is their lower price, higher radiation hardness, and higher mechanical stability. The reflectivity of their polished surface can be increased by applying a NiMo coating.

Using the same TOF setup as in the subsection above, the transmissivity of electropolished, NiMo-coated stainless steel tubes from the Nocado company[8] with an outer diameter of ∅70 mm and an inner diameter of ∅66 mm was measured by comparing the UCN transmission through an assembly of i) 189 cm and ii) 289 cm of Nocado tubes. The measurements were carried out at the PF2-TEST beam port, see Fig. 4.21.

Fig. 4.22 shows the transmissivity of electropolished, NiMo-coated stainless steel tubes. The error bars for the stainless steel tube data were estimated to be 2%, based on the statistical error and a systematic error due to the different cleanliness and dust on the surface of the two beam guides.

[8]Nocado GmbH, Delmenhorst, Germany; Nocado tubes of “Hygieneklasse 4”

Figure 4.21: The UCN Turbine (blue) is at the top of this image. On the right, the PF2-TEST beamline is shown with the TOF setup used to measure the transmissivity of electropolished, NiMo-coated stainless steel tubes. To the left is the PF2-EDM beamline with its ~3 m of electropolished, NiMo-coated stainless steel tubes. The PF2-UCN beamline is located behind the scaffold on the left.

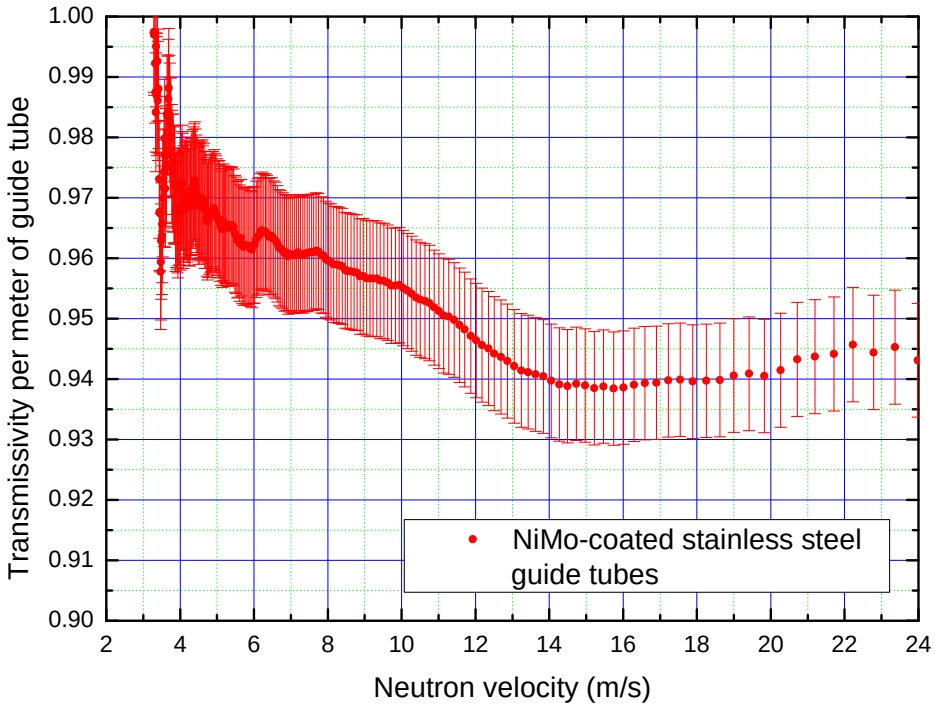

Figure 4.22: Transmissivity of electropolished, NiMo-coated stainless steel tubes for UCNs depending on their velocity. The transmissivity is given per meter of UCN guide tube and refers to the neutron flux at the end of the tube divided by the neutron flux at the front end of the tube.

4.10 UCN spectra of the Turbine's beam ports

Many experiments of the kinds described in Section 1.4 were and still are carried out at the ILL's Turbine. During preparation of these experiments, it is useful to know the neutron spectrum provided at each of the four beam ports. After commissioning of the Turbine, Steyerl et al. [16] measured the neutron flux and density *inside* the Turbine vessel. To the knowledge of both the author and the instrument scientist, there has so far not been any systematic measurement and comparison of the neutron spectrum at the Turbine's *beam ports*, i.e. the experimental positions.

Within this thesis, the neutron spectra at typical experimental positions (up to about 3 meters away from the Turbine shutter) at the beam ports PF2-TEST, PF2-EDM and PF2-UCN were measured in a TOF experiment using the beam guide setups shown in Fig. 4.23. At the PF2-UCN beam port, experimental setups can be put close to the Turbine, while experiments at the PF2-EDM port have to be about three meters away from the Turbine exit due to the current design of the support platform and the limited space around the Turbine. The beam port PF2-MAM was permanently occupied by the long-term experiment "Gravitrap" [155] and thus its spectrum could not be measured.

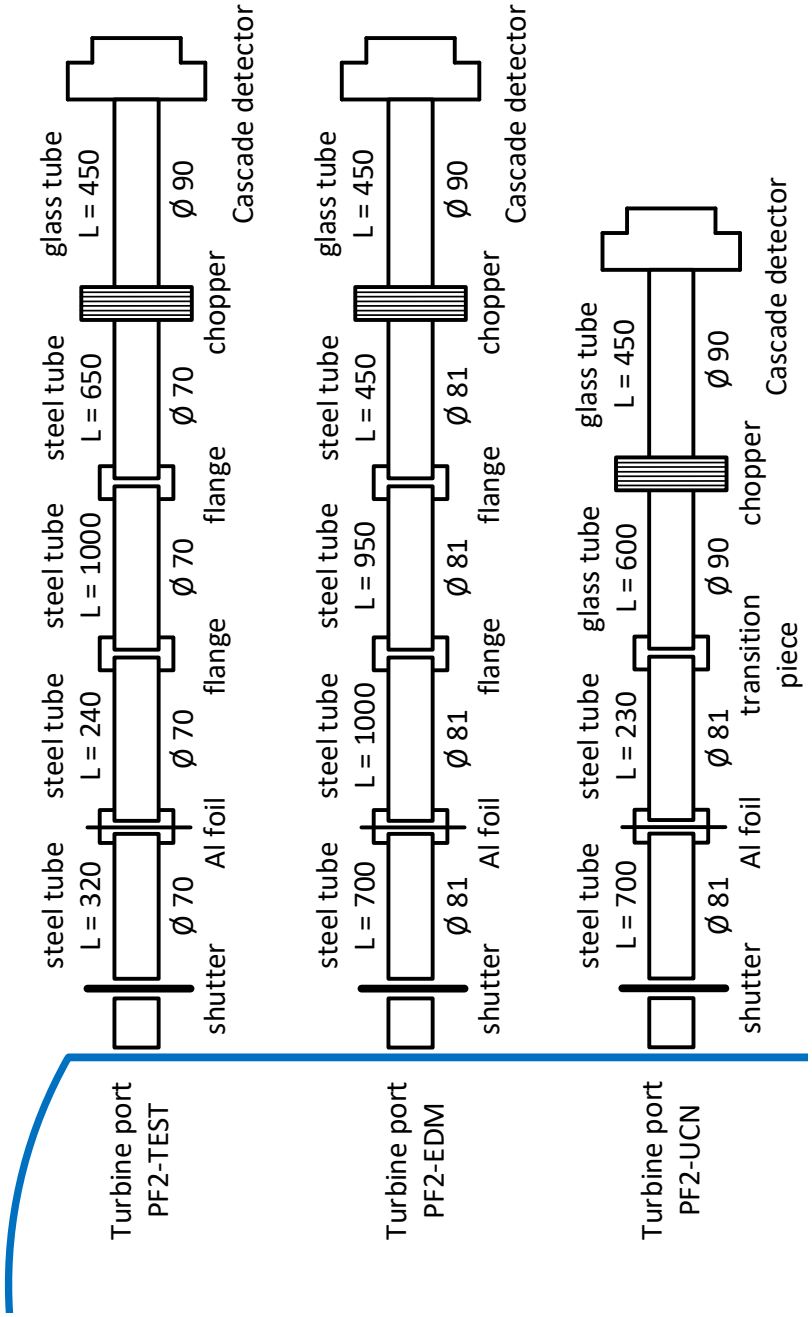

Figure 4.23: Beam tube configurations as they were for comparing the flux of the three Turbine beam ports PF2-TEST, PF2-EDM, and PF2-UCN.

Fig. 4.24 shows the neutron spectra of three Turbine beam ports corrected for transmission losses in the neutron guide tubes as discussed in Section 4.9 and extrapolated back to the position of the safety foil made from aluminum.

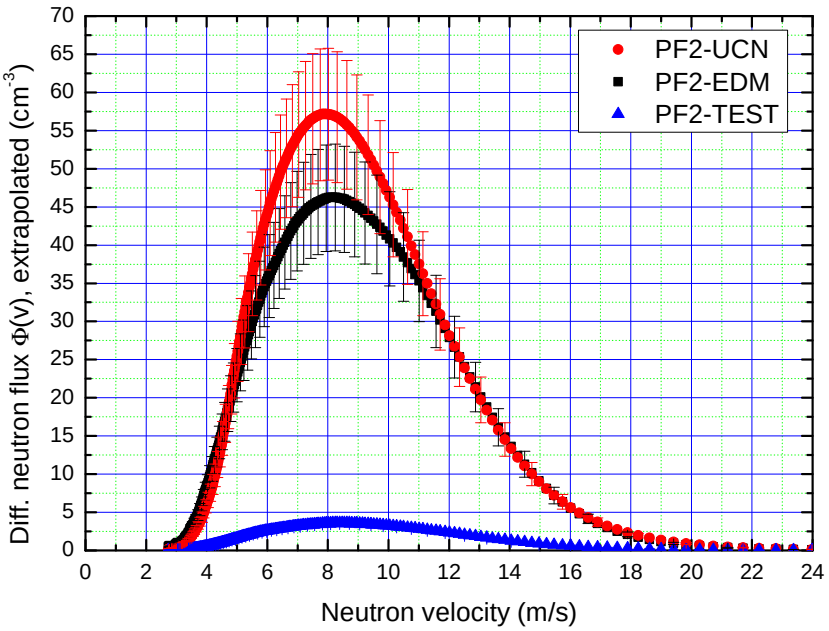

Figure 4.24: Comparison of the neutron fluxes at the beam ports PF2-EDM, PF2-UCN, and PF2-TEST. The inner diameter of the beam guide exiting from the safety foil of the two former ports was 77 mm, that of the latter was 66 mm. Of the error bars, a systematic error of 15% is due to the uncertainty of the absolute Cascade detector efficiency for UCNs. Some error bars have been removed for better legibility.

The transmissivity values measured for electropolished stainless steel tubes of 70 mm outer diameter were also used for those with 81 mm outer diameter installed at the PF2-UCN and PF2-EDM beamline. Besides the beam guide transmissivity, the extrapolation took into account the 3.94% duty cycle as measured with neutrons for the 8 ms chopper setting, see Subsection 4.7.2; the geometric opening of the chopper of 36%, and the 34% absolute detection efficiency of the Cascade detector, see Subsection 4.6.1. The surface roughness of the aluminum foil used as an entrance window in the Cascade detector introduces a systematic error to the extrapolation estimated to be around 10%. All in all, the beamline and TOF setup reduce the usable number of UCNs to ~0.5% of the original flux at the safety foil position. It is surprising that the PF2-UCN beam port has the highest neutron flux as the PF2-EDM beam port was hitherto believed to be the strongest. The neutron fluxes presented in Fig. 4.24 were all measured at a reactor power of 55.8 ± 0.2 MW.

As a by-product of the measurements described above, the evolution of the neutron spectrum during the start-up phase of the Turbine was measured at the PF2-EDM beam position, see Fig. 4.25. The evolution of the shape of the spectrum might be different at other beam ports. In the future, this TOF setup can be used

to optimize the UCN output of the Turbine by varying the number of rotations per minute between 240 and 260.

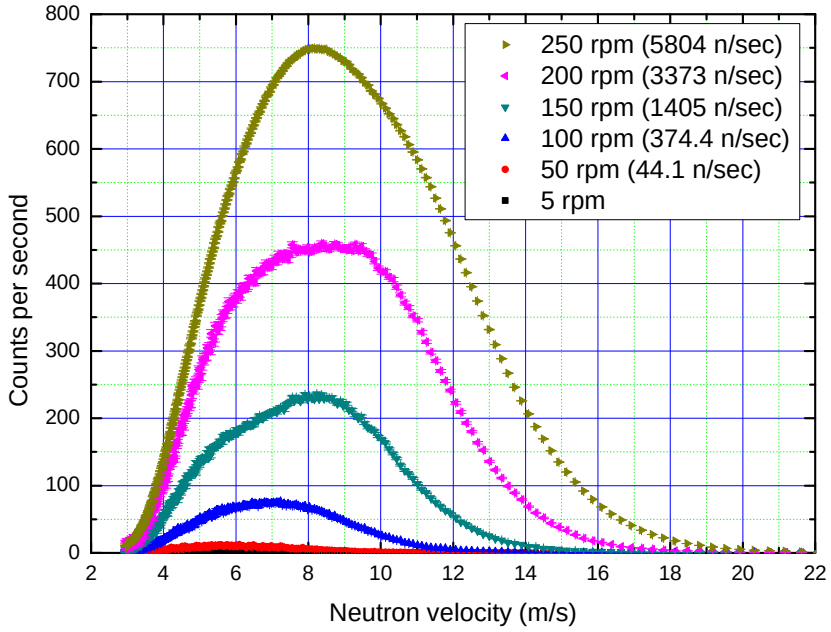

Figure 4.25: Evolution of the neutron spectrum at PF2-EDM during start-up of the Turbine. The beam guide consisted of 2.4 m of Nocado tube downstream of the safety foil and a TOF setup with a 500 mm absorbing TiB_2-coated glass guide. The legend gives the rotational speed of the Turbine as well as the integrated neutron count rate over the entire spectrum.

4.11 UCN losses on gases

Vacuum pumping is a time-consuming factor in cryogenic experiments. While pumping, it is normally not possible to collect useful data. It is therefore important to attain an acceptable vacuum as quickly as possible. It needs to be ensured that the residual gas pressure in the neutron guides is low enough not to cause significant losses of UCNs, e.g. $< 1\%$. Furthermore, the cryostat's isolation vacuum needs to be as good as possible before cool-down to prevent the freezing out of nitrogen, oxygen and water onto the sample container (typically $p_{vac} < 10^{-5}$ mbar). Last, but not least, the closed-cycle refrigerator needs a certain vacuum pressure to function properly ($p_{vac} < 10^{-2}$ mbar). Typical pumping times to achieve a 10^{-5} mbar vacuum inside the cryostat at room temperature and 10^{-3} mbar in the beam guide were in the range of 5 to 7 hours. After twice the time, one order of magnitude was usually gained. Considering beam times of days to a few weeks, i.e.

the time of real data-taking, this is a lot of pumping time that is necessary after each change of the sample container.

A series of UCN transmission experiments was conducted to estimate the losses of UCNs due to residual gas in the neutron quide. To this end, a simple time-of-flight experiment was set up. A stainless-steel neutron guide delivered UCNs to the chopper–guide–detector system. The guide between the chopper and Cascade detector was a glass guide with an inner replica coating of NiMo. The entire system was kept at different air pressures (10^{-3} to 200 mbar) and UCN TOF spectra were recorded.

These TOF spectra were recorded without a collimator and were not corrected for diffuse scattering from the inner walls of the neutron guide. In any case, they gave a good estimate of the highest acceptable residual gas pressure for starting UCN TOF experiments, $p_{\mathrm{gas}} \leq 0.4\,\mathrm{mbar}$. Fig. 4.26 shows the evolution of the PF2-EDM neutron spectrum under various air pressures. Note that no UCNs with $v < 3.2\,\mathrm{m/s}$, the critical velocity of aluminum, are present in the spectrum due to the aluminum safety foil at the Turbine exit and the Cascade detector entrance foil.

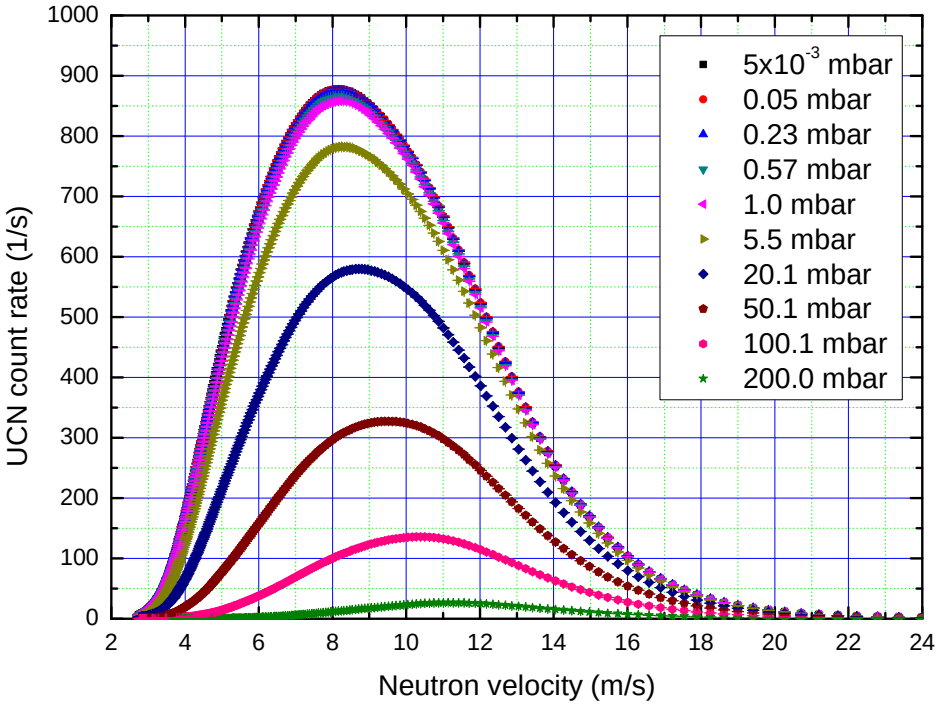

Figure 4.26: Comparison of the neutron spectrum at the end of 310 cm of electropolished stainless steel neutron guides at the PF2-EDM beam port at various air pressures inside the neutron guide. The data for pressures 5×10^{-3}, 0.05, and 0.23 mbar overlap very well indicating a loss of UCNs of less than 1% for residual air pressures of $\leq 0.4\,\mathrm{mbar}$.

5 Design and Development of a Transparent Sample Container

Stets findet Überraschung statt
Da, wo man's nicht erwartet hat;
Doch dass dieselbe überall
Grad angenehm, ist nicht der Fall.
Gar oft erschreckt uns eine sehr,
Und eine andre noch viel mehr.
— Wilhelm Busch

Determining the transmission of slow neutrons through cryogenic liquids and solids of interest, for example hydrogen (H_2) and deuterium (D_2), requires sample containers with thin, highly polished (as motivated in Section 3.5) and optically transparent windows. One of the most difficult sealing problems is that of light gases like hydrogen and helium at low temperatures against a high vacuum. In this chapter the need for an improved sample container is explained and the steps of its design are shown. For the experiments described in this thesis, a new sample container was built, which consisted of a copper body (Electrolytic Tough Pitch copper) and two 1 mm thin amorphous silica windows cold-welded to aluminum clamps using indium wire O-rings, in order to form a simple, reusable and hydrogen-tight cryogenic seal. It withstood up to 2 bar hydrogen gas pressure against 10^{-5} to 10^{-7} mbar cryo-vacuum at temperatures down to 4.5 K.

5.1 Thermal properties of the sample container body

Aluminum, e.g. AlMg3 or other alloys, seems to be the material of choice for cryogenic sample cells used in UCN production and transmission measurements up to now [55, 69, 113, 118, 156]. The poor heat conductivity of commercial pure aluminum (~99% purity) is at the same time its advantage and disadvantage: an advantage because condensing cryogenic liquids into the container is easier at large temperature gradients ($\Delta T \approx 3$ K in this case); a disadvantage because these gradients remain during the measurement and result in a poorly defined sample state. This worsens the quality of transmission measurements in both liquid and

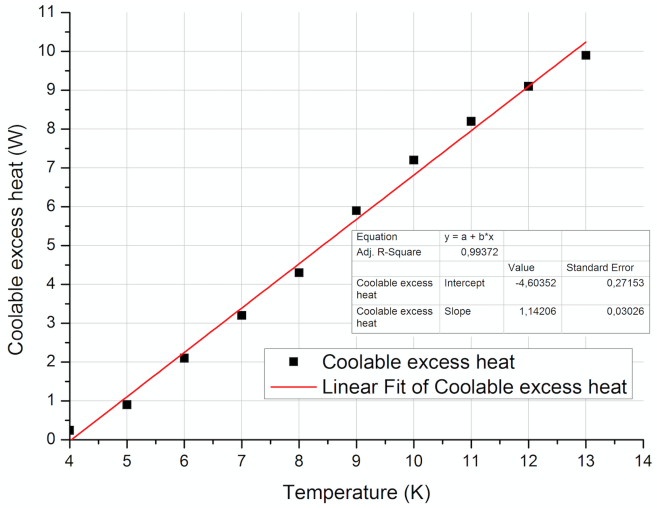

Figure 5.1: Coolable excess heat against the resulting temperature at the bottom of the copper sample container. The lower resistive heater and the lower temperature sensor were inserted into the sample container as in later experiments. The container was used without windows and without a gas fill spiral attached.

solid deuterium. Sample containers made from copper, e.g. Electrolytic Tough Pitch (ETP) copper, on the other hand, provide very small temperature gradients, see Tab. 4.1. Due to these small gradients, the solidification of cryogenic liquids proceeds not from the bottom of the sample container upward, but rather from the edge of the container inward, see Section 5.7. They, therefore, require more skill and patience when growing a solid cryogenic sample.

The coolable excess heat to the sample container vs. the temperature of the cold head's second stage, see Fig. 5.1, was experimentally determined in the exact same setup that was later used for UCN transmission measurements. These data take into account the thermal heat load from the outer cryostat cylinder and the thermal shielding by an aluminum cylinder wrapped in six layers of superinsulation foil (aluminized polyester foil, a few μm thick), which was connected to the first cooling stage ($T = 40$ K) of the cold head. The actual performance matched well the heat load map provided by Sumitomo, the manufacturer of the cold head and compressor unit. The data from Fig. 5.1, as well as the heat conductivities of solids at cryogenic temperatures from [157, 158] were used in simulations of the temperature gradient across the sample container. These simulations were carried out by Jürgen Hingerl as part of an internship he did with me for six months.

The three-dimensional heat gradient in homogenous, isotropic media is described by the heat equation,

$$\frac{\partial T}{\partial t} = \frac{\lambda(T)}{c_\mathrm{p}(T)\rho}\nabla^2 T, \tag{5.1}$$

where T stands for temperature, t for time, λ is the thermal conductivity of the respective medium, c_p its specific heat capacity at constant pressure, and ρ its mass density. ∇^2 is the Laplace operator. While the mass density can be seen as constant on a wide range from ambient to very low temperatures, the specific heat capacity and thermal conductivity strongly depend on the temperature of the material. In pure metals, the heat conductivity is predominantly influenced by electron transport (Wiedemann–Franz law). It falls into the following temperature ranges [140]

$$\lambda(T) \propto \begin{cases} T & \text{, for } T \lll \Theta_\mathrm{D} \\ T^{-4} & \text{, for } T \ll \Theta_\mathrm{D} \\ \text{const.} & \text{, for } T \gg \Theta_\mathrm{D}. \end{cases} . \tag{5.2}$$

To simulate the temperature distribution in the sample container, the heat equation, Eq. 5.2, was solved for the geometry of the sample container taking into account the changing thermal properties at low temperatures. The simulations were carried out using the simulation feature of the commercially available mechanical drawing software Solidworks[1].

The simulation included the two heaters of the sample container: the wire heater surrounding the top of the container just below the upper temperature sensor with the power P_wire, and the resistive heater in the base of the container with the power P_res. The sample container's temperature at the connective interface with the cold head (container bottom) was set to a fixed value T_bottom at the beginning of the simulation and was made subject to the power–temperature curve that had been determined experimentally, see Fig. 5.1. The temperature readings of the sample container were taken at the spots of the upper T_upper and lower temperature sensors T_lower to compare them with the experimental data.

For the old container design using an aluminum body [118], the aluminum clamps as well as the spacer rings (see the description of the sample container below), the curve "Aluminum-2" for commercial aluminum from [157] (~99% purity) was used. To compare the performance of an aluminum body to a copper body, the simulations were repeated for annealed ETP copper of 99.5% purity as the body material. The heat conductivity curves used for the simulation described here are shown in Fig. 5.2.

The heat load at the gas inlet was approximated by setting the top end of the tube on the gas inlet flange, see Fig. 4.2, to a constant temperature of 35 K, which is close to the 40 K of the thermal shield through which it was fed. The flange was made of stainless steel, which had a poor heat conductivity and therefore its exact temperature did not have a large influence on the temperature gradient across the sample container. The long spiral-shaped gas fill tube was also made of stainless steel and served as an effective thermal barrier to the cryostat's outer cylinder.

[1] SolidWorks is a computer-aided design (CAD) computer program published by Dassault Systèmes.

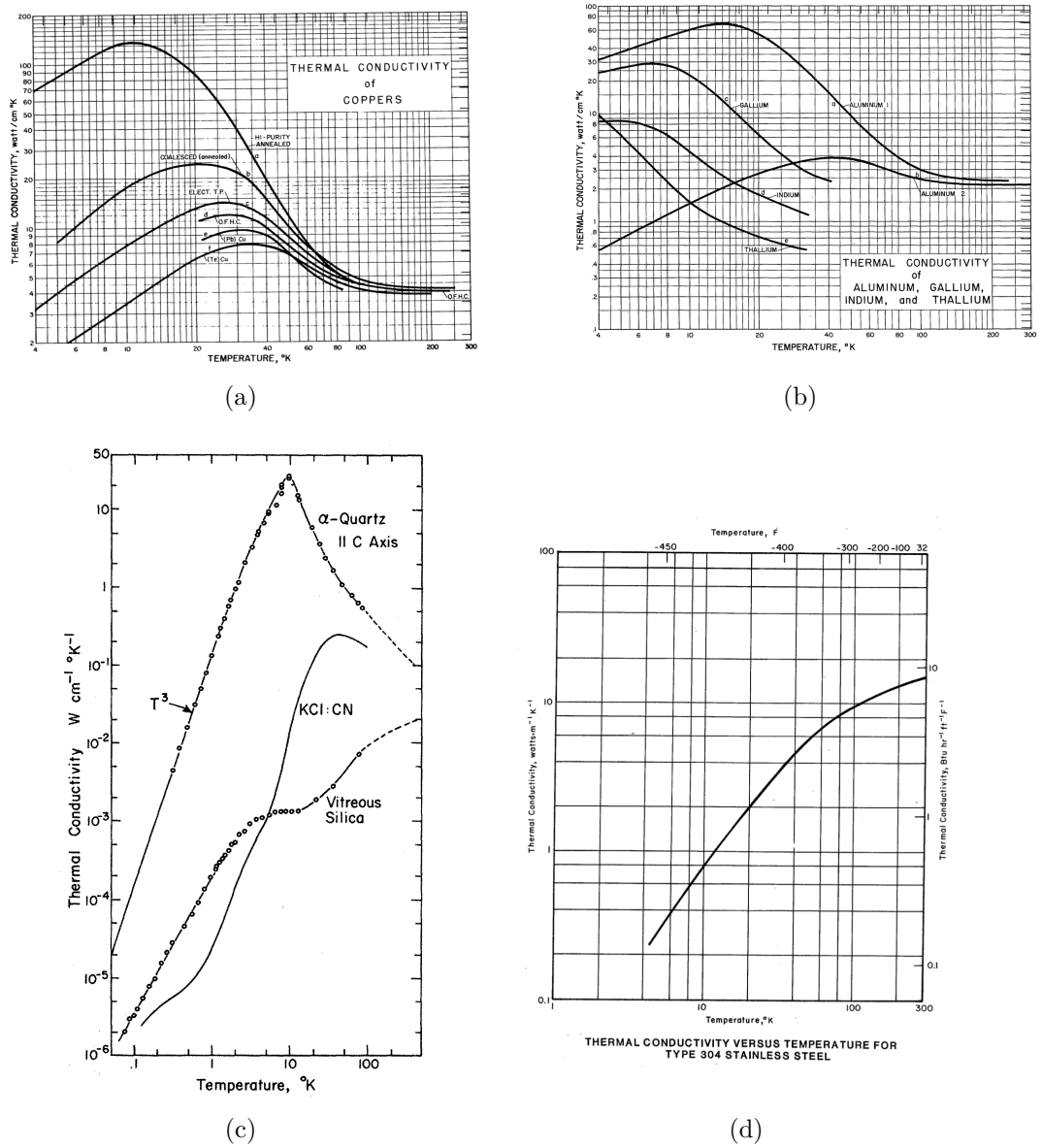

Figure 5.2: Thermal conductivity curves for (a) ETP copper, (b) commercial pure aluminum and single-crystal indium, both taken from [157], (c) for amorphous and crystalline silica [158], and (d) type 304 stainless steel, also taken from [157].

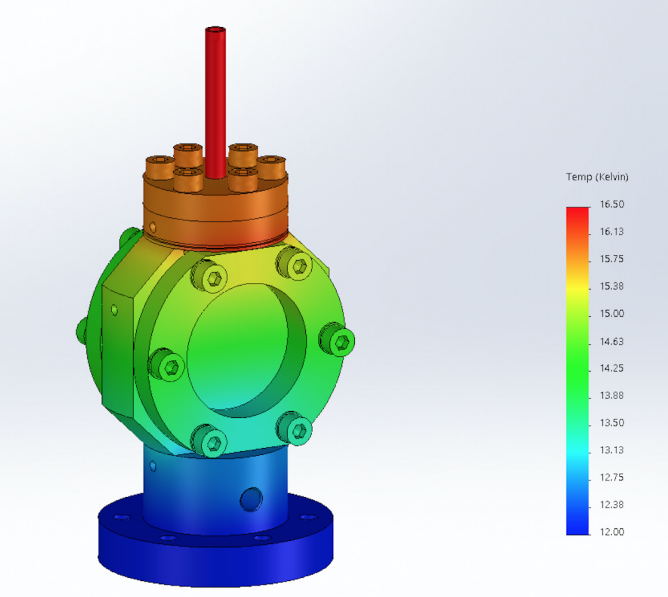

Figure 5.3: Simulated heat map for an aluminum sample container as used in Döge et al. [118] for the boundary conditions $P_{\text{wire}} = 5.7$ W, $P_{\text{res}} = 4.2$ W and $T_{\text{bottom}} = 11.8$ K. The gradient between the two temperature sensors T_{upper} and T_{lower} is 3.2 K.

5.1.1 Reproduction of the experimental values of the aluminum sample container

The simulations were carried out for different power settings of the heaters, P_{wire} and P_{res}, and fixed temperatures on top of the gas inlet flange and the container bottom, which together formed the boundary conditions for the simulation. The numerical solutions of the heat equation, Eq. 5.1, were visualized as heat maps of the entire sample container.

To benchmark the simulations, the thermal conditions from earlier experiments with an aluminum sample container [118] were reproduced. Using a power input of $P_{\text{wire}} = 5.7$ W and $P_{\text{res}} = 4.2$ W, and a fixed bottom temperature $T_{\text{bottom}} = 10$ K, a temperature gradient between the upper T_{upper} and lower T_{lower} temperature sensors of $\Delta T = T_{\text{upper}} - T_{\text{lower}} = 3.2$ K was observed, see Fig. 5.3. This is in good agreement with the experimental data from Herold [114] and Döge et al. [118].

As the thermal conductivity of aluminum with a purity of 99% is less than 1/5 of that of copper at cryogenic temperatures, see Fig. 5.2, a sample container body made from copper promised a much lower temperature gradient across the sample area.

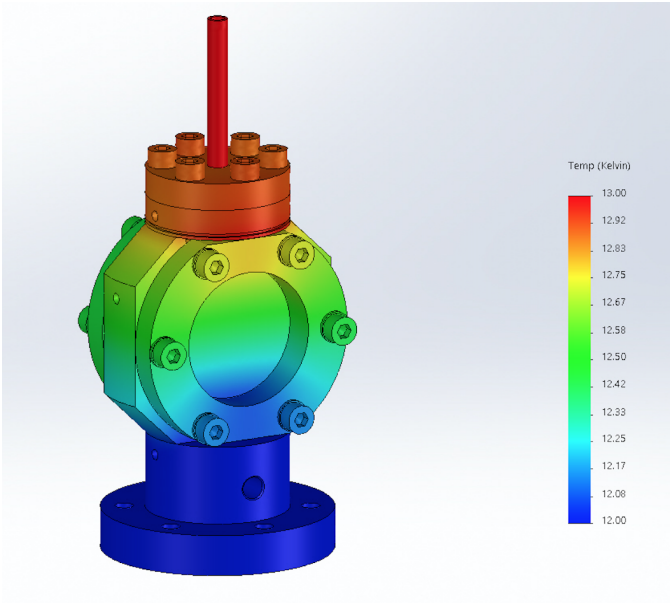

Figure 5.4: Simulated heat map for a copper sample container with the same geometry as used in Döge et al. [118] for the boundary conditions $P_{\text{wire}} = 5.7$ W, $P_{\text{res}} = 4.2$ W and $T_{\text{bottom}} = 11.8$ K. The gradient between the two temperature sensors T_{upper} and T_{lower} is 0.9 K, see line 1 in Tab. 5.1.

5.1.2 Thermal simulation of a sample container made from copper

The same simulations as explained above were carried out for a sample container body made from copper. An example with both heaters turned on is shown in Fig. 5.4. The full simulation results for various power inputs are listed in Tab. 5.1. The maximum temperature gradient is achieved when the upper heater is working at full power and the lower heater is turned off.

After simulations had indicated a small temperature gradient, two new sample containers were machined from copper. They were the ones with the help of which all experimental results presented in this thesis were obtained. A comparison between the simulations and the actual performance of the sample container made from copper is shown in Tab. 5.2. When both heaters are turned on, the upper and lower temperature of the sample container are in excellent agreement with the simulation (± 0.1 K). When both heaters are turned off, the simulation predicted that there would be almost no temperature gradient. However, under real conditions the gradient is 0.6 K. This difference is likely due to heat radiation impinging on the sample container and the fact that the cooling power of the cold head is only slightly above 1 W at 4 K, while it is around 10 W for 12 K, see the capacity map in Fig. 4.3. Heat radiation was neglected in the simulation. Another reason

P_{wire} [W]	P_{res} [W]	T_{bottom} [K]	$T^{\text{sim}}_{\text{lower}}$ [K]	$T^{\text{sim}}_{\text{upper}}$ [K]	ΔT [K]
5.7	4.2	11.8	12.0	12.9	0.9
5.7	3.3	10.0	11.2	10.2	1.0
5.7	0.0	9.0	9.2	10.3	1.1
0.0	0.0	4.0	4.0	4.02	0.02

Table 5.1: Power settings and results of the simulation of a copper sample container.

P_{wire} [W]	P_{res} [W]	$T^{\text{exp}}_{\text{lower}}$ [K]	$T^{\text{exp}}_{\text{upper}}$ [K]	ΔT^{exp} [K]	ΔT^{sim} [K]
5.74	4.2	12.0	12.8	0.8	0.9
5.74	3.3	10.2	11.3	0.9	1.0
5.74	0.00	9.3	9.9	0.6	1.1
0.00	0.00	4.0	4.6	0.6	0.02

Table 5.2: Experimental performance of the sample container made from copper compared to the simulation results from Tab. 5.1 represented in the rightmost column.

could be slight differences between the thermal properties used in the simulation and those of the real sample container.

5.2 Transparent, polished, hydrogen-tight windows for the sample container

Machined, rough-surface aluminum windows[2] for sample containers are fairly easy to make and have been used in UCN transmission experiments before [106, 107, 113, 118, 131].

Aluminum alloys have a favorable post-irradiation behavior (short half-life of 2.5 min of the ^{28}Al isotope, which is created by ^{27}Al capturing a neutron), low neutron scattering and absorption cross sections, and are easily workable. Thermal and

[2]The first VCN transmission experiments through sD_2 at PNPI Gatchina (Russia) [20] used a rough-surface titanium sample container that had much the same disadvantages as the aluminum windows discussed here. The coherent scattering length of natural titanium $b^{\text{Ti}}_{\text{coh}} = -3.438$ fm has the same magnitude as that of aluminum, but is negative, $b^{\text{Ti}}_{\text{coh}} \approx -b^{\text{Al}}_{\text{coh}}$. The same is true for the neutron-optical potentials U_{opt}, respectively. Since the elastic scattering of UCNs on rough metal–vacuum surfaces depends on the squared difference of the coherent scattering lengths at the boundary, its magnitude is almost the same for rough aluminum and titanium surfaces.

cold neutrons have wavelengths of 1 to 10 Ångström and are therefore practically insensitive to the aluminum's neutron-optical potential, material inhomogeneities and surface roughness.

Slow neutrons – especially ultracold neutrons (UCNs), with a velocity of only a few meters per second and a wavelength of several hundred Ångström – are, however, sensitive to surface roughness [132], material [15, 92] and magnetic inhomogeneities [159]. Besides that, aluminum windows are not optically transparent and thus do not allow for an on-line control of the sample. In UCN applications, the advantage of the low neutron-optical potential of aluminum (54 neV) is more than offset by the drawbacks that the use of this material entails.

As tests with single-side polished aluminum[3] windows and unpolished as well as polished aluminum foils (R_a in the range of a few μm) have shown, they are not suitable for UCN transmission experiments because of significant UCN scattering from the vacuum–aluminum and aluminum–sample interfaces due to surface roughness, see Fig. 5.5.

In addition, thin aluminum windows in the range of 0.15 to 0.3 mm tend to bulge at a pressure difference of about one bar. This results in a poorly defined sample thickness, which translates directly to a large error in the scattering cross section. Atchison et al. [106, 107] used an initial sample thickness of 10.0 mm. However, after bulging of the windows, computer simulations suggested an "effective thickness" of 11.1 mm. Considering the relation of sample thickness d and the total cross section σ_{tot} in the transmission equation (Eq. 5.3, where I_0 is the transmitted UCN flux through an empty sample container, and $I(d)$ is the transmitted UCN flux through a sample of thickness d, N_v is the molecular number density of the sample), one immediately understands the importance of a well defined sample thickness.

$$\frac{I(d)}{I_0} = \mathrm{e}^{-N_v \sigma_{\text{tot}} d} \tag{5.3}$$

If one wants to measure the transmission of ultracold neutrons through a cryogenic liquid or solid, the windows of the sample container need to be as highly polished as possible (center-line average roughness $R_a < 10$ Å) in order to minimize undesired scattering from surfaces. Besides a low surface roughness, these windows for UCN transmission experiments should be made from a material with low absorption cross section to maximize the neutron flux to the sample, and with a low neutron-optical potential [42, 43] to transmit UCNs with an as low as possible energy. All materials are practically impervious to UCNs with a kinetic energy below their respective neutron-optical potential. Materials of choice are

[3] Even though polishing aluminum windows can seem to make them shinier and reduce their roughness, hard polishing grains can become implanted into the soft aluminum surface during the polishing process. They can then lead to additional (defect) scattering of UCNs counteracting the effect of a smoother surface.

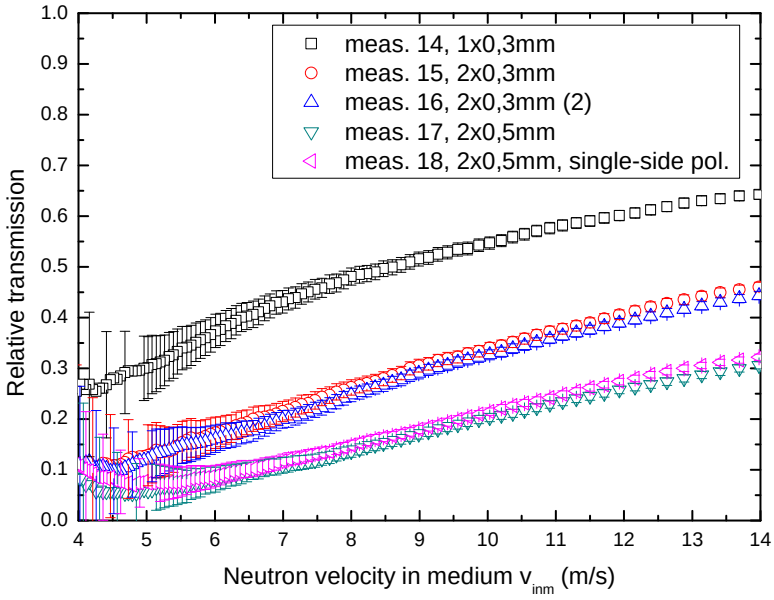

Figure 5.5: Relative transmission of UCNs through one and two AlMg3 windows of 0.3 mm and 0.5 mm thickness at room temperature relative to the direct UCN beam ($T = I/I_0$). The red circles and blue up triangles represent the sample container configuration used in [118]. Both sets of windows are identical and have an identical transmissivity within the experimental uncertainty. The green down triangles represent a sample container with thicker 0.5 mm windows that bulge less under pressure than the 0.3 mm windows. Two of the latter were polished on one side each. The polished sides had a mirror finish but neutron data showed that these windows (purple left triangles) have only a slightly better transmissivity for UCNs than the completely unpolished ones. For all data points below $v = 5$ m/s only every fifth error bar is shown to improve legibility of the plot.

thus silicon, transparent vitreous silica and synthetic quartz (SiO_2; naming convention suggested by Laufer [160] to clarify the naming variations of quartz [161]), and sapphire (Al_2O_3). The latter three are optically transparent and allow for an observation of the condensation and crystal growth processes in the sample container along the neutron beam axis. Amorphous silica has the unique advantage of not producing small-angle scattering inside the material [162]. In our sample containers we used transparent vitreous silica wafers purchased from Plan Optik AG, Elsoff, Germany. All of the following reported results were obtained using sample containers with these wafers.

The fact that the surfaces of the silica windows have a negligible influence on the measured UCN transmission is demonstrated by the virtually identical transmissiv-

ity through one $d = 1.0$ mm window and two $d = 0.525$ mm windows, see Fig. 5.6. If the surfaces had a large impact, four vacuum–silica interfaces would transmit substantially less UCNs than two such interfaces. The neutron-optical potential [42, 43, 44] of the amorphous silica windows used here was calculated based on the volumetric mass density provided by the manufacturer ($\rho = 2.203$ g/cm^3). Its value is 90.6 neV at room temperature and the same at cryo-temperatures due to a volume contraction of less than one per mille.

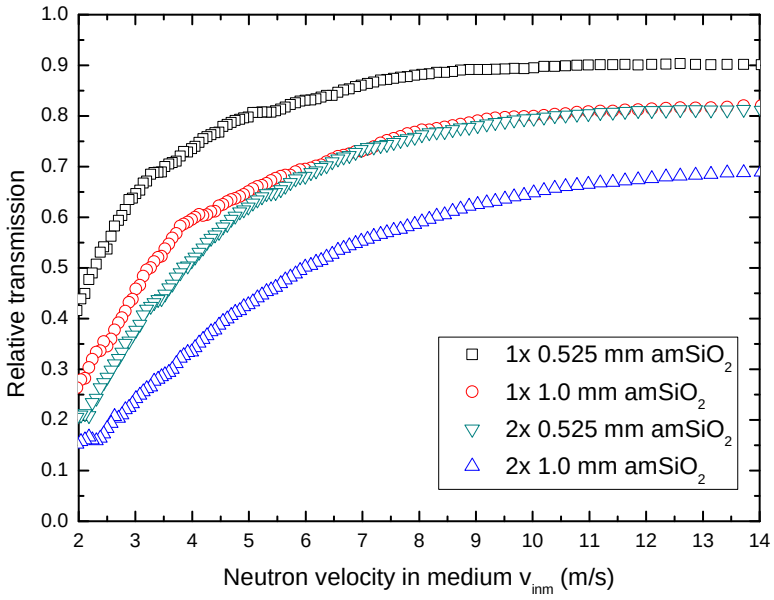

Figure 5.6: Relative transmission of UCNs through one and two amorphous silica windows of 1.0 mm and 0.525 mm thickness at room temperature relative to the direct UCN beam ($T = I/I_0$). The blue up triangles represent the final (empty) sample container.

Since the aforementioned suitable materials are commonly supplied as flat wafers and it is very difficult to make them into one-piece structures (like a flat window plus clamp with screw holes) that would fit into our sample container [118], a hydrogen-tight seal had to be developed to join the flat wafers and the clamps made from aluminum alloy AlMg3 (AA5754)[4]. This became the sample container for the main measurements carried out within this PhD thesis.

[4] AlMg3 is an aluminum alloy with about 3 mass-% of magnesium and a few 0.1 mass-% of chromium, copper, iron, manganese, and silicon each.

5.3 Design requirements for the sample container and optical access

A thick and therefore mechanically strong glass slab or collar does not present an obstacle in experiments with visible light. By contrast, in UCN experiments the glass windows need to be as thin as possible to minimize the absorption of neutrons. Initially, 0.5 mm thick vitreous silica windows were tried out in the sample container, but they imploded in a vacuum test at about 800 mbar pressure difference. Windows of the same size, but with a thickness of 1.0 mm, withstood a pressure difference of 1 bar and more, and thus became the window material of choice for this thesis.

In brief, the design requirements were:

- highly polished and thin windows ($d = 1$ mm), the windows need to be easily removable
- optically transparent windows with a low neutron-optical potential and of high purity (no scattering length density inhomogeneities in the material)
- vacuum seal needs to be easily demountable and hydrogen-tight down to 4.5 K
- sample thickness needs to be well defined, the same across the entire sample area, and adjustable over a wide range within the same sample container
- sample container needs to withstand 2 bar hydrogen pressure against high vacuum with a maximum pressure of 10^{-3} mbar, preferably in the range of 10^{-5} to 10^{-7} mbar, in order for the closed-cycle refrigerator to work smoothly and to minimize UCN up-scattering on residual gas molecules.

The foot of the sample container was designed to be mounted onto the two-stage cold-head of the cryostat described in Döge et al. [118] with a number of modifications: The stainless steel neutron guides facing directly the sample container were removed. An illumination unit with nine white LEDs was mounted on one side of the sample container, see Fig. 5.7. The LED support had a recess for a 50.8 mm double-side polished undoped silicon wafer that served as a reflector for heat radiation coming from the neutron guide. The LED support, and with it the heat reflector, were thermally connected to the cryo-shield on the 1$^{\text{st}}$ stage of the cold head (40 K). The uncovered side of the container could be observed optically through a glass window in the neutron guide and a polished-silicon mirror that could be raised and lowered into the neutron beam through a vacuum feed-through. The mirror was attached to a shaft that could be turned around 360°, which allowed to find the best mirror position for sample observation.

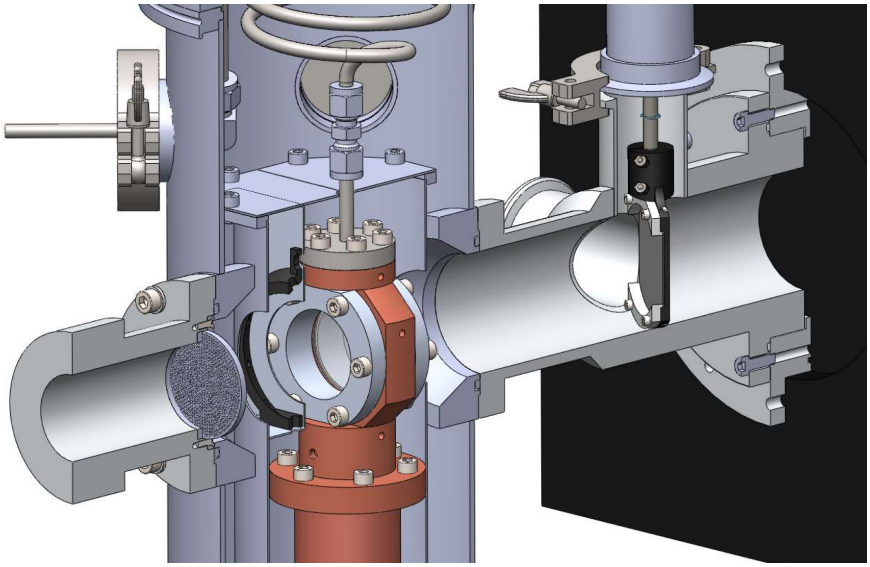

Figure 5.7: The cryostat is shown with the transparent sample container mounted. From left to right the components are: neutron guide adapter, neutron collimator, outer cryostat body, cryo-shield connected to the 1st cooling stage of the cold-head, LED support and heat reflector (not shown), transparent sample container (with gas feed line) mounted on the 2nd cooling stage, neutron guide with horizontal viewport (glass flange) and vertical vacuum feed-through for the shaft and mirror (only black plastic mirror support is shown), and the neutron detector (black box on the right).

5.4 Indium seal

Since the sample container and its windows needed to be sealed against gaseous and liquid hydrogen at temperatures as low as 5 K, the use of rubber O-ring gaskets was not possible. At low temperatures they usually become brittle and leak. Only a few elaborate designs can work with rubber gaskets at low temperatures [163]. The seal for our purposes needed not only to withstand cryogenic temperatures, but it also had to wet the sealing surfaces nearly perfectly. As the smallest molecule in existence, hydrogen is very mobile and can hence escape through even the tiniest scratches in the sealing surfaces. Therefore, the gasket material selected was an indium metal wire gasket (in the literature sometimes referred to as indium O-ring).

Presumably the first mention [164] of indium adhering to glass due to its high wettability was made in 1944. Several years later, in experiments to solder indium metal onto thin films on glass substrates, the adhesiveness of indium to a variety of materials was determined by Belser [165]. Among them were several materials which are of importance to slow neutron scattering – as windows for sample holders: silicon, quartz, aluminum oxide; structural materials: aluminum and copper; and as neutron absorbers: cadmium, titanium and lead. Belser soldered at temperatures around 160 °C to make the adhesive connection between indium and these materials. Our sample container's geometry, however, did not allow for a hot treatment.

Cold-welding an indium seal, i.e. applying only pressure at room temperature to fuse the ends of an indium wire to one another and the whole one-piece ring to a glass surface, appears to have first been reported by Edwards [166]. Following this pioneering work, many designs of cold-welded indium wire seals have been published; mostly for metal-to-metal joints, but also for metal-to-glass joints. The term "glass" here is meant in a broader sense to refer to optically transparent materials and includes quartz, vitreous silica, sapphire, and similar materials. The main advances in the field of metal-to-glass joints that are hydrogen and helium-tight, have been made in the 1950s-1960s [166, 167, 168, 169, 170], among others to seal a large liquid hydrogen bubble chamber [171], and in the 1980s [172, 173, 174, 175]. A substantial overview of published indium seal designs was given by Turkington and Harris-Lowe [173]. All previous designs that describe metal-to-glass joints use, however, flat glass slabs of appreciable thickness – in the range of several millimeters to centimeters – and of corresponding mechanical strength.

5.5 Final design

Two particular restrictions to the design of our sample container made it difficult to achieve good vacuum tightness: (i) The need to have thin windows in combination with a large diameter of 43.8 mm prohibited the exertion of excessive clamping

force on the silica windows. (ii) Depositing a wetting agent like indium, nichrome or platinum onto the rims of the glass flats to improve contact with the indium gasket, as some experimenters have done [170, 172, 174], was not desirable in our case because of frequent demounting of the sample container and some glass breakage that occurred. This meant that the bare indium gasket alone had to provide the required vacuum tightness.

First tests were done with unchamfered aluminum compression clamps for the indium seal and yielded containers that were tight enough to condense air and hydrogen into. However, these seals were not stable over time and proved to fail at overpressures of a few hundred millibar.

The solution to this problem was to machine a 1 mm deep 45° chamfer on the outside of the compression clamp's rim that protrudes into the sample container. The chamfer created a void for the indium to creep into, which could then evenly distribute the clamping force over the whole edge of the silica window. The chamfer greatly improved reproducibility and reliability of the seal.

If the seal were classified according to Lim [174], it would be called a partially trapped O-ring seal.

In UCN transmission experiments it is important to measure samples of two or more well defined different thicknesses so as to separate bulk scattering from scattering at the surface or the sample–window interface. Our copper sample container employs aluminum spacer rings of variable thickness which, combined with a series of different pressure clamps adapted to them, enable quick adjustment of the sample thickness. The two aluminum pressure clamps require a total of four indium wire seals – two inner seals (clamp to silica window) and two outer seals (container body to clamp mating surface).

The clamping force is provided by six equally spaced stainless-steel hexagon socket head cap screws (size M5, 16 mm thread) on each of the two aluminum clamps. To prevent the screws from loosening at cryogenic temperatures, split lock washers are placed between them and the pressure clamps. As the clamps press evenly against the inner and outer indium wire gaskets, the silica windows are held at a constant distance by 2 mm wide (i.e. outside diameter minus inside diameter divided by 2) spacer rings made from aluminum that support the edge of the windows. That distance remains constant even under high pressure. At the top of the spacer ring there is a gap for the gas inlet. The edges of the aluminum spacer rings need to be smoothly rounded off, in order to avoid extreme local strain on the silica windows which can lead to their cracking.

Although spacer rings with a gas inlet gap as large as the diameter of the gas inlet itself would be favorable (9 mm in this case), we found the optimal gap width to be 5 mm. Rings with a 9 mm gap made the silica windows crack due to the larger unsupported fringe area of the windows. It is, however, possible to use rings with 5 mm gaps or no gaps as direct supports for the silica windows and a center ring with a wider gap to allow for a larger gas flow area, see Fig. 5.8.

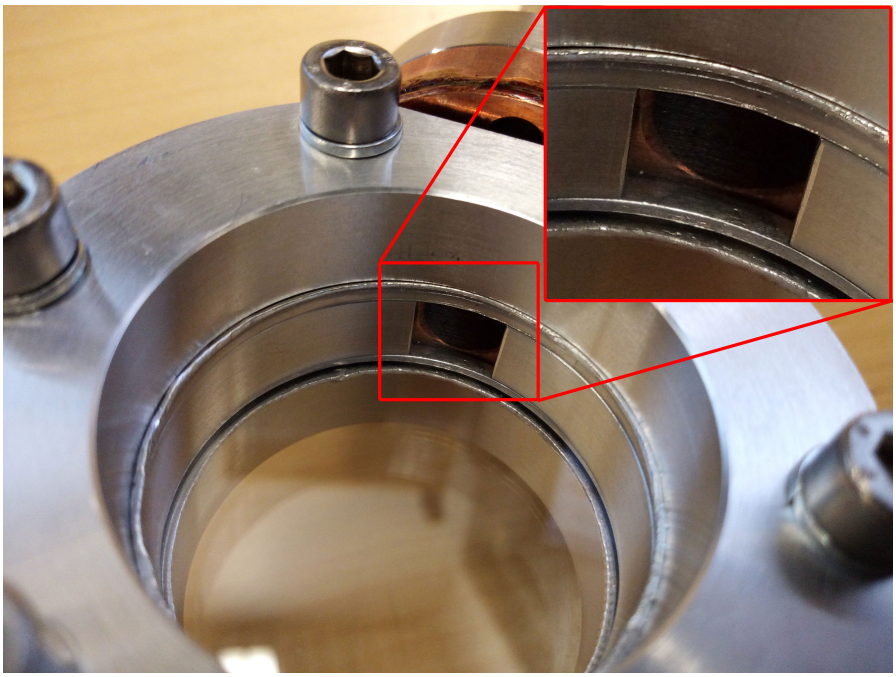

Figure 5.8: Close-up view of the assembled sample container showing the gas inlet and the gap in the central aluminum spacer ring. The layers from the top as shown in the inset are: aluminum clamp, indium wire gasket, silica window, first spacer ring ($d = 1$ mm), second spacer ring ($d = 9$ mm) with 9mm gas inlet gap, third spacer ring ($d = 1$ mm), silica window, indium wire gasket, aluminum clamp.

The length of the compression clamp protruding into the sample container and the thickness of the spacer rings were designed such that the inner indium wire seals (clamp to silica window) were compressed to a thickness of 0.50 to 0.60 mm, and the outer seals (container body to clamp mating surface) to 0.45 to 0.50 mm. With the initial indium wire thickness of 1.5 mm this meant a final gasket compression to 1/3 of the original thickness, see Fig. 5.10 (detail B).

As was pointed out by Turkington and Harris-Lowe [173], to ensure high seal tightness, the surface that is cold-welded to the indium gasket, needs to be either untreated, i.e. utilized as it comes off the lathe, or polished to less than 5 μm roughness. In our seal the vitreous silica wafers were highly polished ($R_a < 3$ Å, as determined by atomic force microscopy, see Fig. 5.9) and the bonding of indium wire to the wafer could be seen after disassembly of the sample container. The aluminum compression clamps were used with the surface finish as they came off the lathe, i.e. with microscopic spiral lines causing a surface roughness of $R_a \approx 7$ μm. The inside surface of the copper container body was equally untreated.

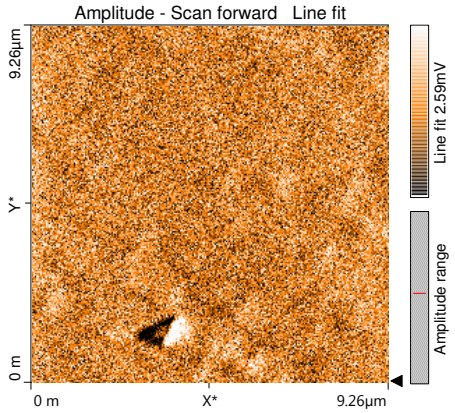

Figure 5.9: 2D atomic force microscopy (AFM) image of an amorphous silica window. The center-line average roughness is 2.85 Å. A second scan of the same sample yielded 1.95 Å. Considering these two measurements and the information from the manufacturer ($R_a < 5$ Å), it is safe to assume 3 Å as the actual maximum roughness.

For sample heating, the container is equipped with two heaters, one 0.1 mm diameter constantan resistive wire recessed in a groove around the top, and one heating resistor in the base of the container. Two Cernox thin film resistance cryogenic temperature sensors take the temperature readings just above and just below the sample volume. They are inserted into holes drilled into the container body, see Fig. 5.10 (detail A).

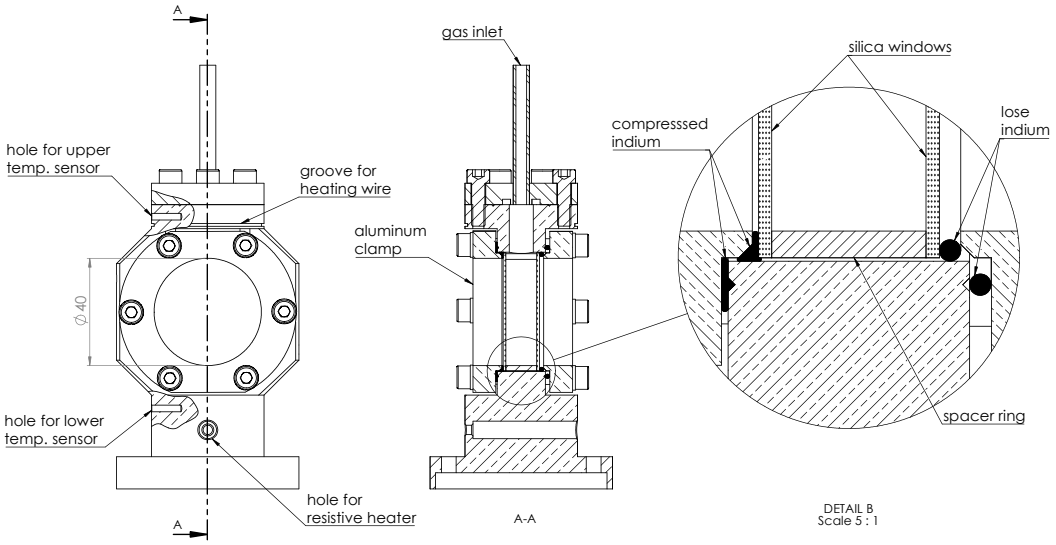

Figure 5.10: Front, side and detailed view of the sample container; each of the two aluminum compression clamps is affixed to the copper sample holder by six stainless steel hex screws (size M5, 16 mm thread). Split lock washers or copper–beryllium washers are placed under the screw heads to prevent loosening of the assembly at cryogenic temperatures. The copper container has one 1 mm deep angular groove at 45° for the outer shallow-groove indium seal [176] on each mating surface. The outside of the rim of the aluminum clamp, which protrudes into the copper container, has a 1 mm × 45° chamfer in order to tightly press the indium against the silica window and the copper container body. The two windows are kept at a precisely determined distance from each other by an aluminum spacer ring between them, which has a thickness of 11.5 mm in this figure. In the sectional view A–A and the detailed view B, the left-side indium wire gaskets are compressed, the right side shows uncompressed indium wire of 1.5 mm diameter. This drawing is to scale, the dimension (40 mm) of the aluminum clamps' inner diameter is indicated on the left.

5.6 Assembly and leak testing at room temperature

Before inserting the aluminum spacer rings, the silica windows, the indium wire gaskets and the aluminum clamps into the sample container, all these items were cleaned. The aluminum parts and the sample container itself were wiped with a lint-free wipe soaked in pure ethanol. The silica windows were pre-cleaned by the manufacturer in a process comprising rinses with a sodium hydroxide solution followed by a phosphoric acid solution. The acid was removed using de-ionized water and the windows were then blow-dried with air. We wiped each of them with ethanol and then blow-dried them with oil-free air to remove any lint from the surface.

Making indium wire more adhesive is achieved by removing the 50 to 100 Å thick oxide layer [177, 178] that forms naturally on the surface. A method proposed by the Indium Corporation [178] (degreasing, wiping with 10 wt.-% hydrochloric acid, rinsing with de-ionized water and acetone) improved the adhesiveness of the indium wire, but proved to be rather time-consuming. Instead, the oxide layer was removed mechanically by scraping it off with a knife that was pulled gently over the wire against the direction of the cutting edge. This treatment improved the adhesiveness to the same extent. The indium wire used in this joint had been recycled from scrap indium of > 99.999 mol-% original purity by the Cryogenics Service of the ILL. Mass spectroscopy analysis of the indium wire showed a purity of 99.7 mol-%, with the main contaminants being Pb, Sn, Ag, Na, and Cd. This is the standard gasket material for cryostats at ILL. Neither the indium wire gaskets, nor the mating surfaces were coated with solder flux or grease, as was the case for some previous seal designs [170].

Indium wire rings of 43.5 mm inside diameter for the two inner seals and of 47.0 mm for the two outer seals were preformed from 1.5 mm diameter indium wire. The wire's butting ends were beveled by cutting them diagonally with a sharp blade at an angle of about 45° to 60°. The exact angle did not seem to have any influence on the seal tightness as long as the cut faces were properly aligned and pressed against each other.

Assembly of the sample container commenced by attaching one of the aluminum compression clamps and the corresponding outer indium wire gasket to the sample container body (inner diameter of 44.5 mm) with 6 hex screws. Then the container was turned around such that all other inserted parts could rest on the protruding rim of that compression clamp. Next the first inner indium wire gasket was inserted into the ledge formed by the rim of the clamp and the inner wall of the sample container. After the indium wire gasket was put in place and leveled, a vitreous silica window and one or more spacer rings made from aluminum were inserted. At this stage it had to be ensured that the gap in the spacer ring was properly aligned with the gas inlet port in the top of the container. The following items were then inserted: the second vitreous silica window and the second inner and

outer indium wire gaskets. The last assembly step was to carefully slip the second compression clamp into the orifice of the sample container and to press lightly but equally against both the inner and outer indium wire gaskets.

After all parts were in place, the container could be returned to an upright position. The stainless steel screws on the pressure clamps were then tightened step by step in a criss-cross pattern to ensure a uniform pressure distribution on the gaskets and the silica windows. The seal was formed as all four indium wire gaskets were gradually compressed.

Since the indium continued to flow slowly each time the screws were tightened, we allowed about five minutes before the next round of tightening.

In the thin-sample configuration ($d < 4.5$ mm), the gas inlet ($d = 9$ mm) overlaps the sandwich of indium wire, window, spacer, window, indium wire and the sample volume is connected to the annular space of about 0.09 cm^3 between the two indium seals through a small gap between the wall of the gas inlet and the compressed indium wire, see the sectional view A–A in Fig. 5.10. During evacuation of the sample container, the annular space is evacuated as well. However, in the thick-sample configuration ($d \geq 4.5$ mm) the annular space is completely trapped between the inner and outer indium seals and can therefore not be evacuated. Air that gets trapped there during assembly of the container, cannot escape. Since the sample container is well evacuated and cooled down to cryogenic temperatures before inserting hydrogen and other gases into the sample volume, this air solidifies inside the annular space and can therefore not contaminate the sample. The trapped air in the annular space did in no way compromise the functionality of the sample container described here. In future designs, a modified shape of the gas inlet can connect the annular space to the sample volume, which can thus be vented during evacuation of the sample container.

The leak rate out of the sample container into the isolation vacuum, where some of the surfaces are at low temperatures, had to be as low as possible. Only below 10^{-1} mbar are the up-scattering losses of ultracold neutrons negligible, see Section 4.11, and only well below 10^{-2} mbar does a cold-head (closed-cycle helium refrigerator) work properly. The isolation vacuum was evacuated by a pre-pump and a turbomolecular pump used in series. A desirable permanent isolation vacuum with the sample container installed and filled is below 10^{-5} mbar.

During extended operation of the cryostat at cryogenic temperatures, gas from small leaks into the isolation vacuum can potentially freeze out on the cold-head and suddenly evaporate during warm-up of the cryostat. To prevent the risk of pressure peaks on the experimental equipment and the UCN source, the cryostat was equipped with an overpressure break foil. In the unlikely event of a sudden pressure increase, it would have opened up and released the gas into the atmosphere. The installation of the break foil was in compliance with the safety regulations in force at Institut Laue-Langevin.

Since the installation of the sample container into the cryostat and the subse-

quent vacuum pumping and cool-down are quite time-consuming, we developed a leak testing method, based on a pressure build-up measurement at room temperature, from which we could reliably deduce the sample container's performance at cold temperatures. After complete assembly and the tightening of the indium seals, the containers were leak-tested by evacuating them down to the 10^{-2} mbar range using an oil-free piston pre-vacuum pump against 1 bar atmospheric pressure. The screws on the pressure clamps were then continuously tightened until the rate of air leaking into the sample container was below $Q_{\mathrm{L}}^{\mathrm{thick}} = 3.4 \times 10^{-5}\,\mathrm{mbar} \times \mathrm{L/s}$ and $Q_{\mathrm{L}}^{\mathrm{thin}} = 9.5 \times 10^{-5}\,\mathrm{mbar} \times \mathrm{L/s}$ for thicker ($d \geq 4.5$ mm) and thinner sample thicknesses, respectively. These values have been corrected for the leak rate of the gas test stand and were calculated over a time period of ten minutes, which is about the time it takes to fill the container with a cryogenic liquid.

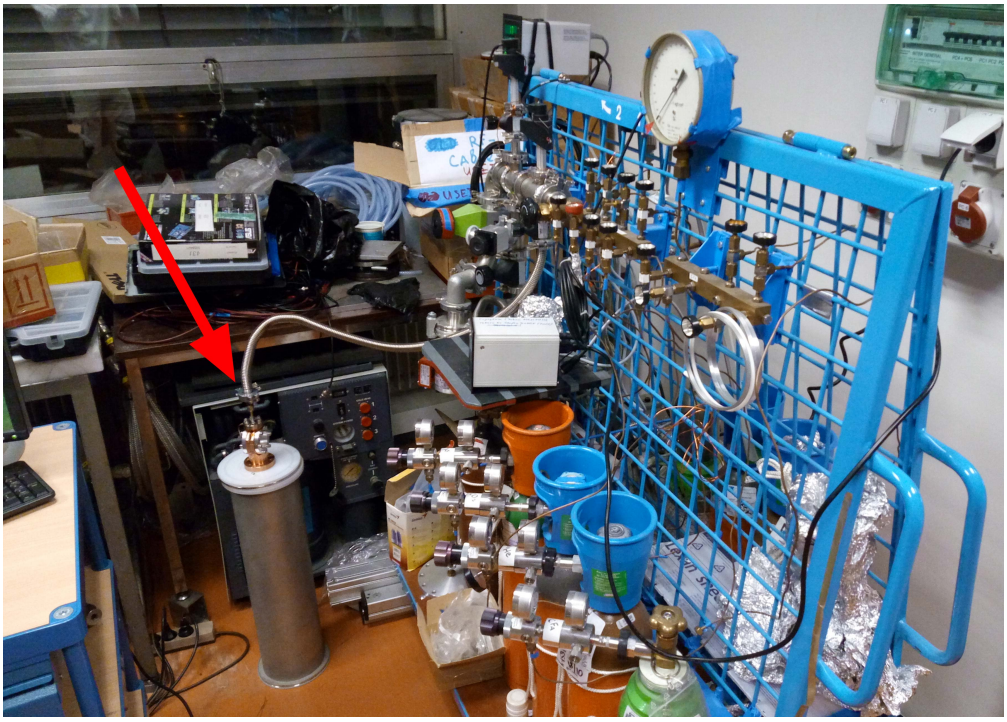

Figure 5.11: The pressure test of the sample container was performed at the gas refill stand of Alexander Strelkov (JINR Dubna) at ILL.

After the vacuum leak test, the sample container was vented and the indium wire was left to creep for 12 to 24 hours. Then the vacuum leak test was repeated and the screws gradually tightened until the leak was again at or below Q_{L}. In this last step, a torque screwdriver may be useful. The maximum final torque applied to the screws was between 0.8 to 1.0 Nm. The last leak test and tightening should be done only shortly before mounting the sample container into the cryostat. The gas test stand used for this testing procedure is shown in Fig. 5.11.

To obtain a general idea of the seal tightness against hydrogen, overpressure tests were performed with a similarly light and viscous, but safer gas – helium. The sample container and the gas system were filled with 1600 mbar of helium against 1 bar of atmospheric pressure. These tests usually lasted for one or two hours. The leak rate of helium out of the sample container and into the atmosphere was typically $\leq 2 \times 10^{-4}\,\mathrm{mbar} \times \mathrm{L/s}$ (corrected for gas test stand leakage) for containers that had been successfully air-leak tested in a pressure build-up measurement.

Sample containers assembled and tested in this manner remained deuterium-tight for four temperature cycles between 5 K and room temperature with deuterium condensed into and evaporated out of the container each time. The tests were discontinued at that point with the container fully functioning, because frequent cycling between room and cryogenic temperatures is not required in our application. As it stands, the container would have likely remained intact during more cyclings.

5.7 Observations at cryogenic temperatures

The first cryogenic tests using this sample container were done by freezing a deuterium crystal out of the gas phase. In order to have the warm gas freeze at all, the container had to be as cold as possible as opposed to being kept just below the freezing point. As the warm gas flowed into the container, it started freezing out on the bottom, but to a large degree also on the side walls and inside the gas inlet – copper parts that were well thermalized to the cold-head temperature. In all attempts the gas inlet froze over before the crystal in the sample container had grown to a sufficient size. That is why freezing from the gas phase was not pursued any further and the crystal was instead grown from the liquid.

Other experimenters, for example Lavelle et al. [113], encountered a similar problem. Due to the use of an optically non-transparent sample container, they were not able to verify whether solid deuterium (sD_2) in a half-filled container rested only in the lower half or whether part of it froze out on the side and upper walls of the container. Our observations support the latter conjecture.

When cryogenic liquids (H_2, D_2) close to the triple point were kept in our sample container, the container and its indium gaskets had to withstand pressure differentials of up to 2 bar. A hydrogen pressure of about 1.5 bar in the sample container increased the pressure of the insulating vacuum of the cryostat to the 10^{-5} mbar range. The seals withstood higher pressures for a few minutes. The pressure inside the container was measured on the gas fill line outside of the cryostat [118].

After the first crystal growing tests in the transparent sample container it quickly became apparent that substances with a higher density in the solid than in the liquid phase will always form bubbles in the freezing process, see Fig. 5.12. In the case of deuterium, the density increases by 12% during the phase transition from liquid to solid, for hydrogen the increase is 11% [46].

According to $\Delta\rho = m/(h \times \Delta A)$ – where $\Delta\rho$ represents the crystal density change, m its mass, h its thickness between the two quartz windows, and ΔA the change in area – this corresponds well to the crystal area decreased by 9 to 10%, see Fig. 5.12. The reason for bubble formation is that the crystal solidifies out of the liquid radially, starting at the inner wall of the sample container and growing inward. The fastest growth of the crystal takes place at the bottom of the sample container, where most heat is removed from the sample by the cold-head. But even on the sides and the top of the sample container, where the temperature is about 1 K higher than at the bottom due to the inflow of warm gas, the liquid starts freezing. When about one third to one half of the sample is frozen, the gas inlet at the top of the sample container freezes over and no additional liquid can enter the sample container. This cannot be avoided, even by heating the top of the sample container with 4 to 5 W, because the power required to keep the gas inlet open would heat up the entire sample to above the freezing point.

After the gas inlet has frozen over and a liquid-filled crystal ring around the inner wall of the sample container has formed, there is a point at which gas bubbles form inside the liquid as the freezing process continues. They rise to the top of the liquid reservoir and are pushed downward by the advancing crystal ring. When all liquid has frozen, the center of the sample container is filled with an irregularly shaped solid–vacuum phase boundary. This is shown in Fig. 5.12 (c) – albeit with a minimal amount of suspended liquid. One might call this phase "snow". UCNs are highly sensitive to phase boundaries and rough surfaces where the neutron-optical potentials of both phases differ by more than ~10 neV. As the highest neutron flux is very much centered in UCN guide tubes, this snow is right inside the UCN beam and significantly distorts the scattering pattern.

The only way that was found to circumvent these complications was to minimize the snow-covered area by employing thaw–refreeze cycles. After about ten such cycles, see Fig. 5.12 (e), during which the snow and the surrounding solid were carefully melted at 0.1 K above the melting point and then slowly refrozen, a single void with a smooth surface was obtained. The void stretched from one sample container window to the other. Blinding out the void by covering it with a flap-shaped cadmium absorber ($d = 0.5$ mm, transmissivity for UCN $\leq 10^{-2}$) and lifting up the sample container by 9 mm to maximize the UCN flux through the pure crystal below the absorber flap was the only way to obtain UCN transmission data through clear cryogenic crystals, see Fig. 5.12 (g-h).

This snow-forming behavior was observed in all substances that were frozen (hydrogen and deuterium) and at various sample thicknesses (1 mm, 2 mm, 4.5 mm, 6.5 mm, 11.5 mm). Although care must be taken when generalizing the behavior of a substance in one specific sample container, it is safe to say that it is very difficult to completely fill any sample container of a few milliliters in volume, such as ours, with a bubble-free crystal.

Fig. 5.12 (e) shows a few radial streaks covering the crystal area. By keeping

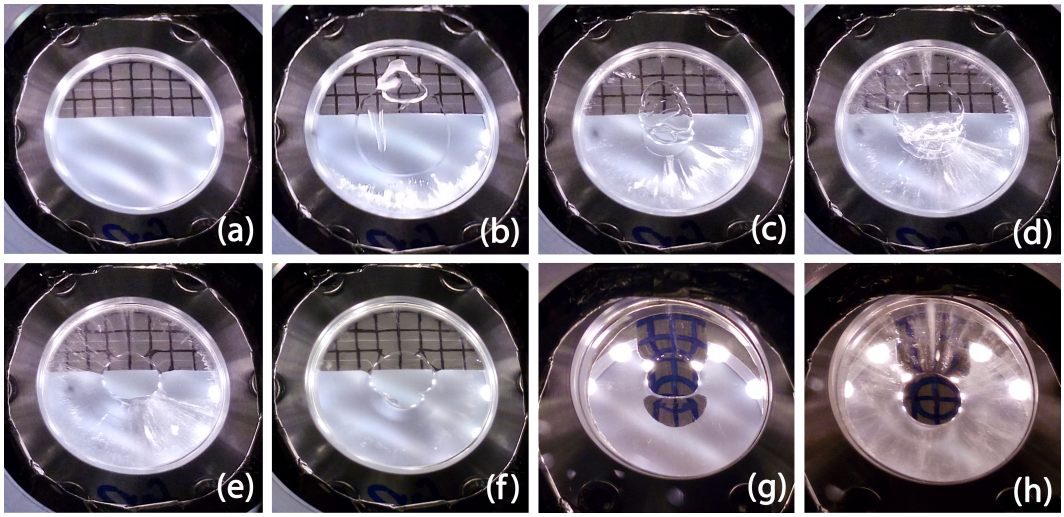

Figure 5.12: View of the sample container along the neutron beam axis as seen through viewport and mirror shown in Fig. 5.7. Parts of the sample container are blinded out for ultracold neutrons by 0.5 mm thick cadmium absorbers. The marking lines on the absorbers are for reference and are 5 mm apart from each other. The sample in (b-f) is 4.5 mm *para*-hydrogen, in (g-h) 6.5 mm *ortho*-deuterium. The images above show (a) an empty sample container with a straight-edge absorber; (b) a liquid-filled *para*-hydrogen crystal ring with bubble formation in the liquid phase; (c) freshly frozen solid *para*-hydrogen, irregular solid–liquid–vacuum phase boundaries ("snow") in the center of the sample container, visible radial streaks; (d) the previous crystal after one thaw–refreeze cycle; (e) the previous crystal after about 10 thaw–refreeze cycles, where the irregular phase boundaries have disappeared and a void with a smooth surface has formed; (f) the previous crystal after 15 hours at constant temperature ($T = 9$ K) and one short thaw–refreeze cycle, the radial marks have disappeared as they were located not in the crystal bulk, but only on the crystal–window interface; (g) a frozen and cycled *ortho*-deuterium crystal at $T = 14.5$ K with a flap-shaped absorber; (h) the previous crystal after cooling to $T = 10$ K.

the crystal just below the melting point and letting heat radiation impinge on the sample container, as well as through melting and refreezing the samples we could establish that these streaks were only present on the crystal–window interface, but not in the bulk of the crystal. A streak-free and absolutely clear *para*-hydrogen crystal is shown in Fig. 5.12 (f).

Whether or not the cryogenic crystal remains in close contact with the vitreous silica window after it has been grown cannot be stated with certainty. However, if

it becomes detached, the smooth surface on which it grew (the roughness of silica windows was less than 3 Å) and its optical transparency mean that a very smooth crystal surface is highly likely.

The determination of precise UCN total cross sections of cryogenic liquids and solids, especially those of solid deuterium, are of great importance to the planning and improvement of UCN sources based on solid *ortho*-deuterium. The larger the mean free path $\lambda_{\mathrm{mfp}} = (N_{\mathrm{v}}\sigma_{\mathrm{tot}})^{-1}$ of UCNs inside the converter material, the higher the UCN flux extractable from the converter. The mean free path of UCNs, and with it the maximum UCN density inside the converter, depends to a large extent on the sD_2 crystal preparation method and holding conditions.

In a previous experiment at the Paul-Scherrer-Institut (PSI) [21, 107], the deuterium crystal was observed perpendicular to the neutron beam axis with blue light from an argon laser. Multiple temperature cyclings between 5 K and 18 K significantly deteriorated the transmission of light and UCNs through that crystal. Applying our above observations, it is conceivable that the crystal surface started melting close to 18 K (even though the temperature sensors were still below the triple point) and then refroze in an uncontrolled fashion. This would have resulted in the gradual formation of a rough crystal surface on the crystal–sapphire interface, causing decreased light transmission, as well as at the crystal–aluminum interface, causing decreased UCN transmission. This scenario is at least a potentially plausible explanation for a significant part of the "additional isotropic elastic scattering" that was entirely attributed to crystal imperfections and subtracted from the total scattering cross section before the final publication of results [107].

Previous experiments on the growth of deuterium crystals in sample containers have not come to an unanimous conclusion as to which freezing method produces the most transparent crystals. However, a literature review on this topic hinted at crystals grown from the liquid phase being more transparent than those grown from the gas phase, while also growing faster and requiring less complex handling. None of the sources reviewed reported that crystals grown from the gas phase were more transparent for light and neutrons. A few reported that those grown from the liquid phase were more transparent [69, 179], while many only investigated those grown from the liquid assuming that they were the most transparent or because these experimenters were not able to grow them from the gas phase [21, 55, 113, 180, 181]. Yet others demonstrated inconclusive results, i.e. similar transparency for crystals grown from the liquid and gaseous phases, for D_2 [19, 58, 182] and for H_2 [183]. However, a large number of reports on sD_2-based UCN sources and other experiments with sD_2 did not mention the – quite important – method of freezing and crystal holding conditions, e.g. [45, 57, 184, 185]. In some sD_2-based UCN sources it is possible to freeze out crystals only from the gas phase due to the source geometry, e.g. at TRIGA Mainz [186, 187] and the planned source at FRM-II Munich [188, 189] (hitherto unpublished technical and authorization

reports)[5].

It should be noted that the silica windows of an empty sample container have a temperature of about 60 K, when the container's body is at 5 K. This is due to the relatively poor heat conductivity of amorphous silica. The corresponding up-scattering cross section for UCNs in amorphous SiO_2, calculated using the incoherent approximation and a Debye temperature of 361 K [190], is 0.8 barn per SiO_2 unit for neutrons with $v = 10$ m/s and can therefore be neglected. As soon as a sample was introduced to the container, the windows adopted the temperature of the sample to within a few 0.1 K.

As is explained in Chapter 1, ultracold neutrons experience an energy step when entering matter from vacuum or going from one material into another. Surface scattering is a coherent elastic process, see Section 3.5. Therefore, the scattering caused by a rough surface depends not only on the magnitude of the roughness R_a, but also on the coherent scattering length b_coh and the particle number density N_V of the surface material. In other words, it depends on the difference of the neutron-optical potential $\Delta U_\mathrm{opt} \propto \Delta(b_\mathrm{coh} N_\mathrm{V})^2$ of the materials on both sides of the rough surface. If the potential difference on both sides is negligible, so is the scattering caused by the surface roughness. In the case of silica (or quartz) windows and deuterium, there is a good matching of neutron-optical potentials, see Tab. 1.2. Even for a rough silica–deuterium boundary, surface scattering would be significantly reduced as compared to aluminum sample cell windows.

For completeness sake, it should be mentioned that UCN transmission experiments were carried out with *para*-hydrogen in addition to those with deuterium. Even though the para-hydrogen content was $c_\mathrm{para} = 99.8\%$, the 1 mm thick sample was almost black to UCNs. The transmission through the sample was so low that it did not allow for a meaningful calculation of the scattering cross section. However, making a thinner sample and using VCNs for transmission measurements will be interesting and should be considered for future experiments.

Note: Large parts of this chapter have been published in a peer-reviewed journal as
S. Döge and J. Hingerl: A hydrogen leak-tight, transparent cryogenic sample container for ultracold-neutron transmission measurements, Review of Scientific Instruments 89, 033903 (2018), also available as pre-print on `https://arxiv.org/abs/1803.10159`.

[5] Andreas Frei (TU Munich, FRM-II), priv. comm.: The deuterium crystals frozen out from the gaseous phase onto a mock vertical UCN "nose" were transparent. Apparently, it is easier to freeze out a transparent deuterium crystal from a gas-infused neutron guide of large volume than inside a small sample container.

6 Raw Data Processing

[...] la moltitudine de' veri concorre all'investigazione, accrescimento e stabilimento delle discipline, e non alla diminuzione o destruzione [...]

— Galileo Galilei, *lettera a Cristina di Lorena, granduchessa di Toscana (1615)*

The treatment of data recorded by the Cascade detector in a TOF setup, see Chapter 4, requires the following steps

- removal of faulty measurement runs
- subtraction of background
- normalization to measurement time
- appropriate binning to achieve a good compromise between time resolution and statistics
- correction of flight time due to the chopper–detector time offset
- conversion of the time spectra into the velocity (v_z) or energy domain ($E_{kin,z}$)
- correction of quantum-mechanical reflection of UCNs from the sample surface
- correction for detector solid angle
- correction for sample impurities

6.1 Background subtraction, normalization and binning

The first step in the treatment of raw transmission data is the addition of all individual runs (120 or 190 s) of each measurement. Faulty runs with a significantly higher or lower UCN count than the normal distribution of runs were discarded. This affected much less than 1% of all runs. Next, the uncorrelated background as shown in Fig. 6.1 was subtracted from each measured spectrum. This background

is always present, regardless of the shielding of the Cascade detector by borated rubber mats. It is largely caused by electronic noise and γ rays, which emanate from the reactor core and especially from the UCN Turbine. Some of it is caused by thermal neutrons. It should be noted that the background radiation on Level D (upmost floor of the ILL reactor) is significantly elevated compared to other experimental areas at the ILL.

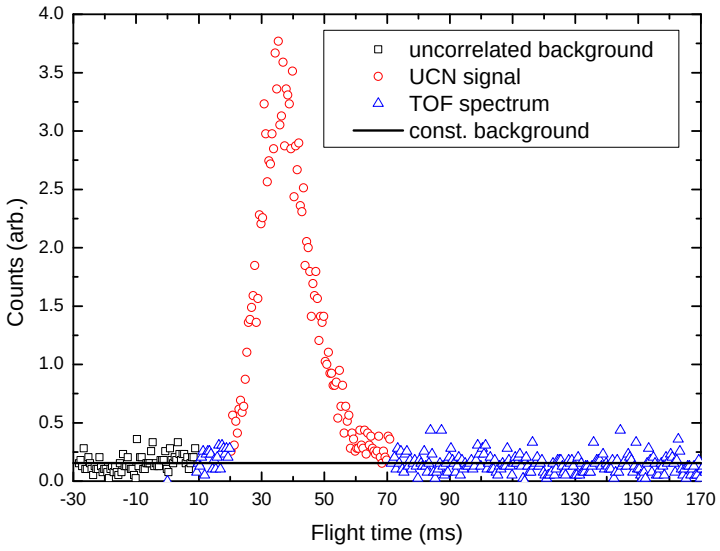

Figure 6.1: The uncorrelated background in the UCN spectra was subtracted by taking the arithmetic average of the counts in channels 1–75 and subtracting it from each channel. This was done for each measurement individually.

As a rule, the data taken for this thesis were binned using a sliding frame of 16 bins of 0.5 ms width each. This binning was taken into account when the error bars were calculated.

Since the transmissivity of the samples is calculated by dividing two UCN spectra one by the other, it is important to make sure these spectra are well aligned. It shall not be concealed that an UCN experiences a slow-down while traversing a sample of a given thickness and a given neutron-optical potential. This slow-down is the consequence of the non-zero index of refraction of the medium, see Eq. 1.15. It can lead to a skewing of the UCN spectrum on the side of slow UCNs as the relative change in velocity is highest for the slow UCNs. A neutron is decelerated when the neutron-optical potential of the matter is is traversing is positive and it is accelerated when the potential is negative. A ratio r is introduced to reflect the apparent in-medium neutron velocity vs. the nominal in-medium neutron velocity

and is defined as

$$r = \frac{d_{\mathrm{TOF}}}{d_{\mathrm{TOF}} - d_{\mathrm{sample}} + d_{\mathrm{sample}} \times \frac{\sqrt{v_{\mathrm{inm}}^2 + v_{\mathrm{crit}}^2}}{v_{\mathrm{inm}}}}. \tag{6.1}$$

For the case of solid deuterium with a potential of 105 neV, i.e. $v_{\mathrm{crit}} = 4.48\,\mathrm{m/s}$, a sample thickness of 10 mmm, and a TOF path length of 455 mm, the ratio r is plotted in Fig. 6.2. For in-medium neutron velocities of 2.1 m/s the difference between apparent and nominal velocity is less than 3%, for 4.2 m/s it is less than 1% and even less than that for faster neutrons. UCNs of 2.1 m/s and less are of little practical importance for the measurements presented here as they lie at the edge of the spectrum where the statistical and systematic errors are high. It can therefore be concluded that a correction of the velocity axis is not necessary for the experiments within this thesis work.

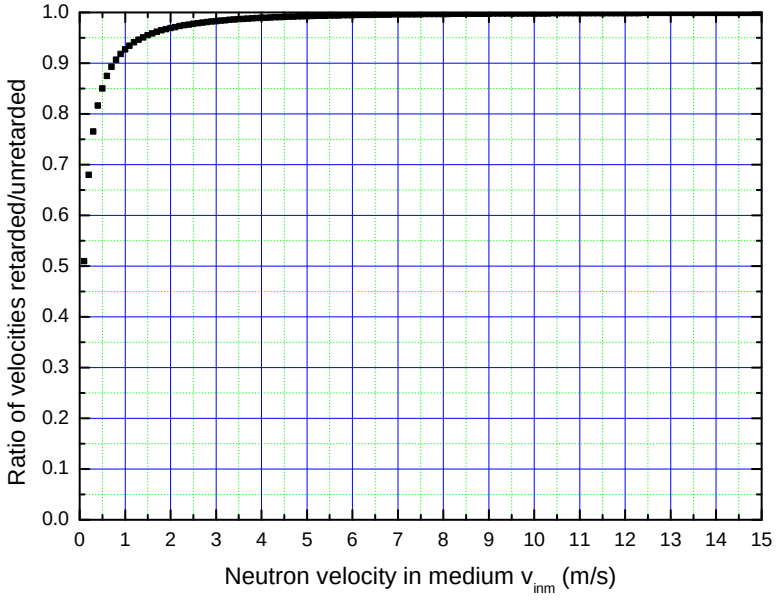

Figure 6.2: Ratio r of apparent vs. nominal UCN velocity over in-medium UCN velocity in solid deuterium. It is obvious that the flight-time retardation only has an effect for the slowest UCNs of ≤ 2.1 m/s.

6.2 Transformation of variables

Before any transformation of variables could take place, the time spectra were corrected by the time offset between the chopper trigger signal, which triggered the Cascade detector, and the actual copper opening. Subsection 4.7.2 describes the two ways of measuring this offset with neutrons and light.

When the domain of the neutron spectrum changes, the channel width is no longer constant as it is in the time domain. Therefore, the count rate per channel needs to be adapted to the new channel width for the respective new domain. In this thesis, neutron spectra and cross sections are, as a rule, presented in the velocity domain (in-medium v_{inm} and out-of-medium velocities v_0).

The differential count rates (or count rates per channel) are transformed from the time domain to the out-of-medium (or vacuum) velocity domain by

$$\frac{\mathrm{d}I}{\mathrm{d}v_0} = \frac{\mathrm{d}I}{\mathrm{d}t}\frac{\partial t}{\partial v_0} = \frac{\mathrm{d}I}{\mathrm{d}t}\frac{d_{\mathrm{TOF}}}{v_0^2} \tag{6.2}$$

and from vacuum to in-medium velocity by

$$\frac{\mathrm{d}I}{\mathrm{d}v_{\mathrm{inm}}} = \frac{\mathrm{d}I}{\mathrm{d}v_0}\frac{\partial v_0}{\partial v_{\mathrm{inm}}} = \frac{\mathrm{d}I}{\mathrm{d}v_0}\frac{v_{\mathrm{inm}}}{v_0}, \tag{6.3}$$

where $v_{\mathrm{inm}} = \sqrt{v_0^2 - v_{\mathrm{crit}}^2}$ and v_{crit} is the critical velocity of the medium, see Tab. 1.2.

6.3 Correction for reflection

When a neutron transcends a phase boundary between two media of different neutron-optical potential, and thus different index of refraction, it has a non-zero probability of being reflected. This effect is more pronounced for very slow neutrons and can be neglected for neutrons with $v_{\mathrm{inm}} > 5$ m/s in deuterium [118, 135].

Steyerl developed a detailed theory of reflection for slow neutrons [191]. The key equations for transmission through a phase boundary is

$$T = \frac{4k\mathrm{Re}(k')}{|k+k'|^2}, \tag{6.4}$$

and for reflection

$$R = \frac{|k-k'|^2}{|k+k'|^2}, \tag{6.5}$$

where k is the neutron wave vector of the incident neutron outside of the sample and k' is the wave vector inside the sample. The wave vectors k and k' can have imaginary parts that signify absorption and inelastic scattering, i.e. up-scattering of UCNs. These imaginary parts are small enough to be neglected in the case of deuterium.

Summed up over the entire sample, i.e. two surfaces, the reflection and transmission of UCNs due to quantum-mechanical effects can respectively be described as

$$\rho = R\frac{1+\alpha^2(T-R)}{1-\alpha^2R^2} \approx \frac{(k-k')^2}{k^2+k'^2} \text{ and} \tag{6.6}$$

$$\tau = \frac{\alpha T^2}{1 - \alpha^2 R^2} \approx \frac{2kk'}{k^2 + k'^2}, \tag{6.7}$$

where α=exp$(-N\sigma_{\mathrm{tot}}d)$ is the attenuation coefficient. The latter equations for both reflection and transmission are valid for negligible absorption and inelastic scattering.

6.4 Correction for detector solid angle

In the transmission experiments presented here, only unscattered and forward-collimated UCNs should be registered by the detector. However, since the detector has a finite, i.e. non-zero, size, neutrons at a small angle with the flight path will also be detected. This means that a forward-collimated neutron that is slightly scattered (low energy transfer, low momentum transfer), will be registered by the detector, although this should not happen. In experiments with faster neutrons, e.g. cold or thermal, the energy transfer can be considerable and the neutron still enters the detector solid angle. With UCNs, however, even a slight transfer of energy will inevitably make the UCNs so fast they are not UCNs any more. And the Cascade detector efficiency for faster neutrons is significantly lower than for UCNs. Therefore, only elastic scattering can lead to falsely detected UCNs.

With the detector solid angle (between the sample container and the detector) known

$$\Omega \approx \frac{A}{L^2} \approx \frac{23.8\,\mathrm{cm}^2}{(28.2\,\mathrm{cm})^2} = 0.03\,\mathrm{sr}, \tag{6.8}$$

the transmission equation can be expanded by a term for unintentionally detected UCNs

$$\frac{I_{\mathrm{meas}}}{I_0} = e^{-N_{\mathrm{v}}\sigma d} e^{-2A} + I_{\mathrm{scat}} \times \frac{\Omega}{4\pi}. \tag{6.9}$$

Inserting typical values for UCN transmission experiments and scattering cross sections, and, most importantly, $\frac{\Omega}{4\pi} = 2.4 \times 10^{-3}$, one quickly recognizes that solid-angle corrections need not be made for this particular TOF setup.

Considering the statistical uncertainties of 5 to 10% in UCN experiments, the <1% effect due to a non-vanishing detector solid angle is negligible.

For the same reasons given above, there needs to be no correction for multiple scattering of UCNs within the sample bulk.

6.5 Sample impurities

6.5.1 Deuterium

In *ortho*-deuterium experiments the relevant impurities are *para*-deuterium and hydrogen. The fraction of *para*-deuterium as determined by Raman spectroscopy

was (2.5±0.2)% for the relevant deuterium samples. Detailed results are presented in Section 4.5. The *para*-deuterium fraction accounts for $1/v \times c_{\mathrm{p}} \times 271\,\mathrm{barn} \times \mathrm{m/s}$ additional cross section due to the rotational transition $J = 1 \rightarrow 0$, see Tab. 3.2. This value is in the single-digit percent range and should be corrected for. The combined coherent and incoherent scattering cross sections of *ortho*-D_2 and *para*-D_2 are similar, 27.5 and 25.5 barn, respectively, and do not introduce an error to the results for *ortho*-D_2, see Section 2.4.

The deuterium purity (grade N30) was indicated as > 99.9% by the supplier, Air Liquide France. To make a conservative estimate and since hydrogen is the worst possible gaseous contaminant for neutron experiments, it was assumed that 0.1% of the deuterium sample were hydrogen. It has an absorption cross section per sample molecule of $1/v \times c_{\mathrm{H_2}} \times 1463\,\mathrm{barn} \times \mathrm{m/s}$. *Ortho*-hydrogen ($J = 1$), even more so than *ortho*-deuterium ($J = 1$), has a tremendous up-scattering cross section of $\sigma_{10}^{0/\pm 1\mathrm{ph}}(10.0\ \mathrm{m/s}) = 1354$ barn/molecule at $T = 10$ K stemming from the rotational transition $J = 1 \rightarrow 0$ [54]. However, as *normal*-deuterium is almost entirely converted to *ortho*-deuterium in the spin converter, see Section 4.4, *normal*-hydrogen is almost entirely converted to *para*-hydrogen, which is the rotational ground state. The other scattering cross sections of *para*-hydrogen multiplied with the hydrogen impurities concentration of 0.1% are negligible for the deuterium measurements.

Absorption in deuterium equals $1/v \times 2.3\,\mathrm{barn} \times \mathrm{m/s}$ per molecule.

6.5.2 Metal foils

The impurities of the various metal foils (Cu, Al, Zr) were taken from the supplier's list of typical impurities, which gives an upper limit of the trace impurities to be expected. Tab. 6.1 lists the foils' typical impurities and also the actual measured impurities for the foils: i) Al 99.99+% 50 μm, ii) Al 99.99+% 100 μm, and iii) Cu 99.9+% 100 μm.

Taking into account the abundance of the impurities listed in Tab. 6.1 as well as their respective absorption cross sections, only one or two impurities per foil actually influence the total absorption cross section of each sample. Tab. 6.2 lists for each sample its respective most relevant impurities. The absorption cross sections at thermal neutron energies were taken from [44]. The resulting additional absorption cross sections were also calculated for thermal neutron energies.

When metals like aluminum and copper are exposed to air at ambient temperature, they form passive oxide layers. For pure bulk copper, a layered CuO/CuO_2 oxide structure of 3.3 nm thickness has been reported [192], while 2.5 to 5.2 nm were found for copper thin films [193] and 6 nm for ultrafine particles [177]. The oxide layer on the surfaces of pure aluminum has been found to be 4 nm for ultrafine particles [177] and between 3 and 4 nm for bulk aluminum [194]. On zirconium, ZrO_2 and sub-stoichiometric oxides have a thickness of about 1.5 nm [195].

Element	Al	Al	Al	Cu	Cu	Zr
	typical	50 μm	100 μm	typical	100 μm	typical
Al	rest	rest	rest	—	—	28
Ag	3	0.1	0.005	500	8	—
B	—	0.2	0.033	—	—	—
Bi	—	1	0.006	< 10	—	—
Ca	4	0.7	0.02	—	—	—
Cu	6	2	0.2	rest	rest	10
Fe	4	2	1	—	2	840
Ga	2	0.2	0.005	—	—	—
Hf	—	—	—	—	—	44
Mg	15	2.0	1.6	—	—	—
Na	0.5	0.5	0.005	—	—	—
Ni	1	0.5	0.03	—	—	35
O	—	30	10	500	5	900
Pb	1	0.5	0.005	< 50	0.2	—
Si	3	2	1.1	—	—	25
other metals	negligible	negligible	negligible	< 300	14.1	negligible

Table 6.1: Typical impurities (in ppm) in the metal foils supplied by Advent Research (United Kingdom) and actual impurities according to the respective certificate of conformity for the foils Al 50 μm and 100 μm as well as Cu 100 μm. Figures with three digits after the decimal point indicate the limits of detection for that particular trace element. The nominal purities of the metal foils for three different thicknesses each were: Al 99.99+%, Cu 99.9+%, Zr 99.8%.

These thicknesses are less than one typical UCN wavelength, see Section 1.2. According to the UCN reflectivity calculations done by Pokotilovski [196], they are small enough to have only negligible influence on the UCN transmission through the sample and can be neglected.

Before the measurement, all metal foils were degreased with isopropyl alcohol and rinsed with de-ionized water. The water was removed by dipping the foil

sample in high-purity acetone and then drying it with a lint-free absorbent paper.

Sample type	Element	Number conc. [%]	$\sigma_{\text{abs}}^{\text{thermal}}$ [barn]	$\sigma_{\text{abs}}^{\text{thermal}}$ [barn] weighted	$\sigma_{\text{abs}}^{\text{thermal}}$ fit [barn]
Al	Al	> 99.99	0.231	0.231	
99.99+%	Ag	3×10^{-4}	63.3	1.9×10^{-4}	
	B	2×10^{-5}	767	1.5×10^{-4}	
	Sum			0.231	0.798 ± 0.350
Cu	Cu	> 99.9	3.78	3.78	
99.9+%	Ag	5×10^{-2}	63.3	3.2×10^{-2}	
	Sum			3.81	3.65 ± 0.33
Zr	Zr	99.8	0.185	0.185	
99.8%	Fe	8.4×10^{-2}	2.56	2.2×10^{-3}	
	Hf	4.4×10^{-3}	104	4.6×10^{-3}	
	Sum			0.192	2.89 ± 1.58

Table 6.2: Impurities from Tab. 6.1 giving rise to some additional absorption cross sections in the metal foil samples i) Al 99.99+%, ii) Cu 99.9+%, and iii) Zr 99.8%. However, due to the high purity of the foils, these additional cross sections are rather low. The cross sections are given for thermal neutron energies. In the right-hand column, the values found experimentally, see Section 7.3, are shown, also extrapolated to thermal energies.

Part III

Results, Discussion and Conclusions

7 Cross Section Results and Comparison with Theory and Previous Experiments

Национальной науки нет, как нет и национальной таблицы умножения.

— Антон Чехов

7.1 Liquid deuterium

The scattering cross sections $\sigma_{\mathrm{tot}}^{\mathrm{D_2}}$ of liquid *ortho*-deuterium ($c_{\mathrm{ortho}} = 0.975$) for UCNs, corrected for absorption in the medium and for reflection at the sample interface, are shown in Fig. 7.1. They include quasi-elastic contributions and 1-phonon up-scattering in *ortho*-deuterium, as well as quasi-elastic and inelastic scattering in *para*-deuterium impurities according to

$$\sigma_{\mathrm{tot}}^{\mathrm{D_2}} = c_{\mathrm{ortho}} \times \sigma_{00} + c_{\mathrm{para}} \times (\sigma_{11} + \sigma_{10}) \,, \tag{7.1}$$

where c_{ortho} and c_{para} are the *ortho*- and *para*-deuterium concentrations and $\sigma_{JJ'}$ the deuterium molecular scattering cross sections.

The experimental data for the temperatures 19.3 K, 20.5 K, 22.0 K and 23.0 K overlap well with the calculation model published by Döge et al. [118]. Instead of the self-diffusion coefficient based on unpublished data, which was used in [118], now the experimentally determined coefficient from O'Reilly and Peterson [197] was used. Quantum simulations by Guarini et al. [198] confirm that value. These new experimental data on liquid deuterium should be considered an improvement of the experimental data published in [118] and [199].

7.2 Solid deuterium

The experimental scattering cross sections of solid *ortho*-deuterium ($c_{\mathrm{ortho}} = 0.975$) for UCNs, corrected for absorption in the medium, for reflection at the sample interface and for up-scattering due to the rotational relaxation $J = 1 \rightarrow 0$ of *para*-deuterium impurities are shown in Fig. 7.2. The temperature uncertainty was

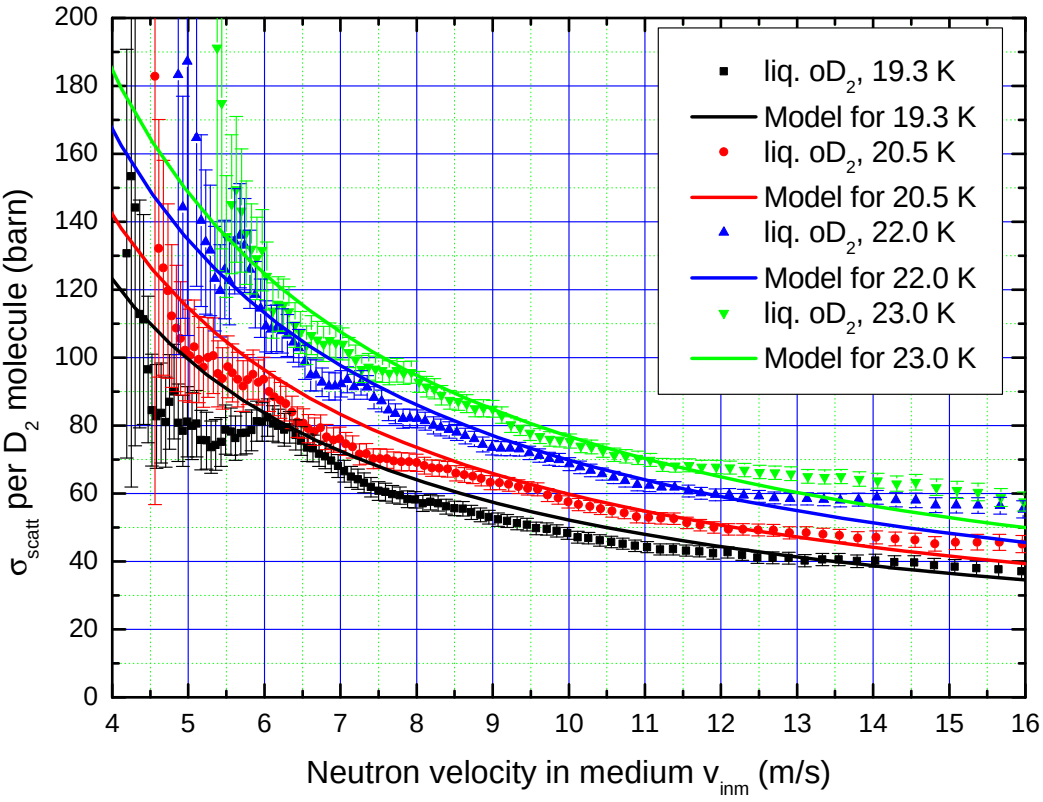

Figure 7.1: Experimental data points (solid colored symbols) for the scattering cross section of liquid *ortho*-deuterium at various temperatures. The theoretical model by Döge et al. [118] was re-calculated for the same temperatures as in the experiment and using $c_{\mathrm{ortho}} = 0.975$ (solid colored lines) and the self-diffusion coefficient for liquid deuterium from O'Reilly and Peterson. The temperature uncertainty was $\Delta T = 0.2$ K. The scattering cross sections were corrected for absorption on H_2 and D_2.

$\Delta T = 0.2$ K. *Normal*-deuterium ($c_{\mathrm{ortho}} = 2/3$, $c_{\mathrm{para}} = 1/3$) at 15 K is represented by black squares. Below them, the red up triangles represent solid *ortho*-deuterium at 10 K and the green down triangles stand for the same crystal at 15.0 K. The blue circles stand for the same crystal after the temperature cycle 10 K $\rightarrow$ 15 K $\rightarrow$ 10 K. It is easy to see that temperature cycling does not lower the scattering cross section of a crystal. In the best case, it remains the same. Qualitatively, similar findings were published in [21, 107]. In the particular case shown here, the cross section increased slightly as a result of temperature cycling.

The red up triangles from Fig. 7.2 (solid *ortho*-deuterium at 10 K) are plotted again in Fig. 7.3. Using the fit model described at the end of Subsection 3.2.2, they are decomposed into their constituents: 1-phonon up-scattering (using the cor-

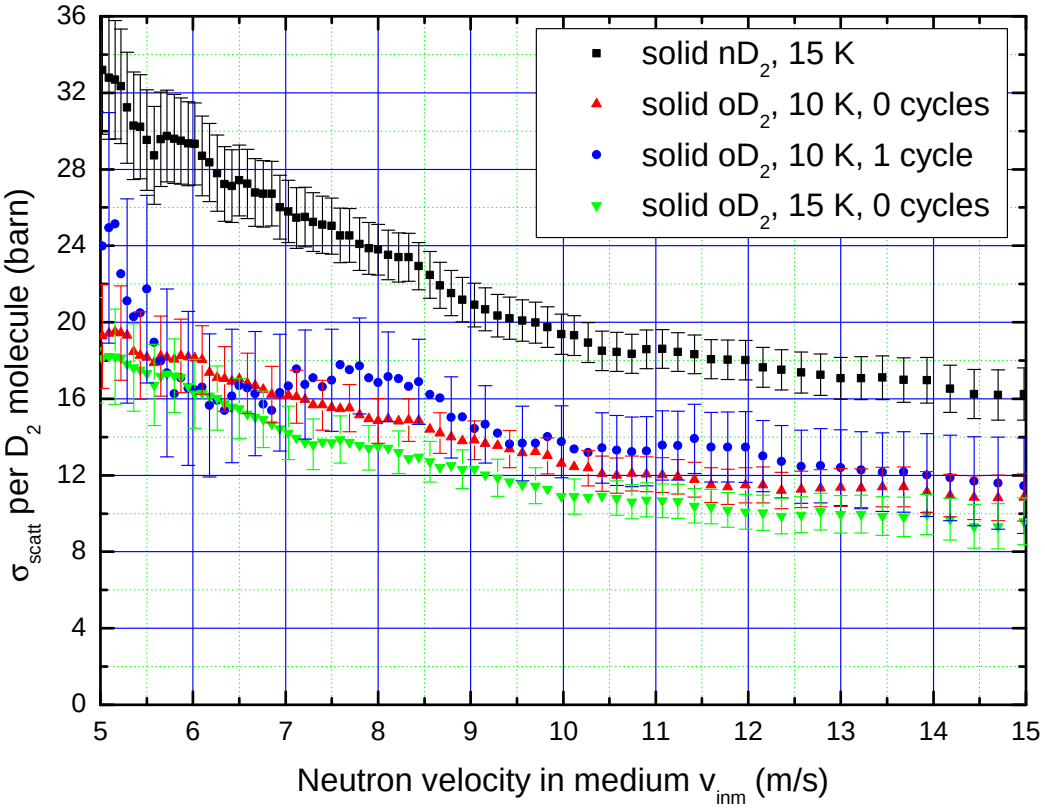

Figure 7.2: Experimental data for solid *normal*- and *ortho*-deuterium at $T = 10$ K and 15 K with and without temperature cycling. The cross sections of *normal*-deuterium lie significantly higher than those of *ortho*-deuterium, due to incoherent up-scattering caused by the rotational relaxation $J = 1 \rightarrow 0$ in the former. For the data points of *ortho*-deuterium below $v = 10$ m/s only every third error bar is shown for better legibility.

rected Incoherent Approximation, see Subsection 3.2.2), incoherent elastic nuclear scattering and elastic scattering contributions from defects (with spherical defect radius $R_\mathrm{d} = 87$ Å and defect concentration $c_\mathrm{p} = 9.5 \times 10^{-11}$ per D_2 molecule) as calculated using the Guinier two-phase model, see Section 3.3. The same fit model yields $R_\mathrm{d} = 117$ Å, $c_\mathrm{p} = 9.7 \times 10^{-12}$ per D_2 molecule for solid *ortho*-deuterium at 15 K, see Fig. 7.4.

This means that the warmer crystal has an order of magnitude fewer defects than the colder crystal while their size undergoes only minor change. This is the first time that an estimation of the size and concentration of defects in deuterium crystals was done for the purposes of UCN scattering.

If instead of the corrected Incoherent Approximation the "old" IA is used for the fit in Fig. 7.3, the Guinier model yields $R_\mathrm{d} = 93$ Å and $c_\mathrm{p} = 6.6 \times 10^{-11}$ per

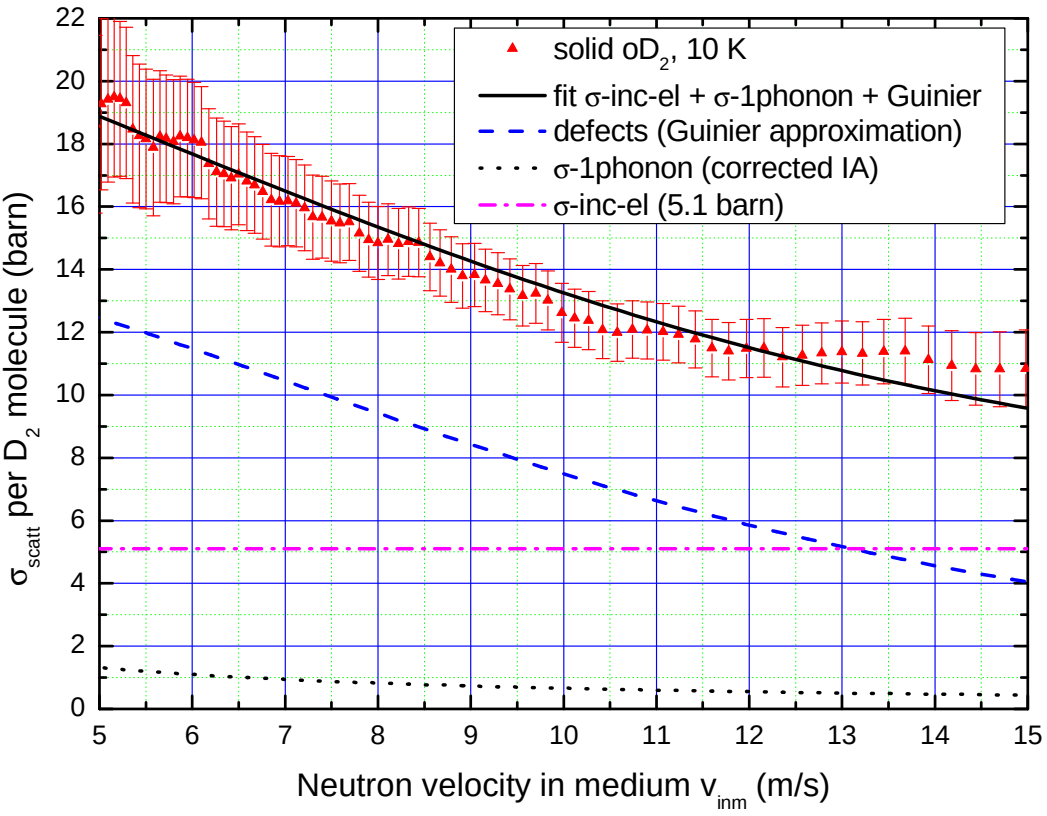

Figure 7.3: Experimental scattering cross section of solid *ortho*-D_2 ($T = 10$ K) and its decomposition into 1-phonon up-scattering (corrected IA), incoherent elastic nuclear scattering and the elastic scattering contributions from defects ($R_d = 87$ Å, $c_p = 9.5 \times 10^{-11}$ per D_2 molecule) as calculated using the Guinier approximation.

D_2 molecule for 10 K, which means significantly fewer defects. For solid *ortho*-deuterium at 15 K, the "old" IA leaves no room for defects at all.

An alternative to the Guinier model is a model using the spherical form factor, which is valid not only in the UCN region, but also for higher energy neutrons. When the data from Fig. 7.3 are fitted using Eq. 3.13, the extracted defect radius is $R_d = 82$ Å and their concentration is $c_p = 1.4 \times 10^{-10}$ per D_2 molecule, see Fig. 7.5. They are very similar to the parameters extracted from the same data using the Guinier model.

The scattering cross sections presented by Atchison et al. [107] for 18 K lie 30% above those presented here for 15 K. This could be a temperature effect or additional scattering on the rough deuterium sample surface, which very likely formed due to the rough-surface aluminum sample container windows used by these experimenters. If, however, surface scattering was deemed to be negligible and the same fit as in Figs. 7.3 and 7.4 (with the corrected IA calculated for 18 K)

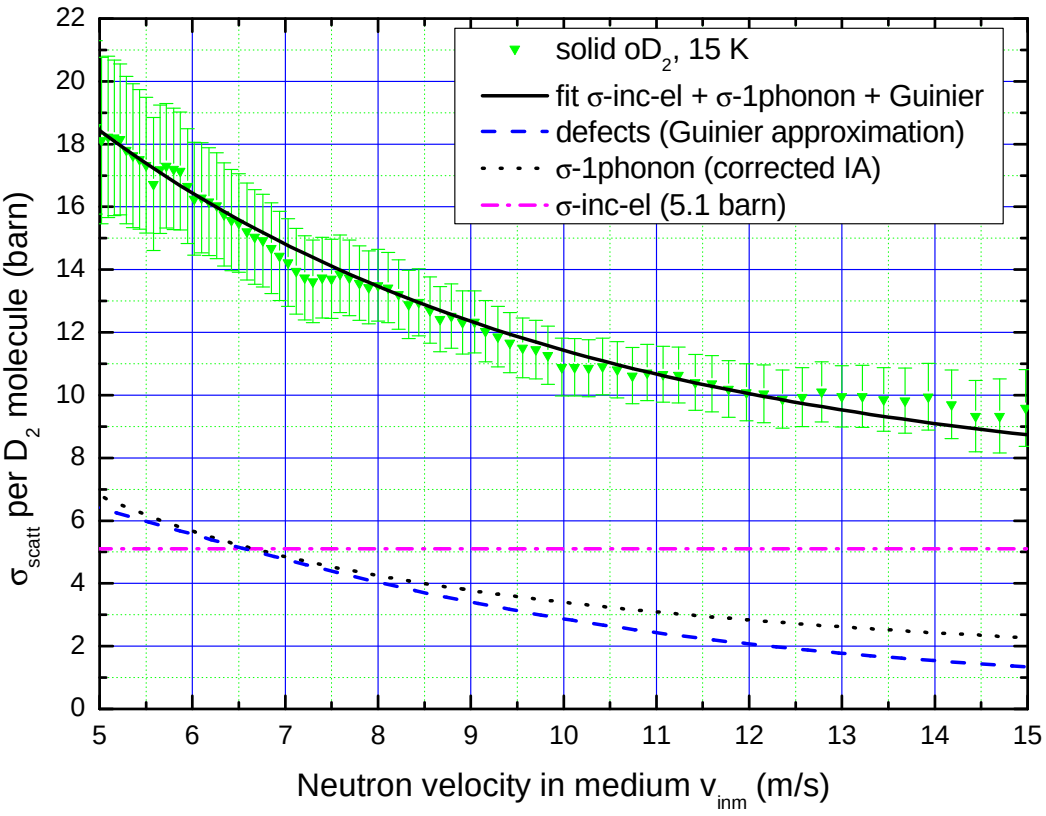

Figure 7.4: Experimental scattering cross section of solid *ortho*-D_2 ($T = 15$ K) and its decomposition into 1-phonon up-scattering (corrected IA), incoherent elastic nuclear scattering and the elastic scattering contributions from defects ($R_d = 117$ Å, $c_p = 9.7 \times 10^{-12}$ per D_2 molecule) as calculated using the Guinier approximation.

was applied, the extracted defect size would be $R_d = 100$ Å and their concentration would be $c_p = 3.9 \times 10^{-11}$. This c_p for 18 K is a factor of 5 higher than the value reported above for 15 K. As shown here and in Brys [21] and Atchison et al. [107], the magnitude of defect scattering should be *lower* for a *warmer* crystal. It stands therefore to reason that at least part of the UCN scattering reported in Atchison et al. is not due to (hypothetical) defects, but uncompensated surface scattering.

Taking the scattering cross sections of liquid and solid deuterium at $v = 10$ m/s from Fig. 7.3 and adding the absorption cross section in D_2 and H_2 as well as the roton relaxation cross section back on, it is possible to plot the mean free path λ_{mfp} for UCNs in a real *ortho*-D_2 crystal over temperature, where $\lambda_{mfp} = (\sigma_{tot} \times N_v)^{-1}$ [200]. In Fig. 7.6 it can be clearly seen that UCNs travel farther in solid deuterium than in its liquid state. For low-energy UCNs, it can be inferred from Fig. 7.3 that elastic defect scattering is the dominant scattering process in the low-temperature solid state. Therefore, λ_{mfp} is dominated essentially by the

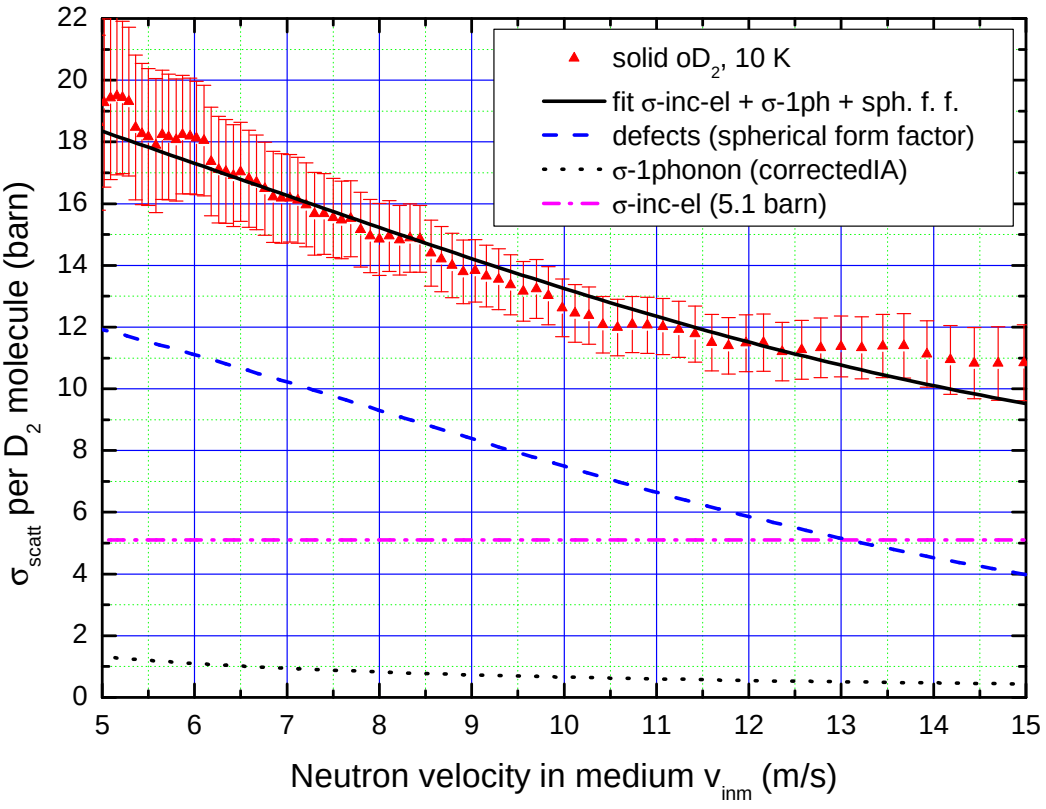

Figure 7.5: Experimental scattering cross section of solid *ortho*-D_2 ($T = 10$ K) and its decomposition into 1-phonon up-scattering (corrected IA), incoherent elastic nuclear scattering and the elastic scattering contributions from defects ($R_d = 82$ Å, $c_p = 1.4 \times 10^{-10}$ per D_2 molecule) as calculated using the spherical form factor model.

number and size of crystal defects. The new value for λ_{mfp} presented here is about a factor of 3 smaller than the experimental value known up to now, 8 cm, from Morris et al. [201]. Earlier calculations even estimated the mean free path of UCNs to be about 15 cm at 6 K [18], while UCN scattering on crystal defects was not taken into account. Kahlenberg et al. [187] wrote that by using values from Leung et al. [202], which were derived for superfluid helium, they extracted a mean free path of UCNs in their sD_2 source of $4.6\,\text{cm} < \lambda_{mfp} < 10.0\,\text{cm}$ at $T \approx 5\,\text{K}$ from simulations. Considering Fig. 7.3, this is likely not the full picture.

These findings reiterate the requirement that UCN converters must be thin-film converters [50, 51] instead of bulk converters. In other words, the active conversion zone, from which UCNs can escape the converter crystal, is only about 1 to 2 cm thick. Most UCNs produced deeper inside the converter cannot escape and thus not be used in experiments.

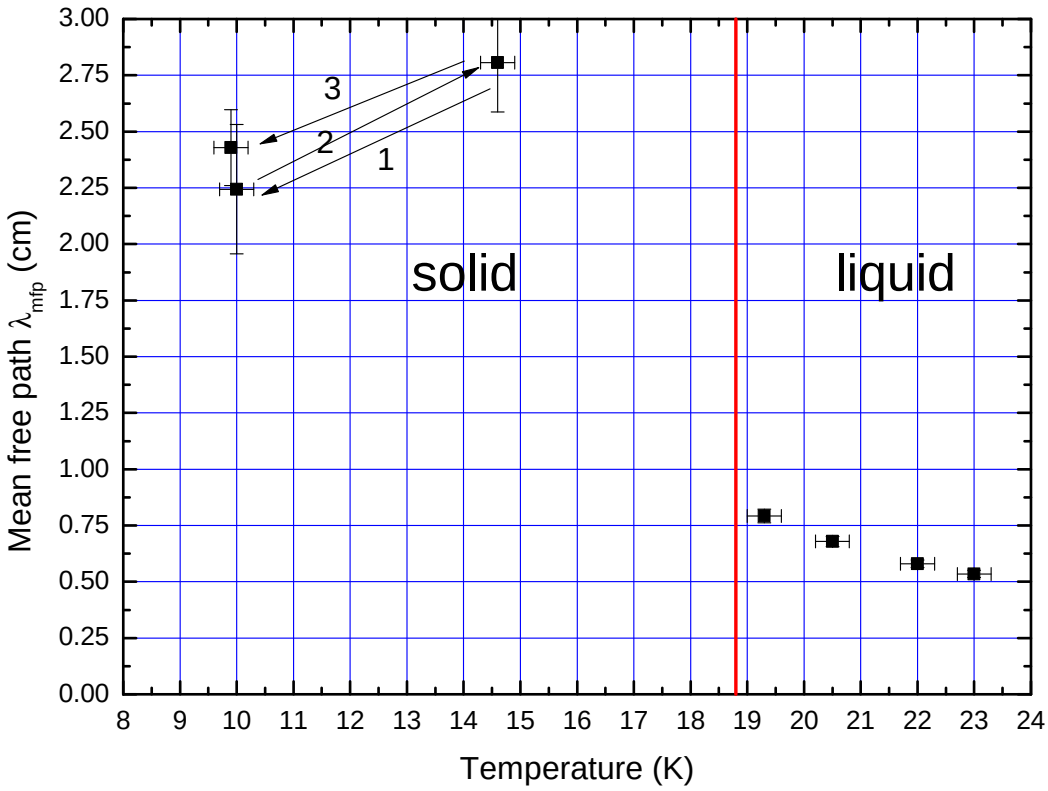

Figure 7.6: Mean free path length λ_{mfp} of UCNs in condensed *ortho*-D_2 ($c_{\mathrm{ortho}} = 0.975$) for $v = 10.0$ m/s at 6 different temperatures. The solid deuterium data are the same as in Fig. 7.2 (here uncorrected for absorption). The arrows 1, 2, 3 represent the temperature cycles of the deuterium crystal.

7.3 Metal Foils

The transmission of UCNs through metal foils of various thickness but with the same surface treatment was carefully recorded. For each foil the transmissivity is given for an out-of-medium (oom) UCN velocity of 7 m/s that was corrected for the neutron-optical potential of each sample, see for example [42], by using the element's corresponding critical velocity v_{crit}

$$v_{\text{in medium}} = \sqrt{(7\mathrm{m/s})^2 - v_{\mathrm{crit}}^2}. \tag{7.2}$$

This logic was chosen in keeping with Atchison et al. [130] to make these data comparable with those presented here. The resulting in-medium (inm) velocities were 6.2 m/s for Al, 4.1 m/s for Cu, and 5.8 m/s for Zr.

As Fig. 7.7 illustrates, two 50 μm thick copper foils with a total of four surfaces have a lower UCN transmissivity than a single foil of 100 μm thickness. If there

Sample	Thickness [μm]	Transmissivity at $v_{\mathrm{oom}} = 7$ m/s
Al-1	50	0.967
Al-2	100	0.859
Al-3	125	0.851
Cu-1	50	0.260
Cu-2	100	0.109
Cu-3	250	0.010
Zr-1	25	0.613
Zr-2	125	0.277
Zr-3	250	0.310

Table 7.1: Measured UCN transmissivity for Al, Cu, and Zr metal foil samples.

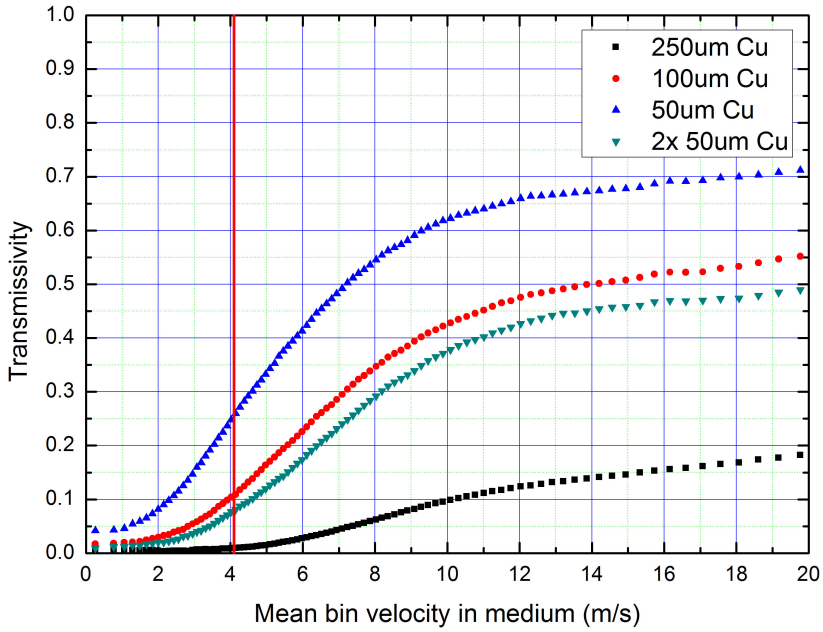

Figure 7.7: Transmissivity of various Cu foils for UCNs plotted over UCN velocity. The in-medium velocity of 4.1 m/s (equivalent to 7 m/s out of medium) is marked with a vertical red line.

were no surface scattering, both sets of foils would have the same transmissivity.

The transmissivities of the 100 μm and the 125 μm Al foils were very similar to each other. Only the transmissivity of the 125 μm foil was taken into account for further treatment and that of the 100 μm thick foil was used to estimate the systematic error of the measurement. The total cross section calculated from the

transmission through foils Al-1 and Al-3 is

$$\sigma_{\mathrm{tot}}^{\mathrm{Al}}(7\,\mathrm{m/s}) = 283 \pm 120\ (\mathrm{sys.})\ \mathrm{barn}\ (\mathrm{Al\text{-}1,Al\text{-}3}). \tag{7.3}$$

After extrapolation to thermal neutron energies, this value is $\sigma_{\mathrm{tot}}^{\mathrm{Al,therm}} = 0.798 \pm 0.350$ barn. The tabulated absorption cross section from Tab. 6.2 is about a factor of 3 lower. The order of magnitude is correct but the agreement between experimental and theoretical values is not satisfactory. The discrepancy is largely due to the fact that the foil thicknesses were too close to each other and thus the transmissivity contrast between them was not good enough.

For zirconium, the situation is similar. Obviously, weakly absorbing samples do not lend themselves easily to this kind of transmission experiment. Also, in the case of zirconium, the thick sample was more a metal sheet than a foil. Although the supplier indicated an equal surface treatment for all three samples, it stands to reason that the actual surface structure of the foil ($d = 50\,\mu$m sample) differed substantially from the surface of the zirconium sheet ($d = 250\,\mu$m). The sheet was so rigid that it had to be cut by electrical discharge machining.

Due to the poor contrast between the thick and thin foils, the experimental average total cross section is far off the tabulated value of 0.192 barn,

$$\sigma_{\mathrm{tot}}^{\mathrm{Zr}}(7\,\mathrm{m/s}) = 1481\ \mathrm{barn}\ (\mathrm{Zr\text{-}1,Zr\text{-}2}) \tag{7.4}$$

$$\sigma_{\mathrm{tot}}^{\mathrm{Zr}}(7\,\mathrm{m/s}) = 706\ \mathrm{barn}\ (\mathrm{Zr\text{-}1,Zr\text{-}3}) \tag{7.5}$$

$$\mathrm{Average:}\ \sigma_{\mathrm{tot}}^{\mathrm{Zr}} = 1094 \pm 390\ (\mathrm{stat.}) \pm 210\ (\mathrm{sys.})\ \mathrm{barn}. \tag{7.6}$$

The above-mentioned average value extrapolated to thermal energies is $\sigma_{\mathrm{tot}}^{\mathrm{Zr,therm}} = 2.89 \pm 1.02\ (\mathrm{stat.}) \pm 0.56\ (\mathrm{sys.})$ barn.

When the transmissivity values are taken from Tab. 7.2 and plugged into Eqs. 3.18ff., the following cross sections for $v_{\mathrm{oom}} = 7\,\mathrm{m/s}$ are obtained for copper

$$\sigma_{\mathrm{tot}}^{\mathrm{Cu}}(7\,\mathrm{m/s}) = 2058\ \mathrm{barn}\ (\mathrm{Cu\text{-}1,Cu\text{-}2}) \tag{7.7}$$

$$\sigma_{\mathrm{tot}}^{\mathrm{Cu}}(7\,\mathrm{m/s}) = 1885\ \mathrm{barn}\ (\mathrm{Cu\text{-}2,Cu\text{-}3}) \tag{7.8}$$

$$\sigma_{\mathrm{tot}}^{\mathrm{Cu}}(7\,\mathrm{m/s}) = 1928\ \mathrm{barn}\ (\mathrm{Cu\text{-}1,Cu\text{-}3}) \tag{7.9}$$

$$\mathrm{Average:}\ \sigma_{\mathrm{tot}}^{\mathrm{Cu}} = 1957 \pm 74\ (\mathrm{stat.}) \pm 100\ (\mathrm{sys.})\ \mathrm{barn}. \tag{7.10}$$

When this average value is extrapolated to thermal neutron energies, i.e. $v_{\mathrm{neutron}} = 2200$ m/s, using the relation $\sigma_{\mathrm{abs}} \times v_{\mathrm{UCN}} = \mathrm{const.}$, $\sigma_{\mathrm{tot}}^{\mathrm{Cu,therm}} = 3.65 \pm 0.14\ (\mathrm{stat.}) \pm 0.19\ (\mathrm{sys.})$ barn are obtained. This value is in very good agreement with the tabulated absorption cross section of 3.81 barn at thermal energies, see Tab. 6.2. Fig. 7.8 shows the transmissivity of copper foils of different thicknesses for UCNs.

When the data points are fitted using the modified transmission equation, Eq. 3.17, and an extrapolation to zero foil thickness is done, the intercept of the fit with the y-axis shows the fraction of UCNs that is lost on both surfaces together, e^{-2A}. It is obvious that a very large share of the total UCN losses is due to surface scattering instead of bulk scattering. In the case of copper foils, the two surfaces alone scatter about 40% of UCNs out of the direct beam.

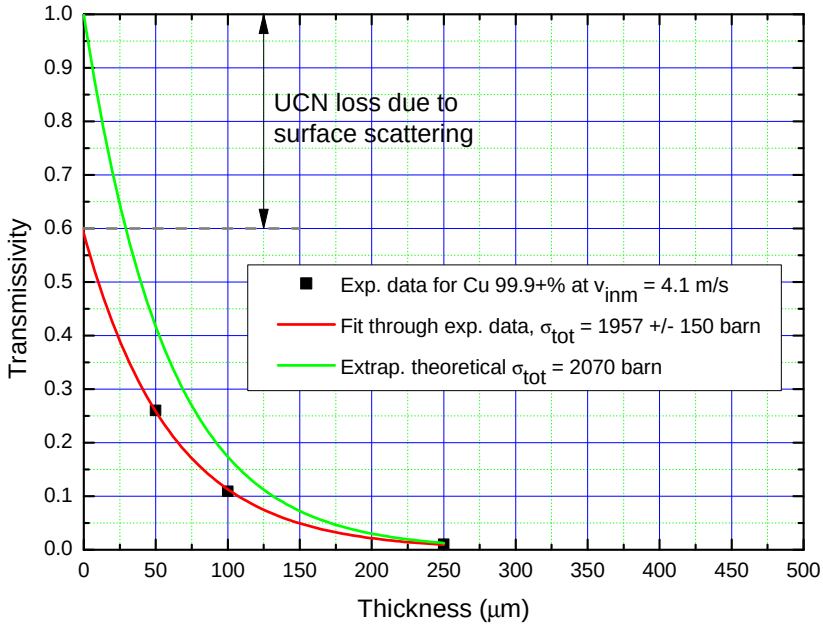

Figure 7.8: Transmissivity of Cu foil of three different thicknesses for UCNs of an in-medium velocity of 4.1 m/s (equivalent to 7 m/s out of medium). The data points were fitted (red line) with the transmission equation including a surface scattering term, Eq. 3.17, and using the average $\sigma_{\mathrm{tot}} = 1957$ barn. The green line represents the transmissivity as expected if there was no surface scattering.

The surface roughness of the metal foil samples as measured by atomic force microscopy (AFM) and extracted from the cross section measurements above and Eq. 3.17 are shown and contrasted in Tab. 7.2. The AFM measurements were carried out at the Joint Institute for Nuclear Research (JINR) in Dubna, Russia, with the help of Yuliya Gorshkova.

From the roughness parameters in Tab. 7.2 it becomes quite clear that the magnitudes of both roughness parameters b and R_{a} do not correlate well. While for copper there is almost one order of magnitude between both, the difference for zirconium is only a factor of two. It stands to assume that neutrons "see" a different spectrum of roughness amplitudes than mechanical or optical means of measurement.

Sample	Roughness Parameter b [Å]	Roughness Parameter R_a [Å]
Al	—	350 ± 100 Å
Cu	77 ± 1 Å	550 ± 150 Å
Zr	205 ± 35 Å	400 ± 100 Å

Table 7.2: Surface roughness of metal foils as extracted from UCN measurements and the theory from Section 3.5 (parameter b), as well as the roughness measured mechanically by AFM (parameter R_a). The neutron measurements above yielded no useful result for aluminum.

AFM scans of the foils used in the experiments described above yielded values of the same order of magnitude reported in the pioneering work of Steyerl [132], 200 to 500 Å. In his work Steyerl noted that the roughness values extracted from electron micrographs were in quantitative agreement with the roughness parameter extracted from neutron measurements but that it was difficult to interpret these micrographs. Also, as mentioned in Section 3.5, one parameter is often not enough to describe a rough surface to a satisfying degree.

Considering the above, it has to be concluded that, with current theories and techniques available, mechanical measurements of sample roughness can at best serve to estimate the order of magnitude of the loss of UCNs due to scattering on rough sample surfaces. The transmission of each foil, used as vacuum barrier or for a different purpose, still has to be measured with UCNs to know its exact transmissivity.

With the methods developed in Section 3.5, the experimental results from Atchison et al. [130] can be re-examined to determine the surface roughness parameter b for those foils as seen by UCNs. For aluminum, the first sample had a thickness of 10 μm and the others were stacks of 100 μm thick foils [1]. The zirconium samples were 100, 250, and 500 μm, layered from foils 50 μm thick. For multiple layers of foil, the right side of Eq. 3.17 needs to be raised to the power of n, which represents the number of foils in the neutron beam. Otherwise the lower transmissivity would be attributed to σ_{tot} and suggested a false higher bulk cross section. Consequently, before calculating the surface roughness parameter b of *one* foil, the n-th root needs to be taken of the surface transmissivity term $\exp^{-2A\times n}$.

Tab. 7.3 gives the experimental transmissivities of Al and Zr foils (second column) as well as the roughness parameter b extracted from those measurements applying the methods developed in this thesis. In the calculation of $e^{-N\sigma_{\text{tot}}d}$, σ_{tot} was taken as presented in the paper; incoherent 1-phonon scattering was neglected. The ratio of measured transmissivity to expected transmissivity (due to absorption

[1] See footnote in Section 3.5.

only), i.e. column 2 divided by column 3, is given in column 4. From this excess loss of transmissivity, the roughness parameter b was calculated.

Sample Thickness d [μm]	Exp. Transm.	Theoretical $\exp^{-N\sigma_{\mathrm{tot}}d}$	Exp. Tr. / Th. Tr. $\exp^{-2A\times n}$	Roughness Parameter b [Å]
Al 10	0.943	0.994	0.949	120
Al 100	0.837	0.940	0.890	177
Al 2 × 100	0.707	0.883	0.801	173
Al 3 × 100	0.612	0.830	0.737	166
Al 4 × 100	0.540	0.780	0.692	158
Al 5 × 100	0.484	0.733	0.660	150
Zr 2 × 50	0.860	0.943	0.912	72
Zr 5 × 50	0.680	0.864	0.787	73
Zr 10 × 50	0.449	0.746	0.602	76

Table 7.3: Surface roughness of metal foils from Atchison et al. [130] as re-analyzed applying the theory from Section 3.5 (roughness parameter b). The uncertainty of b was estimated to be ±15%.

The roughness parameters extracted from the UCN transmission measurements of Atchison et al. [130] are consistent between the individual samples and yield average values of $b(\mathrm{Al}) = 161 \pm 24$ Å for aluminum and of $b(\mathrm{Zr}) = 74 \pm 11$ Å for zirconium. These are in line with the typical roughness parameters from Steyerl [132] and prove conclusively that surface scattering is the reason for the 2.2-fold and 2.6-fold decrease of foil transmissivity compared to theory (taking into account only absorption) for aluminum and zirconium, respectively.

Summing up, it can be concluded from the measurements described above as well as the re-evaluation of data from Atchison et al. that surface scattering is a significant loss channel for UCNs and needs to be taken into account in transmission experiments.

8 Summary of Results and Conclusions

Veritatem inquirenti, semel in vita de omnibus, quantum fieri potest, esse dubitandum.

— René Descartes, *Principia philosophiæ (1644)*

8.1 Summary

Within this thesis, new experimental scattering cross sections of liquid and solid *ortho*-deuterium for ultracold neutrons (UCNs) are presented. They were taken in a sample container with highly polished amorphous silica windows, which suppressed parasitic neutron scattering on surfaces as far as possible. Moreover, that container allowed for an optical inspection of the samples before the neutron measurements were started. It was developed within this thesis specifically for more reliable UCN transmission measurements on cryogenic samples.

The new results for the cross sections of liquid *ortho*-deuterium overlap well with a calculation model published earlier [118], which has no free parameters and uses only the material properties of deuterium.

For solid *ortho*-deuterium, it is demonstrated quantitatively for the first time how the total scattering cross section can be decomposed into its constituents: 1-phonon up-scattering, incoherent elastic scattering, and coherent defect scattering. This decomposition allows for estimating the size and concentration of defects in solid deuterium crystals using the Guinier approximation and the spherical form factor model.

The widely used Incoherent Approximation is shown to be a factor of 2 to 5 too high for ultracold neutron (UCN) scattering in deuterium. Applying a correction to the Incoherent Approximation allows for a realistic decomposition of the scattering cross section. It is also proven that the scattering cross sections reported by Atchison et al. [107] contain contributions from either scattering on rough surfaces or scattering from crystal defects. The proportions of both cannot be determined retroactively.

Converting the experimental cross sections from this work into mean free path lengths for UCNs inside deuterium crystals yields typical values of about 2 cm, which is a factor of 3 to 4 smaller than previously reported values [201]. This

finding supports the requirement that UCN converters be thin-film instead of bulk converters.

As much as neutron scattering on rough surfaces was suppressed for the deuterium samples by using highly polished SiO_2 sample container windows, it was expressly measured in a variety of metal foils. While pure aluminum and zirconium yielded only the order of magnitude of surface scattering, the copper samples demonstrated convincingly that surface scattering needs to be taken into account in all UCN transmission experiments using metal windows or foils. This tremendous effect was also observed in a re-analysis of UCN transmission experiments with foils published by Atchison et al. [130].

As a by-product of the work on this thesis, experimental equipment for UCN transmission was characterized systematically and the absolute neutron flux at three beam ports of the ILL Turbine was measured.

8.2 Conclusions for the operation of solid deuterium-based UCN converters

Lavelle et al. [113] estimated the total UCN losses, i.e. the share of UCNs produced that cannot leave the UCN converter, to be 3/4. These losses are mainly due to UCN up-scattering in the deuterium bulk and losses at aluminum foils used as exit windows. As conjectured earlier and proven in this thesis, they are exacerbated by the trapping of UCNs inside the source due to elastic scattering on defects. In addition, Lavelle et al. reviewed all previously reported UCN yields and their temperature dependence, see Fig. 8.1. Except for the converter at Los Alamos, which does not have an exit window but releases UCNs into the beam tube directly from the sD_2 crystal layer[1], converters showed only a negligible temperature dependence of the UCN yield between 5 and 12 K. Atchison et al. [55] reported only slight gains in UCN output from sD_s-based converters of about 9% for cooling the D_2 crystal from 12 K to 8 K. Only above 12 K does the UCN yield from most converters start to decline significantly with temperature. Earlier calculations using the Incoherent Approximation with higher 1-phonon up-scattering cross sections, see Section 3.2, had estimated the upper saturation temperature at 6 K.

As it seems from these previous findings and the new results reported in Chapter 7, the suppression of 1-phonon up-scattering at low temperatures is counteracted by more (elastic) scattering on defects in the deuterium crystal, which leads to the total cross section being relatively constant over a wide temperature range. The results of this thesis suggest the lowest total cross section (sum of 1-phonon and defect scattering) to be at a deuterium temperature of around 12 K. This is

[1] The UCN sources at the TRIGA reactor at the University of Mainz, Germany, and the source at Los Alamos National Laboratory, USA both have no exit window.

in line with empirical measurements of UCN yields of converters operating at the moment.

Considering what was said above, it stands to reason that an improvement of the crystal growing and curing procedures alone may improve the extractable UCN density of existing sD_2-based sources by a few tens of percent. However, even the best crystal treatment is unlikely to lead to UCN gains of an order of magnitude and finally reach the UCN output that was initially proposed [18, 19].

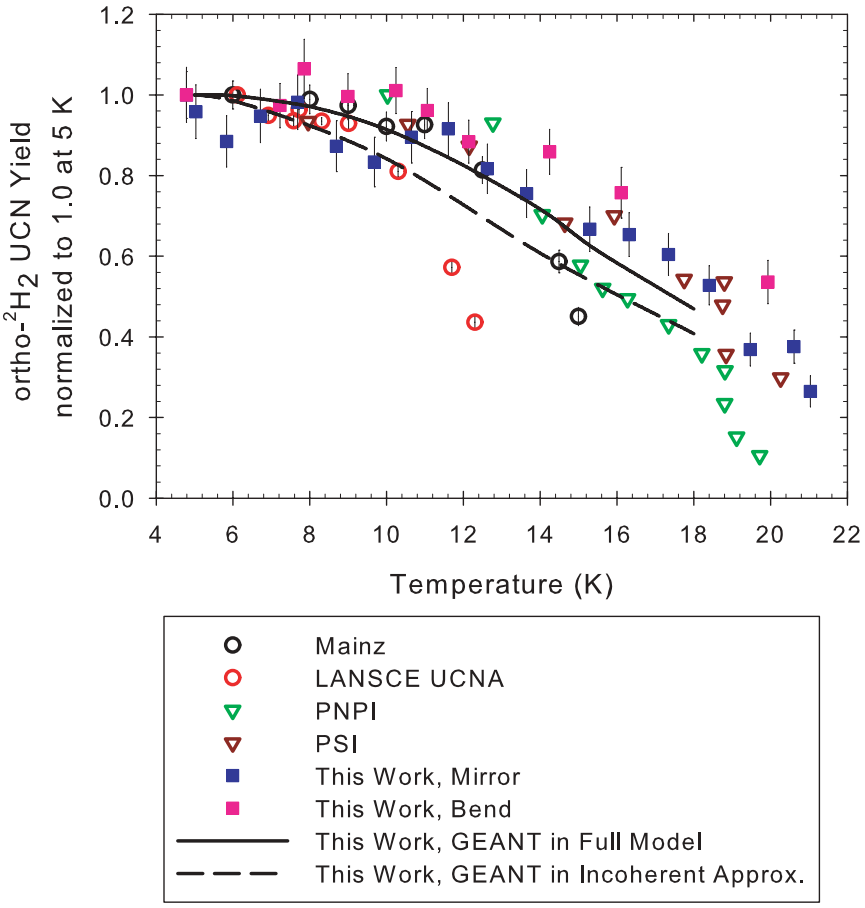

Figure 8.1: The temperature dependence of the UCN yield of various UCN converters after Lavelle et al. ("this work") [113] compared to similar experiments (Mainz [150], LANSCE UCNA [201], PNPI [203], and PSI [55]). All data are scaled to unity at 5 K. Reprinted with permission. Copyrighted by the American Physical Society.

Part IV

Appendix

Appendix A

Proposed Future Experiments

A.1 Defects

For the purposes of this dissertation, the defects inside deuterium crystals were treated as generalized spheres with a radius of gyration R_g. This radius of gyration is a generalized unit of dimension of these defects, which can also be expressed as cylinders, needles and other geometrical shapes. A pure transmission experiment with ultracold neutrons does not allow to make any more detailed determination of the type of defect. A small-angle neutron scattering (SANS) experiment with cold neutrons could elucidate the geometrical shape of these defects.

A.2 Other uses for the sample container

According to Souers [46], the optical refractive index $n(\lambda)$ of solid hydrogen and deuterium had not been measured by 1986. A search of the recent literature has not yielded any pertinent publications either. The sample container presented in Chapter 5 is suitable for performing such a measurement.

A.3 Temperature and time dependence of UCN transmission through fomblin

Fomblin oil and grease, i.e. perfluoropolyether chains with a high molecular weight between 1000 and 10,000 grams per mole, are widely used in storage experiments with ultracold neutrons (UCNs). The neutron-optical potential of fomblin is 106 neV [43]. A vessel coated with fomblin on the inside allows for the near loss-free storage of neutrons with a kinetic energy below this potential. That is why fomblin is the inner wall coating of choice for vessels used in experiments that measure the lifetime of the free neutron [204, 205, 206, 207].

In order to increase the accuracy of the results from these experiments and minimize systematic errors, it is important to know all neutron loss channels to a very high precision, see Subsection 1.4.1. However, to date the exact interaction of slow

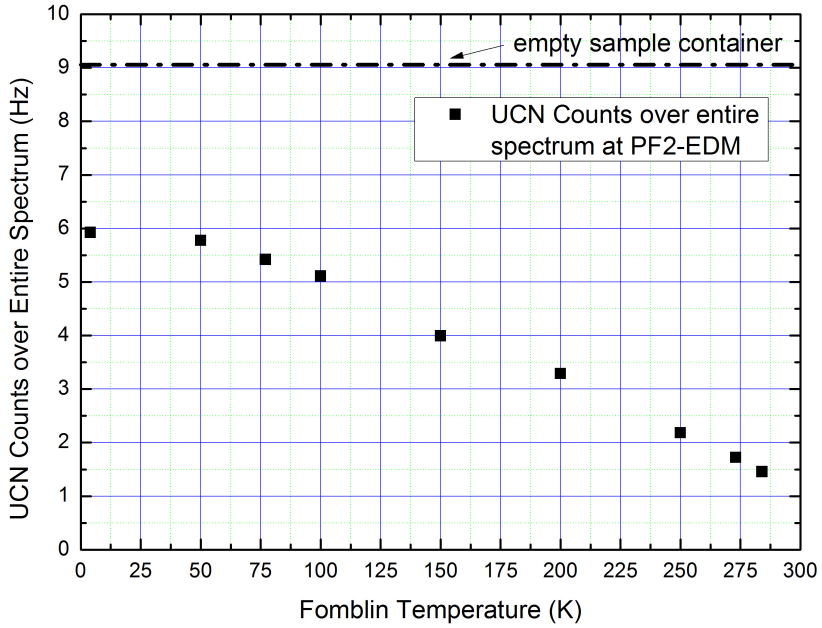

Figure A.1: Temperature dependence of the UCN transmission through the same fomblin as in Fig. A.2. The count rate was integrated over the entire spectrum.

neutrons with fomblin is poorly understood. Moreover, all free-neutron lifetime experiments show that the losses of UCNs on fomblin increase over time and depend on temperature, even if the vacuum in the storage vessel is at 10^{-6} mbar [208].

An overview over various types of fomblin and a simulation of the effect of adsorbed water on neutrons with a kinetic energy in the meV range was recently published by Goremychkin and Pokotilovski [209].

Another UCN loss channel in fomblin is small heating of UCNs through interaction with surface waves [210], which can be pictured as dangling fomblin chains that give UCNs a small energy boost upon collision. At room temperature and below, fomblin is highly viscous and forms a smooth surface, which makes it easy to apply it to walls. At low temperatures, e.g. the boiling point of nitrogen at 77 K, fomblin can, under certain circumstances, form cracks through which UCNs can escape the storage volume [211].

The transmission of UCNs through fomblin is generally believed not to depend much on temperature at low temperatures. However, a test measurement performed on fomblin during experiment no. 3-14-370 [212] showed that the UCN transmission increases almost linearly from room temperature down to just below 50 K, see Fig. A.1. This points to loss channels being present even at liquid nitrogen temperatures.

It is therefore important to measure the UCN transmission through fomblin oils of various molecular weights (2800, 3300 and 6500 g/mole) at a set of temperatures

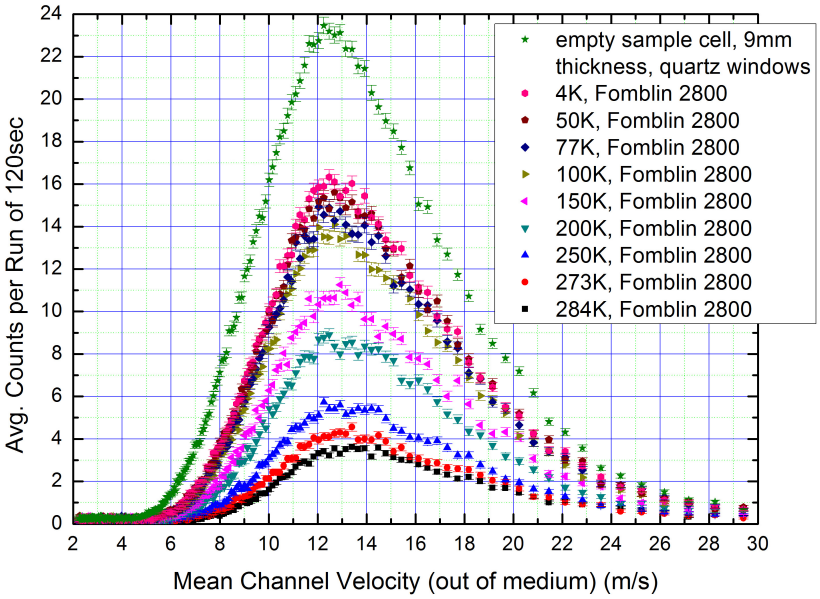

Figure A.2: UCN transmission spectra through a sample of fomblin oil (M = 2800 g/mole, 9.0 mm thick, quartz sample container) as measured in September 2016, data acquisition 3 hours per temperature.

ranging from above room temperature down to ≈ 4 K. The velocity dependence of the UCN transmission needs to be determined by a time-of-flight (TOF) setup like the one described in Section 4.1. Velocity-dependent transmission data for one kind of fomblin are shown in Fig. A.2.

In order to gain a thorough understanding of all UCN losses in fomblin oil, it is necessary to directly measure the temperature dependence of UCN transmission through fomblin at the beamline PF2-EDM at Institut Laue-Langevin using, for example, the experimental equipment described in Chapter 4.

In February 2017, a proposal to measure the transmission of UCN through different types of fomblin was submitted to and accepted by the Subcommittee of College 3 (Nuclear and Particle Physics) at the ILL (proposal no. 3-14-379)[1]. Due to the cancellation of the two last reactor cycles in 2017, these supplementary experiments could not be carried out before the submission of this thesis. The author, however, encourages colleagues in the field to carry out these experiments in the near future.

Prompt gamma activation analysis (PGAA) can be used to measure the amount of hydrogen and water impurities in fresh fomblin oil. Heating and cooling the fomblin sample during a PGAA measurement can be a way of determining an effective degassing procedure. A proposal submitted to the Budapest Neutron

[1]Proposer: Stefan Döge (ILL/TUM), co-proposers: Christoph Morkel (TUM) and Valery Nesvizhevsky (ILL)

Center (BNC) for this purpose was accepted in November 2017. Together with a hydrogen-containing calibration sample of well known thickness and density, e.g. a polyethylene (PE) foil, this experiment will tell how much hydrogen is present in fresh fomblin.

Bibliography

[1] Ya. B. Zel'dovich. Storage of cold neutrons. *Sov. Phys. JETP Lett.*, 9: 1389–90, 1959.

[2] V. I. Lushchikov, Yu. N. Pokotilovsky, A. V. Strelkov, and F. L. Shapiro. Observation of Ultracold Neutrons. *Sov. Phys. JETP Lett.*, 9(1):23–26, 1969. URL `http://www.jetpletters.ac.ru/ps/1639/article_25024.shtml`.

[3] В. И. Лущиков, Ю. Н. Покотиловский, А. В. Стрелков, and Ф. Л. Шапиро. Наблюдение ультрахолодных нейтронов. *Письма в ЖЭТФ*, 9(1):40–45, 1969. URL `http://www.jetpletters.ac.ru/ps/679/article_10540.shtml`.

[4] A. Steyerl. Measurements of total cross sections for very slow neutrons with velocities from 100 m/sec to 5 m/sec. *Physics Letters B*, 29(1):33–35, 1969.

[5] C. Patrignani and others (Particle Data Group). 2017 Review of Particle Physics. *Chin. Phys. C*, 40:100001, 2016 and 2017 update. URL `http://pdg.lbl.gov`.

[6] C. A. Baker, D. D. Doyle, P. Geltenbort, K. Green, M. G. D. van der Grinten, P. G. Harris, P. Iaydjiev, S. N. Ivanov, D. J. R. May, J. M. Pendlebury, J. D. Richardson, D. Shiers, and K. F. Smith. Improved experimental limit on the electric dipole moment of the neutron. *Phys. Rev. Lett.*, 97:131801, Sep 2006. doi: 10.1103/PhysRevLett.97.131801. URL `https://link.aps.org/doi/10.1103/PhysRevLett.97.131801`.

[7] J. M. Pendlebury et al. Revised experimental upper limit on the electric dipole moment of the neutron. *Phys. Rev. D*, 92:092003, Nov 2015. doi: 10.1103/PhysRevD.92.092003. URL `https://link.aps.org/doi/10.1103/PhysRevD.92.092003`.

[8] V. V. Nesvizhevsky, H. G. Börner, A. K. Petukhov, H. Abele, S. Baeßler, F. J. Rueß, T. Stöferle, A. Westphal, A. M. Gagarski, G. A. Petrov, and A. V. Strelkov. Quantum states of neutrons in the Earth's gravitational field. *Nature*, 415:297, 2002. doi: 10.1038/415297a. URL `http://dx.doi.org/10.1038/415297a`.

[9] T. Jenke, P. Geltenbort, H. Lemmel, and H. Abele. Realization of a gravity-resonance-spectroscopy technique. *Nat. Phys.*, 07:468, 2011.

[10] G. Ichikawa, S. Komamiya, Y. Kamiya, Y. Minami, M. Tani, P. Geltenbort, K. Yamamura, M. Nagano, T. Sanuki, S. Kawasaki, M. Hino, and M. Kitaguchi. Observation of the spatial distribution of gravitationally bound quantum states of ultracold neutrons and its derivation using the Wigner function. *Phys. Rev. Lett.*, 112:071101, Feb 2014. doi: 10.1103/PhysRevLett.112.071101. URL `https://link.aps.org/doi/10.1103/PhysRevLett.112.071101`.

[11] K. A. Steinhauser, A. Steyerl, H. Scheckenhofer, and S. S. Malik. Observation of quasibound states of the neutron in matter. *Phys. Rev. Lett.*, 44:1306–1309, May 1980. doi: 10.1103/PhysRevLett.44.1306. URL `https://link.aps.org/doi/10.1103/PhysRevLett.44.1306`.

[12] A. I. Frank. Optics of ultracold neutrons and the neutron-microscope problem. *Phys. Usp.*, 30(2):110–133, 1987. doi: 10.1070/PU1987v030n02ABEH002810. URL `https://ufn.ru/en/articles/1987/2/b/`.

[13] A. I. Frank. Ultracold neutrons and the interaction of waves with moving matter. *Physics of Particles and Nuclei*, 47(4):647–666, Jul 2016. ISSN 1531-8559. doi: 10.1134/S1063779616040067. URL `https://doi.org/10.1134/S1063779616040067`.

[14] G. Bison, M. Daum, K. Kirch, B. Lauss, D. Ries, P. Schmidt-Wellenburg, G. Zsigmond, T. Brenner, P. Geltenbort, T. Jenke, O. Zimmer, M. Beck, W. Heil, J. Kahlenberg, J. Karch, K. Ross, K. Eberhardt, C. Geppert, S. Karpuk, T. Reich, C. Siemensen, Y. Sobolev, and N. Trautmann. Comparison of ultracold neutron sources for fundamental physics measurements. *Phys. Rev. C*, 95:045503, Apr 2017. doi: 10.1103/PhysRevC.95.045503. URL `https://link.aps.org/doi/10.1103/PhysRevC.95.045503`.

[15] A. Steyerl. A "neutron turbine" as an efficient source of ultracold neutrons. *Nuclear Instruments and Methods*, 125(3):461–469, 1975. ISSN 0029-554X. doi: http://dx.doi.org/10.1016/0029-554X(75)90265-7. URL `http://www.sciencedirect.com/science/article/pii/0029554X75902657`.

[16] A. Steyerl, H. Nagel, F.-X. Schreiber, K.-A. Steinhauser, R. Gähler, W. Gläser, P. Ageron, J. M. Astruc, W. Drexel, G. Gervais, and W. Mampe. A new source of cold and ultracold neutrons. *Physics Letters A*, 116(7):347–352, 1986. doi: http://dx.doi.org/10.1016/0375-9601(86)90587-6. URL `http://www.sciencedirect.com/science/article/pii/0375960186905876`.

[17] B. Lauss. Startup of the high-intensity ultracold neutron source at the Paul Scherrer Institute. *Hyperfine Interactions*, 211(1):21–25, May 2012. ISSN

1572-9540. doi: 10.1007/s10751-012-0578-7. URL https://doi.org/10.1007/s10751-012-0578-7.

[18] A. P. Serebrov, V. A. Mityukhlyaev, A. A. Zakharov, T. Bowles, G. Greene, and J. Sromicki. Solid deuterium source of ultracold neutrons based on a pulsed spallation source. *JETP Lett.*, 66(12):802–808, Dec 1997.

[19] F. Atchison, B. Blau, K. Bodek, B. van den Brandt, T. Bryś, M. Daum, P. Fierlinger, A. Frei, P. Geltenbort, P. Hautle, R. Henneck, S. Heule, A. Holley, M. Kasprzak, K. Kirch, A. Knecht, J. A. Konter, M. Kuźniak, C.-Y. Liu, C. L. Morris, A. Pichlmaier, C. Plonka, Y. Pokotilovski, A. Saunders, Y. Shin, D. Tortorella, M. Wohlmuther, A. R. Young, J. Zejma, and G. Zsigmond. Investigation of solid D_2, O_2 and CD_4 for ultracold neutron production. *Nuclear Instruments and Methods in Physics Research Section A: Accelerators, Spectrometers, Detectors and Associated Equipment*, 611(2):252–255, 2009. doi: https://doi.org/10.1016/j.nima.2009.07.072. URL http://www.sciencedirect.com/science/article/pii/S016890020901537X. Particle Physics with Slow Neutrons.

[20] A. P. Serebrov, E. A. Kolomenski, M. S. Lasakov, V. A. Mityukhlyaev, A. N. Pirozhkov, I. A. Potapov, V. E. Varlamov, A. V. Vasiliev, A. R. Young, and A. A. Zakharov. Experimental studies of very cold neutrons passing through solid deuterium. *JETP Lett.*, 74(6):302–305, Sep 2001.

[21] Tomasz Bryś. *Extraction of ultracold neutrons from a solid deuterium source.* PhD thesis, ETH Zürich, Zurich, Switzerland, 2007.

[22] W. D. Harkins. The constitution and stability of atomic nuclei. (A contribution to the subject of inorganic evolution.). *Philosophical Magazine*, 42(249):305–339, 1921. URL http://archive.org/details/londonedinburg6421921lond.

[23] H. Becker and W. Bothe. Die γ-Strahlung von Bor und Beryllium. *Naturwissenschaften*, 20:349–349, May 1932. doi: 10.1007/BF01504733.

[24] J. Chadwick. Possible existence of a neutron. *Nature*, 129:312, 1932.

[25] J. Chadwick. The existence of a neutron. *Proceedings of the Royal Society of London A*, 136:692–708, 1932.

[26] L. de Broglie. Waves and quanta. *Nature*, 112(2815):540, 1923.

[27] L. de Broglie. *Recherches sur la théorie des Quanta.* PhD thesis, Université de Paris, 1924. URL https://tel.archives-ouvertes.fr/tel-00006807.

[28] C. Davisson and L. H. Germer. The scattering of electrons by a single crystal of nickel. *Nature*, 119(2998):558, 1927. URL `http://dx.doi.org/10.1038/119558a0`.

[29] H. von Halban and P. Preiswerk. Preuve expérimentale de la diffraction des neutrons. *Comptes Rendus de l'Académie des Sciences (Paris)*, 203:73–75, 1936.

[30] D. P. Mitchell and P. N. Powers. Bragg reflection of slow neutrons. *Phys. Rev.*, 50:486–487, Sep 1936. doi: 10.1103/PhysRev.50.486.2. URL `https://link.aps.org/doi/10.1103/PhysRev.50.486.2`.

[31] M. Arndt, O. Nairz, J. Vos-Andreae, C. Keller, G. van der Zouw, and A. Zeilinger. Wave–particle duality of C_{60} molecules. *Nature*, 401:680, 1999. URL `http://dx.doi.org/10.1038/44348`.

[32] B. Brezger, L. Hackermüller, S. Uttenthaler, J. Petschinka, M. Arndt, and A. Zeilinger. Matter-Wave Interferometer for Large Molecules. *Phys. Rev. Lett.*, 88:100404, Feb 2002. doi: 10.1103/PhysRevLett.88.100404. URL `https://link.aps.org/doi/10.1103/PhysRevLett.88.100404`.

[33] S. Eibenberger, S. Gerlich, M. Arndt, M. Mayor, and J. Tuxen. Matter-wave interference of particles selected from a molecular library with masses exceeding 10 000 amu. *Phys. Chem. Chem. Phys.*, 15:14696–14700, 2013. doi: 10.1039/C3CP51500A. URL `http://dx.doi.org/10.1039/C3CP51500A`.

[34] J. Halpern, I. Estermann, O. C. Simpson, and O. Stern. The scattering of slow neutrons by liquid ortho- and parahydrogen. *Phys. Rev.*, 52:142, Jul 1937. doi: 10.1103/PhysRev.52.142. URL `http://link.aps.org/doi/10.1103/PhysRev.52.142`.

[35] V. F. Turchin. *Slow Neutrons*. Israel program for scientific translations. Sivan Press, Jerusalem, 1965. Russian original: Медленные нейтроны, Госатомиздат, Moscow, 1963.

[36] D. Emendörfer and K. H. Höcker. *Theorie der Kernreaktoren, Band 1: Der stationäre Reaktor*. Bibliographisches Institut AG, Zürich, 1982.

[37] A. Furrer, J. Mesot, and T. Strässle. *Neutron Scattering in Condensed Matter Physics*. World Scientific, Singapore, 2009.

[38] V. F. Sears. Neutron Slowing Down and Thermalization. In *Intnernational Worjshop on Cold Neutron Sources*, page 157. Los Alamos National Laboratory, UC-413, 1991.

[39] A. Steyerl and S. S. Malik. Sources of ultracold neutrons. *Nuclear Instruments and Methods in Physics Research Section A: Accelerators, Spectrometers, Detectors and Associated Equipment*, 284(1):200–207, 1989. ISSN 0168-9002. doi: https://doi.org/10.1016/0168-9002(89)90282-9. URL `http://www.sciencedirect.com/science/article/pii/0168900289902829`.

[40] A. Steyerl. Ultracold neutrons: Production and experiments. *Physica B: Condensed Matter*, 156–157(0):528–533, 1989. ISSN 0921-4526. doi: http://dx.doi.org/10.1016/0921-4526(89)90722-9. URL `http://www.sciencedirect.com/science/article/pii/0921452689907229`.

[41] В. К. Игнатович. *Физика ультрахолодных нейтронов*. Наука, Москва, 1986.

[42] V. K. Ignatovich. *The Physics of Ultracold Neutrons*. Clarendon Press, Oxford, 1990.

[43] R. Golub, D. J. Richardson, and S. K. Lamoreaux. *Ultra-Cold Neutrons*. Adam Hilger, Bristol, 1991.

[44] V. F. Sears. Neutron scattering lengths and cross sections. *Neutron News*, 3(3):26–37 (Special Feature), 1992. URL `http://www.ncnr.nist.gov/resources/n-lengths/`.

[45] I. Altarev, F. Atchison, M. Daum, A. Frei, E. Gutsmiedl, G. Hampel, F. J. Hartmann, W. Heil, A. Knecht, J. V. Kratz, T. Lauer, M. Meier, S. Paul, Y. Sobolev, and N. Wiehl. Direct experimental verification of neutron acceleration by the material optical potential of solid $^2H_2$. *Phys. Rev. Lett.*, 100:014801, Jan 2008. doi: 10.1103/PhysRevLett.100.014801. URL `http://link.aps.org/doi/10.1103/PhysRevLett.100.014801`.

[46] P. C. Souers. *Hydrogen Properties for Fusion Energy*. University of California Press, 1986.

[47] E. Fermi and W. H. Zinn. Articles 217 and 220. In Edoardo Amaldi et al., editors, *Note e memorie (Collected papers)*, volume 2 (United States, 1939–45), pages 425–434. The University of Chicago Press, 1965.

[48] R. Golub and J. M. Pendlebury. Super-thermal sources of ultra-cold neutrons. *Physics Letters A*, 53(2):133–135, 1975. ISSN 0375-9601. doi: https://doi.org/10.1016/0375-9601(75)90500-9. URL `http://www.sciencedirect.com/science/article/pii/0375960175905009`.

[49] I. S. Altarev, Yu. V. Borisov, A. B. Brandin, V. F. Ezhov, S. N. Ivanov, G. K. Kunstman, V. M. Lobashev, V. A. Nazarenko, V. L. Ryabov, A. P. Serebrov, and R. R. Taldaev. A liquid hydrogen source of ultra-cold neutrons.

Physics Letters A, 80(5):413–416, 1980. ISSN 0375-9601. doi: https://doi.org/10.1016/0375-9601(80)90784-7. URL http://www.sciencedirect.com/science/article/pii/0375960180907847.

[50] R. Golub and K. Böning. New type of low temperature source of ultra-cold neutrons and production of continous beams of UCN. *Zeitschrift für Physik B Condensed Matter*, 51(2):95–98, Jun 1983.

[51] Z-Ch. Yu, S. S. Malik, and R. Golub. A thin film source of ultra-cold neutrons. *Zeitschrift für Physik B Condensed Matter*, 62(2):137–142, Jun 1986.

[52] A. Frei, E. Gutsmiedl, C. Morkel, A. R. Müller, S. Paul, S. Rols, H. Schober, and T. Unruh. Understanding of ultra-cold-neutron production in solid deuterium. *EPL (Europhysics Letters)*, 92(6):62001, 2010. URL http://stacks.iop.org/0295-5075/92/i=6/a=62001.

[53] A. P. Serebrov, V. A. Mityukhlyaev, A. A. Zakharov, V. V. Nesvizhevsky, and A. G. Kharitonov. Is it possible to produce next generation of UCN sources with density 10^3 – 10^4 cm^{-3}? *JETP Lett.*, 59:757, 1994.

[54] C.-Y. Liu, A. R. Young, and S. K. Lamoreaux. Ultracold neutron upscattering rates in a molecular deuterium crystal. *Phys. Rev. B*, 62(6):R3581, 2000. doi: 10.1103/PhysRevB.62.R3581. URL https://link.aps.org/doi/10.1103/PhysRevB.62.R3581.

[55] F. Atchison, B. van den Brandt, T. Bryś, M. Daum, P. Fierlinger, P. Hautle, R. Henneck, S. Heule, M. Kasprzak, K. Kirch, J. A. Konter, A. Michels, A. Pichlmaier, M. Wohlmuther, A. Wokaun, K. Bodek, U. Szerer, P. Geltenbort, J. Zmeskal, and Y. Pokotilovskiy. Production of ultracold neutrons from a cold neutron beam on a $^2H_2$ target. *Phys. Rev. C*, 71:054601, May 2005. doi: 10.1103/PhysRevC.71.054601. URL https://link.aps.org/doi/10.1103/PhysRevC.71.054601.

[56] A. P. Serebrov. Solid deuterium and UCN factory: application to the neutron electric dipole moment measurement. *Nuclear Instruments and Methods in Physics Research Section A: Accelerators, Spectrometers, Detectors and Associated Equipment*, 440(3):653–657, 2000. ISSN 0168-9002. doi: https://doi.org/10.1016/S0168-9002(99)01057-8.

[57] A. Saunders, J. M. Anaya, T. J. Bowles, B. W. Filippone, P. Geltenbort, R. E. Hill, M. Hino, S. Hoedl, G. E. Hogan, T. M. Ito, K. W. Jones, T. Kawai, K. Kirch, S. K. Lamoreaux, C.-Y. Liu, M. Makela, L. J. Marek, J. W. Martin, C. L. Morris, R. N. Mortensen, A. Pichlmaier, S. J. Seestrom, A. Serebrov, D. Smith, W. Teasdale, B. Tipton, R. B. Vogelaar, A. R. Young, and J. Yuan. Demonstration of a solid deuterium source

of ultra-cold neutrons. *Physics Letters B*, 593(1):55–60, 2004. ISSN 0370-2693. doi: https://doi.org/10.1016/j.physletb.2004.04.048. URL http://www.sciencedirect.com/science/article/pii/S0370269304006781.

[58] A. Frei, E. Gutsmiedl, C. Morkel, A. R. Müller, S. Paul, M. Urban, H. Schober, S. Rols, T. Unruh, and M. Hölzel. Density of states in solid deuterium: Inelastic neutron scattering study. *Phys. Rev. B*, 80:064301, Aug 2009. doi: 10.1103/PhysRevB.80.064301. URL http://link.aps.org/doi/10.1103/PhysRevB.80.064301.

[59] R. Golub and J. M. Pendlebury. The interaction of ultra-cold neutrons (UCN) with liquid helium and a superthermal UCN source. *Physics Letters A*, 62(5):337–339, 1977. ISSN 0375-9601. doi: https://doi.org/10.1016/0375-9601(77)90434-0. URL http://www.sciencedirect.com/science/article/pii/0375960177904340.

[60] P. Ageron, W. Mampe, R. Golub, and J. M. Pendelbury. Measurement of the ultra cold neutron production rate in an external liquid helium source. *Physics Letters A*, 66(6):469–471, 1978. ISSN 0375-9601. doi: https://doi.org/10.1016/0375-9601(78)90399-7. URL http://www.sciencedirect.com/science/article/pii/0375960178903997.

[61] P. V. E. McClintock. Ultra-cold neutrons in superfluid helium. *Nature*, 275:174–175, 1978. doi: http://dx.doi.org/10.1038/275174a0.

[62] O. Zimmer, F. M. Piegsa, and S. N. Ivanov. Superthermal source of ultracold neutrons for fundamental physics experiments. *Phys. Rev. Lett.*, 107:134801, Sep 2011. doi: 10.1103/PhysRevLett.107.134801. URL https://link.aps.org/doi/10.1103/PhysRevLett.107.134801.

[63] H. Yoshiki, K. Sakai, M. Ogura, T. Kawai, Y. Masuda, T. Nakajima, T. Takayama, S. Tanaka, and A. Yamaguchi. Observation of ultracold-neutron production by 9-å cold neutrons in superfluid helium. *Phys. Rev. Lett.*, 68:1323–1326, Mar 1992. doi: 10.1103/PhysRevLett.68.1323. URL https://link.aps.org/doi/10.1103/PhysRevLett.68.1323.

[64] H. Yoshiki, K. Sakai, T. Kawai, and S. Goto'o. Three metre long horizontal cryostat producing ultracold neutrons using superfluid liquid helium at 0.5 K (Mark 3000). *Cryogenics*, 34(4):277–286, 1994. ISSN 0011-2275. doi: https://doi.org/10.1016/0011-2275(94)90107-4. URL http://www.sciencedirect.com/science/article/pii/0011227594901074.

[65] R. Picker and TRIUMF collaboration. How the minuscule can contribute to the big picture: the neutron electric dipole moment project at TRIUMF. 2016. URL http://arxiv.org/abs/1612.00875. arXiv:physics.ins-det/1612.00875v1.

[66] C.-Y. Liu and A. R. Young. Ultra-cold neutron production in anti-ferromagnetic oxygen solid. 2004. URL `http://arxiv.org/abs/nucl-th/0406004`. arXiv:nucl-th/0406004v1.

[67] E. Gutsmiedl, F. Böhle, A. Frei, A. Maier, S. Paul, A. Orecchini, and H. Schober. Production of ultra-cold neutrons in solid α-oxygen. *EPL (Europhysics Letters)*, 96(6):62001, 2011. URL `http://stacks.iop.org/0295-5075/96/i=6/a=62001`.

[68] D. J. Salvat, E. Gutsmiedl, C.-Y. Liu, P. Geltenbort, A. Orecchini, S. Paul, and H. Schober. Investigating solid α-$^{15}N_2$ as a new source of ultra-cold neutrons. *EPL (Europhysics Letters)*, 103(1):12001, 2013. URL `http://stacks.iop.org/0295-5075/103/i=1/a=12001`.

[69] F. Atchison, B. Blau, K. Bodek, B. van den Brandt, T. Bryś, M. Daum, P. Fierlinger, P. Geltenbort, P. Hautle, R. Henneck, S. Heule, A. Holley, M. Kasprzak, K. Kirch, A. Knecht, J. A. Konter, M. Kuźniak, C.-Y. Liu, A. Pichlmaier, C. Plonka, Y. Pokotilovski, A. Saunders, D. Tortorella, M. Wohlmuther, A. R. Young, J. Zejma, and G. Zsigmond. Production of ultracold neutrons from cryogenic $^2H_2$, O_2 , and C^2H_4 converters. *EPL (Europhysics Letters)*, 95(1):12001, 2011. URL `http://stacks.iop.org/0295-5075/95/i=1/a=12001`.

[70] E. V. Lychagin, A. Yu. Muzychka, G. V. Nekhaev, V. V. Nesvizhevsky, E. I. Sharapov, and A. V. Strelkov. UCN Source at an External Beam of Thermal Neutrons. *Advances in High Energy Physics*, 2015:547620, 2015. doi: http://dx.doi.org/10.1155/2015/547620.

[71] V. V. Nesvizhevsky, M. Dubois, Ph. Gutfreund, E. V. Lychagin, A. Yu. Nezvanov, and K. N. Zhernenkov. Effect of nanodiamond fluorination on the efficiency of quasispecular reflection of cold neutrons. *Phys. Rev. A*, 97: 023629, Feb 2018. doi: 10.1103/PhysRevA.97.023629. URL `https://link.aps.org/doi/10.1103/PhysRevA.97.023629`.

[72] O. Zimmer. Neutron conversion and cascaded cooling in paramagnetic systems for a high-flux source of very cold neutrons. *Phys. Rev. C*, 93:035503, Mar 2016. doi: 10.1103/PhysRevC.93.035503. URL `https://link.aps.org/doi/10.1103/PhysRevC.93.035503`.

[73] В. К. Игнатович. Ультрахолодные нейтроны — открытие и исследование. *Успехи физических наук*, 166(3):303–326, 1996. URL `http://ufn.ru/ru/articles/1996/3/d/`.

[74] H. Abele. The neutron. its properties and basic interactions. *Progress in Particle and Nuclear Physics*, 60(1):1–81, 2008. ISSN 0146-6410. doi: https:

//doi.org/10.1016/j.ppnp.2007.05.002. URL http://www.sciencedirect.com/science/article/pii/S0146641007000622.

[75] D. Dubbers and M. G. Schmidt. The neutron and its role in cosmology and particle physics. *Rev. Mod. Phys.*, 83:1111–1171, Oct 2011. doi: 10.1103/RevModPhys.83.1111. URL https://link.aps.org/doi/10.1103/RevModPhys.83.1111.

[76] M. Tanabashi and others (Particle Data Group). 23. Big-Bang Nucleosynthesis. *Phys. Rev. D*, 98:030001, 2018. URL http://pdg.lbl.gov/2018/reviews.

[77] F. E. Wietfeldt and G. L. Greene. Colloquium: The Neutron Lifetime. *Rev. Mod. Phys.*, 83:1173–1192, Nov 2011. doi: 10.1103/RevModPhys.83.1173. URL https://link.aps.org/doi/10.1103/RevModPhys.83.1173.

[78] A. T. Yue, M. S. Dewey, D. M. Gilliam, G. L. Greene, A. B. Laptev, J. S. Nico, W. M. Snow, and F. E. Wietfeldt. Improved determination of the neutron lifetime. *Phys. Rev. Lett.*, 111:222501, Nov 2013.

[79] S. Materne, R. Picker, I. Altarev, H. Angerer, B. Franke, E. Gutsmiedl, F. J. Hartmann, A. R. Müller, S. Paul, and R. Stoepler. PENeLOPE – on the way towards a new neutron lifetime experiment with magnetic storage of ultra-cold neutrons and proton extraction. *Nuclear Instruments and Methods in Physics Research Section A: Accelerators, Spectrometers, Detectors and Associated Equipment*, 611(2):176–180, 2009. ISSN 0168-9002. doi: https://doi.org/10.1016/j.nima.2009.07.055. URL http://www.sciencedirect.com/science/article/pii/S0168900209015204. Particle Physics with Slow Neutrons.

[80] P. Schmidt-Wellenburg. The quest for an electric dipole moment of the neutron. *AIP Conference Proceedings*, 1753(1):060002, 2016. doi: 10.1063/1.4955363. URL http://aip.scitation.org/doi/abs/10.1063/1.4955363.

[81] S. Baeßler, V. V. Nesvizhevsky, K. V. Protasov, and A. Yu. Voronin. Constraint on the coupling of axionlike particles to matter via an ultracold neutron gravitational experiment. *Phys. Rev. D*, 75:075006, Apr 2007. doi: 10.1103/PhysRevD.75.075006. URL https://link.aps.org/doi/10.1103/PhysRevD.75.075006.

[82] G. Cronenberg, P. Brax, H. Filter, P. Geltenbort, T. Jenke, G. Pignol, M. Pitschmann, M. Thalhammer, and H. Abele. Acoustic Rabi oscillations between gravitational quantum states and impact on symmetron dark energy. *Nature Physics*, Jul 2018. doi: 10.1038/s41567-018-0205-x. URL https://doi.org/10.1038/s41567-018-0205-x.

[83] C. G. Shull. Wave properties of the neutron. In *The Neutron and its Applications*, pages 157–168. Institute of Physics Conference Series No. 64: Section 3, 1982.

[84] А. И. Франк. Оптика ультрахолодных нейтронов и проблема нейтронного микроскопа. *Усп. физ. наук*, 151(2):229–272, 1987. doi: 10.3367/UFNr.0151.198702b.0229. URL `https://ufn.ru/ru/articles/1987/2/b/`.

[85] A. I. Frank. Ultracold-neutron microscopy. *Soviet Atomic Energy*, 66(2):106–114, Feb 1989. ISSN 1573-8205. doi: 10.1007/BF01121798. URL `https://doi.org/10.1007/BF01121798`.

[86] И. М. Франк. *Природа*, 9:24, 1972.

[87] Ф. Л. Шапиро. Ультрахолодные нейтроны. *Препринт ОИЯИ Дубна*, pages R3–7135, 1973.

[88] P. Herrmann, K.-A. Steinhauser, R. Gähler, A. Steyerl, and W. Mampe. Neutron Microscope. *Phys. Rev. Lett.*, 54:1969–1972, May 1985. doi: 10.1103/PhysRevLett.54.1969. URL `https://link.aps.org/doi/10.1103/PhysRevLett.54.1969`.

[89] A. Steyerl, W. Drexel, T. Ebisawa, E. Gutsmiedl, K.-A. Steinhauser, R. Gähler, W. Mampe, and P. Ageron. Neutron Microscopy. *Revue de Physique Appliquée*, 23:171–180, 1988. URL `https://hal.archives-ouvertes.fr/jpa-00245760/document`.

[90] Pierre Bouguer. *Essai d'optique sur la gradation de la lumière*. Claude Jombert, Paris, 1729.

[91] August Beer. Bestimmung der Absorption des rothen Lichts in farbigen Flüssigkeiten. *Annalen der Physik und Chemie*, 86:78–88, 1852.

[92] Yu. N. Pokotilovski, M. I. Novopoltsev, P. Geltenbort, and T. Brenner. A differential time-of-flight spectrometer of very slow neutrons. *Instruments and Experimental Techniques*, 54(1):16–22, Jan 2011. ISSN 1608-3180. doi: 10.1134/S0020441210061077. URL `https://doi.org/10.1134/S0020441210061077`.

[93] W. Heisenberg. Mehrkörperprobleme und Resonanz in der Quantenmechanik. II. *Zeitschrift für Physik A Hadrons and Nuclei*, 41(4):239–267, Aug 1927. ISSN 0939-7922. doi: 10.1007/BF01391241. URL `https://doi.org/10.1007/BF01391241`.

[94] R. Mecke. Zur Struktur einer Klasse von Bandenspektra. *Zeitschrift für Physik*, 31(1):709–712, Feb 1925. ISSN 0044-3328. doi: 10.1007/BF02980625. URL https://doi.org/10.1007/BF02980625.

[95] F. Hund. Zur Deutung der Molekelspektren. II. *Zeitschrift für Physik*, 42 (2):93–120, Feb 1927. ISSN 0044-3328. doi: 10.1007/BF01397124. URL https://doi.org/10.1007/BF01397124.

[96] A. Eucken. Die Molekularwärme des Wasserstoffs bei tiefen Temperaturen. *Sitzber. Preuss. Akad. Wiss.*, page 141, 1912.

[97] I. F. Silvera. The solid molecular hydrogens in the condensed phase: Fundamentals and static properties. *Rev. Mod. Phys.*, 52:393–452, Apr 1980. doi: 10.1103/RevModPhys.52.393. URL http://link.aps.org/doi/10.1103/RevModPhys.52.393.

[98] D. M. Dennison. A note on the specific heat of the hydrogen molecule. *Proceedings of the Royal Society of London. Series A, Containing Papers of a Mathematical and Physical Character*, 115(771):483–486, 1927. ISSN 09501207. URL http://www.jstor.org/stable/94849.

[99] T. Steinhauser, D. Hoffmann, J. James, and B. Friedrich. *Hundert Jahre an der Schnittstelle von Chemie und Physik: das Fritz-Haber-Institut der Max-Planck-Gesellschaft zwischen 1911 und 2011.* De Gruyter, 2011.

[100] K. F. Bonhoeffer and P. Harteck. Über Para- und Orthowasserstoff. *Zeitschrift für physikalische Chemie B*, 4(1):113–141, 1929. doi: http://dx.doi.org/10.1515/zpch-1929-0408. URL https://www.degruyter.com/view/j/zpch.1929.4.issue-1/zpch-1929-0408/zpch-1929-0408.xml.

[101] F. Atchison, P. Beaud, T. Bryś, M. Daum, P. Fierlinger, R. Henneck, T. Hofmann, K. Kirch, G. Kühne, G. Knopp, A. Pichlmaier, A. Serebrov, H. Spitzer, J. Wambach, J. Wimmer, A. Wokaun, K. Bodek, P. Geltenbort, M. Giersch, J. Zmeskal, and K. Mishima. Ortho-para equilibrium in a liquid D_2 neutron moderator under irradiation. *Phys. Rev. B*, 68:094114, Sep 2003. doi: 10.1103/PhysRevB.68.094114. URL http://link.aps.org/doi/10.1103/PhysRevB.68.094114.

[102] C.-Y. Liu, S. K. Lamoreaux, A. Saunders, D. Smith, and A. R. Young. An apparatus to control and monitor the para-D_2 concentration in a solid deuterium, superthermal source of ultra-cold neutrons. *Nuclear Instruments and Methods in Physics Research Section A: Accelerators, Spectrometers, Detectors and Associated Equipment*, 508(3):257–267, 2003. ISSN 0168-9002. doi: https://doi.org/10.1016/S0168-9002(03)01666-8.

[103] H. W. Wooley, R. B. Scott, and F. G. Brickwedde. Compilation of thermal properties of hydrogen in its various isotopic and ortho-para modifications. *J. Res. Nat. Bur. Stand.*, 41:379–475, 1948.

[104] M. Hamermesh and J. Schwinger. The Scattering of Slow Neutrons by Ortho- and Paradeuterium. *Phys. Rev.*, 69:145–154, Mar 1946.

[105] J. A. Young and J. U. Koppel. Slow Neutron Scattering by Molecular Hydrogen and Deuterium. *Phys. Rev.*, 135:A603–A611, Aug 1964. doi: 10.1103/PhysRev.135.A603.

[106] F. Atchison, B. van den Brandt, T. Bryś, M. Daum, P. Fierlinger, P. Hautle, R. Henneck, K. Kirch, J. Kohlbrecher, G. Kühne, J. A. Konter, A. Pichlmaier, A. Wokaun, K. Bodek, M. Kasprzak, M. Kuźniak, P. Geltenbort, M. Giersch, J. Zmeskal, M. Hino, and M. Utsuro. Measured total cross sections of slow neutrons scattered by gaseous and liquid $^2H_2$. *Phys. Rev. Lett.*, 94:212502, Jun 2005. doi: 10.1103/PhysRevLett.94.212502. URL `https://link.aps.org/doi/10.1103/PhysRevLett.94.212502`.

[107] F. Atchison, B. Blau, B. van den Brandt, T. Bryś, M. Daum, P. Fierlinger, P. Hautle, R. Henneck, S. Heule, K. Kirch, J. Kohlbrecher, G. Kühne, J. A. Konter, A. Pichlmaier, A. Wokaun, K. Bodek, M. Kasprzak, M. Kuźniak, P. Geltenbort, and J. Zmeskal. Measured total cross sections of slow neutrons scattered by solid deuterium and implications for ultracold neutron sources. *Phys. Rev. Lett.*, 95:182502, Oct 2005. doi: 10.1103/PhysRevLett.95.182502. URL `http://link.aps.org/doi/10.1103/PhysRevLett.95.182502`.

[108] Yu. N. Pokotilovski. UCN transport simulation in solid deuterium crystals. *Nuclear Instruments and Methods in Physics Research Section A: Accelerators, Spectrometers, Detectors and Associated Equipment*, 675(Supplement C):29–33, 2012. ISSN 0168-9002. doi: https://doi.org/10.1016/j.nima.2012.01.070. URL `http://www.sciencedirect.com/science/article/pii/S0168900212001301`.

[109] I. I. Gurevich and L. V. Tarasov. *Low-Energy Neutron Physics*. North-Holland Publishing Company, 1968.

[110] J. Schwinger and E. Teller. The scattering of neutrons by ortho- and parahydrogen. *Phys. Rev.*, 51:775–775, May 1937. doi: 10.1103/PhysRev.51.775. URL `https://link.aps.org/doi/10.1103/PhysRev.51.775`.

[111] J. Schwinger and E. Teller. The scattering of neutrons by ortho- and parahydrogen. *Phys. Rev.*, 52:286–295, Aug 1937. doi: 10.1103/PhysRev.52.286. URL `https://link.aps.org/doi/10.1103/PhysRev.52.286`.

[112] Wulf-Dieter Seiffert. *Messung der Streuquerschnitte von flüssigem und festem Wasserstoff, Deuterium und Deuteriumhydrid für thermische Neutronen.* PhD thesis, Technische Universität München, Munich, Germany, 1970. Also Euratom report no. EUR 4455 d.

[113] C. M. Lavelle, C.-Y. Liu, W. Fox, G. Manus, P. M. McChesney, D. J. Salvat, Y. Shin, M. Makela, C. Morris, A. Saunders, A. Couture, and A. R. Young. Ultracold-neutron production in a pulsed-neutron beam line. *Phys. Rev. C*, 82:015502, Jul 2010. doi: 10.1103/PhysRevC.82.015502. URL `https://link.aps.org/doi/10.1103/PhysRevC.82.015502`.

[114] Christian Herold. *Messung von Streuquerschnitten ultrakalter Neutronen in festem Deuterium.* Diploma thesis, Technische Universität München, Munich, Germany, 2013.

[115] W. Bernnat, J. Keinert, and M. Mattes. Evaluation of scattering laws and cross sections for calculation of production and transport of cold and ultracold neutrons. In H. Conrad, editor, *Forschungszentrum Jülich Matter and Materials 20*, pages 9–42. Forschungszentrum Jülich, 2004.

[116] W. Mehringer. Thermal and subthermal neutron scattering. *Zeitschrift für Physik*, 210(5):434–456, Mar 1968. ISSN 0044-3328. doi: 10.1007/BF02083661. URL `https://doi.org/10.1007/BF02083661`.

[117] P. H. Handel. Recoilless spin-flip in the magnetic scattering of cold neutrons. *Zeitschrift für Naturforschung A*, 24:1646–1659, 1969.

[118] Stefan Döge, Christian Herold, Stefan Müller, Christoph Morkel, Erwin Gutsmiedl, Peter Geltenbort, Thorsten Lauer, Peter Fierlinger, Winfried Petry, and Peter Böni. Scattering cross sections of liquid deuterium for ultracold neutrons: Experimental results and a calculation model. *Phys. Rev. B*, 91:214309, Jun 2015. doi: 10.1103/PhysRevB.91.214309. URL `http://link.aps.org/doi/10.1103/PhysRevB.91.214309`.

[119] M. Nielsen and H. Bjerrum Møller. Lattice dynamics of solid deuterium by inelastic neutron scattering. *Phys. Rev. B*, 3:4383–4385, Jun 1971. doi: 10.1103/PhysRevB.3.4383. URL `http://link.aps.org/doi/10.1103/PhysRevB.3.4383`.

[120] M. Nielsen. Phonons in solid hydrogen and deuterium studied by inelastic coherent neutron scattering. *Phys. Rev. B*, 7:1626–1635, Feb 1973. doi: 10.1103/PhysRevB.7.1626. URL `http://link.aps.org/doi/10.1103/PhysRevB.7.1626`.

[121] A. V. Stepanov. On the coefficient of absorption of ultracold neutrons in a medium bounded by a rough surface. *Theoretical and Mathematical Physics*, 22(3):299–303, Mar 1975. ISSN 1573-9333. doi: 10.1007/BF01037809. URL https://doi.org/10.1007/BF01037809.

[122] C.-Y. Liu, A. R. Young, C. M. Lavelle, and D. Salvat. Coherent neutron scattering in polycrystalline deuterium and its implications for ultracold neutron production. pages arXiv:1005.1016 [nucl–th], 2010. URL https://arxiv.org/abs/1005.1016v1.

[123] G. Placzek and L. Van Hove. Interference effects in the total neutron scattering cross-section of crystals. *Il Nuovo Cimento (1955-1965)*, 1(1): 233–256, Jan 1955. ISSN 1827-6121. doi: 10.1007/BF02731767. URL https://doi.org/10.1007/BF02731767.

[124] А. В. Степанов. Оптический потенциал для ультрахолодных нейтронов. *Физика элементарных частиц и атомного ядра*, 7:989–1038, 1976.

[125] A. Guinier and G. Gournet. *Small Angle Scattering of X-Rays*. John Wiley and Sons, Ltd., 1955.

[126] G. Kostorz. Small-angle scattering and its applications to materials science. In G. Kostorz, editor, *Neutron Scattering*, volume 15 of *Treatise on Materials Science and Technology*, pages 227–289. Elsevier, 1979. doi: https://doi.org/10.1016/B978-0-12-341815-9.50013-6. URL http://www.sciencedirect.com/science/article/pii/B9780123418159500136.

[127] F. Atchison, M. Daum, R. Henneck, S. Heule, M. Horisberger, M. Kasprzak, K. Kirch, A. Knecht, M. Kużniak, B. Lauss, A. Mtchedlishvili, M. Meier, G. Petzoldt, C. Plonka-Spehr, R. Schelldorfer, U. Straumann, and G. Zsigmond. Diffuse reflection of ultracold neutrons from low-roughness surfaces. *The European Physical Journal A*, 44(1):23–29, Apr 2010. ISSN 1434-601X. doi: 10.1140/epja/i2010-10926-x. URL https://doi.org/10.1140/epja/i2010-10926-x.

[128] P. Schmidt-Wellenburg, J. Barnard, P. Geltenbort, V. V. Nesvizhevsky, C. Plonka, T. Soldner, and O. Zimmer. Efficient extraction of a collimated ultra-cold neutron beam using diffusive channels. *Nuclear Instruments and Methods A*, 577(3):623–625, 2007. ISSN 0168-9002. doi: https://doi.org/10.1016/j.nima.2007.03.032. URL http://www.sciencedirect.com/science/article/pii/S0168900207006535.

[129] Andreas Frei. *Untersuchung ausgewählter Elemente der UCN-Quelle Mini-D2*. Diploma thesis, Technische Universität München, Munich, Germany, 2002.

[130] F. Atchison, B. Blau, A. Bollhalder, M. Daum, P. Fierlinger, P. Geltenbort, G. Hampel, M. Kasprzak, K. Kirch, S. Köchli, B. Kuczewski, H. Leber, M. Locher, M. Meier, S. Ochse, A. Pichlmaier, C. Plonka, R. Reiser, J. Ulrich, X. Wang, N. Wiehl, O. Zimmer, and G. Zsigmond. Transmission of very slow neutrons through material foils and its influence on the design of ultracold neutron sources. *Nuclear Instruments and Methods in Physics Research Section A: Accelerators, Spectrometers, Detectors and Associated Equipment*, 608(1):144–151, 2009. doi: https://doi.org/10.1016/j.nima.2009.06.047. URL `http://www.sciencedirect.com/science/article/pii/S0168900209013047`.

[131] S. Döge et al. Measurement of the UCN scattering cross sections of liquid and solid deuterium, 2015. Institut Laue–Langevin, Grenoble, France, experimental report no. 3-14-351.

[132] A. Steyerl. Effect of surface roughness on the total reflexion and transmission of slow neutrons. *Zeitschrift für Physik A Hadrons and Nuclei*, 254(2):169–188, 1972. ISSN 0939-7922. doi: 10.1007/BF01380066. URL `http://dx.doi.org/10.1007/BF01380066`.

[133] C. Y. Poon and B. Bhushan. Comparison of surface roughness measurements by stylus profiler, AFM and non-contact optical profiler. *Wear*, 190(1):76–88, 1995. ISSN 0043-1648. doi: https://doi.org/10.1016/0043-1648(95)06697-7. URL `http://www.sciencedirect.com/science/article/pii/0043164895066977`. Macro and Micro-Tribology and Mechanics of Magnetic Storage Systems.

[134] E. S. Gadelmawla, M. M. Koura, T. M. A. Maksoud, I. M. Elewa, and H. H. Soliman. Roughness parameters. *Journal of Materials Processing Technology*, 123(1):133–145, 2002. ISSN 0924-0136. doi: https://doi.org/10.1016/S0924-0136(02)00060-2. URL `http://www.sciencedirect.com/science/article/pii/S0924013602000602`.

[135] Stefan T. Döge. *Measurement of the Scattering Cross Section of Ultracold Neutrons in Liquid Deuterium*. Master's thesis, Technische Universität München, Munich, Germany, 2014.

[136] C. Morkel, S. Döge, et al. Measurement of UCN scattering cross sections of liquid and solid ortho-deuterium, 2013. Institut Laue–Langevin, Grenoble, France, experimental report no. 3-14-311.

[137] M. Hartl, R. C. Gillis, L. Daemen, D. P. Olds, K. Page, S. Carlson, Y. Cheng, T. Hugle, E. B. Iverson, A. J. Ramirez-Cuesta, Y. Lee, and G. Muhrer. Hydrogen adsorption on two catalysts for the ortho- to parahydrogen conversion: Cr-doped silica and ferric oxide gel. *Phys. Chem.*

Chem. Phys., 18:17281–17293, 2016. doi: 10.1039/C6CP01154C. URL http://dx.doi.org/10.1039/C6CP01154C.

[138] N. S. Sullivan, D. Zhou, and C. M. Edwards. Precise and efficient in situ ortho→para-hydrogen converter. *Cryogenics*, 30(8):734–735, 1990. ISSN 0011-2275. doi: https://doi.org/10.1016/0011-2275(90)90240-D. URL http://www.sciencedirect.com/science/article/pii/001122759090240D.

[139] N. Hild and B. Lauss. Report on the Raman measurements of H_2 and D_2 during the ILL run from 8.2.-7.3.2017. Technical report, Paul Scherrer Institut (PSI), Villigen, Switzerland, 2017.

[140] R. Gross and A. Marx. *Festkörperphysik*. Oldenbourg Verlag, Munich, Germany, 2012.

[141] D. A. Long. *The Raman Effect: A Unified Treatment of the Theory of Raman Scattering by Molecules*. John Wiley and Sons, Ltd., 2002.

[142] M. Klein and C. J. Schmidt. CASCADE, neutron detectors for highest count rates in combination with ASIC/FPGA based readout electronics. *Nuclear Instruments and Methods in Physics Research Section A: Accelerators, Spectrometers, Detectors and Associated Equipment*, 628(1):9–18, 2011. ISSN 0168-9002. doi: http://dx.doi.org/10.1016/j.nima.2010.06.278. URL http://www.sciencedirect.com/science/article/pii/S0168900210014683. VCI 2010 Proceedings of the 12th International Vienna Conference on Instrumentation.

[143] F. Sauli. The gas electron multiplier (GEM): Operating principles and applications. *Nuclear Instruments and Methods in Physics Research Section A: Accelerators, Spectrometers, Detectors and Associated Equipment*, 805(Supplement C):2–24, 2016. ISSN 0168-9002. doi: https://doi.org/10.1016/j.nima.2015.07.060. URL http://www.sciencedirect.com/science/article/pii/S0168900215008980. Special Issue in memory of Glenn F. Knoll.

[144] M. Klein. Cascade Detector Technologies (CDT), Heidelberg, Germany. 2018. priv. comm. and CDT website.

[145] Jürgen S. Hingerl. *A Versatile Device for Studying Ultracold Neutrons and Testing Cryogenic Storage Volumes*. Master's thesis, Technische Universität München, Munich, Germany, 2019.

[146] A. V. Strelkov. Joint Institute of Nuclear Research (JINR), Dubna, Russia. 2018. priv. comm.

[147] A. Frei. Technische Universität München, Munich, Germany. 2018. priv. comm.

[148] Damien Roulier. *Production et détection de neutrons ultra-froids pour le spectromètre GRANIT*. PhD thesis, Université Grenoble Alpes, Grenoble, France, 2015.

[149] Gwendal Rogel. *Développement de détecteurs de neutrons ultra-froids et d'un système d'analyse de polarisation pour la mesure de l'EDM du neutron*. PhD thesis, Université Grenoble Alpes, Grenoble, France, 2009.

[150] Thorsten Lauer. *Investigation of a superthermal ultracold neutron source based on a solid deuterium converter for the TRIGA Mainz reactor*. PhD thesis, Universität Mainz, Mainz, Germany, 2010.

[151] M. Daum, B. Franke, P. Geltenbort, E. Gutsmiedl, S. Ivanov, J. Karch, M. Kasprzak, K. Kirch, A. Kraft, T. Lauer, B. Lauss, A. R. Müller, S. Paul, P. Schmidt-Wellenburg, T. Zechlau, and G. Zsigmond. Transmission of ultra-cold neutrons through guides coated with materials of high optical potential. *Nuclear Instruments and Methods in Physics Research Section A: Accelerators, Spectrometers, Detectors and Associated Equipment*, 741:71–77, 2014. ISSN 0168-9002. doi: https://doi.org/10.1016/j.nima.2013.12.050. URL `http://www.sciencedirect.com/science/article/pii/S0168900213017580`.

[152] S. Wlokka, P. Fierlinger, A. Frei, P. Geltenbort, T. Huber, S. Paul, K. Schreckenbach, and R. Stoepler. Investigation of guides for ultracold neutrons. *Journal of Neutron Research*, 18:109–116, 2015. doi: 10.3233/JNR-160029.

[153] S. Wlokka, P. Fierlinger, A. Frei, P. Geltenbort, S. Paul, T. Pöschl, F. Schmid, W. Schreyer, and D. Steffen. Consistent description of UCN transport properties. 2017. URL `http://arxiv.org/abs/1701.07431`. arXiv:1701.07431v1 [physics.ins-det].

[154] Tobias Rechberger. *Ramsey Spectroscopy of Gravitationally Bound Ultracold Neutrons*. PhD thesis, Technische Universität Wien, Vienna, Austria, 2018.

[155] A. P. Serebrov, E. A. Kolomensky, A. K. Fomin, I. A. Krasnoshchekova, A. V. Vassiljev, D. M. Prudnikov, I. V. Shoka, A. V. Chechkin, M. E. Chaikovskiy, V. E. Varlamov, S. N. Ivanov, A. N. Pirozhkov, P. Geltenbort, O. Zimmer, T. Jenke, M. Van der Grinten, and M. Tucker. Neutron lifetime measurements with a large gravitational trap for ultracold neutrons. *Phys. Rev. C*, 97:055503, May 2018. doi: 10.1103/PhysRevC.97.055503. URL `https://link.aps.org/doi/10.1103/PhysRevC.97.055503`.

[156] K. Bodek, B. van den Brandt, T. Bryś, M. Daum, P. Fierlinger, P. Geltenbort, M. Giersch, P. Hautle, R. Henneck, M. Kasprzak, K. Kirch, J. A. Konter, G. Kühne, M. Kuźniak, K. Mishima, A. Pichlmaier, D. Rätz, A. Serebrov, and J. Zmeskal. An apparatus for the investigation of solid D with respect to ultra-cold neutron sources. *Nuclear Instruments and Methods in Physics Research Section A: Accelerators, Spectrometers, Detectors and Associated Equipment*, 533(3):491–504, 2004. ISSN 0168-9002. doi: http://dx.doi.org/10.1016/j.nima.2004.06.157. URL http://www.sciencedirect.com/science/article/pii/S0168900204015621.

[157] J. E. Jensen, R. B. Stewart, W. A. Tuttle, H. Brechna, and A. G. Prodell. *Selected Cryogenic Data Notebook*, volume 1. Brookhaven National Laboratory, 1980. BNL 10200-R.

[158] R. C. Zeller and R. O. Pohl. Thermal conductivity and specific heat of noncrystalline solids. *Phys. Rev. B*, 4:2029–2041, Sep 1971. doi: 10.1103/PhysRevB.4.2029. URL https://link.aps.org/doi/10.1103/PhysRevB.4.2029.

[159] R. Lermer and A. Steyerl. Investigation of ferromagnetic domains and bloch walls by very-low-energy neutron transmission. *Physica Status Solidi A*, 33 (2):531–541, 1976. ISSN 1521-396X. doi: 10.1002/pssa.2210330212. URL http://dx.doi.org/10.1002/pssa.2210330212.

[160] J. S. Laufer. High silica glass, quartz, and vitreous silica. *J. Opt. Soc. Am.*, 55(4):458–460, Apr 1965. doi: 10.1364/JOSA.55.000458. URL http://www.osapublishing.org/abstract.cfm?URI=josa-55-4-458.

[161] Georgius Agricola. *De Natura Fossilium, Book V. Quartz.* Froben, Basel, 1546.

[162] M. Roth. The small-angle scattering of neutrons by surface imperfections. *Journal of Applied Crystallography*, 10(3):172–176, Jun 1977. doi: 10.1107/S0021889877013181. URL https://doi.org/10.1107/S0021889877013181.

[163] R. F. Robbins and P. R. Ludtke. Review of static seals for cryogenic systems. *Journal of Spacecraft and Rockets*, 1:253, 1964.

[164] K. Rose. Metals in industry: Versatile indium. *Scientific American*, 170(4):154–156, April 1944. ISSN 0036-8733 (print), 1946-7087 (electronic). doi: http://dx.doi.org/10.1038/scientificamerican0444-154. URL http://www.nature.com/scientificamerican/journal/v170/n4/pdf/scientificamerican0444-154.pdf.

[165] R. B. Belser. A technique of soldering to thin metal films. *Review of Scientific Instruments*, 25(2):180–183, 1954. doi: 10.1063/1.1771017.

[166] M. H. Edwards. The index of refraction of liquid helium. *Canadian Journal of Physics*, 34(8):898–900, 1956. doi: 10.1139/p56-099. URL `http://dx.doi.org/10.1139/p56-099`.

[167] J. Willis. Low-temperature optical window seal used at 80° K. *Review of Scientific Instruments*, 29(11):1053–1053, 1958. doi: 10.1063/1.1716058.

[168] N. H. Horwitz and H. V. Bohm. Metal-to-glass vacuum seal for low temperatures. *Review of Scientific Instruments*, 32(7):857–858, 1961. doi: 10.1063/1.1717535.

[169] F. J. Smith, J. K. Smith, and S. P. McGlynn. Low temperature double path absorption cell. *Review of Scientific Instruments*, 33(12):1367–1371, 1962. doi: 10.1063/1.1717781. URL `http://dx.doi.org/10.1063/1.1717781`.

[170] F. R. Lipsett. Cold welded indium low temperature window seal. *Review of Scientific Instruments*, 37(2):229–229, 1966. doi: 10.1063/1.1720139.

[171] L. R. Lucas and H. P. Hernandez. Inflatable gasket for the 72-in. bubble chamber. *Review of Scientific Instruments*, 30(10):941–942, 1959. doi: 10.1063/1.1716391.

[172] B. M. Abraham and C. M. Falco. Demountable ^{4}He film stopper for dilution refrigerators. *Review of Scientific Instruments*, 47(2):253–254, 1976. doi: 10.1063/1.1134600. URL `http://dx.doi.org/10.1063/1.1134600`.

[173] R. R. Turkington and R. F. Harris-Lowe. Note on the design of simple indium O-ring seals. *Review of Scientific Instruments*, 55(5):803–805, 1984. doi: 10.1063/1.1137806.

[174] C. C. Lim. Indium seals for low-temperature and moderate-pressure applications. *Review of Scientific Instruments*, 57(1):108–114, 1986. doi: 10.1063/1.1139130.

[175] R. H. Haycock, S. Tritchew, and P. Jennison. Compact indium seal for cryogenic optical windows. *Proc. SPIE*, 1340:165–175, 1990. doi: 10.1117/12.23067. URL `http://dx.doi.org/10.1117/12.23067`.

[176] D. B. Fraser. Special indium seal for cryogenic use. *Review of Scientific Instruments*, 33(7):762–763, 1962. doi: 10.1063/1.1717959.

[177] K. Tamura, Y. Kimura, H. Suzuki, O. Kido, T. Sato, T. Tanigaki, M. Kurumada, Y. Saito, and C. Kaito. Structure and thickness of natural oxide

layer on ultrafine particle. *Japanese Journal of Applied Physics*, 42(12R): 7489, 2003. URL http://stacks.iop.org/1347-4065/42/i=12R/a=7489.

[178] Indium Corporation, 34 Robinson Rd, Clinton, NY 13323, USA.

[179] Malgorzata Kasprzak. *Ultracold Neutron Converters*. PhD thesis, Universität Wien, Vienna, Austria, 2008.

[180] Malgorzata Kasprzak. *Thermal up-scattering of very cold and ultra-cold neutrons in solid deuterium*. Master's thesis, Jagiellonian University, Krakow, Poland, 2004.

[181] D. Bondoux, H. G. Börner, V. Ermilov, J. P. Gonzales, E. Kulagin, S. Kulikov, E. Lelièvre-Berna, V. Melikhov, V. V. Nesvizhevsky, T. Soldner, F. Thomas, and E. Shabalin. Investigation of the energy accumulation rate in solid deuterium irradiated with fast electrons. *Nuclear Instruments and Methods in Physics Research Section A: Accelerators, Spectrometers, Detectors and Associated Equipment*, 606(3):637–644, 2009. ISSN 0168-9002. doi: https://doi.org/10.1016/j.nima.2009.04.026. URL http://www.sciencedirect.com/science/article/pii/S0168900209007815.

[182] Axel R. Müller. *Characterization of solid D_2 as source material for ultra cold neutrons and development of a detector concept for the detection of protons from the neutron decay*. PhD thesis, Technische Universität München, Munich, Germany, 2008.

[183] S. Ishimoto, T. Kobayashi, K. Morimoto, I. Nomura, A. Ozawa, S. Suzuki, Y. Takahashi, I. Tanihata, and T. Tsuru. Windowless solid hydrogen target. *Nuclear Instruments and Methods in Physics Research Section A: Accelerators, Spectrometers, Detectors and Associated Equipment*, 480(2):304–314, 2002. ISSN 0168-9002. doi: https://doi.org/10.1016/S0168-9002(01)00951-2. URL http://www.sciencedirect.com/science/article/pii/S0168900201009512.

[184] F. Atchison, B. Blau, K. Bodek, B. van den Brandt, T. Bryś, M. Daum, P. Fierlinger, A. Frei, P. Geltenbort, P. Hautle, R. Henneck, S. Heule, A. Holley, M. Kasprzak, K. Kirch, A. Knecht, J. A. Konter, M. Kuźniak, C.-Y. Liu, C. L. Morris, A. Pichlmaier, C. Plonka, Y. Pokotilovski, A. Saunders, Y. Shin, D. Tortorella, M. Wohlmuther, A. R. Young, J. Zejma, and G. Zsigmond. Cold neutron energy dependent production of ultracold neutrons in solid deuterium. *Phys. Rev. Lett.*, 99:262502, Dec 2007. doi: 10.1103/PhysRevLett.99.262502. URL https://link.aps.org/doi/10.1103/PhysRevLett.99.262502.

[185] A. Saunders, M. Makela, Y. Bagdasarova, H. O. Back, J. Boissevain, L. J. Broussard, T. J. Bowles, R. Carr, S. A. Currie, B. Filippone, A. García, P. Geltenbort, K. P. Hickerson, R. E. Hill, J. Hoagland, S. Hoedl, A. T. Holley, G. Hogan, T. M. Ito, S. K. Lamoreaux, C.-Y. Liu, J. Liu, R. R. Mammei, J. Martin, D. Melconian, M. P. Mendenhall, C. L. Morris, R. N. Mortensen, R. W. Pattie Jr., M. Pitt, B. Plaster, J. Ramsey, R. Rios, A. Sallaska, S. J. Seestrom, E. I. Sharapov, S. Sjue, W. E. Sondheim, W. Teasdale, A. R. Young, B. VornDick, R. B. Vogelaar, Z. Wang, and Yanping Xu. Performance of the Los Alamos National Laboratory spallation-driven solid-deuterium ultra-cold neutron source. *Review of Scientific Instruments*, 84(1):013304, 2013. doi: 10.1063/1.4770063. URL `https://doi.org/10.1063/1.4770063`.

[186] J. Karch, Yu. Sobolev, M. Beck, K. Eberhardt, G. Hampel, W. Heil, R. Kieser, T. Reich, N. Trautmann, and M. Ziegner. Performance of the solid deuterium ultra-cold neutron source at the pulsed reactor TRIGA Mainz. *The European Physical Journal A*, 50(4):78, Apr 2014. ISSN 1434-601X. doi: 10.1140/epja/i2014-14078-9. URL `https://doi.org/10.1140/epja/i2014-14078-9`.

[187] J. Kahlenberg, D. Ries, K. U. Ross, C. Siemensen, M. Beck, C. Geppert, W. Heil, N. Hild, J. Karch, S. Karpuk, F. Kories, M. Kretschmer, B. Lauss, T. Reich, Y. Sobolev, and N. Trautmann. Upgrade of the ultracold neutron source at the pulsed reactor TRIGA Mainz. *The European Physical Journal A*, 53(11):226, Nov 2017. ISSN 1434-601X. doi: https://doi.org/10.1140/epja/i2017-12428-9.

[188] A. Frei. Systembeschreibung JBU00: Die Quelle für ultrakalte Neutronen (UCN-Quelle) am FRM II. Systembeschreibung OPA00381, Forschungs-Neutronenquelle Heinz Maier-Leibnitz (FRM II), 2014.

[189] A. Frei. Betrieb einer Quelle zur Erzeugung ultrakalter Neutronen. Sicherheitsbericht OPA00524, Forschungs-Neutronenquelle Heinz Maier-Leibnitz (FRM II), 2017.

[190] M. Fukuhara, A. Sanpei, and K. Shibuki. Low temperature-elastic moduli, Debye temperature and internal dilational and shear frictions of fused quartz. *Journal of Materials Science*, 32(5):1207–1211, 1997. ISSN 1573-4803. doi: 10.1023/A:1018583918380. URL `http://dx.doi.org/10.1023/A:1018583918380`.

[191] A. Steyerl. A time-of-flight spectrometer for ultracold neutrons. *Nuclear Instruments and Methods*, 101(2):295–314, 1972. ISSN 0029-554X. doi: https://doi.org/10.1016/0029-554X(72)90204-2. URL `http://www.sciencedirect.com/science/article/pii/0029554X72902042`.

[192] P. Keil, D. Lützenkirchen-Hecht, and R. Frahm. Investigation of Room Temperature Oxidation of Cu in Air by Yoneda-XAFS. *AIP Conference Proceedings*, 882(1):490–492, 2007. doi: 10.1063/1.2644569. URL https://aip.scitation.org/doi/abs/10.1063/1.2644569.

[193] I. Platzman, R. Brener, H. Haick, and R. Tannenbaum. Oxidation of Polycrystalline Copper Thin Films at Ambient Conditions. *The Journal of Physical Chemistry C*, 112(4):1101–1108, 2008. doi: 10.1021/jp076981k. URL https://doi.org/10.1021/jp076981k.

[194] J. Evertsson, F. Bertram, F. Zhang, L. Rullik, L. R. Merte, M. Shipilin, M. Soldemo, S. Ahmadi, N. Vinogradov, F. Carlà, J. Weissenrieder, M. Göthelid, J. Pan, A. Mikkelsen, J.-O. Nilsson, and E. Lundgren. The thickness of native oxides on aluminum alloys and single crystals. *Applied Surface Science*, 349(Supplement C):826–832, 2015. ISSN 0169-4332. doi: https://doi.org/10.1016/j.apsusc.2015.05.043. URL http://www.sciencedirect.com/science/article/pii/S0169433215011617.

[195] I. Bespalov, M. Datler, S. Buhr, W. Drachsel, G. Rupprechter, and Y. Suchorski. Initial stages of oxide formation on the Zr surface at low oxygen pressure: An in situ FIM and XPS study. *Ultramicroscopy*, 159:147–151, 2015. doi: 10.1016/j.ultramic.2015.02.016. URL http://www.ncbi.nlm.nih.gov/pmc/articles/PMC4691236/.

[196] Yu. N. Pokotilovski. Effect of oxide films and structural inhomogeneities on transmission of ultracold neutrons through foils. *Eur. Phys. J. Appl. Phys.*, 73(2):20302, 2016. doi: 10.1051/epjap/2016150073. URL https://doi.org/10.1051/epjap/2016150073.

[197] D. E. O'Reilly and E. M. Peterson. Self-diffusion of liquid hydrogen and deuterium. *The Journal of Chemical Physics*, 66(3):934–937, 1977. doi: 10.1063/1.434001. URL https://doi.org/10.1063/1.434001.

[198] E. Guarini, M. Neumann, U. Bafile, M. Celli, D. Colognesi, S. Bellissima, E. Farhi, and Y. Calzavara. Velocity autocorrelation by quantum simulations for direct parameter-free computations of the neutron cross sections. II. liquid deuterium. *Phys. Rev. B*, 93:224302, Jun 2016. doi: 10.1103/PhysRevB.93.224302. URL https://link.aps.org/doi/10.1103/PhysRevB.93.224302.

[199] S. Döge, C. Herold, E. Gutsmiedl, C. Morkel, and P. Geltenbort. New experimental results for the scattering cross sections of liquid and solid deuterium for ultracold neutrons and an approach to their calculation. *ISINN-23 Conference Proceedings*, pages 119–130, 2016. URL http://isinn.jinr.ru/proceedings/isinn-23.html.

[200] B. Davison and J. B. Sykes. *Neutron Transport Theory*. Oxford University Press, 1958.

[201] C. L. Morris, J. M. Anaya, T. J. Bowles, B. W. Filippone, P. Geltenbort, R. E. Hill, M. Hino, S. Hoedl, G. E. Hogan, T. M. Ito, T. Kawai, K. Kirch, S. K. Lamoreaux, C.-Y. Liu, M. Makela, L. J. Marek, J. W. Martin, R. N. Mortensen, A. Pichlmaier, A. Saunders, S. J. Seestrom, D. Smith, W. Teasdale, B. Tipton, M. Utsuro, A. R. Young, and J. Yuan. Measurements of Ultracold-Neutron Lifetimes in Solid Deuterium. *Phys. Rev. Lett.*, 89:272501, Dec 2002. doi: 10.1103/PhysRevLett.89.272501.

[202] K. K. H. Leung, S. Ivanov, F. M. Piegsa, M. Simson, and O. Zimmer. Ultracold-neutron production and up-scattering in superfluid helium between 1.1 K and 2.4 K. *Phys. Rev. C*, 93:025501, Feb 2016. doi: 10.1103/PhysRevC.93.025501. URL `https://link.aps.org/doi/10.1103/PhysRevC.93.025501`.

[203] A. Serebrov, V. Mityukhlyaev, A. Zakharov, A. Kharitonov, V. Shustov, V. Kuz'minov, M. Lasakov, R. Tal'daev, A. Aldushchenkov, V. Varlamov, A. Vasil'ev, M. Sazhin, G. Greene, T. Bowles, R. Hill, S. Seestrom, and P. Geltenbort. Studies of a solid-deuterium source for ultra-cold neutrons. *Nuclear Instruments and Methods in Physics Research Section A: Accelerators, Spectrometers, Detectors and Associated Equipment*, 440(3):658–665, 2000. ISSN 0168-9002. doi: https://doi.org/10.1016/S0168-9002(99)01058-X.

[204] W. Mampe, L. N. Bondarenko, V. I. Morozov, Yu. N. Panin, and A. I. Fomin. Measuring neutron lifetime by storing ultracold neutrons and detecting inelastically scattered neutrons. *JETP Lett.*, 57:82–87, 1993. [Russian original: Письма в ЖЭТФ, 57, 77 (1993)].

[205] S. Arzumanov, L. Bondarenko, S. Chernyavsky, P. Geltenbort, V. Morozov, V.V. Nesvizhevsky, Yu. Panin, and A. Strepetov. A measurement of the neutron lifetime using the method of storage of ultracold neutrons and detection of inelastically up-scattered neutrons. *Physics Letters B*, 745 (Supplement C):79–89, 2015. ISSN 0370-2693. doi: https://doi.org/10.1016/j.physletb.2015.04.021. URL `http://www.sciencedirect.com/science/article/pii/S0370269315002646`.

[206] A. Serebrov, V. Varlamov, A. Kharitonov, A. Fomin, Yu. Pokotilovski, P. Geltenbort, J. Butterworth, I. Krasnoshchekova, M. Lasakov, R. Tal'daev, A. Vassiljev, and O. Zherebtsov. Measurement of the neutron lifetime using a gravitational trap and a low-temperature Fomblin coating. *Physics Letters B*, 605(1):72–78, 2005. ISSN 0370-2693. doi: https://doi.org/10.1016/j.physletb.2004.11.013. URL `http://www.sciencedirect.com/science/article/pii/S0370269304015552`.

[207] A. P. Serebrov, V. E. Varlamov, A. G. Kharitonov, A. K. Fomin, Yu. N. Pokotilovski, P. Geltenbort, I. A. Krasnoschekova, M. S. Lasakov, R. R. Taldaev, A. V. Vassiljev, and O. M. Zherebtsov. Neutron lifetime measurements using gravitationally trapped ultracold neutrons. *Phys. Rev. C*, 78:035505, Sep 2008. doi: 10.1103/PhysRevC.78.035505. URL `https://link.aps.org/doi/10.1103/PhysRevC.78.035505`.

[208] E. Kolomensky. PNPI Gatchina, Russia. 2017. priv. comm.

[209] E. A. Goremychkin and Yu. N. Pokotilovski. Neutron lifetime and density of states of fluoropolymers at low temperatures. *JETP Letters*, 105(8):548–551, Apr 2017. doi: 10.1134/S0021364017080045. URL `https://doi.org/10.1134/S0021364017080045`.

[210] Yu. N. Pokotilovski. Interaction of ultracold neutrons with liquid surface modes as a possible reason for neutron energy spread during long storage in fluid wall traps. *Physics Letters A*, 255(3):173–177, 1999. ISSN 0375-9601. doi: https://doi.org/10.1016/S0375-9601(99)00122-X. URL `http://www.sciencedirect.com/science/article/pii/S037596019900122X`.

[211] S. Chernyavsky. Kurchatov Institute, Moscow, Russia. 2015. priv. comm. and ILL experimental report 3-14-350.

[212] S. Döge et al. Measurement of the UCN/VCN cross sections of liquid and solid para-hydrogen, 2017. Institut Laue–Langevin, Grenoble, France, experimental report no. 3-14-370.

Acknowledgement

Keine Schuld ist dringender als die, Dank zu sagen.
— fake Cicero *quote created in the 21st Century*

Without the precious support of many scientists, technicians, colleagues and friends, as well as my parents Tilo and Kathrin, the work on this thesis would not have been possible. Therefore, I will try to name all those who helped my thesis to move forward in one way or another, and simply made my three and a half years at the Institut Laue–Langevin (ILL) worthwhile.

First and foremost, I extend my gratitude to Christoph Morkel of TU München for uncounted deep scientific discussions in Grenoble and Munich, Stephan Paul for being my official TU München thesis supervisor, Winfried Petry from FRM II for helping fund my PhD position and his interest in the progress of my thesis, and ILL director Helmut Schober for hosting and co-supervising me in Grenoble.

Over the course of the thesis work, I had the pleasure of meeting many scientists distinguished in the field of ultracold neutron scattering and thank them for sharing their knowledge and results with me, among others: Valery V. Nesvizhevsky (ILL), Alexander V. Strelkov, Yuri N. Pokotilovski, Alexander I. Frank, Egor V. Lychagin, Kirill N. Zhernenkov (all from JINR, Dubna), Sergey M. Chernyavsky (Kurchatov Institute, Moscow), Evady A. Kolomensky, Anatoly P. Serebrov (PNPI, Gatchina), Andreas Frei (TU München FRM II), and Albert Young and Ekaterina I. Korobkina (both from North Carolina State University). I also thank Ralf Engels of Forschungszentrum Jülich for fruitful discussions about deuterium and fomblin, and Eleonora Guarini of Università degli Studi di Firenze for providing me with the diffusion constant and Einstein frequency of liquid deuterium based on her group's quantum simulations.

For help with additional experiments, I am indebted to Yuliya E. Gorshkova (AFM measurements at JINR, Dubna), Michael Schneider of Swiss Neutronics (AFM measurements), and Bernhard Lauss and Nicolas Hild from Paul Scherrer Institut (Raman measurements of deuterium).

Thanks is also due to my summer students and interns Henrik Thoma (2015, TU München) and Pierre Rambourg (2016, ENS des Mines de Nantes); and especially to George Chappell (2016, University of Bath) for his programming support and help during the legendary fomblin incident (which followed the measurement presented in Fig. A.2), and to Jürgen Hingerl (2016-17, TU München) for mechanical drawings, computer simulations and support during three reactor cycles.

Valuable advice and support in optimizing the cryostat and gas-handling system was provided to me by members of the ILL Cryogénie group: Xavier Tonon, Eric Bourgeat-Lami, Olivier Losserand, Simon Baudoin, and Eddy Lelièvre-Berna.

I am also grateful to ILL technicians Didier Berruyer and Thomas Brenner for machining parts for my experiments and logistical support. Furthermore, I thank Peter Hartung of Ludwig-Maximilians-Universität Munich for the original mechanical drawings of the cryostat.

For three and a half years, I enjoyed the hospitality of the Nuclear and Particle Physics group at ILL and thank group leader Oliver Zimmer for discussions and Michael Jentschel for general advice on my thesis work and his support with optical measurements.

The instrument scientists of PF2 (the Turbine), Tobias Jenke and Peter Geltenbort, provided general support to this thesis work.

During the past two years of my PhD research, I enjoyed the company of PhD and undergraduate students from TU Wien. For many memorable night shifts at the Turbine on Level D and uncountable pizzas "Chez Emilie", I am grateful to Tobias Rechberger, Joachim Bosina, Jakob Micko, Richard Wagner, and Peter Salajka.

My special thanks goes out to Christoph Morkel, Dennis Wilmsen, Helmut Schober, and Tobias Jenke for taking the time to proof-read the manuscript with a critical eye.

The PhD contract covering most of the work on this thesis was co-financed by the Institut Laue–Langevin in Grenoble (France) and the Forschungsneutronenquelle Heinz Maier-Leibnitz (FRM II) in Munich (Germany). Other parts of this thesis benefited from financial support by TU München Physik-Department E18, TU München Graduate School, Leonhard-Lorenz-Stiftung Munich under grants no. 930/16 and 940/17, Deutscher Akademischer Austauschdienst (DAAD), and the Russian Fond for Basic Research under grant no. РФФИ 17-32-50024-мол-нр.

The majority of the experimental equipment used for this thesis was provided and/or paid for by TU München Physik-Department E18, FRM II, the group of Peter Fierlinger (TU München Universe Cluster), and the ILL.